



**INSTITUTO POTOSINO DE INVESTIGACIÓN
CIENTÍFICA Y TECNOLÓGICA, A.C.**

POSGRADO EN CIENCIAS APLICADAS

**Hierarchy in 1D Carbon Nanostructures:
*from theoretical design and properties calculation
to experimental synthesis and characterization***

Tesis que presenta

José Manuel Romo Herrera

Para obtener el grado de

Doctor en Ciencias Aplicadas

En la opción de

Nanociencias y Nanotecnología

Codirectores de la Tesis:

Dr. Mauricio Terrones Maldonado

Dr. Humberto Terrones Maldonado

Dr. Vincent Meunier

San Luis Potosí, S.L.P., Febrero de 2008

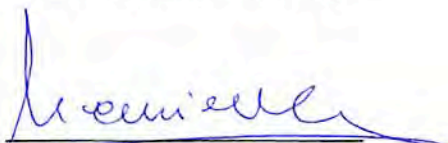


Constancia de aprobación de la tesis

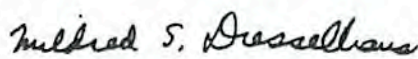
La tesis "**Hierarchy in 1D Carbon Nanostructures: *from theoretical design and properties calculation to experimental synthesis and characterization***" presentada para obtener el Grado de Doctor en Ciencias Aplicadas en la opción de Nanociencias y Nanotecnología fue elaborada por **José Manuel Romo Herrera** y aprobada el **25 de Febrero de 2008** por los suscritos, designados por el Colegio de Profesores de la División de Materiales Avanzados del Instituto Potosino de Investigación Científica y Tecnológica, A.C.

Dr. Mauricio Terrones Maldonado
(Codirector de la tesis)

Dr. Humberto Terrones Maldonado
(Codirector de la tesis)



Dr. Vincent Meunier
(Codirector de la tesis)



Dr. Mildred Dresselhaus
(Sinodal externo)



Créditos Institucionales

Esta tesis fue elaborada en el Laboratorio de (Nombre del Laboratorio) de la División de Materiales Avanzados para la Tecnología Moderna del Instituto Potosino de Investigación Científica y Tecnológica, A.C., bajo la codirección de los doctores Mauricio Terrones Maldonado, Humberto Terrones Maldonado y Vincent Meunier.

Durante la realización del trabajo el autor recibió una beca académica del Consejo Nacional de Ciencia y Tecnología (No. de registro 182403) y del Instituto Potosino de Investigación Científica y Tecnológica, A. C.



IPICYT

Instituto Potosino de Investigación Científica y Tecnológica, A.C.

Acta de Examen de Grado

El Secretario Académico del Instituto Potosino de Investigación Científica y Tecnológica, A.C., certifica que en el Acta 024 del Libro Primero de Actas de Exámenes de Grado del Programa de Doctorado en Ciencias Aplicadas en la opción de Nanociencias y Nanotecnología está asentado lo siguiente:

En la ciudad de San Luis Potosí a los 25 días del mes de febrero del año 2008, se reunió a las 10:00 horas en las instalaciones del Instituto Potosino de Investigación Científica y Tecnológica, A.C., el Jurado integrado por:

Dr. Mauricio Terrones Maldonado	Presidente	IPICYT
Dr. Humberto Terrones Maldonado	Secretario	IPICYT
Dr. Florentino López Urías	Sinodal	IPICYT
Dra. Mildred S. Dresselhaus	Sinodal externo	MIT, E.U.A.
Dr. Vincent Meunier	Sinodal externo	ORNL, E.U.A.
Dra. Yadira Itzel Vega Cantú	Sinodal	IPICYT

a fin de efectuar el examen, que para obtener el Grado de:

**DOCTOR EN CIENCIAS APLICADAS
EN LA OPCIÓN DE NANOCIENCIAS Y NANOTECNOLOGÍA**

sustentó el C.

José Manuel Romo Herrera

sobre la Tesis intitulada:

Hierarchy in Carbon Nanostructures: from theoretical design to experimental synthesis and characterization

que se desarrolló bajo la dirección de

Dr. Humberto Terrones Maldonado
Dr. Mauricio Terrones Maldonado
Dr. Vincent Meunier (Oak Ridge National Laboratory)

El Jurado, después de deliberar, determinó

APROBARLO

Dándose por terminado el acto a las 12:55 horas, procediendo a la firma del Acta los integrantes del Jurado. Dando fé el Secretario Académico del Instituto.

A petición del interesado y para los fines que al mismo convengan, se extiende el presente documento en la ciudad de San Luis Potosí, S.L.P., México, a los 25 días del mes de febrero de 2008.

L.C.C. Ivonne Lizette Cuevas Velez
Jefa del Departamento de Asuntos Escolares

Dr. Marcial Bonilla Marín
Secretario Académico



Agradecimientos

Una tesis de Doctorado ... se puede ver como un documento, un requisito más que cumplir para la obtención del grado, la compilación de cuatro años de trabajo, aportaciones científicas, la propuesta de una nueva línea de investigación, el cierre de una etapa en la vida personal y hasta como la culminación de una larga formación académica ... cual de todas ellas es mi manera de verla? ... no lo se, me supongo que en distintos momentos cada una de ellas ha pasado por mi mente ... lo que si puedo decir es que no ha resultado tarea sencilla y sin lugar a dudas no imagino poder haber terminádola sin el apoyo y ayuda de tanta pero tanta gente que de una u otra manera han sido parte de estos cuatro años y medio de trabajo.

Más que agradecer, comienzo compartiendo este logro con mi Familia sin la cual esta experiencia nunca hubiera comenzado y mucho menos llegado a un buen final. A mi Madre y mi Padre, quienes siempre han estado ahí para animarnos y motivarnos a seguir creciendo por cualquiera que sea el rumbo que elijamos y para apoyarnos en cada uno de nuestros tropiezos, y hablo en plural porque siempre lo han hecho con cada uno de sus tres hijos por igual. Gracias por siempre brindarnos esa fuente de seguridad llamada hogar. Gracias Charlie y Diana por siempre estar ahí, para pelearnos, regañarnos y después reir y apoyarnos.

Y si a alguien se le debe este logro es sin lugar a dudas a mis asesores. Gracias Dr. Mauricio Terrones ... gracias Dr. Humberto Terrones ... gracias Dr. Vincent Meunier ... por la oportunidad, los proyectos asignados, el apoyo académico y económico, gracias por el tiempo brindado a mi formación y por cada uno de los conocimientos compartidos. Parece que fue ayer cuando hace cinco años comenzaba a contemplar la posibilidad de hacer el postgrado en nanotecnología y el hecho de poder combinar "teoría y experimento" era una inquietud a la cual no quería renunciar. La recomendación principal era el extranjero, pero se comenzaba a hablar de dos jóvenes investigadores que comenzaban como pioneros a desarrollar el área en el país. Recuerdo haberme sorprendido gratamente cuando al leer algunos de sus trabajos encontré justo lo que buscaba, experimento y teoría complementados en el estudio de nanoestructuras. Tan grato ese recuerdo, como la impresión causada por el Dr. Mauricio Terrones cuando decidí venir a conocer el instituto, quien a su más puro estilo de torbellino en medio de 20 000 proyectos por concluir se dio tiempo para recibir al escuincle de 23 años, con su muy característica amabilidad y sentido de motivación logró convencerme de regresar a hacer maletas para comenzar esta aventura que terminaría cinco años más tarde con la obtención de este grado académico. Después del primer año de materias ya trabajábamos el protocolo para la propuesta de proyecto Doctoral bajo la supervisión del Dr. Mauricio y el Dr. Humberto y finalmente medio año después llegaría la colaboración con el Dr. Vincent Meunier quien se incorporaría a mi comité de coasesores ... académicamente no había más que uno pudiera pedir: experto en síntesis y

caracterización, experto en diseño de estructuras y cristalografía, y experto en cálculos teóricos todo alrededor de nanoestructuras de carbono. Si bien es cierto que tengo que agradecerles todo mi crecimiento académico durante estos cuatro años y medio ... agradezco más aún el haber estado trabajando a lado de seres humanos como los tres siempre lo demostraron ... gracias Mauricio, gracias Humberto, gracias Vincent ... y gracias también por todos esos detalles de apoyo brindados más allá del terreno laboral ... gracias Mauricio.

Mucho del trabajo presentado en este proyecto ha sido gracias a todo un grupo de trabajo detrás, comenzando por los incansables: Daniel, Grisel, Lisette y Gabi siempre al pie del cañón con su característica eficiencia ... pasando por cada uno de mis compañeros de trabajo: Lalo, Ana Laura, Zamudio, Julio, Andres, Jessica y Aarón. Así como consejos, asesoría y discusiones del Dr. Florentino López, Dr. Emilio Muñoz, Dra. Yadira Vega y Dr. Fernando Rodríguez. Así como enriquecedoras discusiones con Samuel y Jaime. Cada uno de ellos en menor o mayor medida son partícipes del crédito correspondiente a todos los resultados presentados en este documento.

Gracias a estar en un grupo de investigación como el de los Hermanos Terrones me permitió realizar estancias de investigación en grupos colaboradores para el desarrollo del presente proyecto. Gracias al Dr. Vincent Meunier y el Dr. Bobby Sumpter por su asesoría durante las estancias en Oak Ridge National Laboratory, en Tennessee EUA; así como a los compañeros y amigos conocidos como Sefa Dag y Dominic Biava. Gracias al Prof. David Smith y la Dra. Molly McCarthy por recibirme en Arizona State University, en Tempe Arizona EUA; así como a David Cullen por su colaboración y amistad brindada durante la visita.

Esta etapa de formación académica fue fuertemente enriquecida también por el grupo del Prof. Manfred Rühle en Max-Planck-Institut für Metallforschung en Stuttgart Alemania, gracias Fabio Lupo por la amistad y apoyo brindado; gracias Paul, Saso, Elena y Vesna. Así como por la visita al grupo de la Prof. Mildred Dresselhaus en Massachusetts Institute of Technology, gracias Prof. Millie por el tiempo, interés, consejos e ideas brindadas a mi investigación; gracias Xiaoting por tu eficiencia y gran disponibilidad. Gracias Federico, Mario, Alfonso y Hootan por su hospitalidad y discusiones.

Así mismo agradezco al grupo de colaboradores del Prof. Ruiz en el Instituto de Física de la UASLP, en especial a Edgar, gracias por la disposición y el trabajo duro siempre puesto a los proyectos en común.

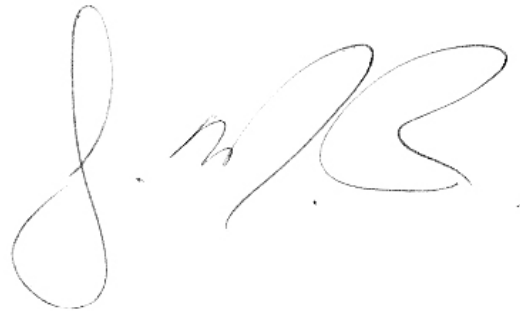
Muchas gracias también a Paola Ayala, por haber sido parte de esta etapa de formación académica.

No quisiera dejar pasar la oportunidad para agradecer al Dr. Ernesto Cota, el Dr. Fernando Rojas, el Dr. Jesús Antonia Díaz, el Dr. Eugenio Méndez y el Dr. Roberto Vázquez, por haberme brindado las herramientas básicas lo suficientemente sólidas en mi etapa de formación básica durante la Licenciatura, y quienes sin lugar a dudas contribuyeron como fuente de motivación y ejemplos de rectitud en distintas áreas de la investigación científica. Y bueno que decir de mi

Padre, sin quien seguramente nunca hubiera nacido mi interés por la investigación científica.

Al final del día es una etapa de vida la que comprende un Doctorado y a través de ella he tenido la oportunidad de conocer y compartir momentos de todo tipo con muy buenas personas ... gracias a todos y cada uno de ustedes que bien saben quienes son y prefiero omitir enlistarlos para evitar cualquier tipo de injusticia que mi memoria y torpeza seguramente ocasionarían. Gracias por todos los buenos y no tan buenos momentos que compartimos juntos, por todas las fiestas, viajes, risas, preocupaciones y experiencias de vida compartidas durante esta etapa.

... y solo concluir con un par de frases que he escuchado por ahí, quizás con palabras un poquitín más altisonantes en su versión original, pero bueno palabras más palabras menos, algunos dicen por ahí que “no cualquier ‘tonto’ llega a ser Doctor” pero quizás yo me quedo más con la que dice que “lo Doctor no nos quita lo ‘tonto’”.

A handwritten signature in black ink, consisting of a large, stylized initial 'J' followed by a series of loops and flourishes that suggest the name 'J. M. B.' or similar.

Acknowledgements

More than to thank for, I should start sharing this achievement with my Family, without them this experience never would have started and a successful ending would had been impossible. To my Mother and Father, who always have been there to cheer us up and motivate us to keep growing through which ever is the way that we had choosen, and to support us in every obstacle. Thanks for always provide us with that safety source called home. Thanks Charlie and Diana for always being there to fight, to argue, and then laugh and help.

This achievement is totally owed to my advisors. Thanks Dr. Mauricio Terrones, thanks Dr. Humberto Terrones, thanks Dr. Vincent Meunier for the opportunity, the asigned projects, the academic and economic support, thanks for all the time provided to my education and for every single knowledge shared with me. Thanks to Dr. Mauricio and Dr. Humberto for generating the possiblity to work in a theory-experiment project. Thanks for supply me with a first level advisors team and all the working needs. But I thank the most to have had the opportunity to work along three human beings, as you always behaved ... thanks Mauricio, thanks Humberto, thanks Vincent.

Most of the work presented here is thanks to a whole group of people, starting from the always hard workers: Daniel, Grisel, Lisette and Gabi always ready with their characteristic efficiency ... as well as each of my groupmates: Lalo, Ana Laura, Zamudio, Julio, Andres, Jessica y Aarón. Similarly, thanks to advises, and discussions with Dr. Florentino López, Dr. Emilio Muñoz, Dra. Yadira Vega and Dr. Fernando Rodríguez. Thanks for fruitful discussions to Samuel and Jaime too. Every single one of them is participant of the credit from all the results presented in this document.

The Terrones group collaborations allowed to perform part of this project in foreign research groups. Thanks Dr. Vincent Meunier and Dr. Bobby Sumpter for their advises during my academic stays at Oak Ridge National Laboratory; thanks to Sefa Dag and Dominic Biava. Thanks to Prof. David Smith and Dra. Molly McCarthy for receving me in Arizona State University in a characterization stay; thanks so much to David Cullen for his efficient collaboration and the friendship provided.

This academic formation stage was also strongly enriched by Porf. Manfred Rühle group at Max-Planck-Institut für Metallforschung, thanks Fabio Lupo for all the support and the friendship provided; thanks Paul, Saso, Elena and Vesna. And for the visit to Prof. Mildred Dresselhaus group at Massachusetts Institute of Technology, thanks Prof. Millie for all the time, interest, advises and ideas provided to my reserach; thanks Xiaoting for all your great availability and efficiency. Thanks Federico, Mario, Alfonso and Hootan for the hospitality and fruitful discussions.

I also thank to the collaborator group from Prof. Ruiz at Instituto de Física from UASLP, specially to Edgar, thanks for all your hard work and interest always put to our common projects.

Thanks so much to Paola Ayala, she certainly was part of this academic formation stage.

I could not miss the opportunity to say thanks to Dr. Ernesto Cota, Dr. Fernando Rojas, Dr. Jesús Antonio Díaz, Dr. Eugenio Mendez and Dr. Roberto Vazquez, since they provided me with all the solid enough basic tools during my undergraduate formation, and without a doubt, who contributed as a motivation source and honesty examples in different lines from scientific research. And of course, to my Dad, without whom the scientific research interest never would have been born in me.

At the end of the road, a Ph.D. is a life stage and through it I have had the opportunity to meet and share all kind of moments with very good people ... thanks to every single of you, you perfectly know who you are and myself prefer to omit listing you to avoid any type of injustice that my stupidity and memory would probably cause. Thanks for every single good and not so good moment that we share together, for all the parties, travels, laughs, worries and life experiences shared during this stage.

Sincerely, Thanks so much ...

Pepe
(J.M.Romo-Herrera)

Contents

Agradecimientos	ix
Acknowledgments	xiii
Abstract	xxiii
Resumen	xxv
Chapter 1: General Introduction	1
1.1 Basic Idea: Hierarchy and 1D building blocks.	2
1.2 2D and 3D ordered arrays from biological and 0D (clusters) building blocks.	4
1.3 1D building blocks: from isolated devices to their strategic assembly.	7
1.4 Carbon nanotubes as building blocks	9
1.4.1 Geometrical properties.	9
1.4.2 Electronic properties.	9
1.4.3 Mechanical properties	10
1.4.4 Coalescence of CNTs	10
1.4.5 Review of CNTs synthesis.	11
1.5 Contributions of the present Ph.D. work.	12
References	14
Chapter 2: 2D and 3D Ordered Networks based on 1D nanostructures: <i>from design to properties calculations</i>	17
2.1 Hierarchy algorithm	19
2.1.1 SuperSquare network	19
2.1.2 SuperGraphene network.	20
2.1.3 SuperCubic network	20
2.1.4 SuperDiamond network	20
2.1.5 Computational and conceptual tools.	22
2.2 Stability of the ON-CNTs	23
2.2.1 Configuration energy calculations	23
2.2.2 Experimental observations.	27
2.3 Quantum conductance.	28
2.3.1 2D ON-CNTs: <i>SuperSquare and SuperGraphene</i>	28
2.3.2 3D ON-CNTs: <i>SuperCubic and SuperDiamond</i>	31
2.4 Mechanical properties	35
2.4.1 Volumetric compression	35
2.4.2 Axial compression	37
2.5 Surface area.	40
Appendix: <i>Calculation Methods</i>	43
References	53
Chapter 3: Defects engineering in ON-CNTs: <i>guiding current</i>	55
3.1 Introduction	57
3.2 Effect of one Stone-Wales (SW) defect in a perfect CNT	59

3.2.1 One SW and its implications at the eigen channel level	59
3.2.2 Different types of SWs produces different eigen channel behavior	64
3.2.3 Increasing the amount of SWs.	66
3.3 Proposal of patch of defects (Haeckelite) in ON-CNTs	70
3.4 Enhancement of current through specific paths.	71
3.4.1 One Stone Wales case.	73
3.4.2 Asymmetric effect	76
3.4.3 Enhancement of specific path	78
3.5 Conclusions	86
References	87

Chapter 4: CVD synthesis of CNT junctions and its Branching **89**

Mechanism	
4.1 Introduction	91
4.1.1 Reviewing the literature	92
4.2 Experimental setup	93
4.2.1 Experimental method	93
4.2.2 Characterization techniques	95
4.3 CNT junctions results and discussion	95
4.3.1 Materials obtained in the external zone of the reactor.	95
4.3.2 Material collected from the thermic insulator #1 zone (TI1)	98
4.3.2.1 Tree –like branches and Y junctions	98
4.3.2.2 Metallic balls entangled with carbon nanofibres	99
4.3.3 Effects of catalysts in the branching morphology	104
4.3.3.1 Termination of CNTs when using Fe as catalyst.	105
4.3.3.2 CNTs junctions	107
4.3.4 Effects of flow rates (thiophene concentration)	111
4.3.4.1 Minimum Ar flux through thiophene	111
4.3.4.1.a Random networks of 1D carbon blocks	111
4.3.4.1.b Micro tubular Junctions	112
4.3.4.2 Medium Ar flux through thiophene	114
4.3.4.2.a Micro Patterns	114
4.3.4.2.b Sea urchin –like nanostructures	115
4.3.5 Summary of junctions produced.	118
4.4 Branching Mechanism.	119
4.4.1 Type of junctions	119
4.4.2 Experimental and theoretical evidence	120
4.4.2.1 Detailed characterization at the branching points	120
4.4.2.2 DFT calculations: The importance of sulfur	122
4.4.2.3 HRTEM observations.	124
4.4.3 Branching Mechanism and discussion.	125
4.5 Conclusions	126
4.6 Open Issues.	127
Calculation Methods.	127
References	128

Chapter 5: 1D Superlattices: nitrogen doped and undoped segments	131
5.1 Introduction	133
5.2 Experimental setup	135
5.2.1 Experimental device	135
5.2.2 Experimental method	136
5.2.3 Characterization techniques	136
5.3 Calibration experiments.	137
5.3.1 Temperature and carrier flux.	137
5.3.2 Reaction time	139
5.4 1D Superlattices.	146
5.4.1 Interface between two segments.	146
5.4.1.a Continuity along CNTs	147
5.4.1.b Elbow structure.	149
5.4.2 Analytical (EDX) measurement	152
5.4.3 Multiple segments	155
5.4.4 Failed experiments.	156
5.5 Conclusions	157
References	158
Perspectives	161
Reserach Articles	162

List of Tables

2.i	Stability energy values obtained using DFT calculations	24
2.ii	Stability energy values obtained using.	24
2.iii	Porosity and surface area values calculated for the ON-CNTs	40
3.i	Conductance values at the eigenchannel level for strategic energy values	60
3.ii	Conductance values at the eigenchannel level for the different type of SW cases	66
3.iii	Conductance values at the eigenchannel level as the amount of SWs is increased	68

List of Figures

1.1 Schematic representation of the core idea of the thesis	3
1.2 Networks from biological building blocks.	4
1.3 Networks from 0D building blocks (atomic clusters)	6
1.4 Ordered arrays from 1D building blocks	8
2.1 Illustration of Hierarchy algorithm	21
2.2 The nine constructor blocks to build the ON-CNTs	22
2.3 Configuration energy values per atom for each ON-CNT	23
2.4 Local strain energy on the nodes conforming the 2D networks	25
2.5 Local strain energy on the nodes conforming the 3D networks	26
2.6 Experimental junctions obtained by CVD	27
2.7 Conductance, electronic density of states, structure and defect positions for SS blocks	28
2.8 Conductance, electronic density of states, structure and defect positions for SG blocks	30
2.9 Conductance, electronic density of states, structure and defect positions for SC blocks	31
2.10 LDOS of the (6,6) SC block.	32
2.11 Conductance, electronic density of states, structure and defect positions for SD blocks	33
2.12 Architecture dictates the final electronic and conductance properties.	34
2.13 Volumetric compression applied to the 3D networks	36
2.14 Strain energy vs axial strain for the 3D ON-CNTs.	37
2.15 Rigidity or flexibility of the networks imposed by the architecture	38
2.16 Rigidity along the [111] axial compression of the SD network.	39
2.17 Illustration of the van der Waals and Connolly surface area	41
3.1 One and none SW on (6,6) CNT conductance and DOS graphs	59
3.2 Scattered wave function at the eigenchannel level on the (6,6) CNT	61
3.3 Schematic explanation of the symmetry argument governing the scattering process in a SW defect	63
3.4 The two inequivalent SW positions along an armchair CNT.	64
3.5 DOS and conductance graphs of the inequivalent SW cases.	65
3.6 DOS and conductance graphs as the amount of SW is increased	67
3.7 LDOS plot of the (6,6) CNT as the amount of SWs is increased	67
3.8 LDOS and scattered wave plot as the amount of SWs is increased showing a delocalization of the quasibound charge into rings.	68
3.9 LDOS and scattered wave plot of the 4SW case	69
3.10 Proposal of patch of defects strategically located along a ON-CNT.	70
3.11 The hybrid blocks designed from the (6,6) SG building block.	71
3.12 Conductance and DOS graphs of the (6,6) SG hybrid blocks.	72
3.13 Schematic illustration of the one by one SW incorporation	73
3.14 The two inequivalent positions for one SW in a (6,6) SG block.	73
3.15 DOS and conductance for one SW case in a (6,6) SG block	74
3.16 LDOS for one SW case in a (6,6) SG block	75

3.17 SW positions at the sides of the superbond to produce asymmetries in the conduction.	76
3.18 Analysis of the conductance peaks appearing due to asymmetries.	77
1.19 Analysis of the assymmetric 5SW case.	78
3.20 Analysis of the conductance enhancement by incorporation of SWs by rings (4SWs at each ring)	79
3.21 Analysis of the conductance enhancement by incorporating one by one SWs	80
3.22 Patch of defects effect: <i>Charge delocalization</i>	82
3.23 Analysis of the current guiding at the eigenchannel level due to the defects positions	84
3.24 Analysis of the current guiding at the eigenchannel level due to the defects positions	85
4.1 Experimental setup and temperature zones definition	94
4.2 SEM and TEM of the material obtained from the exterior zone.	96
4.3 TEM and EDX of the carbon spheres showing roudness as function of Ni presence	97
4.4 SEM from the tree branches –like material	98
4.5 SEM from the carbon fibres entanglement with Ni particles	99
4.6 TEM from the carbon fibres.	100
4.7 TEM from the Ni particles.	101
4.8 EDX elemental map showing Ni balls with S composition	102
4.9 EDX high resolution line scans on metallic particles	102
4.10 HRTEM from metallic particles	103
4.11 HRTEM showing the interface between two different crystalline domain coexisting in the metallic particle.	103
4.12 SEM images of metallic spheres coated by CNTs	104
4.13 Termination of CNTs when Fe and S are present in the system	105
4.14 EDX high resolution line scan of the metallic particle trapped at the CNTs tip.	106
4.15 CNTs Y-junctions	107
4.16 Concentric cylinders structure of the Y-junctions obtained	108
4.17 EDX high resolution line scan of the Y-junction and its catalyst	108
4.18 Detailed HRTEM analysis of a catalyst particle trapped right at the junction point	109
4.19 SEM of random networks composed of carbon microtubes	111
4.20 SEM of Carbon microtube junctions with different geometries	112
4.21 TEM of the carbon microtube junctions, showing layered material.	112
4.22 EDX high resolution linescan showing S content on the microtubes.	113
4.23 SEM images showing micropattern of flakes composed by different type of nanostructures	114
4.24 SEM of sea urchin –like nanostructures entangled with C fibres.	115
4.25 TEM and HRTEM with the structure of the sea urchin –like material.	116
4.26 EELS elemental mapping of the sea urchin –like material	116
4.27 EDX high resolution line scans of the metallic particle in the sea urchin –like material.	117
4.28 HRTEM of the metallic particle in the sea urchin –like material.	117

4.29	Types of junctions and synthesis conditions	118
4.30	General morphology of the cone stacked Y junctions	119
4.31	High resolution characterization of the branching point.	121
4.32	Sulfur role in the Branching Mechanism	123
4.33	HRTEM characterization of a developing Y-junction	124
4.34	Schematic illustration of the Branching Mechanism.	125
5.1	Experimental setup to perform intermitent-CVD.	135
5.2	Most efficient carrier flux and temperature parameters	137
5.3	CNTs length dependence on the temperature.	139
5.4	General morphology of CNx sample as function of the reaction time.	140
5.5	General morphology of MW sample as function of the reaction time	141
5.6	CNTs length dependence on the reaction time	142
5.7	CNTs diameters distribution as function of the reaction time	144
5.8	Schematic representation of the growth mechanism of CNTs by aerosol CVD	145
5.9	Low mag SEM of the interface between the CNx-MW interface	146
5.10	Higher mag SEM of the interface between the CNx-MW interface	147
5.11	Diameters distribution along the CNx-MW interface	148
5.12	Elbow –like defects observed at the CNx-MW interface zone	149
5.13	TEM of the elbow –like structure	150
5.14	HRTEM along the elbow –like zone.	151
5.15	EDX analysis before and after the CNx-MW interface	152
5.16	Schematic representation of the kinetics in the CNTs flakes growth.	153
5.17	EDX measurements showing a nitrogen doping gradient along the CNTs axis.	154
5.17	SEM and EDX analysis of multiple segments CNTs arrays	155
5.18	Representative results illustrating failed experiments.	156

Abstract

A key challenge in nanotechnology is the assembly of nanostructured components (**building blocks**; such as DNA molecules, 0D clusters and 1D nanowires) into well ordered arrays. Based on this research trend, the core proposal of the present Ph.D. work has been to use 1D nanostructures as building blocks (e.g. nanowires and nanotubes) to design and synthesize 1D superlattices as well as 2D and 3D networks.

These assembled arrays can be seen as a new type of material at the microscale, exhibiting characteristic properties tuned up by the building block properties and their specific architectures. Unfortunately, little was known regarding the different ways networks can be created and their physico-chemical properties as a function of their architecture. In this context, a general algorithm (Hierarchy algorithm) to design and generate ideal models (xyz coordinates) of networks from 1D nanostructures (e.g. nanowires or nanotubes) as building blocks was proposed [1].

An emphasis is made on carbon nanotubes (CNTs) as building blocks, since they possess highly desirable properties: an extremely high Young's modulus and remarkable flexibility, could behave as ballistic conductors or semiconductors, possess high surface area and coalesce with each other under appropriate conditions.

The Hierarchy algorithm was applied to CNTs to design a set of Ordered Networks based on CNTs (ON-CNTs) to study in detail the physico-chemical properties of the networks (electronic transport, mechanical, porosity and surface area properties) as a function of their architecture. This revealed outstanding mechanical properties, together with selective electronic conductance paths [2], complemented by low mass densities, high surface areas, and continuous porosity; where the properties were largely dominated by the specific architecture [1]. A subsequent study focuses on electronic nanocircuits, exploiting the advantage that ON-CNTs offer when including nanowires and nanodevices all self-integrated within the network. It is shown that arrays containing topological defects (non hexagonal rings in the sp^2 carbon network composing the CNTs) can perform as intradevices to guide current along specific trajectories, thus showing ON-CNTs as potential organic nanocircuits working as addressable arrays [3].

In the experimental part of the thesis, the details of the node formation is necessary towards the synthesis of CNTs networks. Therefore, a full study on the CNT branching phenomena has been performed, including CNT junction synthesis and detailed high-resolution characterization which was complemented with first principles density functional theory calculations. Here, the Branching Mechanism of CNTs at the atomistic level by the presence of sulfur atoms is elucidated [4]. The CVD synthesis work, turned out with five different types of covalent Y-junctions, when different experimental conditions were used (amount of sulfur source or type of catalyst) [5].

Finally a synthesis study is presented to obtain 1D Superlattices (1D structures composed of axially alternated segments) using nitrogen-doped and undoped CNTs as building blocks [6]. The characterization of these structures

exhibited how continuous CNTs can be obtained with nitrogen-doped segments and undoped segments of variable lengths. The synthesis method should motivate further experimental work exploring the electronic properties of this type of material.

These results together try to illustrate the intriguing field of “*playing LEGO*” with 1D nanostructures, to motivate research work with the vast range of combinations that building block composition, length and diameter, architecture type and dimensionality offer to explore with creativity and scientific knowledge.

[1] Romo-Herrera, J.M., Terrones, M., Terrones, H., Dag, S. & Meunier, V. "Covalent 2D and 3D Networks from 1D Nanostructures". **NanoLetters** **7(3)**: 570-576 (2007).

[2] Romo-Herrera, J.M., Terrones, M., Terrones, H. & Meunier, V. "Transport properties of ordered networks based on carbon nanotubes (ON-CNTs)". (submitted).

[3] Romo-Herrera, J.M., Terrones, H., Terrones, M., & Meunier, V. "Defects engineering in ON-CNTs: guiding current". (to be submitted).

[4] Romo-Herrera, J.M., Sumpter, B.G., Cullen, D.A., Terrones, H., Cruz-Silva, E., Smith, D.J., Meunier, V. & Terrones, M. "An Atomistic Branching Mechanism for Carbon Nanotubes: Sulfur as triggering agent". (in press; **Angewandte Chemie**).

[5] Romo-Herrera, J.M., Cruz-Silva, E., Cullen, D.A., Terrones, H., Smith, D.J. & Terrones, M. "Temperature gradient and flux effect effect in the Pyrolysis of Thiophene and Nickelocene: from sea urchin -like nanostructures to five different types of Y-junctions". (to be submitted).

[6] Romo-Herrera, J.M., Zamudio, A., Cruz-Silva, E., Cullen, D.A., Smith, D.J., Terrones, H., Terrones, M., "1D Superlattices from nitrogen-doped and undoped CNTs segments". (in progress).

Resumen

El ensamblaje de componentes nanoestructurados (*bloques constructores*; tales como moléculas de DNA, agregados atómicos 0D y nanoalambres 1D) en arreglos bien ordenados corresponde a un reto actual en nanotecnología. Basados en esta tendencia de investigación, la principal propuesta de este trabajo de Doctorado ha sido utilizar nanoestructuras 1D como bloques constructores (e.g. nanoalambres y nanotubos) para diseñar y sintetizar nanoalambres intermitentes 1D (1D superlattices) así como redes en 2D y 3D.

Estos arreglos ensamblados pueden ser vistos como un nuevo tipo de material en la microescala, exhibiendo propiedades intrínsecas provenientes de las propiedades de los bloques constructores utilizados y sus arquitecturas específicas. Desafortunadamente, poco era conocido con respecto a la manera en que diferentes redes pueden ser creadas y sus propiedades fisico-químicas como función de su arquitectura. En este contexto, un algoritmo general (algoritmo de Jerarquía) para diseñar y generar modelos ideales (coordenadas xyz) de redes a partir de nanoestructuras 1D (e.g. nanoalambres o nanotubos) como bloques constructores fue propuesto [1].

Un especial énfasis es puesto en nanotubos de carbono (CNTs) como bloques constructores, debido a que poseen propiedades sumamente deseadas: un módulo de Young extremadamente alto y extraordinaria flexibilidad, pueden comportarse como conductores balísticos o semiconductores, poseen un alta área superficial y bajo condiciones apropiadas coalescen entre ellos.

Por consiguiente, el algoritmo de Jerarquía fue aplicado a CNTs para diseñar un conjunto de *redes ordenadas basadas en CNTs* (ON-CNTs) que permitieran estudiar por completo las propiedades fisico-químicas de las redes (propiedades de transporte electrónico, mecánico, porosidad y área superficial) como función de su arquitectura. Esto reveló extraordinarias propiedades mecánicas, junto con selectivas trayectorias de conductancia electrónica [2], complementado por bajas densidades de masa, altas áreas superficiales y porosidad continua; donde las propiedades fueron fuertemente dominadas por la arquitectura específica del arreglo [1]. Un estudio posterior se concentró en nanocircuitos electrónicos, explotando la ventaja que ON-CNTs ofrecen al incluir nanoalambres y nanodispositivos todo auto-integrado a través de la red. Es mostrado que arreglos que contengan defectos topológicos (anillos no hexagonales en la red sp^2 de carbono que compone a los CNTs) pueden funcionar como intra-dispositivos para guiar corriente a lo largo de trayectorias específicas, por lo cual se muestra a las ON-CNTs como potenciales nanocircuitos orgánicos que pudieran trabajar con funciones de memoria (addressable arrays) [3].

En la parte experimental, los detalles de la formación de un nodo es necesaria para poder sintetizar redes CNTs. Por ende, un estudio completo sobre el fenómeno de ramificación de CNTs fue realizado; incluyendo la síntesis de uniones de CNTs y una detallada caracterización de alta-resolución, lo cual fue complementado con cálculos de primeros principios con la teoría del funcional de la densidad. En este trabajo, está elucidado el mecanismo de ramificación de los CNTs a nivel atómico debido a la presencia de azufre [4]. El trabajo de síntesis por

CVD arrojó cinco diferentes tipos de uniones Y cuando diferentes condiciones experimentales fueron utilizadas (cantidad de fuente de azufre o tipo de catalizador) [5].

Finalmente es presentado un estudio de síntesis para obtener nanoalambres intermitentes 1D (estructuras 1D compuestas por segmentos axialmente alternados) utilizando como bloques constructores CNTs dopados con nitrógeno y sin dopaje [6]. La caracterización de estas estructuras exhibió que CNTs continuos, con segmentos de longitud variable dopados con nitrógeno y sin dopaje, pueden ser obtenidos. El método de síntesis debiera motivar futuro trabajo experimental para explorar las propiedades electrónicas de este tipo de materiales.

Todos estos resultados juntos intentan ilustrar el emocionante campo de “jugar al LEGO” con nanoestructuras 1D, para así motivar trabajo de investigación con el enorme rango de combinaciones que la composición del bloque constructor, longitud y diámetro, tipo de arquitectura y dimensionalidad, ofrecen por explorar con creatividad y conocimiento científico.

[1] Romo-Herrera, J.M., Terrones, M., Terrones, H., Dag, S. & Meunier, V. "Covalent 2D and 3D Networks from 1D Nanostructures". **NanoLetters** 7(3): 570-576 (2007).

[2] Romo-Herrera, J.M., Terrones, M., Terrones, H. & Meunier, V. "Transport properties of ordered networks based on carbon nanotubes (ON-CNTs)". (submitted).

[2] Romo-Herrera, J.M., Terrones, H., Terrones, M., & Meunier, V. "Defects engineering in ON-CNTs: guiding current". (in progress).

[3] Romo-Herrera, J.M., Sumpter, B.G., Cullen, D.A., Terrones, H., Cruz-Silva, E., Smith, D.J., Meunier, V. & Terrones, M. "An Atomistic Branching Mechanism for Carbon Nanotubes: Sulfur as triggering agent". (accepted; **Angewante Chemie**).

[4] Romo-Herrera, J.M., Cruz-Silva, E., Cullen, D.A., Terrones, H., Smith, D.J. & Terrones, M. "Temperature gradient and flux effect effect in the Pyrolysis of Thiophene and Nickelocene: from sea urchin -like nanostructures to five different types of Y-junctions". (to be submitted).

[5] Romo-Herrera, J.M., Zamudio, A., Cruz-Silva, E., Cullen, D.A., Smith, D.J., Terrones, H., Terrones, M., "1D Superlattices from nitrogen-doped and undoped CNTs segments". (in progress).

Chapter 1. General Introduction

1.1 Basic Idea: Hierarchy and 1D building blocks	2
1.2 2D and 3D ordered arrays from biological and 0D (clusters) building blocks	4
1.3 1D building blocks: from isolated devices to their strategic assembly	7
1.4 Carbon nanotubes as building blocks	9
1.4.1 Geometrical properties	9
1.4.2 Electronic properties	9
1.4.3 Mechanical properties	10
1.4.4 Coalescence of CNTs	10
1.4.5 Review on CNTs synthesis.	11
1.5 Contributions of the present Ph. D. work	12
References	14

1.1 Basic Idea: *Hierarchy and 1D building blocks*

A current key challenge in nanotechnology is the assembly of nanostructured components (***building blocks***; such as DNA molecules, 0D clusters and 1D nanowires) into well ordered arrays. At first, nanoscience research has focused on the synthesis, observations, and study of isolated nanostructures and their properties. A next step, currently under development, corresponds to the assembly of such nanostructured building blocks into ordered microarrays.

The following quotes reflect the current trends in the field (2003-2007):

“Control of the detailed structure of matter on the finest possible scale is a major goal of chemistry, material science and nanotechnology. This goal may be approached in two steps: first, the construction of individual molecules through synthetic chemistry; and second, the arrangement of molecular building blocks into larger structures“.

E.Winfree, F.Liu, L.A.Wenzler and N.C.Seeman
Nature 394: 539-544 (1998)

“Semiconductor Nanowires and carbon nanotubes represent promising building blocks for the bottom-up assembly of integrated electronic systems ...“.

“... Yet to move forward and possibly go beyond existing technologies will require the development of approaches that enable controlled assembly and integration of these building blocks on a scale far beyond that of individual devices ...“.

D.Whang, S.Jin, Y.Wu and C.M.Lieber
Nano Letters 3 (9): 1255-1259 (2003)

“Although carbon nanotubes promise to have a wide range of applications, better control is needed over the building and organization of nanotube-based architectures“.

**B.Q.Wei, R.Vajtai, Y.Jung, J.Ward,
R.Zhang, G.Ramanath and P.M.Ajayan**
Nature 416: 495-496 (2002).

Based on this research trend, the core idea of the present Ph.D. work is to use 1D nanostructures as building blocks (e.g. nanowires and nanotubes) to design and synthesize 1D superlattices as well as 2D and 3D networks (see [Figure 1.1](#)). These assembled arrays can be seen as a new type of material at the microscale exhibiting characteristic properties tuned up by the properties of the building blocks employed and their specific architectures. An emphasis is made on carbon nanotubes (CNTs) as building blocks, although the general idea can be extrapolated to any 1D nanostructures.

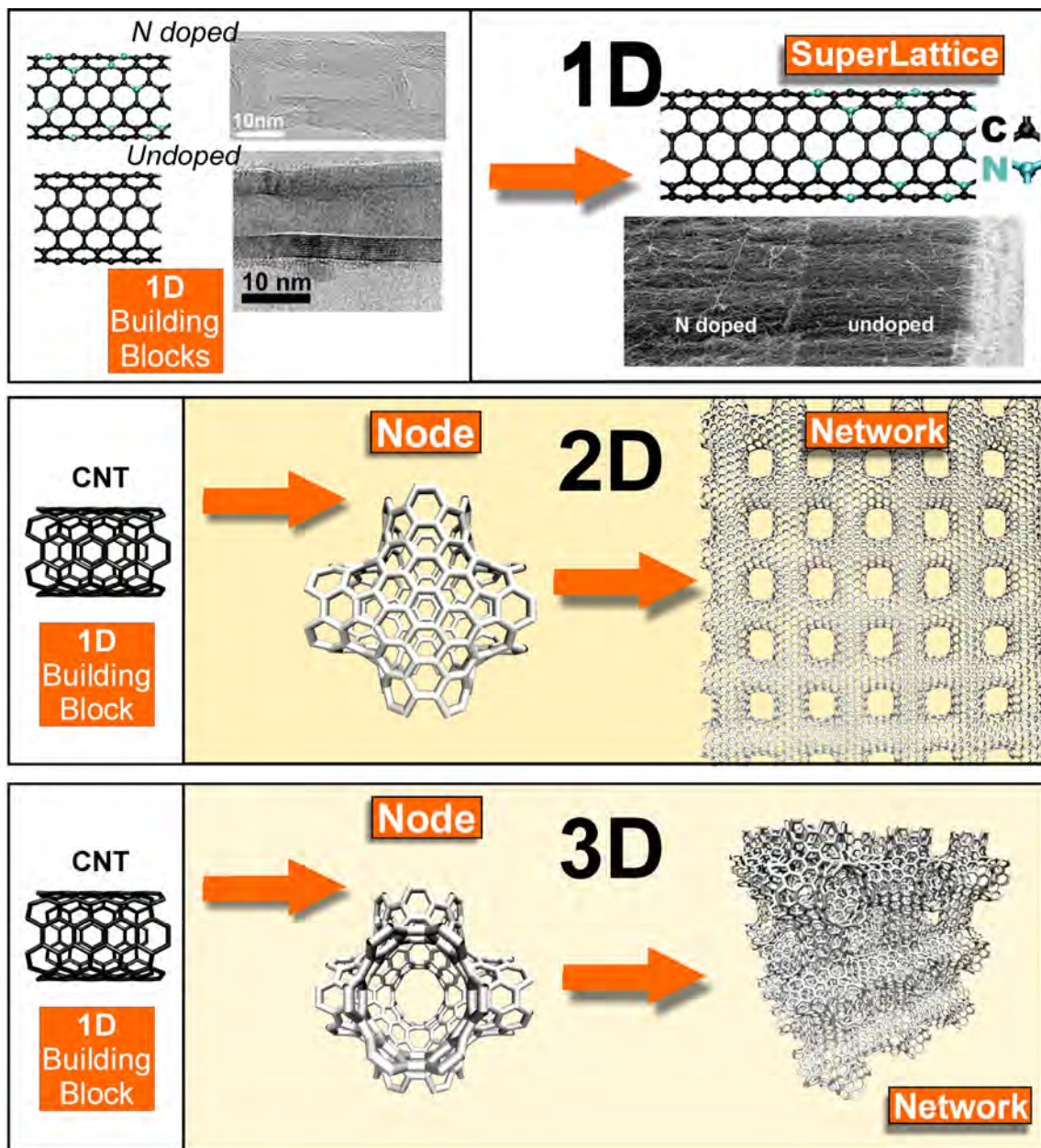


Figure 1.1. Schematic representation of the core idea of the thesis. 1D Superlattices were obtained experimentally from nitrogen doped and undoped CNTs; while 2D and 3D networks made from nanotubes are proposed and their properties are calculated in detail.

1.2 2D and 3D ordered arrays from biological and 0D (clusters) building blocks

Some results have been reported in the literature, in which ordered arrays are assembled from different types of building blocks such as: bio-building blocks (DNA and RNA) and 0D clusters.

The DNA has been explored in materials science as a building block, due to its powerful molecular recognition ability which can be used in nanotechnology to direct the assembly of highly structured materials with specific nanoscale features [1]. Along this line, branched DNA molecules with *sticky ends* (a short single-stranded overhang protruding from the end of a double-stranded helical DNA molecule; like flaps of Velcro) have been used as Wang tiles that assemble in solution into 2D crystals with well defined subunit structure [2]. More recently, a 2D nanogrid was assembled from tiles composed by four four-arm DNA branched junctions (*Holliday Junctions* [1]) pointing in four directions [3]. Even RNA planar networks have been achieved, from squared-shaped RNA supramolecules (*tecto RNA* [1]) with sticky interacting tails [4].

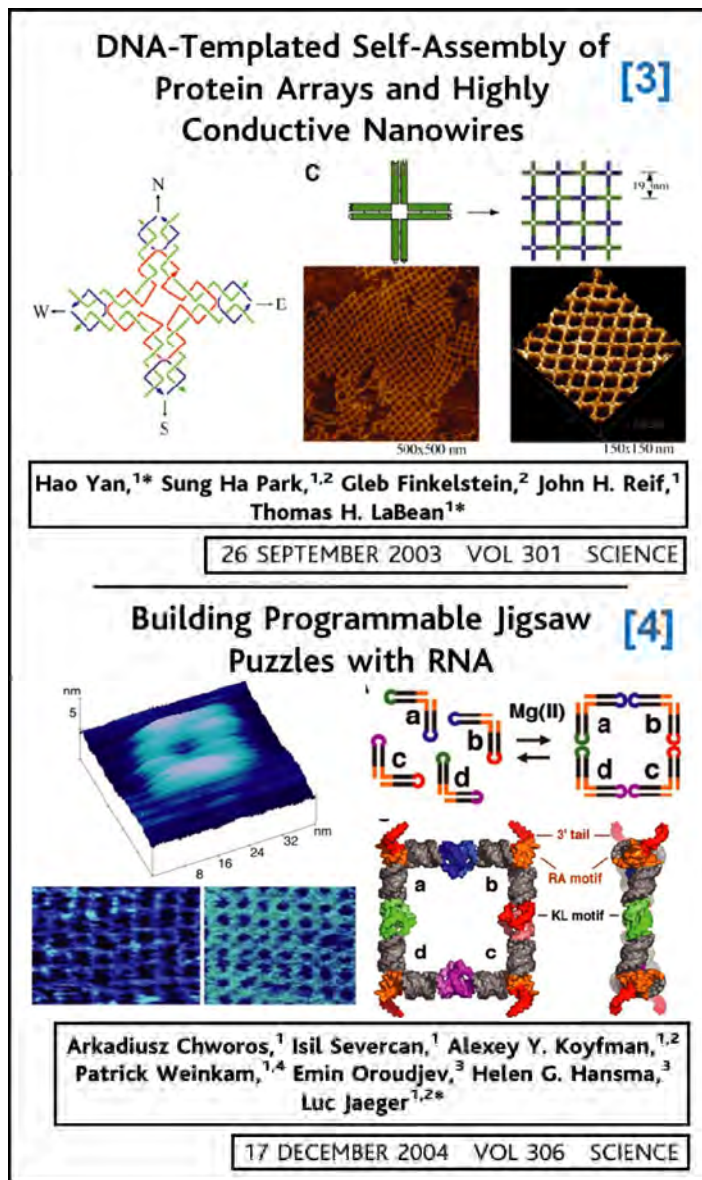
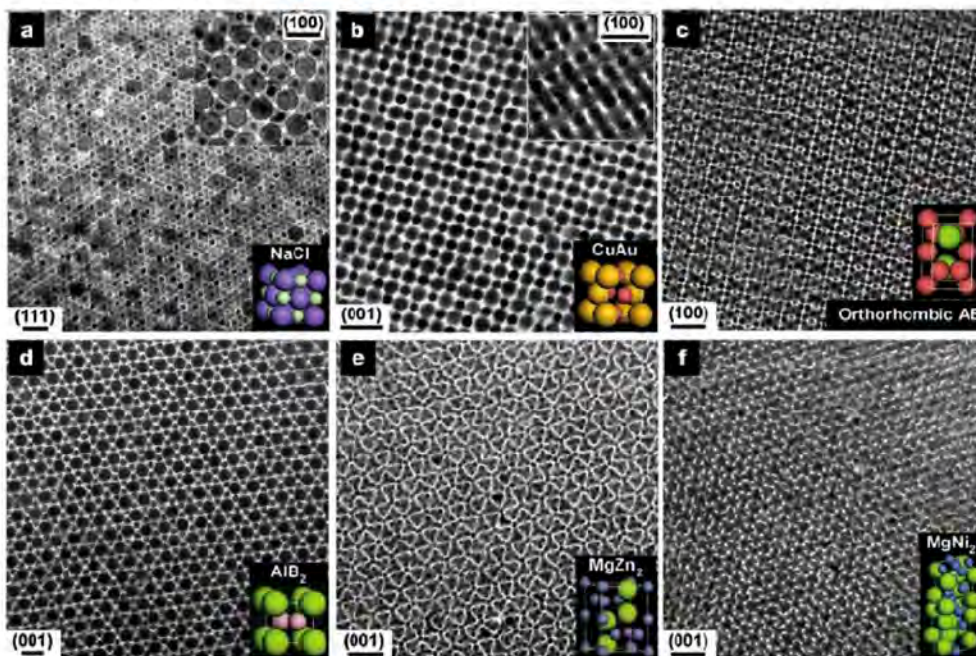


Figure 1.2. Networks built up from biological building blocks. The first work [3] assembles DNA strands into a multiterminal cross, which is repeated to obtain a SuperSquare architecture, as the one measured by AFM. The second work [4] starts from basic RNA pieces, which are assembled into a square as the one shown in the model and measured by AFM, this RNA squares possess tails at the corners which helped them to connect them in a higher level of hierarchy into a RNA SuperSquare architecture.

A step forward has also been explored, when using DNA material as a template to anchor inorganic quantum dots (0D clusters). This idea has been used to interconnect microelectrodes to a silver nanowire obtained by a two-step procedure: first the hybridization of DNA molecules with surface bound oligonucleotides is used to stretch it between two gold electrodes, subsequently this DNA molecule is used as a template to anchor silver aggregates [5]. In addition, it has been possible to organize quantum dots (Au clusters) into spatially defined structures. This was carried out by interconnecting clusters with DNA oligonucleotides capped with sulfur groups following Watson-Crick base pairing interactions [6,7]. In 2000, a noncovalent DNA-based strategy was reported for controlling a stepwise growth of layered nanoparticles (e.g. Au clusters) arrays layer-by-layer to obtain multilayered structures [8]. A different approach followed using *bacterial S-layers* (self assembled 2D ordered films of proteins that are present in many bacterial cell walls and which possess pores of identical size arranged in an oblique, square or hexagonal lattice symmetry) as templates, in order to achieve an *in situ* nucleation of 2D ordered arrays of cadmium sulphide (CdS) clusters [9]. A similar porous template idea was explored from genetically engineering proteins called *chaperonins* (proteins that self-assemble into regular double-ring structures and can be crystallized into higher-order structures such as 2D crystals) to direct the organization of metallic (Au) and semiconductor (CdZn/ZnS; core/shell) clusters [10].

The inorganic assembly of inorganic quantum dots has also been developed, to promote the formation of 2D and even 3D Superlattices. The first attempts used double ended organic molecules as interconnects to rigidly stabilize a close packed monolayer array of gold passivated aggregates [11]. Some spherical arrays ($\sim\mu\text{m}$) obtained from the assembly of gold passivated particle ($\sim 2\text{nm}$) subunits have also been synthesized [12]. Recently, this research method yielded spectacular results related to the generation of 3D superlattices. Four years ago, the co-assembly of binary 3D superlattices was reported, from PbSe semiconductor clusters and Fe_2O_3 magnetic nanocrystals, exhibiting AB_2 (AlB_2) and AB_{13} (NaZn_{13}) crystal structures [13]. Last year, various binary nanoparticle superlattices were produced, forming 15 different crystal structures (close packed), from various combinations of PbSe, PbS, Fe_2O_3 , CoPt_3 , Bi, Au, Ag and Pd clusters (semiconducting, metallic and magnetic) by tuning the cluster charge (from surfactant molecules), because the Coulomb energy determines the stoichiometry of the growing superlattices [14]. Finally last year, a diamond –like structure was obtained with self-assembling charged, equally sized, metal nanoparticles of two different types (Au and Ag); this was due to the change in electrostatic interactions in the nanoscopic regime, where the thickness of the screening layer becomes commensurate with the dimensions of the assembling particles, thus favouring non close packed sphalerite structures (diamond –like) [15].

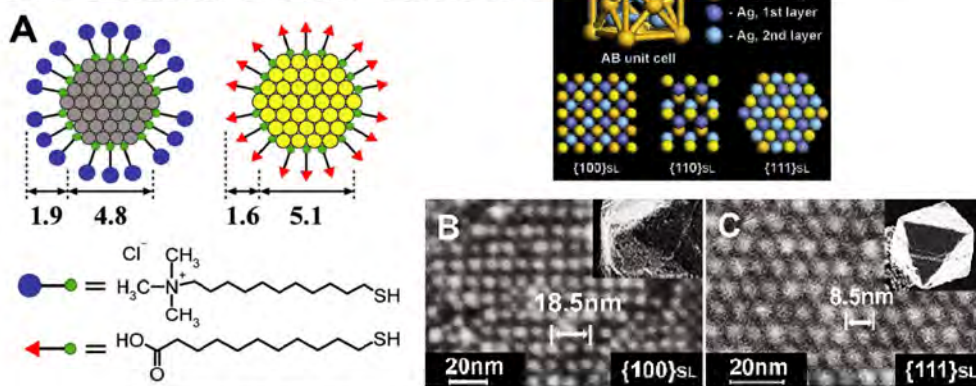
Structural diversity in binary nanoparticle superlattices [14]



Elena V. Shevchenko^{1,2,*}, Dmitri V. Talapin^{1,†}, Nicholas A. Kotov³, Stephen O'Brien² & Christopher B. Murray¹

NATURE | Vol 439 | 5 January 2006

Electrostatic Self-Assembly of Binary Nanoparticle Crystals with a Diamond-Like Lattice [15]



Alexander M. Kalsin, Marcin Fialkowski, Maciej Paszewski, Stoyan K. Smoukov, Kyle J. M. Bishop, Bartosz A. Grzybowski*

21 APRIL 2006 VOL 312 SCIENCE

Figure 1.3. Networks built up from 0D building blocks (inorganic clusters). All type of crystallographic arrays have been obtained assembling atomic clusters, the first work [14] shows the wide diversity in crystal arrays achieved. The second work [15] reports the Diamond-like lattice, so hard to be obtained and finally assembled from 0D building blocks.

1.3 1D building blocks: from isolated devices to their strategic assembly

1D nanostructures, such as nanowires (NWs), nanorods and nanotubes (NTs) represent another group of building blocks which should give different types of properties to the assemblies due to the morphological difference imposed by their one-dimensionality.

Basic electronic components based on isolated 1D building blocks have been demonstrated, such as molecular quantum wires using an individual single walled nanotube (SWNT) [16]; a single electron transistor with a bundle of SWNTs [17] and a room temperature Field Effect Transistor (FET) based on an individual semiconductor SWNT [18]. Intramolecular devices were proposed with CNTs heterojunctions (chirality change within a single tube by 5-7 pair topological defects), where metal/semiconductor and semiconductor/semiconductor junctions can be achieved [19-21]. These structures were later observed by TEM (transmission electron microscopy) [22] and local electrical measurements (scanning tunneling microscopy; STM) along individual SWNTs [23], showing a rectifying diode behaviour when a semiconductor/metallic junction was presented in the electrical transport measurement [24]. Carbon nanotube inter- and intramolecular logic gates have been fabricated by interconnecting a p-type CNT-FET to a n-type CNT-FET or by n-doping only a given section of an originally p-type CNT-FET to obtain NOT logic gates along a single tube [25]. CNTs and NWs have also been shown to perform as sensors when changing their conductance when external molecules are attached, either sensing chemical gases (NO_2 or NH_3) with SWNTs [26], as a pH (potential of hydrogen) nanosensor with functionalized Si NWs [27], or as biomolecular sensors by functionalizing Si NWs with biological species [27]. A bistable (on/off) switch device was demonstrated by molecular-gating NWs; this was achieved by functionalizing with redox active molecules NW-FETs (p-Si, n-InP and n-GaN) showing hysteresis loops in the conductance vs voltage graphs. The latter allowed to address an *on* or *off* state by voltage pulses (since the redox-active molecules can store charge and maintain the activated state) [28]. A further step was achieved when these 1D building blocks were arranged into an overlapping cross configuration. A light-emitting diode was obtained when using p-n cross junctions with NWs (n-type: Te-doped InP NW; p-type: Zn-doped InP NW) which exhibit rectifying behavior, emitting light strongly from the junction region [29]. An individual cross configuration of overlapping CNTs was also electrically studied (metallic-metallic, semiconductor-semiconductor and metallic-semiconductor), exhibiting a rectifying Schottky barrier in the metallic-semiconductor case [30]; as where a cross of overlapping NWs (n-CdS and p-Si) behaves as a nanoscale avalanche photodiode [31]. However, the latter examples constitute the first step towards integrated systems. The next challenge is to assemble such building blocks on functional and more complex arrays.

The assembly of inorganic NWs has recently witnessed significant progress towards the production of non-covalent ordered arrays. One of the first successful approaches used a fluid flow and a mold containing fluidic channels in order to obtain aligned monolayers of inorganic nanowires (InP and Si) [32]. Subsequently,

a method to produce ultrahigh dense arrays of aligned metal and semiconductor NWs was reported (Superlattice Nanowire Pattern Transfer; SNAP) [33]. This method creates superlattices of GaAs/Al_{0.8}Ga_{0.2}As on silicon wafers by molecular beam epitaxy. In a second step AlGaAs fringes are selectively removed to evaporate the metal directly onto the GaAs fringes. Finally, the synthesized NWs are transferred to a silicon wafer by contacting a heat-curable epoxy film [33]. A more general approach based on self-assembly by Langmuir Blodgett technique, reported the generation of Si NW networks (not bonded covalently) by uniaxially compressing NWs on a surfactant monolayer on an aqueous subphase. This is a promising method capable of controlling building blocks, NW pitch and NW orientation [34]. The first applications of this type of network have been demonstrated using a 3x1 network (3 nodes) that perform as AND or NOR logic gates [35]. An addressable decoder nanosystem was also reported with a 4x4 network (16 nodes), in which the devices were field effect transistors obtained at every nanowire crossing. By selective chemical modifications on specific cross points, it was possible to define a code that enables nanowire input lines to turn on and turn off specific output lines [36].

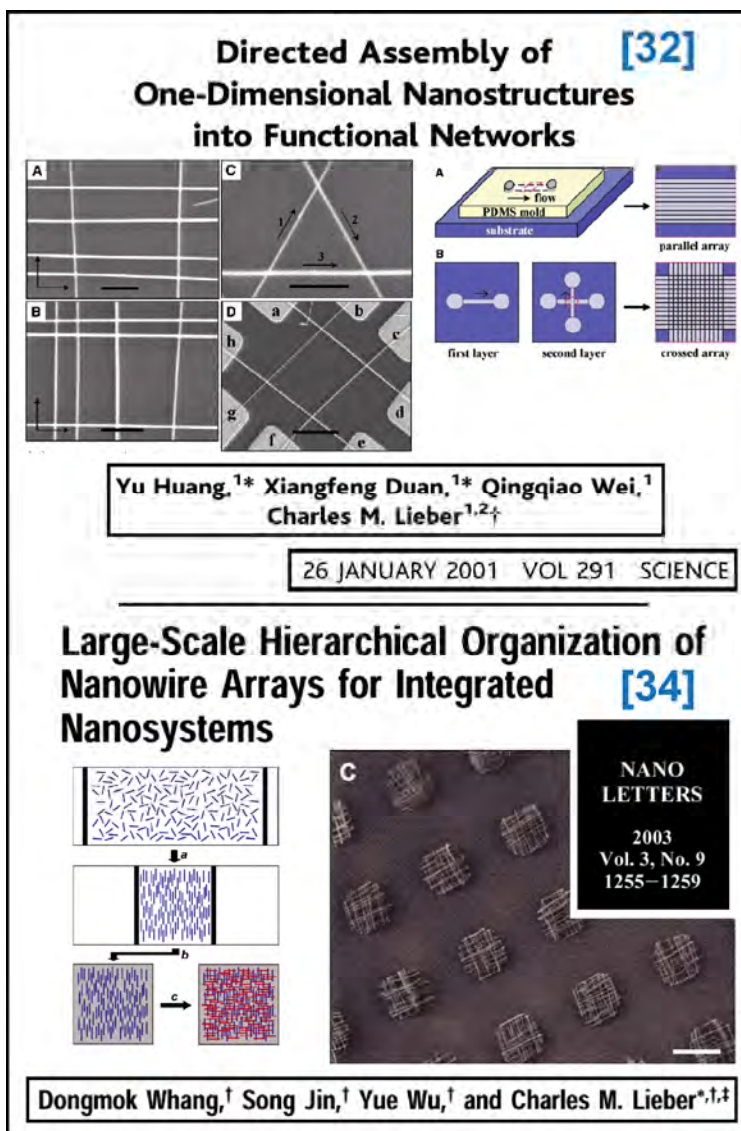


Figure 1.4. The first attempts to arrange 1D building blocks into ordered networks have been reported with inorganic NWs. The first work [32] reported small networks built from a layer-by-layer approach. The second work [34] reported a Langmuir-Blodgett technique to assemble millions of NWs by a layer-by-layer approach, where the nanowires are stacked one over the other without covalent junctions.

Even though the development of 1D building blocks has focused on inorganic NWs, there have been initial efforts to fabricate CNTs 2D networks arranged in a square geometry. This has been achieved experimentally by orthogonal self-assembly of CNTs crossbar architectures by simultaneous graphoepitaxy (CNT horizontal aligned growth following high atomic steps of miscut C-plane sapphire surfaces) and field directed growth (from SiO₂ islands previously deposited on the substrate) in a single step of CVD [37]. Although this result is remarkable, the substrate preparation possesses an important limitation for the production of this type of non covalent CNT networks. Nevertheless, the effort along this research line is just starting, and some applications for this specific 2D square non-covalent networks have been proposed as a Nonvolatile Random Access Memory (RAM) for molecular computing [38].

1.4 Carbon Nanotubes as building blocks

Carbon Nanotubes have caught the attention of numerous scientists in the last 15 years due to their fascinating physico-chemical properties such as electronic, mechanical and geometrical characteristics. If these tubes are interconnected covalently, a wide variety of networks can be produced.

1.4.1 Geometrical properties

A single walled nanotube (SWNT) is conceptually obtained by rolling a single graphene sheet into a cylinder. The obtained system corresponds to a tube composed of sp² hybridized carbon atoms (each atom bonded to the three nearest neighbors). An important concept in these nanostructures is *curvature*, since it corresponds to a curved graphene surface. Two dimensional surfaces immersed in 3D space exhibit a mathematical concept known as Gaussian curvature (K), and three different types of geometries can be obtained: Euclidean geometry (K=0; plane surface geometry such as the graphene sheet), spherical geometry (K>0; positive curvature surfaces such as Fullerenes); and hyperbolic geometry (K<0; negative curvature surfaces, these are saddle point surfaces) [39]. For SWNTs, it is possible to join nanotubes at different angles and obtain complex multi-terminal networks (see [Chapter 2](#)).

A multi walled carbon nanotube (MWNT) consists of concentric cylindrical graphene layers (or nested tubes). The intertube spacing is ~0.34nm and they usually exhibit a turbostratic arrangement (the arrangement of concentric tubes are not correlated in the radial direction).

Carbon Nanotubes (CNTs) could exhibit lengths of up to centimeters and diameters in the nm range, this corresponds to high aspect ratios stamping them the 1D characteristic.

Since the CNTs correspond to hollow cylindrical structures, it is possible to divide space in two surfaces with an “outside” and an “inside” and therefore it is possible to encapsulate different types of materials.

1.4.2 Electronic properties

One of the main issues that motivated the intensive research on CNTs, was the predicted electronic structure of SWNTs, in which depending on the tube

chirality (*i.e.* the way the hexagons are oriented along the tube axis) the tubes could exhibit metallic, semi-metallic or semiconductor behaviour [40-42]. This prediction was confirmed experimentally six years later, using Scanning Tunneling Microscopy (STM) and Scanning Tunneling Spectroscopy (STS) to show the direct arrangement of carbon hexagons together with measurements of the electronic structure of the nanotubes [43-44].

In addition to offering semiconductor and metallic building blocks, CNTs behave as ballistic transport conductors (electricity conduction with coherence length larger than their physical length). Along this line, it has been demonstrated different types of nanodevices made from CNTs (see [section 1.3](#)).

1.4.3 Mechanical properties

An outstanding property of carbon nanotubes corresponds to their exceptional mechanical behavior because CNTs combine high stiffness [45-48], and an extraordinary flexibility [49-51] in addition to resistance to fracture [51].

The Young's modulus of CNTs have been experimentally measured from thermal vibration in cantilevered nanotubes inside a Transmission Electron Microscope (TEM). The studies estimated a 1.8 ± 1.4 TPa value [45]. A subsequent study reported a value of 1.28 ± 0.59 TPa, by measuring the lateral force applied by bending the cantilevered nanotubes with an Atomic Force Microscope (AFM) tip [46]. These experimental values are in good agreement with theoretically calculated Young modulus obtained using non-orthogonal tight binding formalism (with a predicted value of 1.26 TPa) [47] and by *ab initio* calculations (values on the order of 1 TPa) [48].

The bending of CNTs has been observed by High Resolution TEM (HRTEM) and studied by atomic simulations, and revealed morphology deformations by the presence of *kinks* at high bending angles [49]. Experimentally it was demonstrated that CNTs can be bent at high angles ($\sim 180^\circ$ and then -360°) even twenty times without catastrophic deformations, performed with an AFM [50]. The compression of CNTs was also studied theoretically beyond the plastic regime. These studies revealed a strain release mechanism occurring by abrupt morphology deformations (*buckles*), thus demonstrating that CNTs could sustain extreme strains with no signs of brittleness [51].

1.4.4 Coalescence of CNTs

The coalescence behavior of CNTs corresponds to the merging of two adjacent nanotubes through atomic rearrangements. This is an important property that should allow the covalent joining of a large number of nanotubes if they have been previously assembled strategically, into ordered networks.

The coalescence in CNTs was first observed in bundles of SWNTs under electron irradiation at high temperatures inside a HRTEM, where neighboring tubes coalesce axially into one of larger diameter [52]. Coalescence has also been observed in double walled nanotubes (DWNTs) [53]. Coalescence is not restricted to parallel nanotubes, it was later demonstrated that two crossed and overlapping SWNTs could be merged in order to form junctions at different angles [54]. Molecular dynamics simulations demonstrated that the driving force for

coalescence corresponds to the presence of defects (vacancies, dangling bonds and non-hexagon rings) generated from the high energy electron beam, which induces formation of vacancies followed by surface reconstruction [52,54]. A zipper mechanism has been proposed for the fast coalescence observed in parallel SWNTs under HRTEM irradiation at high temperatures [55]. Recently, it has been demonstrated that boron atoms could act as welders during heat annealing of DWNTs, in which the coalescence phenomenon is triggered by boron and results in the reduction of the merging temperature [56].

1.4.5 Review on CNTs Synthesis

The starting point of CNTs is usually referred to a report published in 1991 by S. Iijima, showing HRTEM images and electron diffraction patterns of concentric tubes with diameters of nanometers made of carbon atoms [57]. However, the first clear observation of CNTs had been already reported 15 years earlier by Oberlin A., Endo M. and Koyama T. These authors described such carbon hollow tubes as “annular ring structure of a tree” [58]. Even more, the first TEM evidence for a tubular nano-sized carbon filaments was reported in 1952 in the Journal of Physical Chemistry of Russia [60-61]; although at the time TEM resolution was not able to distinguish the arrangement of graphene layers in the nanotube walls. Another interesting historical data was written by T.W. Ebbesen [59], he described how a paper predicting the electronic structure of a nanotube made by rolling a graphene sheet [40] was submitted in 1991, and to some people this work was too speculative for publication since the synthesis of nanotubes seemed unlikely ... months later the synthesis report was published by S. Iijima [57]. These pioneering results were followed by theoretical predictions that a carbon nanotube could be a metal or a semiconductor, simply by the different helical arrangement of the carbon atoms along the axis [40-42].

A first main challenge at the time was to improve the synthesis methods, since the CNTs were only available in minute quantities and coexisted with large amounts of impurities in the samples. The synthesis of graphitic nanotubes in gram quantities was reported in 1992, by optimizing the arc discharge method [62]. The next landmark was achieved in 1993, when the synthesis of SWNTs was reported using the same arc discharge technique [63-64]. Three years later the synthesis of SWNTs in high yields of more than 70% by the laser ablation technique was reported [65]. The subsequent year (1997), the arc discharge technique was optimized to obtain a similar sample quality to the one reported from the laser ablation technique, suggesting that the growth mechanism for SWNTs must be independent of the details of the technique used [66]. More recently, SWNT strands with lengths >10 cm were obtained [67] and even continuous spinning of fibers made from carbon nanotubes directly from the chemical vapor deposition (CVD) synthesis zone has been achieved [68]. Regarding the quality of the samples, the use of ethanol as an additive in the CVD synthesis allowing less contamination, increased lengths and crystallinity of MWCNTs [69] while a 99.98% purity sample of SWNTs was reported with a 2.5 mm long nanotube forest by a water-assisted CVD method [70].

1.5 Contributions of the present Ph. D. work

Following the current developing trend of fabricating well ordered arrays from nanostructured building blocks, within the bottom-up approach, the present Ph.D. work focuses on the integration of 1D nanostructures into organized architectures such as 1D superlattices as well as 2D and 3D networks made of nanotubes. The first part ([Chapter 2](#) and [Chapter 3](#)) focuses on theoretically designing nanotube networks and presents novel calculations of their physico-chemical properties. The second part ([Chapter 4](#) and [Chapter 5](#)) reports experimental work to fully understand the node formation (*i.e.* Branching Mechanism of CNTs; [Chapter 4](#)) and to synthesize 1D Superlattices (axially intermittent) using nitrogen-doped and undoped CNTs as building blocks ([Chapter 5](#)).

In particular, [chapter 2](#) starts with the proposal of a general algorithm (Hierarchy Algorithm) to generate ideal models (xyz coordinates) of networks from 1D nanostructures (e.g. nanowires or nanotubes) as building blocks. Subsequently this idea is extrapolated to design a set of Ordered Networks based on CNTs (ON-CNTs) and to fully study the physico-chemical properties of the networks (electronic transport, mechanical, porosity and surface area properties) as a function of their architecture. [Chapter 3](#) focuses on electronic nanocircuits, exploiting the advantage that ON-CNTs offer when including nanowires and nanodevices all self-integrated along the network. It is shown that arrays containing topological defects (non-hexagonal rings) can perform as intradevices to guide current along specific paths, thus showing ON-CNTs as potential organic nanocircuits working as addressable arrays.

The experimental synthesis of CNT networks, a challenging issue, can be greatly facilitated by studying the details of the formation mechanism and the branching nanotube phenomena during growth. In this context, [chapter 4](#) presents a full study on the CNTs branching phenomena, including detailed high-resolution characterization which is complemented by first principles density functional theory calculations. Here, the Branching Mechanism of CNTs is elucidated at the atomistic level in the presence of sulfur atoms. The chemical vapor deposition (CVD) synthesis work turned out with five different types of covalent Y-junctions when different experimental conditions were used (amount of the sulfur source or type of catalyst). In addition, other types of nanostructures were obtained in these experiments: sea urchin –like, encapsulated metal spheres in carbon onions and carbon fibers.

By interconnecting nitrogen-doped and undoped CNTs as the building blocks, it is possible to generate 1D Superlattices. [Chapter 5](#) presents the experimental demonstration of 1D Superlattices by adapting an intermittent aerosol CVD system. The characterization of these structures shows how continuous CNTs can be obtained with nitrogen-doped segments and undoped segments of variable length. The synthesis method should motivate further experimental work exploring the electronic properties of this type of material (as electronic wires with self-integrated devices along its axis).

The research field on ordered micro-arrays built from 1D building blocks is just a recent area that is still in its infancy, in which by combining different types of 1D nanostructures (e.g. carbon-NTs, boron nitride-NTs, doped CNTs, or inorganic NWs) together with different types of architectures (crystallographic arrays) fascinating and novel materials would result. The applications of such heteronetworks range from electronic nanocircuits with nanowires and nanodevices (see Chapter 2 and Chapter 3), long nanowires with intradevices (see Chapter 5), molecular shock absorbers (see Chapter 2), chemical [26-27] or biological [27] sensors, filters or molecular storage devices (see Chapter 2) among others. All these potential applications demand further experimental work.

A major challenge to be achieved in the near future is the controlled production of ON-CNTs. Along this line, the experimental assembly of inorganic nanowires into stacked (non covalent) ordered arrays using the Langmuir-Blodgett technique has been demonstrated [34]. While these nanowires were not connected covalently, it is shown theoretically and experimentally in this work that CNT networks are stable and feasible. CNTs can be coalesced (merged covalently), individually using controlled electron irradiation at high temperatures [54], or randomly in higher yields using atomic welders (e.g. B atoms) during heat treatments [56]. Therefore, by extrapolating the concept of welding CNTs into self-assembled arrays, it should be possible to obtain novel architectures consisting of *covalently bonded* 2D and 3D CNTs networks when using CNTs as building blocks.

References

- [1] Seeman, N.C. DNA in a material world. **Nature** **421**, 427-431 (2003).
- [2] Winfree, E., Liu, F., Wenzler, L.A. & Seeman, N.C. Design and self-assembly of two-dimensional DNA crystals. **Nature** **394**, 539-544 (1998).
- [3] Yan, H., Park, S.H., Finkelstein, G., Reif, J.H. & LaBean, T.H. DNA-Templated Self-Assembly of Protein Arrays and Highly Conductive Nanowires. **Science** **301**, 1882-1884 (2003).
- [4] Chworos, A., et al. Building Programmable Jigsaw Puzzles with RNA. **Science** **306**, 2068-2072 (2004).
- [5] Braun, E., Eichen, Y., Sivan, U. & Ben-Yoseph, G. DNA-templated assembly and electrode attachment of a conducting silver wire. **Nature** **391**, 775-778 (1998).
- [6] Mirkin, C.A., Letsinger, R.L., Mucic, R.C. & Storhoff, J.J. A DNA-based method for rationally assembling nanoparticles into macroscopic materials. **Nature** **382**, 607-609 (1996).
- [7] Alivisatos, A.P., et al. Organization of 'nanocrystal molecules' using DNA. **Nature** **382**, 609-611 (1996).
- [8] Taton, T.A., Mucic, R.C., Mirkin, C.A. & Letsinger, R.L. The DNA-Mediated Formation of Supramolecular Mono- and Multilayered Nanoparticle Structures. **J. Am. Chem. Soc.** **122**, 6305-6306 (2000).
- [9] Shenton, W., Pum, D., Sleytr, U.B. & Mann, S. Synthesis of cadmium sulphide superlattices using self-assembled bacterial S-layers. **Nature** **389**, 585-587 (1997).
- [10] Andrew Mcmillan, R., Paavola, C.D., Howard, J., Chan, S.L., Zaluzec, N.J. & Trent, J.D. Ordered nanoparticle arrays formed on engineered chaperonin protein templates. **Nature** **1**, 247-252 (2002).
- [11] Andres, R.P., et al. Self-Assembly of a Two-Dimensional Superlattice of Molecularly Linked Metal Clusters. **Science** **273**, 1690-1693 (1996).
- [12] Boal, A.K., et al. Self-assembly of nanoparticles into structured spherical and network aggregates. **Nature** **404**, 746-748 (2000).
- [13] Redl, F.X., Cho, K.-S., Murria, C.B. & O'Brien S. Three-dimensional binary superlattices of magnetic nanocrystals and semiconductor quantum dots. **Nature** **423**, 968-970 (2003).
- [14] Shevchenko, E.V., Talapin, D.V., Kotov, N.A., O'Brien, S. & Murray, C.B. Structural diversity in binary nanoparticle superlattices. **Nature** **439**, 55-59 (2006).
- [15] Kalsin, A.M., et al. Electrostatic Self-Assembly of Binary Nanoparticle Crystals with a Diamond-Like Lattice. **Science** **312**, 420-424 (2006).
- [16] Tans, S.J., et al. Individual single-wall carbon nanotubes as quantum wires. **Nature** **386**, 474-477 (1997).
- [17] Bockrath, M., et al. Single-Electron Transport in Ropes of Carbon Nanotubes. **Science** **275**, 1922-1925 (1997).
- [18] Tans, S.J., et al. Room-temperature transistor based on a single carbon nanotube. **Nature** **393**, 49-52 (1998).
- [19] Chico, L., Crespi, V.H., Benedict, L.X., Louie, S.G. & Cohen, M.L. Pure Carbon Nanoscale Devices: Nanotube Heterojunctions. **Phys. Rev. Lett.** **76** (6), 971-974 (1996).
- [20] Lambin, Ph., Fonseca, A., Vigneron, J.P., Nagy, J.B. & Lucas, A.A. Structural and electronic properties of bent carbon nanotubes. **Chem. Phys. Lett.** **245** (1), 85-89 (1995).
- [21] Terrones, H., Terrones, M. & Hsu, W.K. Beyond C₆₀: Graphite Structures for the Future. **Chem. Soc. Rev.** **24**, 341-350 (1995).
- [22] Terrones, M., et al. Graphitic structures: from planar to spheres, toroids and helices. **Phil.Trans.R.Soc.Lond.A** **354**, 2025-2054 (1996).
- [23] Collins, P.G., Zettl, A., Bando, H., Thess, A. & Smalley R.E. Nanotube Nanodevice. **Science** **278**, 100-103 (1997).
- [24] Yao, Z., Postma, H.W.Ch., Balents, L. & Dekker, C. Carbon nanotube intramolecular junctions. **Nature** **402**, 273-276 (1999).
- [25] Derycke, V., Martel, R., Appenzeller, J. & Avouris, Ph. Carbon Nanotube Inter- and Intramolecular Logic Gates. **Nano Lett.** **1** (9), 453-456 (2001).
- [26] Kong, J., et al. Nanotube Molecular Wires as Chemical Sensors. **Science** **287**, 622-625 (2000).

- [27] Cui, Y., Wei, Q., Park, H. & Lieber C.M. Nanowire Nanosensors for Highly Sensitive and Selective Detection of Biological and Chemical Species. **Science** **293**, 1289-1292 (2001).
- [28] Duan, X., Huang, Y. & Lieber, C.M. Nonvolatile Memory and Programmable Logic from Molecule-Gated Nanowires. **Nano Lett.** **2** (5), 487-490 (2002).
- [29] Duan, X., Huang, Y., Cui, Y., Wang, J. & Lieber, C.M. Indium phosphide nanowires as building blocks for nanoscale electronic and optoelectronic devices. **Nature** **409**, 66-69 (2001).
- [30] Fuhrer, M.S., et al. Crossed Nanotube Junctions. **Science** **288**, 494-497 (2000).
- [31] Hayden, O., Agarwal, R. & Lieber, C.M. Nanoscale avalanche photodiodes for highly sensitive and spatially resolved photon detection. **Nature Materials** **5**, 352-356 (2006).
- [32] Huang, Y., Duan, X., Wei, Q. & Lieber, C.M. Directed Assembly of One-Dimensional Nanostructures into Functional Networks. **Science** **291**, 630-633 (2001).
- [33] Melosh, N.A., et al. Ultrahigh-Density Nanowire Lattices and Circuits. **Science** **300**, 112-115 (2003).
- [34] Whang, D., Jin, S., Wu, Y. & Lieber C.M. Large-Scale Hierarchical Organization of Nanowire Arrays for Integrated Nanosystems. **Nano Lett.** **3** (9), 1255-1259 (2003).
- [35] Huang, Y., et al. Logic Gates and Computation from Assembled Nanowire Building Blocks. **Science** **294**, 1313-1317 (2001).
- [36] Zhong, Z., Wang, D., Cui, Y., Bockrath, M.W. & Lieber, C.M. Nanowire Crossbar Arrays as Address Decoders for Integrated Nanosystems. **Science** **302**, 1377-1379 (2003).
- [37] Ismach, A. & Joselevich, E. Orthogonal Self-Assembly of Carbon Nanotube Crossbar Architectures by Simultaneous Graphoepitaxy and Field-Directed Growth. **Nano Lett.** **6** (8), 1706-1710 (2006).
- [38] Rueckes, T., et al. Carbon Nanotube-Based Nonvolatile Random Access Memory for Molecular Computing. **Science** **289**, 94-97 (2000).
- [39] Terrones, H., Terrones, M. & Moran-Lopez, J.L. Curved Nanomaterials. **Curr.Sci.** **81** (9), 1011-1029 (2001).
- [40] Mintmire, J.W., Dunlap, B.I. & White, C.T. Are Fullerene Tubules Metallic?. **Phys. Rev. Lett.** **68** (5), 631-634 (1992).
- [41] Hamada, N., Sawada, S. & Oshiyama, A. New One-Dimensional Conductors: Graphitic Microtubules. **Phys. Rev. Lett.** **68** (10), 1579-1581 (1992).
- [42] Saito, R., Fujita, M., Dresselhaus, G. & Dresselhaus, M.S. Electronic Structure of chiral graphene tubules. **Appl. Phys. Lett.** **60**, 2204-2206 (1992).
- [43] Odom, T.W., Huang, J.-L., Kim, P. & Lieber, C.M. Atomic structure and electronic properties of single-walled carbon nanotubes. **Nature** **391**, 61-64 (1998).
- [44] Wildoer, J.W.G., Venema, L.C., Rinzler, A.G., Smalley, R.E. & Dekker, C. Electronic structure of atomically resolved carbon nanotubes. **Nature** **391**, 59-61 (1998).
- [45] Treacy, M.M.J., Ebbesen, T.W. & Gibson, J.M. Exceptionally high Young's modulus observed for individual carbon nanotubes. **Nature** **381**, 678-680 (1996).
- [46] Wong, E.W., Sheehan, P.E & Lieber, C.M. Nanobeam Mechanics: Elasticity, Strength and Toughness of Nanorods and Nanotubes. **Science** **277**, 1971-1975 (1997).
- [47] Hernández, E., Goze, C., Bernier, P. & Rubio, A. Elastic Properties of C and B_xC_yN_z Composite Nanotubes. **Phys. Rev. Lett.** **80** (20), 4502-4505 (1998).
- [48] Sánchez-Portal, D., Artacho, E., Soler, J.M., Rubio, A. & Ordejón, P. Ab initio structural, elastic, and vibrational properties of carbon nanotubes. **Phys. Rev. B** **59** (19), 12678-12688 (1999).
- [49] Iijima, S., Brabec, C. Maiti, A. & Bernholc, J. Structural flexibility of carbon nanotubes. **J. Chem. Phys.** **104**, 2089-2092 (1996).
- [50] Falvo, M.R., et al. Bending and buckling of carbon nanotubes under large strain. **Nature** **389**, 582-584 (1997).
- [51] Yakobson, B.I., Brabec, C.J. & Bernholc, J. Nanomechanics of Carbon Tubes: Instabilities beyond Linear Response. **Phys. Rev. Lett.** **76** (14), 2511-2514 (1996).
- [52] Terrones, M., Terrones, H., Banhart, F., Charlier, J.-C. & Ajayan, P.M. Coalescence of Single-Walled Carbon Nanotubes. **Science** **288**, 1226-1229 (2000).
- [53] Endo, M., et al. Coalescence of Double-Walled Carbon Nanotubes: Formation of Novel Carbon Bicables. **Nano Lett.** **4** (8), 1451-1454 (2004).

-
- [54] Terrones, M., et al. Molecular Junctions by Joining Single-Walled Carbon Nanotubes. **Phys. Rev. Lett.** **89** (7), 075505 (2002).
- [55] Yoon, M., et al. Zipper Mechanism of Nanotube Fusion: Theory and Experiment. **Phys. Rev. Lett.** **92** (7), 075504 (2004).
- [56] Endo, M., et al. Atomic Nanotube Welders: Boron Interstitials Triggering Connections in Double-Walled Carbon Nanotubes. **Nano Lett.** **5**, 1099-1105 (2005).
- [57] Iijima, S. Helical microtubules of graphitic carbon. **Nature** **354**, 56-58 (1991).
- [58] Oberlin, A., Endo, M. & Koyama, T. Filamentous growth of carbon through benzene decomposition. **J. Cryst. Growth.** **32**, 335-349 (1976).
- [59] Ebbesen, T.W. Carbon Nanotubes. **Phys. Today**, **June**, 26-32 (1996).
- [60] Radushkevich, L.V. & Lukyanovich, V.M. O strukture ugleroda, obrazujucesja pri termiceskom razlozenii okisi ugleroda na zeleznom kontakte. **Zurn Fisis Chim** **26**, 88-95 (1952).
- [61] Monthieux, M. & Kuznetsov, V.L. Who should be given the credit for the discovery of carbon nanotubes?. **Carbon** **44**, 1621 (2006).
- [62] Ebbesen, T.W. & Ajayan, P.M. Large-scale synthesis of carbon nanotubes. **Nature** **358**, 220-222 (1992).
- [63] Bethune, D.S., et al. Cobalt-catalysed growth of carbon nanotubes with single-atomic-layer walls. **Nature** **363**, 605-607 (1993).
- [64] Iijima, S. & Ichihashi, T. Single-shell carbon nanotubes of 1-nm diameter. **Nature** **363**, 603-605 (1993).
- [65] Thess, A., et al. Crystalline Ropes of Metallic Carbon Nanotubes. **Science** **273**, 483-487 (1996).
- [66] Journet, C., et al. Large-scale production of single-walled carbon nanotubes by the electric-arc technique. **Nature** **388**, 756-758 (1997).
- [67] Zhu, H.W., et al. Direct Synthesis of Long Single-Walled Carbon Nanotube Strands. **Science** **296**, 884-886 (2002).
- [68] Li, Y.-L., Kinloch, I.A. & Windle A.H. Direct Spinning of Carbon Nanotube Fibers from Chemical Vapor Deposition Synthesis. **Science** **304**, 276-278 (2004).
- [69] Botello, A.R., et al. Controlling the Dimensions, Reactivity and Crystallinity of Multiwalled Carbon Nanotubes using Low Ethanol Concentrations. **Chem. Phys. Lett.** (*in press*).
- [70] Hata, K., et al. Water-Assisted Highly Efficient Sintesis of Impurity-Free Single-Walled Carbon Nanotubes. **Science** **306**, 1362-1364 (2004).

Chapter 2. 2D and 3D Ordered Networks based on 1D nanostructures: *from design to properties calculations*

Abstract

The main goal of the theoretical part of this thesis corresponds to the study of the physico-chemical properties of Ordered Networks based on Carbon Nanotubes (ON-CNTs). As a starting point, there are necessary *ideal models*. On this line, it was started from “*scratch*” with the proposal of a general algorithm to generate ideal models of 2D and 3D networks (xyz coordinates) from 1D nanostructures as constructor blocks. Following the algorithm a set of ON-CNTs were generated and their electronic transport, mechanical, porosity, and surface area properties were calculated.

The electronic transport results revealed more favourable electronic paths along the nodes (multi-terminal junctions) suggesting a way to guide current along specific trajectories through this type of networks. The density of states (DOS) and local DOS (LDOS) analysis showed that the distribution of the electronic states plays a crucial role for the final conductance of the different electronic paths.

The mechanical properties calculations proved that the strength of the networks is correlated with the specific architecture independently of the chirality of the CNTs. The local strain analysis exposes that most of the strain concentrates at the nodes, therefore the final strength of the network is directly dependent of the geometry of the junctions imposed by the architecture. The axial compression revealed that these types of networks are able to support a length reduction four times larger than isolated CNTs.

Finally, the Connolly and van der Waals surface areas of the set of networks was calculated showing values as high as 2700 m²/g and 2800 m²/g respectively. The porosity of the studied systems makes them good candidates for exploring novel catalysts, sensors, filters or molecular storage properties.

2.1 Hierarchy algorithm	19
2.1.1 SuperSquare network	19
2.1.2 SuperGraphene network	20
2.1.3 SuperCubic network	20
2.1.4 SuperDiamond network	20
2.1.5 Computational and conceptual tools	22
2.2 Stability of the ON-CNTs	23
2.2.1 Configuration energy calculations	23
2.2.2 Experimental observations	27
2.3 Quantum conductance	28
2.3.1 2D ON-CNTs: <i>SuperSquare and SuperGraphene</i>	28
2.3.2 3D ON-CNTs: <i>SuperCubic and SuperDiamond</i>	31
2.4 Mechanical properties	35
2.4.1 Volumetric compression	35
2.4.2 Axial compression.	37
2.5 Surface area	40
Appendix: <i>Calculation Methods</i>	43
References	53

The main goal of the theoretical part of this thesis corresponds to the study of the physico-chemical properties of Ordered Networks based on Carbon Nanotubes (ON-CNTs). As a starting point, there are necessary *ideal models*. Along this line, it was started from “*scratch*” with the proposal of a general algorithm to generate ideal models of 2D and 3D networks (xyz coordinates) from 1D nanostructures as constructor blocks. Following the algorithm a set of ON-CNTs were generated and their electronic transport, mechanical, porosity, and surface area properties were calculated.

Ordered networks of 1D nanostructures (ON-1DNs) are attractive since they present features such as: i) the nodes (covalent junctions of 1D nanostructures) provide rigidity or flexibility to the network; ii) the electronic properties of the 1D blocks, once assembled can generate a nanocircuit or an addressable array; iii) the proposed networks are analogous to a porous material, and can therefore be used as catalytic supports, molecular sieves, or gas storage components, and iv) the pore size can be varied as a function of the architecture, the length of the super bond, and its diameter.

2.1 Hierarchy algorithm

The design of 2D and 3D periodic networks has been extended into a generalized algorithm able to build novel supercrystals from 1D nanostructures (e.g. nanotubes, nanowires or nanorods).

Covalent networks are designed by selecting 1D nanostructures as building blocks. A multi-terminal node can be generated by applying point group operations to these 1D building blocks. Subsequently, the concept of *hierarchy* is introduced, to use these nodes as the new building blocks, which by a new set of rules (space group operations) will result in complex architectures. These conceptual steps (schematically illustrated with CNTs in [Figure 2.1](#)) represent the *Hierarchy algorithm* able to generate crystallographically different types of 2D and 3D supercrystal models from 1D blocks.

The hierarchy algorithm can be employed to interconnect carbon nanotubes covalently, by adding nonhexagonal carbon rings (e.g. pentagons, heptagons or octagons; [marked in red in Figure 2.1](#)) [1] in various ways (dictated by *Euler's law*, see appendix with illustrative examples) to form planar squared or hexagonal supersheets (Super-square **SS** or super-graphene **SG**) or 3D superlattices (Super-cubic **SC** or super-diamond **SD**).

2.1.1 SuperSquare network

This network can be obtained by repeating, with translation operations, a multi-terminal cross-junction node. This node is built by joining pairs of CNTs at an angle of 90° using pentagons, heptagons, and octagons ([colored in red in Figure 2.1](#)).

The SuperSquare (SS) block made up of (6,6) CNTs is constructed by inserting two vertical (6,6) tubes and two horizontal (6,6) tubes. Each horizontal tube requires a tubular rim containing four heptagons, two octagons, and two pentagons in order to keep the connectivity of the node ([see red rims shown in Figure 2.1](#)). The (10,0) SS block is built in a similar manner, but in this case the tubular rims require four octagons, four pentagons, and two heptagons (dictated by *Euler's law*, [see appendix](#) with illustrative examples). An additional hybrid SS block

was constructed by combining (6,6) and (10,0) CNTs, providing an alternative possibility of metal-semiconductor nanotube network. The latter hybrid networks is generated by connecting two vertical (6,6) tubes and two horizontal (10,0) tubes with three heptagons per quadrant.

2.1.2 SuperGraphene network

This particular architecture includes a pair of 3-terminal nodes interconnected covalently by a superbond made up of a straight CNT. Three CNTs are joined at 60° angles (similar to a Y junction) with a pair of heptagons embedded in each 60° angle (see Figure 2.1). This node is reflected by a mirror plane so as to complete a 2D SG building block. It is interesting that SG networks can be obtained when adding only heptagons (two per 60° angle) connecting either (6,6) or (10,0) CNTs.

2.1.3 SuperCubic network

The building blocks for the SC architecture stem from six CNTs, and are arranged perpendicularly from each face of a cubic cell. In order to interconnect (6,6) CNTs, octagons need to be positioned at each 90° angle between the tubes (the total number of octagons is 12; see Figure 2.1). Similarly, (10,0) CNTs require a pair of heptagons in each 90° angle between tube pairs in order to construct the SC block. These SC architecture resembles the Schwarzite type P [2], from their topological equivalency.

2.1.4 SuperDiamond network

The SD building blocks are constructed when joining four CNTs tetrahedrally. Each tube emerges from the faces of a tetrahedron on the [111], [-1-11], [1-1-1], and [-11-1] directions (mimicking the atomic carbon diamond geometry). For the (6,6) SD block, we are restricted to insert an octagon at the intersection between each pair of CNTs in order to maintain the threefold coordination of each atom (a total number of six octagons are required; Figure 2.1); whereas the (9,0) SD block requires a triplet of heptagons at the intersection of three tubes (a total of four triplets of heptagons are required). The SD architecture presents a topological equivalency with Schwarzite type D [2].

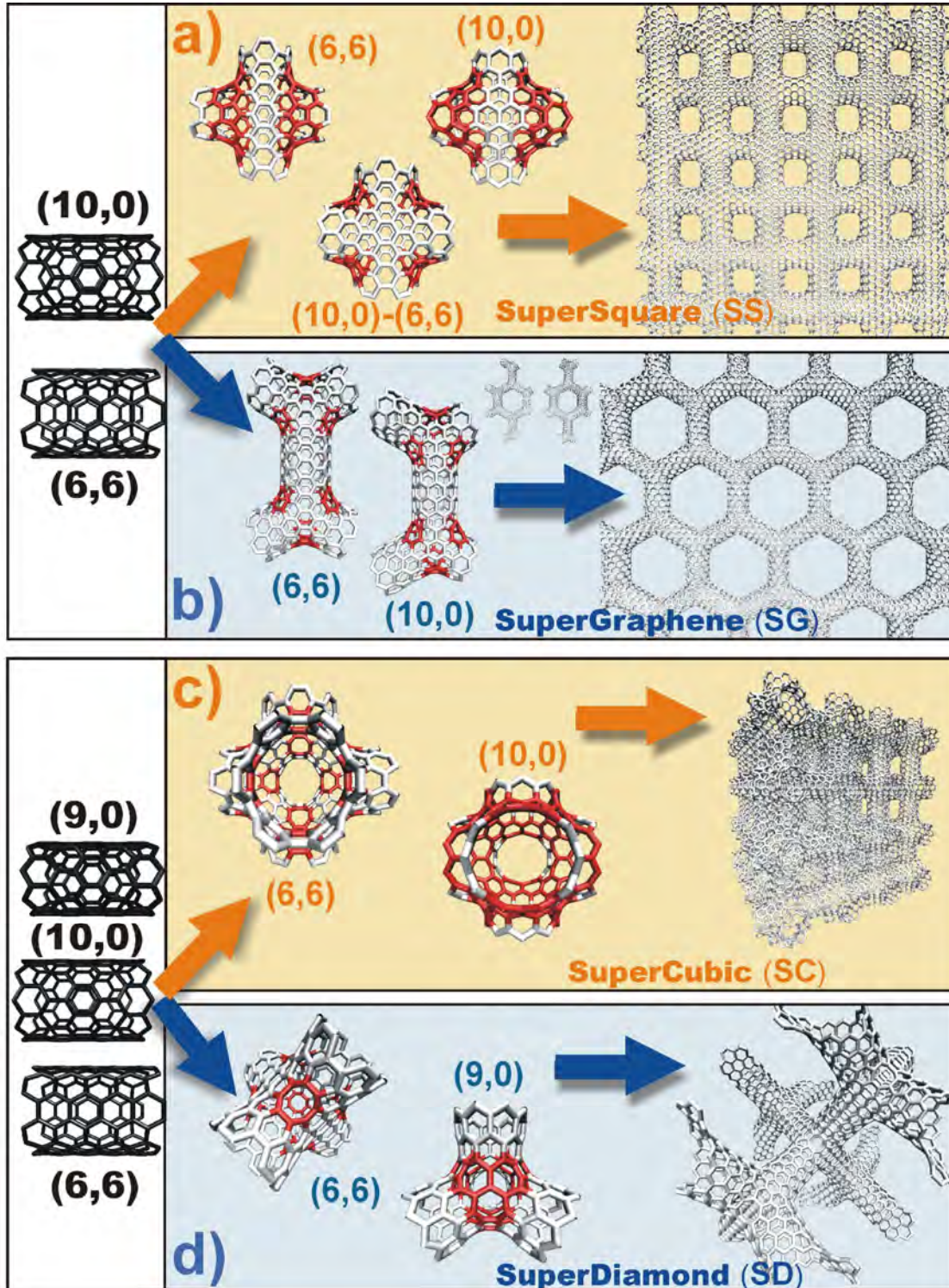


Figure 2.1 Illustration of the Hierarchy Algorithm. Starting with a 1D building block and following symmetry rules (point group operations) multi-terminal devices are obtained. An additional level of hierarchy is accomplished when the multi-terminal devices become the new building blocks, then a different set of rules (translation operations) is applied in order to obtain the ON-CNTs. Marked with red are the topological defects (non hexagonal rings) necessary to induce curvature. Section a) depicts the SuperSquare architecture, b) the SuperGraphene network; c) the SuperCubic array while d) the SuperDiamond type.

This set of networks to explore in this work is illustrated on the right column of Figure 2.1. Each of the four architectures have an *armchair* version and a *zigzag* version. Then the ON-CNTs set is composed of eight different networks and a ninth element designed from a mixture of armchair and zigzag nanotubes, in the case of the SS architecture. The nine multi-terminal blocks (which by translation operations build the networks) are presented in Figure 2.2.

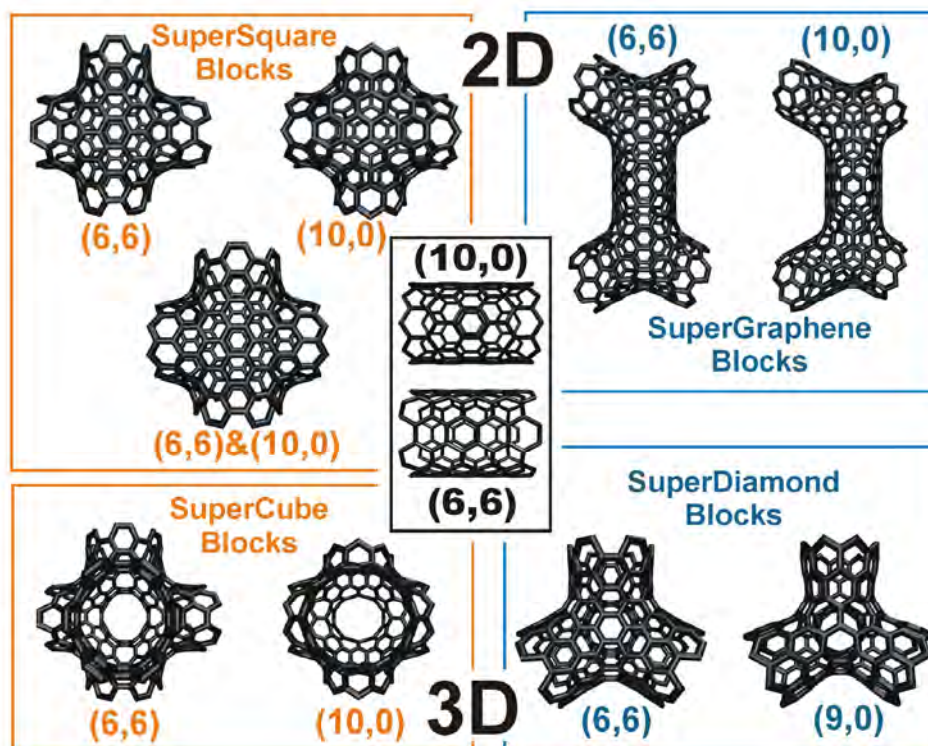


Figure 2.2 The nine constructor blocks to build the ON-CNTs. Repeating them by translation operations the 2D and 3D networks are obtained.

2.1.5 Computational and conceptual tools

Some computational tools together with crystallography concepts were needed in the design of the ON-CNTs (some examples applying the Gaussian curvature concepts to specific networks are included in the Appendix of the present chapter).

i) genera_SWNT.for : A program written in Fortran 77 to construct CNTs of a given chirality and number of atoms given by the user (*the software is based on space mappings from the cartesian coordinates into cylindrical coordinates, transforming graphene coordinates into a Carbon Nanotube*).

ii) rotaYtraslada.for : A program written in Fortran 77 to rotate and translate any structure in space by the angles and translation vectors defined by the user (*based on the Rotation Matrix and simple Translations*).

iii) General concepts of Crystallography : Point groups and space groups, specially from the graphite and diamond structure.

iv) Gaussian curvature concepts, specifically applied to sp^2 carbon sheets [3].

2.2 Stability of the ON-CNTs

2.2.1 Configuration energy calculations

The *configuration energy* of the networks was calculated, and compared with already existing structures in nature in order to confirm their plausible existence.

The stability of the systems was calculated using the empirical many-body *Tersoff-Brenner potential* [4-5], which has proven to be remarkably reliable for energetics of sp^2 -hybridized carbon structures [6] and is accurate to reproduce lattice constants, binding energies, and the elastic constants of both graphite and diamond [5]. The quality of the energetic stability values obtained from the empirical potential were verified with DFT calculations.

The constructor blocks were first optimized (relaxed) using periodic boundary conditions (*i.e.* relaxing the full networks) by a conjugated gradient algorithm to obtain the minimum energy configuration. The configuration energy values obtained were normalized by the amount of atoms in each structure. The energies per atom are presented in [Figure 2.3](#).

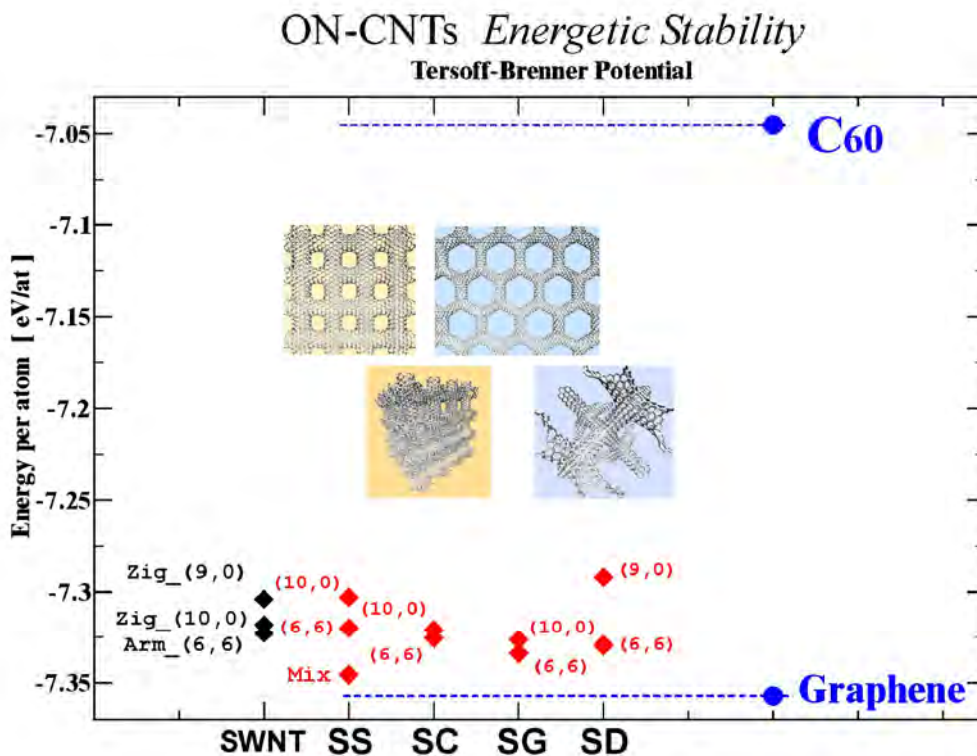


Figure 2.3 Configuration energy values per atom for each network. It is indicated by dashed lines the limiting values for the fullerene and graphene. The left column corresponds to SWNTs. All calculations were performed using the Tersoff-Brenner potential.

The limiting values of graphene and fullerene C₆₀ calculated with the same empirical potential can be seen in [Figure 2.3](#) with dashed lines. The energy values for all the structures are less than the energy value for the fullerene, identified in nature [7]. In addition, the networks are close in energy to graphene and completely in the energy range for the three single wall nanotubes calculated

[(6,6), (10,0) and (9,0)]. These results give plausibility to the ON-CNTs designed.

Compare the values obtained from the two different formalisms, in [Table 2.i](#) (DFT calculations values) and [Table 2.ii](#) (values obtained using the empirical potential).

	DFT	Energetic	Stability
	Energy per atom [eV/lat]	$E_{\text{Network}}-E_{\text{Graphite}}$ [eV/lat]	$E_{\text{Network}}-E_{\text{C60}}$ [eV/lat]
single C atom	-0.078		
C ₆₀ Fullerene	-9.74		
(6,6)-(10,0) SS	-9.98	0.145	-0.240
(6,6) SS	-9.94	0.185	-0.200
(10,0) SS	-9.92	0.205	-0.180
(10,0) SG	-9.97	0.155	-0.230
(6,6) SC	-9.92	0.205	-0.180
(10,0) SC	-9.86	0.265	-0.120
Graphite	-10.13		

Table 2.i Stability energy values obtained using DFT calculations. The difference with respect to the Graphite and Fullerene are shown in the different columns as a comparison with reference structures.

	Tersoff-Brenner Energetic Stability	
	$E_{\text{Network}}-E_{\text{Graphene}}$ [eV/lat]	$E_{\text{Network}}-E_{\text{C60}}$ [eV/lat]
(6,6)-(10,0) SS	0.032	-0.300
(6,6) SS	0.057	-0.275
(10,0) SS	0.074	-0.258
(6,6) SG	0.043	-0.289
(10,0) SG	0.051	-0.281
(6,6) SC	0.052	-0.280
(10,0) SC	0.056	-0.276
(6,6) SD	0.048	-0.285
(9,0) SD	0.085	-0.247
(6,6) CNT	0.054	-0.278
(10,0) CNT	0.059	-0.273
(9,0) CNT	0.073	-0.259

Table 2.ii Stability energy values obtained using Tersoff-Brenner potential. The networks energy values are compared with isolated CNTs (the three last lines). The values correspond to the difference with respect to Graphene and Fullerene.

Following the Tersoff-Brenner potential, the energy at each atomic site was obtained. From this type of local information, a parameter that can be interpreted as the *strain energy* is obtained, due to deformations on the carbon mesh (strictly speaking, the strain energy is usually defined as the difference between the local energy value obtained on a site and the value for a carbon atom immersed in the perfect sheet of graphene).

The strain energy is presented by a color scale on the different constructor blocks. The main trend observed is that plane regions have the lowest values of strain energy, as the curvature is higher around pentagon rings, the strain energy increases.

The strain energy for the SS and SG blocks is shown in Figure 2.4. It can be seen how the regions without defects (*i.e.* arrays of hexagons which induce planar regions) have a minimum value of strain energy; while the defects, specially the pentagons, induce the higher values of strain energy.

The SC and SD blocks in Figure 2.5 have lower value of strain energy, presenting hereby good stability for such structures. The (9,0) SD block is the only one showing few points with higher value of strain energy. These are points located at the defective region formed by the triplets of heptagons (necessary to induce the negative gaussian curvature).

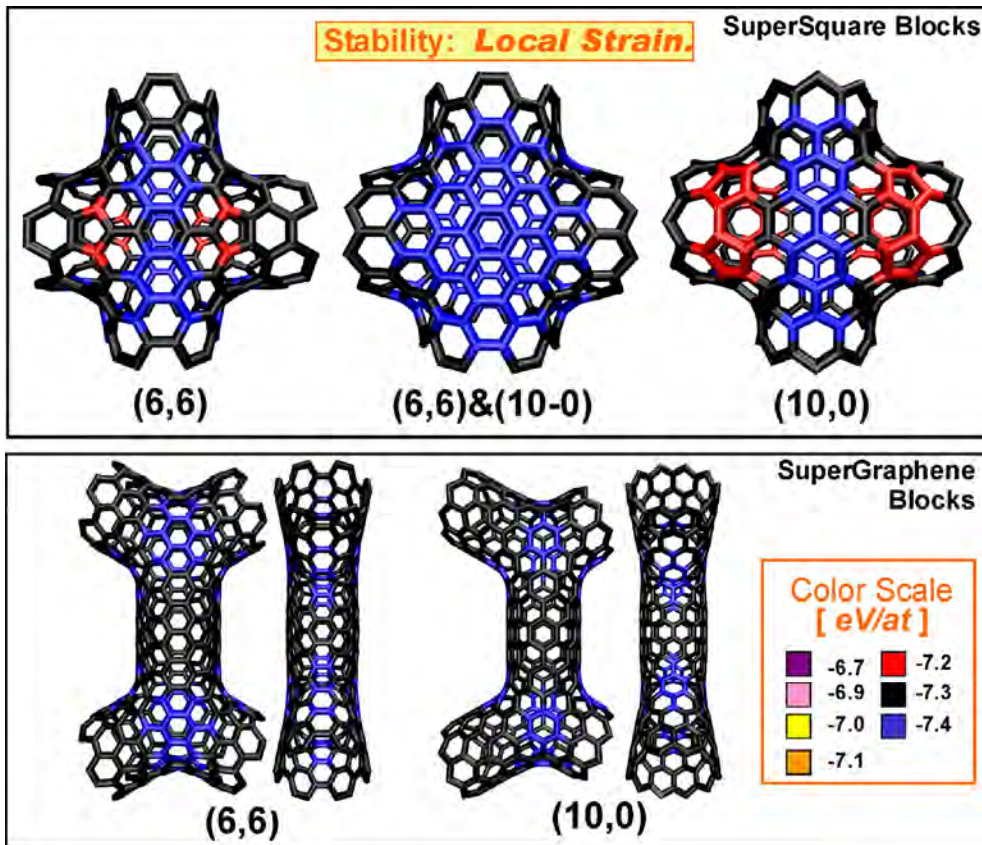


Figure 2.4 Local strain energy on the multi-terminal nodes conforming to the 2D networks. The values are calculated as a difference between the local energy value obtained on a site and the value for a carbon atom immersed in the graphene sheet. The color scale points out that the regions around the pentagons are less stable due to the induced curvature.

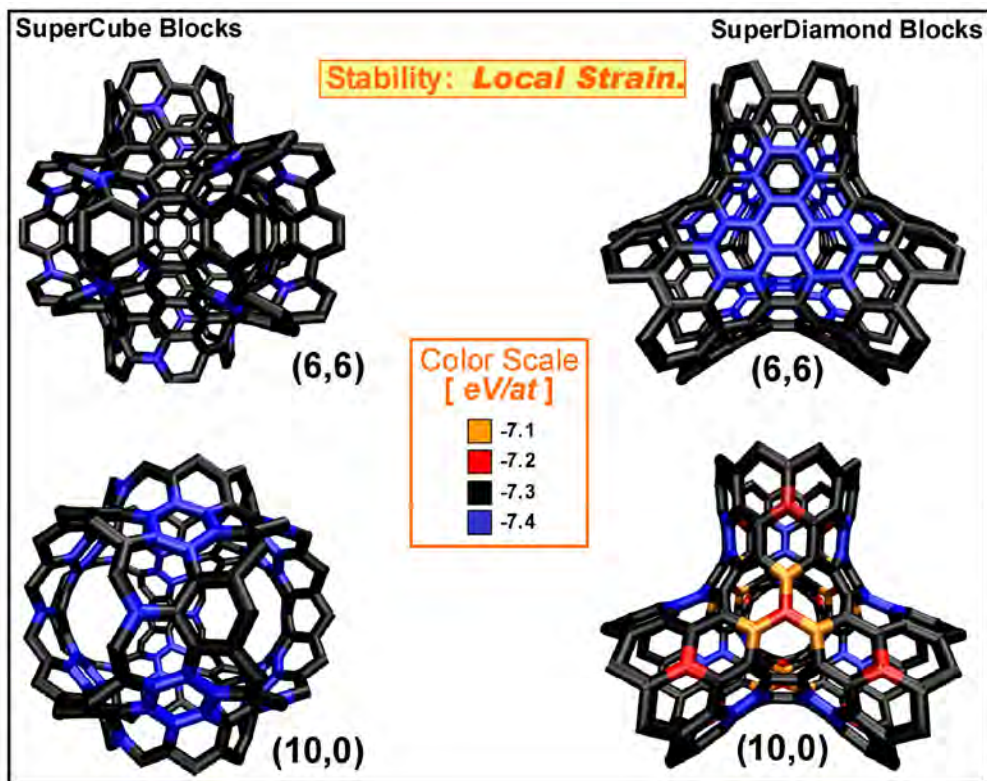


Figure 2.5 Local strain energy on the multi-terminal nodes conforming the 3D networks. The most stable regions (blue) correspond to the planar points along the structure.

2.2.2 Experimental observations

Experimental junctions were obtained from chemical vapor deposition (CVD) methods involving the thermolysis of nickelocene (NiCp_2) powder in conjunction with thiophene ($\text{C}_4\text{H}_4\text{S}$) in an argon atmosphere at $1000\text{ }^\circ\text{C}$; explained in detail in Chapter 4.

The branched carbon arrays were experimentally observed by SEM to study their morphology and specifically the angles in the most stable junctions in order to propose novel theoretical models. Even when the experimental junctions correspond to isolated nodes of thicker 1D carbon blocks (concentric carbon tubes micrometers in diameter; see Chapter 4 for more details), they represent evidence of specific branching geometries stable in nature as a starting point for the theoretical design of plausible models.

Figure 2.6 shows that the junctions are covalently connected in a variety of stable ways, such as a junction with the geometry of a 3D SC network node (see Fig. 2.6.b), a T-junction and a cross-junction with the geometry needed in a 2D SS network (Fig. 2.6.c and 2.6.d), a 3-terminal junction with the necessary angles in a 2D hexagonal network (Fig. 2.6.e), and a 4-terminal junction with a tetrahedral-like architecture (Fig. 2.6.f)

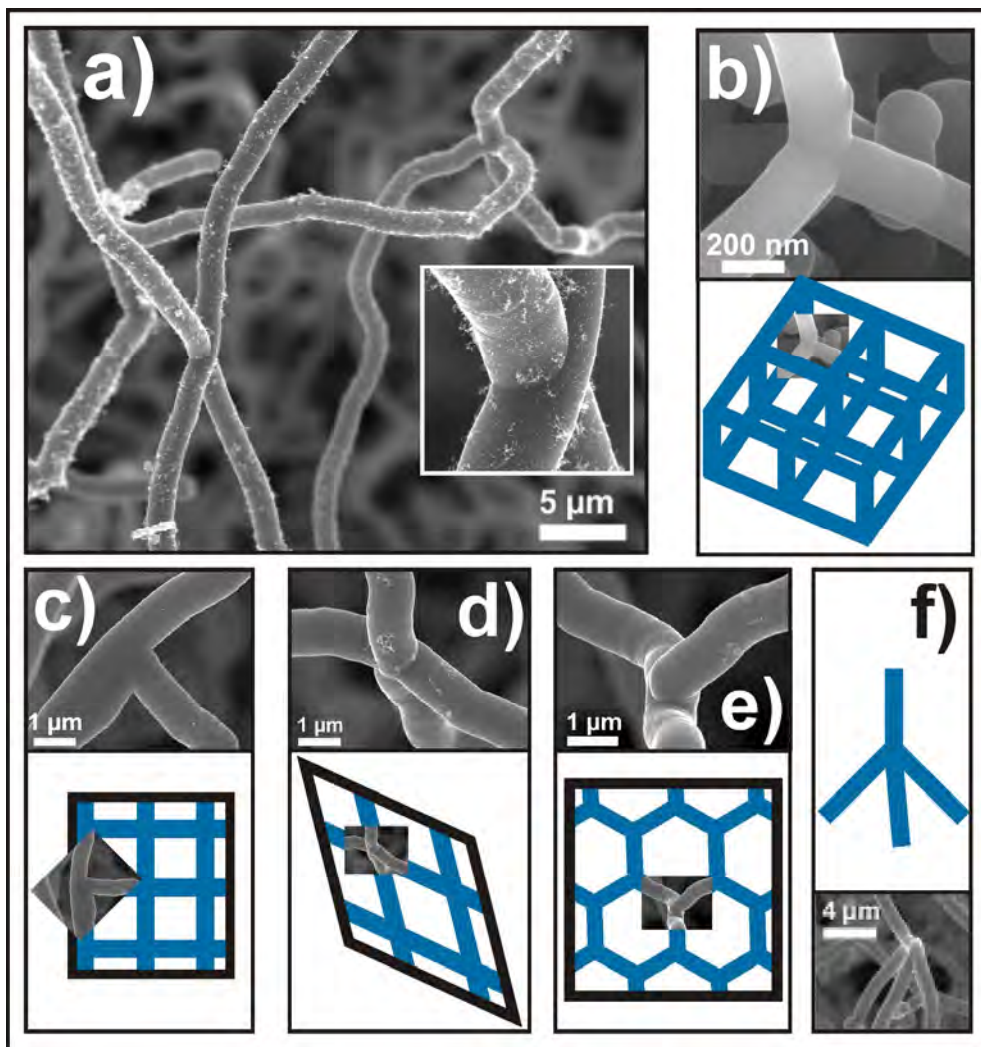


Figure 2.6 Experimental junctions obtained by CVD (see chapter 4). Their angles and geometries are similar to the b) SC, c) SS, d) SS, e) SG or f) SD architecture, respectively.

2.3 Quantum conductance properties

The electronic transport properties of the proposed ON-CNTs were explored using the Landauer-Buttiker formalism [8] together with equilibrium Green functions. A four orbital per atom tight-binding Hamiltonian, parametrized for carbon sp^2 networks, was used to calculate the electronic properties [9] (see [calculation methods appendix](#) for more details). The basic multi-terminal blocks (nodes of the networks) were considered and analyzed as multi-terminal devices.

2.3.1 2D ON-CNTs: *SuperSquare* and *SuperGraphene*

□ *SuperSquare* network

Three different networks with SS architecture were constructed from: (6,6) armchair nanotubes, (10,0) zigzag nanotubes and a mixture of (6,6) armchair and (10,0) zigzag nanotubes. [Figure 2.7](#) presents the conductance graphs, together with the basic blocks analyzed in the upper panel where the defective rings (pentagons, heptagons or octagons) from one of the octants are marked in red (repeated by 3 mirror planes bisectors of the structure: the plane on which the octant is situated and the two planes perpendicular to the first one, which contain the axis of one of the tubes).

The multi-terminal devices studied show three inequivalent paths: going straight and crossing through the “belt of defects” [A \leftrightarrow B], going straight without crossing “belt of defects” [D \leftrightarrow E], and turning 90° at the node (joining point) [A \leftrightarrow D].

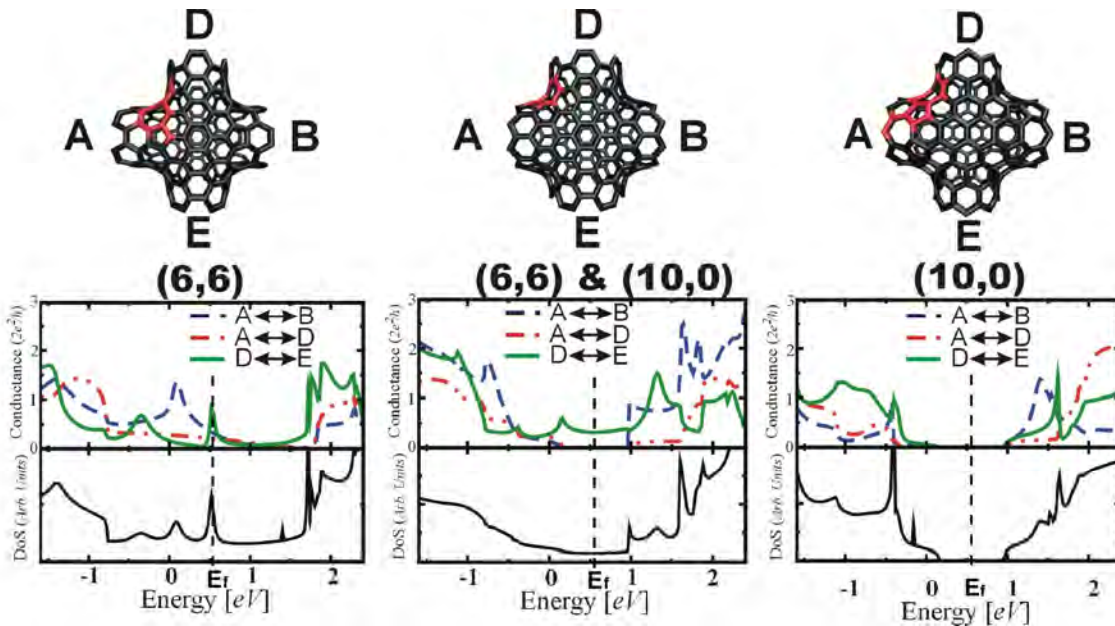


Figure 2.7 Conductance, electronic density of states, structure and defect positions for SS blocks. Remarkably the conductance result obtained for the (6,6)&(10,0) SS block, where only path D \leftrightarrow E is conducting (green continuous line) around the Fermi level, while path A \leftrightarrow B and A \leftrightarrow D present a conductance gap; therefore suggesting that the electronic current can be guided through specific paths along this type of networks.

The constructor block for the (6,6) SS network presents a peak of $\sim 1[2e^2/h]$ at the Fermi level (~ 0.5 eV) for the $D \leftrightarrow E$, as well as a small conductance for the $A \leftrightarrow B$ and $A \leftrightarrow D$; corresponding then to a conductor node. The most favourable path is the $D \leftrightarrow E$, which is the path with fewer defects. It is worthy to mention the peak from path $A \leftrightarrow B$ at ~ 0.06 eV, where the most favourable path has totally changed in a relative short range of energy. This brings the idea of a “switching” mechanism between terminals by tuning the energy of the travelling electrons.

The (10,0) SS block presents a gap of ~ 0.75 eV, consistent with the electronic structure of the isolated (10,0) nanotubes.

The (6,6)&(10,0) SS block shows a remarkable result, since there is a conductor path through $D \leftrightarrow E$ (the armchair path) and conductance gaps for the other two paths; therefore a selectivity of a trajectory for the electrons to travel along the network is obtained. It could then be envisioned, by designing appropriately a network (bottom-up approach), to guide current along nanocircuits.

□ **SuperGraphene network**

Two versions of the SG architecture were analyzed: one constructed from (6,6) armchair nanotubes and a second version build from (10,0) zigzag nanotubes. Three inequivalent paths due to their conductance are observed in [Figure 2.8](#): the shortest path [$A \leftrightarrow E$] and two different paths crossing the nanotube connecting the two joining points in the constructor block [$A \leftrightarrow B$ and $A \leftrightarrow D$].

Both networks present a gap in the conductance curves. The (10,0) SG block reveals a conductance gap consistent with the semiconducting properties present in the density of states (DOS) graph.

The (6,6) SG block shows a conductance gap even when there are states all around the Fermi level in the DOS graph. The distribution of electronic states at 0.30eV (Local Density of States (LDOS); [see Figure 2.8](#)) exhibits a lack of states at the nanotube connecting both joining points, which explains the zero conductance through paths $A \leftrightarrow B$ and $A \leftrightarrow D$. On the $A \leftrightarrow E$ path we can see blue rings concentric to the tube axes with almost no states plus some isolated white spots (which give the contribution to the DOS curve), showing not only the existence of electronic states at the DOS graph but also their distribution on the block plays a crucial role in the selectivity of conduction paths.

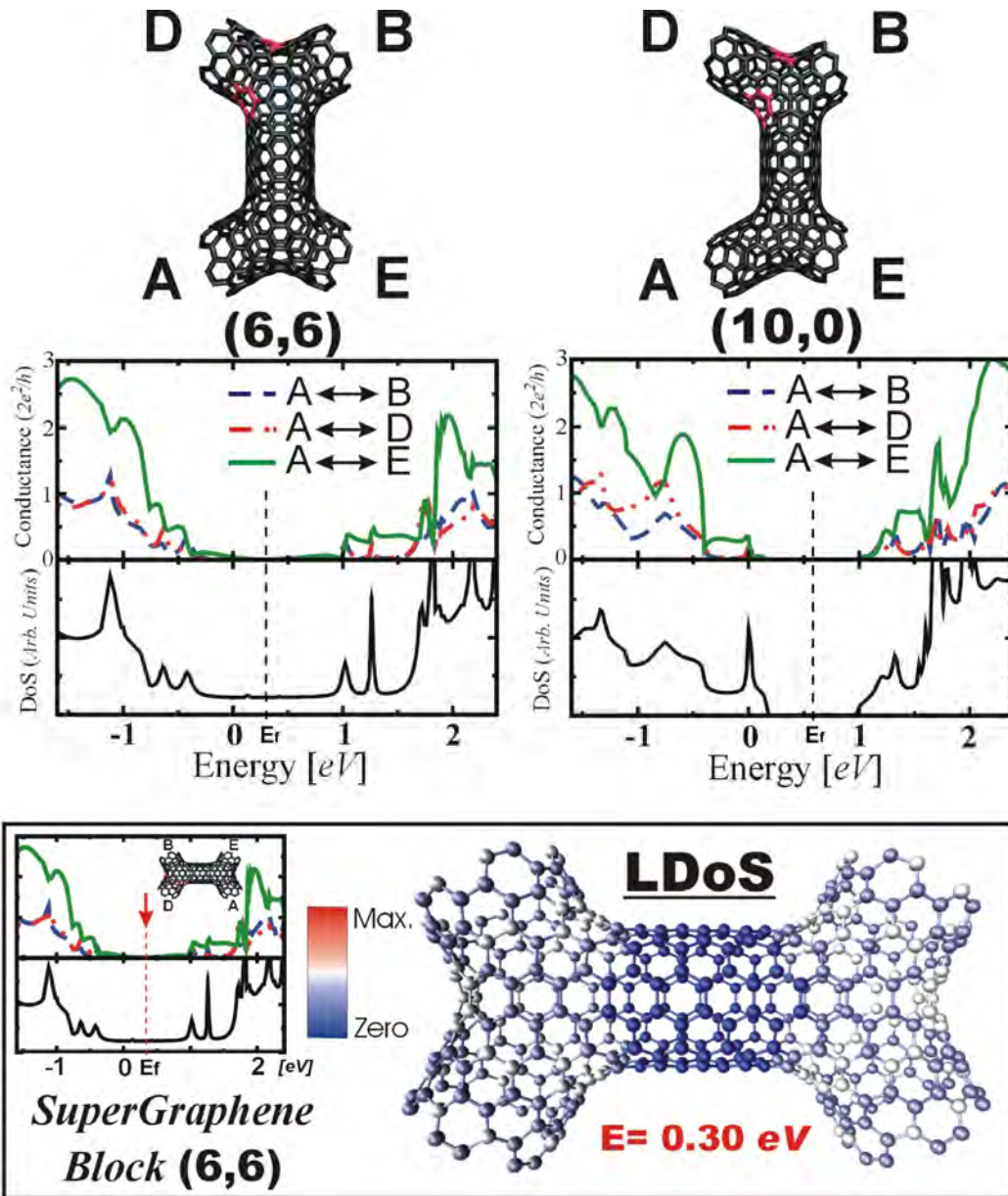


Figure 2.8 Conductance, electronic density of states, structure, and defect positions for SG blocks are presented in the upper panel. The lowest panel shows the LDoS at 0.30eV of the (6,6) SG block, revealing that even with the existence of electronic states in the DOS curve, their spatial distribution plays a crucial role to explain the zero conductance around the Fermi level. The (10,0) SG block shows a gap in the DOS curve around the Fermi energy, characteristic of the (10,0) chirality.

2.3.2 3D ON-CNTs: SuperCubic and SuperDiamond

□ SuperCubic network

Using the same (6,6) armchair and (10,0) zigzag nanotubes two SC network versions were designed. The conductance curves together with the structure of the basic blocks are presented in Figure 2.9 (the defect rings remarked with red color).

Two inequivalent paths are obtained: going straight [$A \leftrightarrow B$] and turning 90° at the node [$A \leftrightarrow D$].

The (6,6) SC network presents, at ~ 0.8 eV over and under the Fermi energy, an equivalent conductance for any of the possible paths that the travelling electrons could take; meanwhile, around the Fermi level the conductance is increased considerably for the $A \leftrightarrow B$ path. This points out a “switching” mechanism between paths, by tuning the energy of the travelling electrons, envisioning the possibility of guiding electronic current through the network.

The (10,0) SC block shows an electronic structure with a semiconductor gap of ~ 0.75 eV.

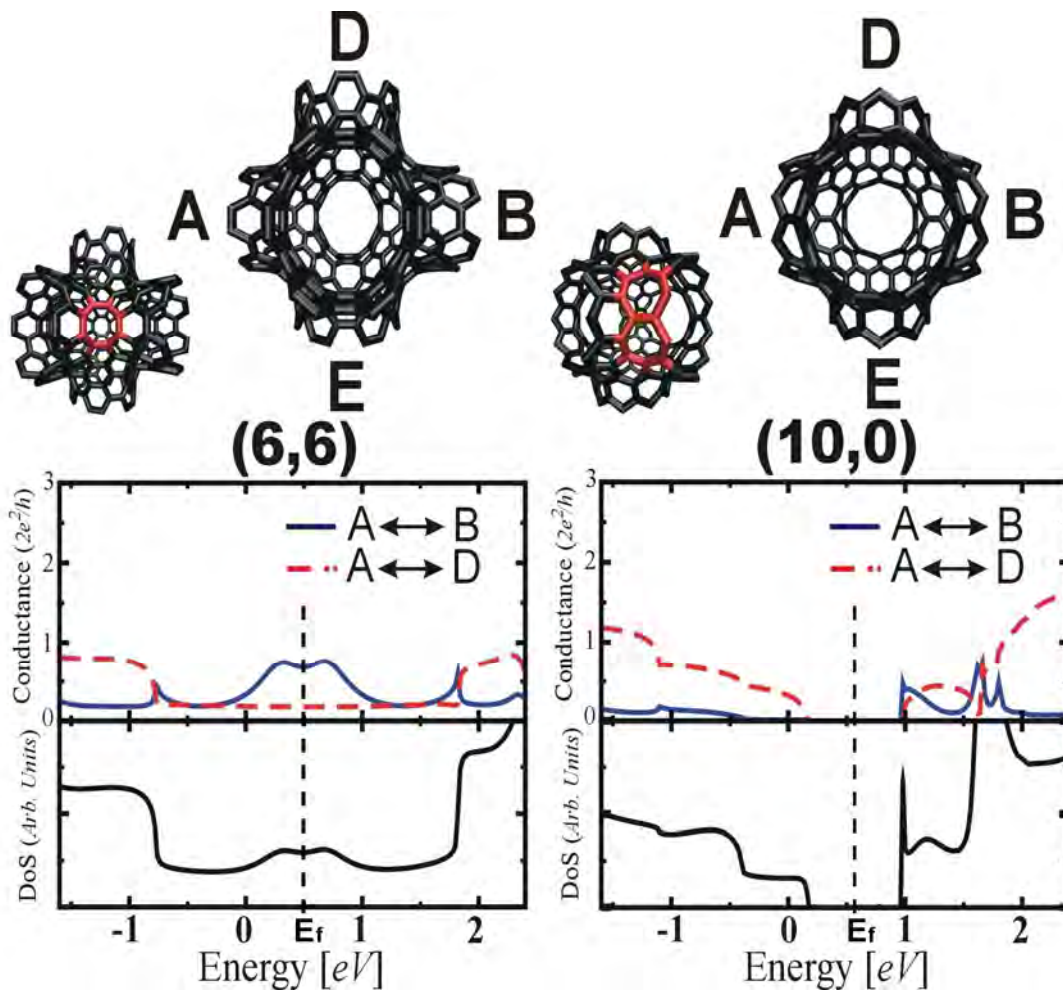


Figure 2.9 Conductance, density of states, structure and defect positions for SC blocks. The (6,6) SC block presents a dominant conductance behavior, electronic paths $A \leftrightarrow B$ and $A \leftrightarrow D$ present equivalency at certain energy ranges while inequivalency at the energy domain around the Fermi level; this suggests a switching concept that could be activated by tuning the energy.

The LDOS allows us to understand in more detail the electronic transport properties of the (6,6) SC block, when the distribution of electronic states at $E = -0.38\text{eV}$ (all equivalent paths) and around the Fermi level $E = 0.50\text{eV}$ ($A \leftrightarrow B$ the favoured path) is compared in Figure 2.10. It can be seen at $E = 0.50\text{eV}$, that the defect rings (octagons) are activated and the SC architecture constrains their positions in such a manner that their distribution opens a straight path of allowed states coming from three different octagons close enough to overlap or communicate between them (indicated by an arrow on the figure).

An isolated octagon causes a localized amount of states at certain energy values, playing the role of scatterers [10]; in contrast, the SC architecture connects the electronic states from the octagons delocalizing them and raising up an electronic trajectory through the block.

Therefore, the distribution of defects plays a dominant role in the conductance of networks. In addition, this distribution will be constrained by the specific architecture, giving different conductance properties to the networks depending on their specific architecture.

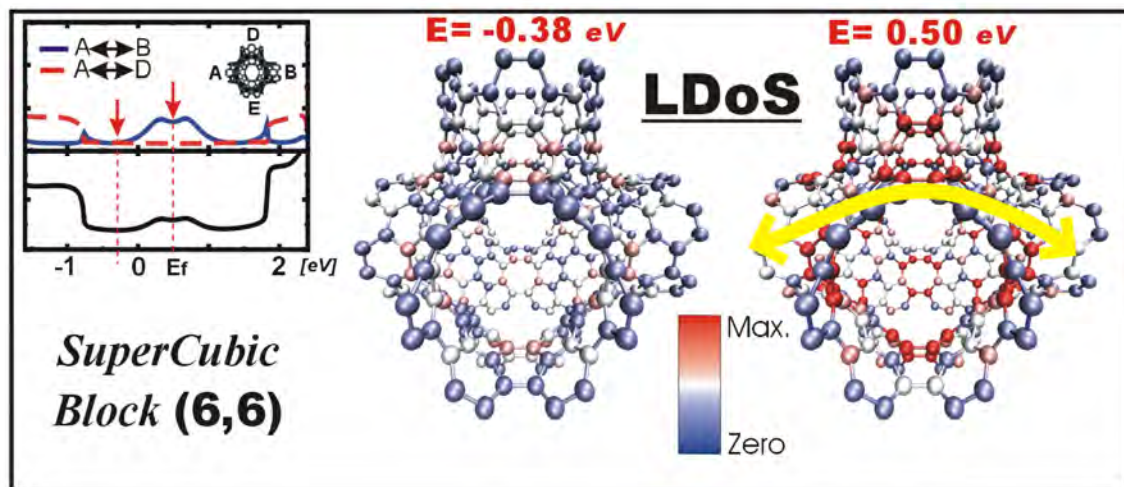


Figure 2.10 Comparison of the LDOS of the (6,6) SC block at -0.38eV and 0.50eV showing that the position of the octagons constrained by the SC architectures plays a crucial role opening a conductance path and therefore increasing the conductance through path $A \leftrightarrow B$ at 0.50eV (around the Fermi level).

SuperDiamond network

The SD architecture is a special case, the zigzag version has been built from (9,0) nanotubes, since the Diamond geometry imposes tubes with a symmetry axis C_3 along the nanotube axis; this automatically imposes only conductors zigzag tubes to obtain this architecture. The armchair version was built from the same (6,6) nanotubes.

The SD architecture revealed that all the possible electronic paths are equivalent in conductance, as shown in Figure 2.11.

The (6,6) SD block presents zero conductance around the Fermi level, even when electronic states are present, as can be seen on the DOS graph.

The (9,0) SD block shows semimetallic properties, with a tiny gap in the range of meV.

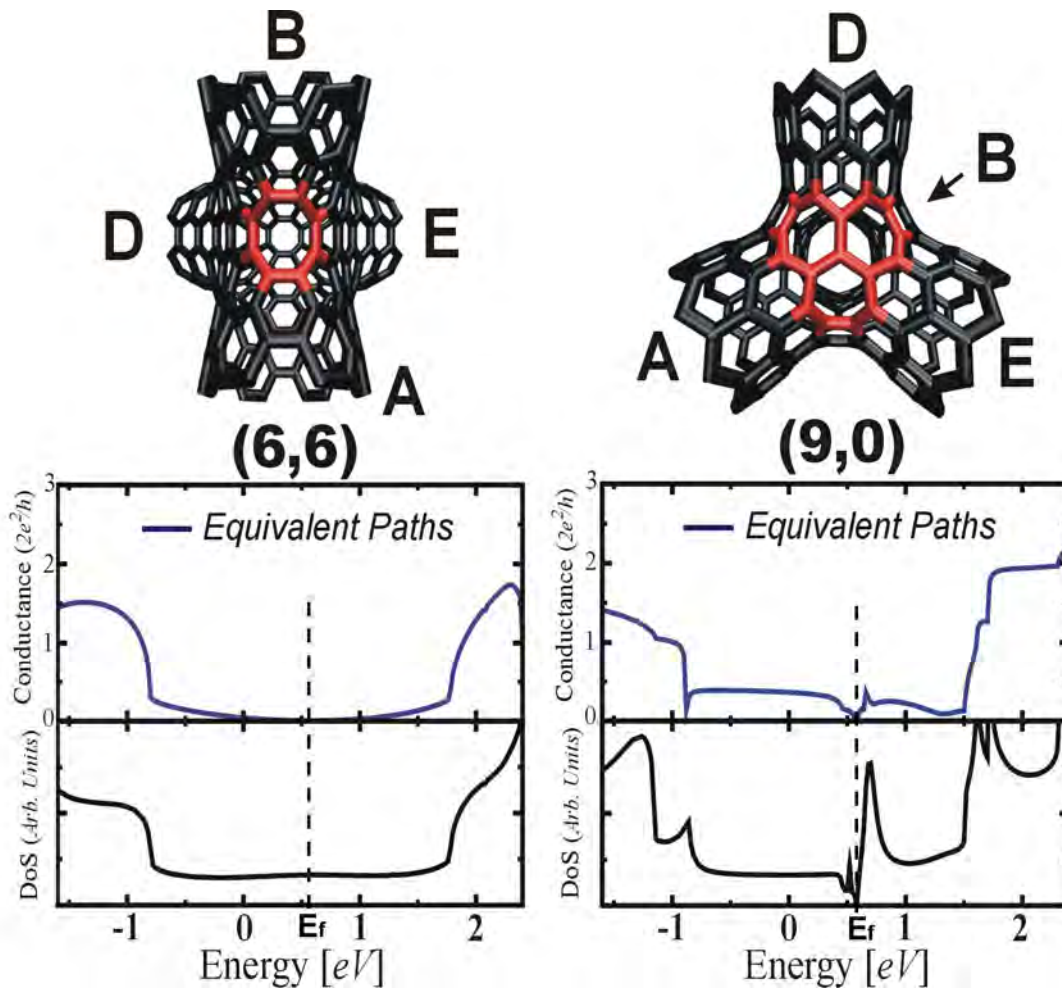


Figure 2.11 Conductance, density of states, structure and defect positions for SD blocks. The SD architecture imposes conductance equivalency along all the different electronic paths. The (6,6) SD architecture presents zero conductance around the Fermi energy even with the existence of electronic states in the DOS curve. The (9,0) SD block presents a semi-metallic behaviour.

Some general trends can be emphasized:

i) The distribution of the LDOS along the structure plays a crucial role to understand the conductance through the different paths along the basic blocks (nodes).

ii) The distribution of defects plays a critical role in the conductance of networks. This distribution is constrained by the specific architecture. Therefore the specific architecture dictates different conductance properties to the networks.

iii) Depending on the architecture, different paths through different terminals show conductance inequivalencies. As a consequence, a travelling electron will have more favourable paths to cross the block at each node in the network. Therefore, one could think of having specific paths over the whole network with more electronic flux.

iv) This idea allows to envision how to control and lead electronic current through specific trajectories for organic electronic nanocircuits.

Figure 2.12 explicitly shows how the specific architecture dictates different electronic and conductance properties for each network.

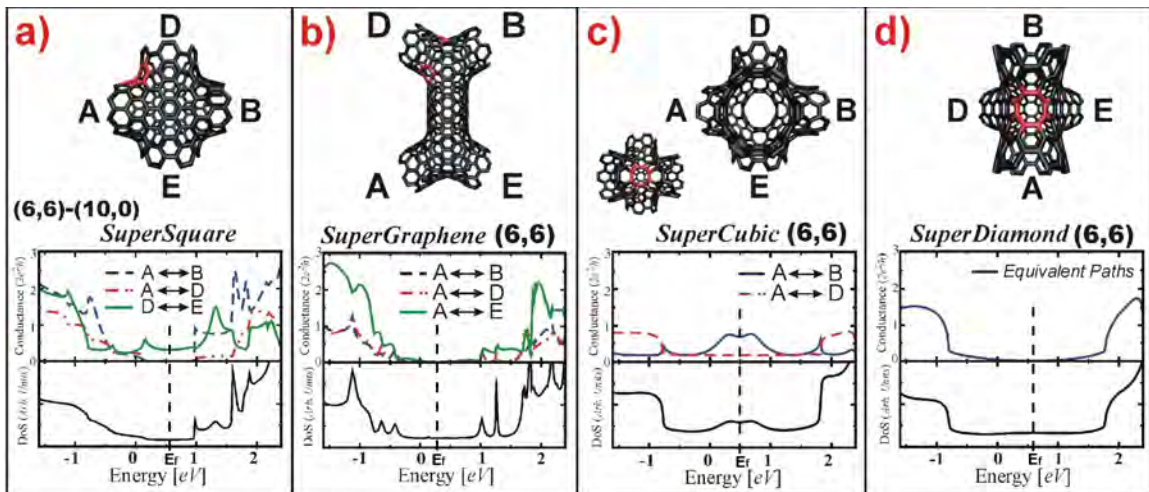


Figure 2.12 Architecture dictates the final electronic and conductance properties of the networks. Four different architectures built up from the same building block (a (6,6) CNT) present completely different DOS characteristics and conductance properties. a) corresponds to the SS, b) to the SG, c) to the SC and d) to the SD architecture.

2.4 Mechanical properties

The mechanical properties of the ON-CNTs were calculated using the Tersoff-Brenner potential [4-5], which has proven to be remarkably reliable for energetics of sp^2 -hybridized carbon structures [6] and is accurate when describing geometrical transformations under mechanical strain [11-12]. Systematic structural studies of these systems using first principles calculations, such as density functional theory (DFT), are in general precluded because of their large number of atoms per unit cell. Mechanical properties results based on the Tersoff-Brenner potential have been reported to be in close agreement with more sophisticated ab initio [13-15] or tight binding values [14], as well as with recent experimental observations [16].

The mechanical study was performed under volumetric and uniaxial compression of the 3D networks.

2.4.1 Volumetric Compression

The strain energy (energy difference with respect to the equilibrium configuration) vs. strain curves for both the (6,6) and (10,0) SC networks are very similar (overlapped red and black continuous curves on Figure 2.13). A similar trend is observed for both the (6,6) and (9,0) SD networks (see overlapped green and blue curves on Figure 2.13). These results reveal that the bulk mechanical properties of the networks are independent of the nanotube chirality and are dictated by the specific architecture.

The estimated volumetric modulus is ca. 63 GPa for the SC architecture and ca. 80 GPa for the SD architecture (note that our calculations were also able to reproduce the results reported on individual nanotubes performed by Yakobson *et al.* [11] and Hernandez *et al.* [14]).

A fine analysis indicates that the local strain energy due to volumetric compression of the networks leads to a maximal stress concentrated on the nodes (see Figure 2.13.b). The ultimate strength of the nanotube network is therefore dominated by the strength of the nodes, as illustrated with the snapshots in Figure 2.13.b where the networks finally collapse right at the node.

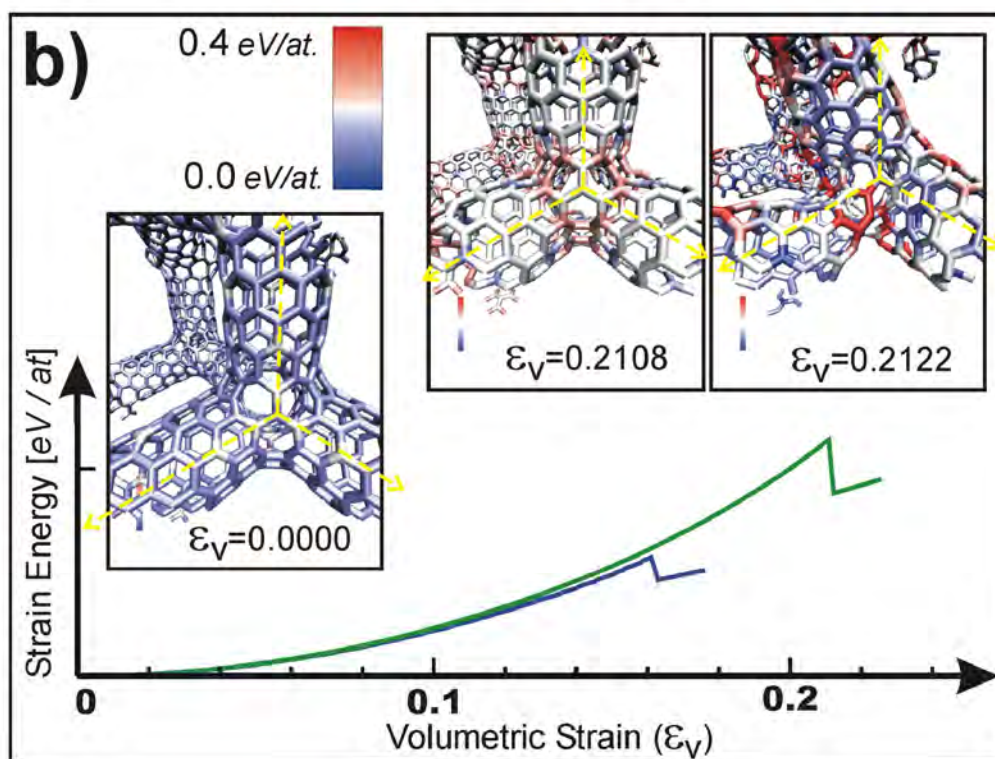
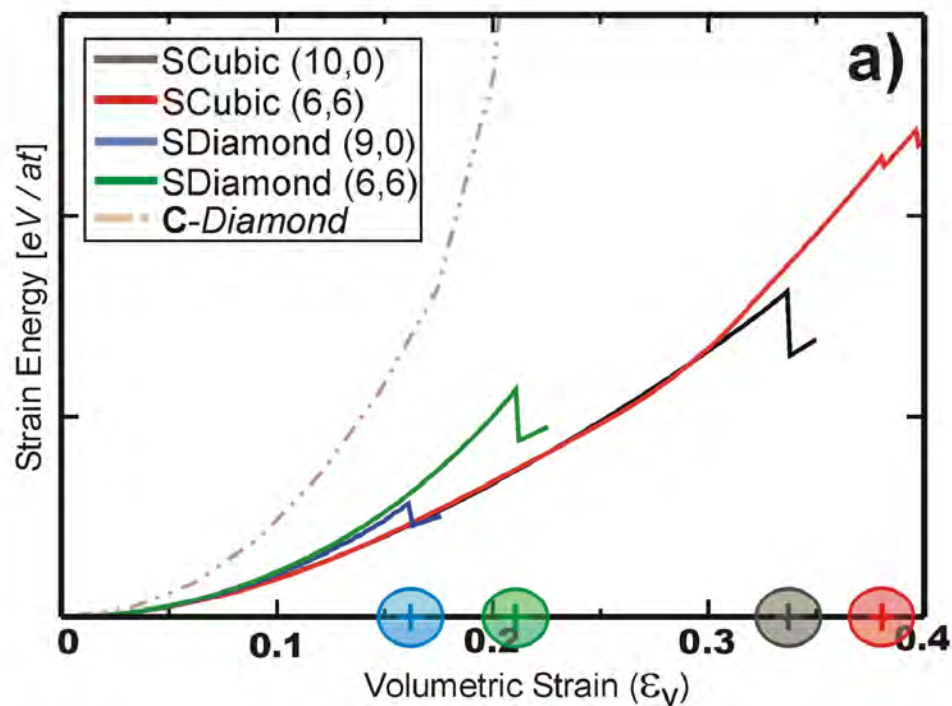


Figure 2.13 Volumetric compression applied to the 3D networks. Graph in a) shows the strain energy vs. volumetric strain obtained, note that is dictated by the architecture and is independent of chirality. Figure b) shows how the strain concentrates right at the nodes, therefore the properties of the network depend on the node geometry.

2.4.2 Axial compression

The same trend was observed when axial (unidirectional) compression was applied, a similar mechanical behaviour for the same architecture networks independent of the chirality of the nanotubes (see graphs in Figure 2.14). The estimated Young modulus (under axial compression along the [001] axis) for the SC architecture corresponds to ca. 100 GPa for both chiralities; while for the SD architecture (under unidirectional compression along the [111] and [001] axis) they correspond to ca. 120 GPa and 75 GPa respectively.

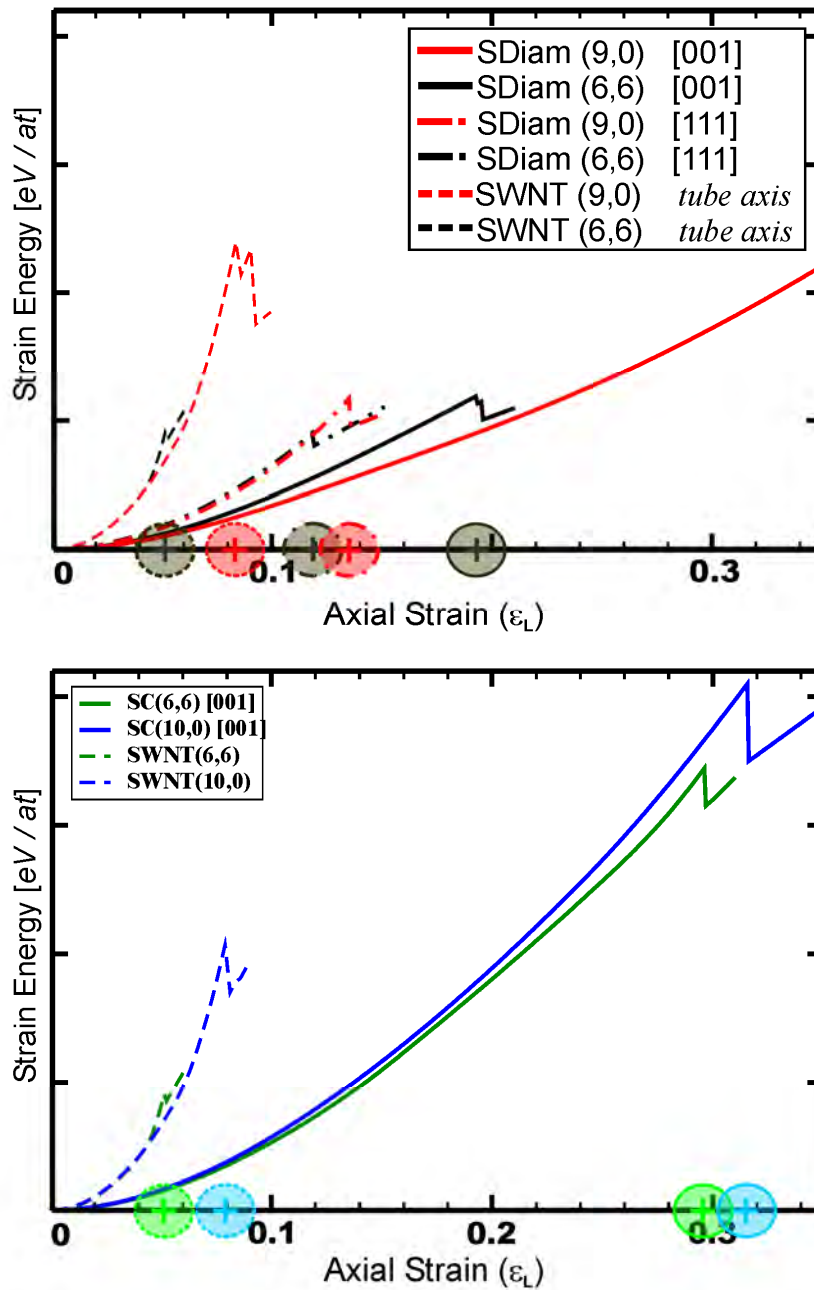


Figure 2.14 Strain energy vs. axial strain obtained for the 3D ON-CNTs. It is remarkable that the networks support twice and even five times more axial strain than isolated CNTs (maximum strain supported is marked by circles on the strain axis).

When studying the axial compression, the networks are able to support extremely high axial strains: a SD network is able to support elastically a reduction of 50% of the initial length along the [001] direction, and ~13% along the [111], whereas the SC network is able to stand ~30% along [001] axis (marked by circles on the axial strain axis; corresponding to the graph first discontinuity where energy is released by an irreversible deformation of the structure). In comparison, isolated carbon nanotubes are only able to support ~7% of the initial length along the tube axis. The snapshots in Figure 2.15 show the length reduction along the [001] axis for the SC and SD networks (the first three snapshots correspond to strains before the irreversible deformation while the fourth one is after it). It is remarked by a green line in the SD network the astonishing reduction in length, helped by an accordion-like compression of the network (an animation is available as Supporting Information at <http://materials.ipicyt.edu.mx/galeria/>) due to the strategic assembly imposed by the architecture, exploiting then the fascinating flexibility of the CNTs [17].

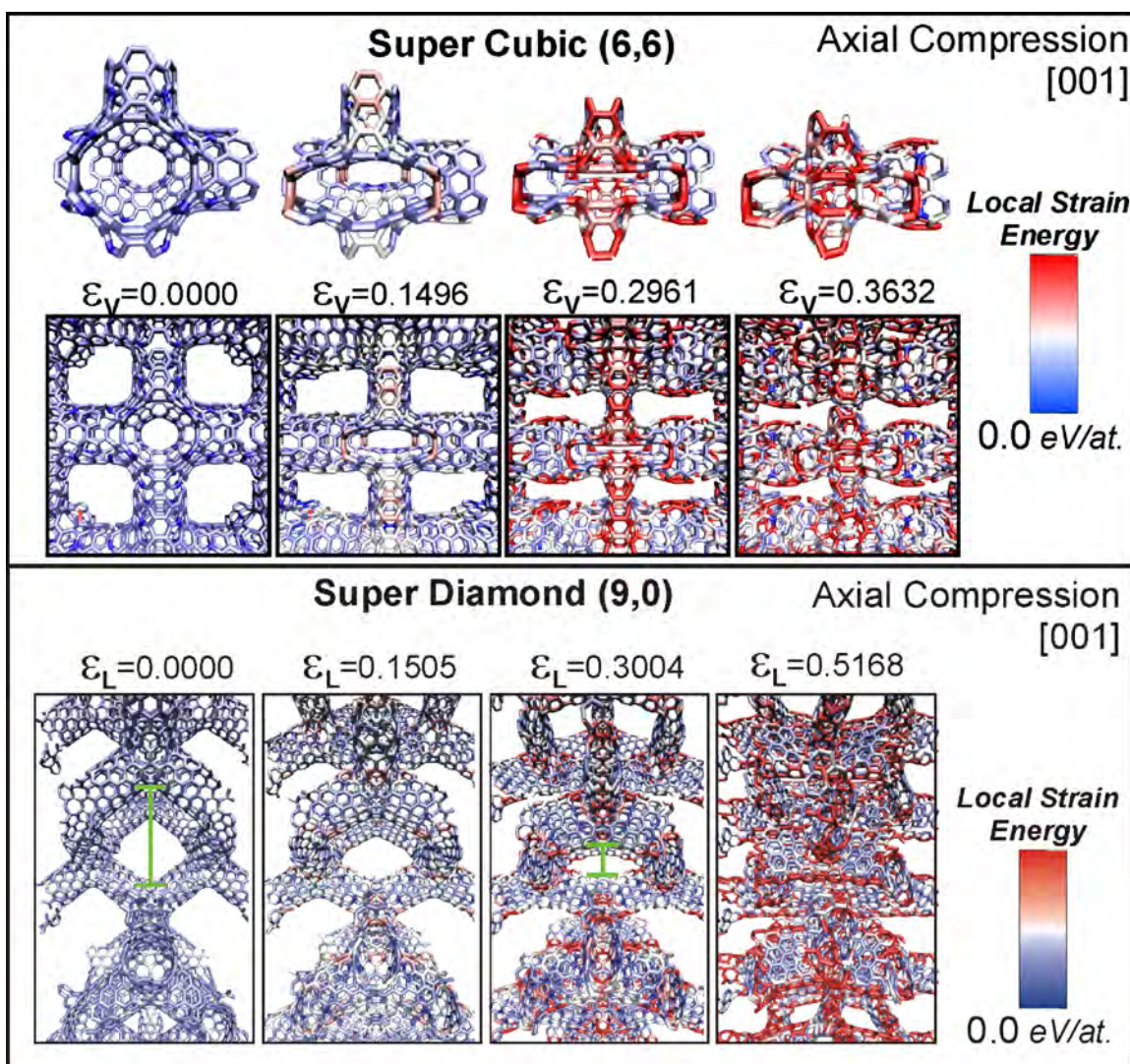


Figure 2.15 This figure shows how the rigidity of the constructor block (CNTs) is exploited when strategic assembly imposed by the architecture is achieved. The color scale represents the local strain energy along the network. Remarkably, in the bottom panel, the accordion-like compression experienced by the (9,0) SD network, due to the strategic assembly imposed by the specific architecture and the intrinsic flexibility of the initial material (CNTs).

Figure 2.16 shows the axial compression of the SD network on the [111] axis, where certain CNTs reside parallel to this direction. Following the local strain color scale (maximum local strain colored by red, then white until blue is reached on the zero local strain relative to plane Graphite) we observe that most of the strain resides on these CNTs, which play the role of supporting columns on this specific architecture.

A main conclusion is the important role of the specific architecture, which together with the original mechanical properties of the basic block (in this case CNTs) dictate and enhance the mechanical properties of the network. We can envision tuning the mechanical properties of materials by choosing a correct combination of basic blocks and architectures.

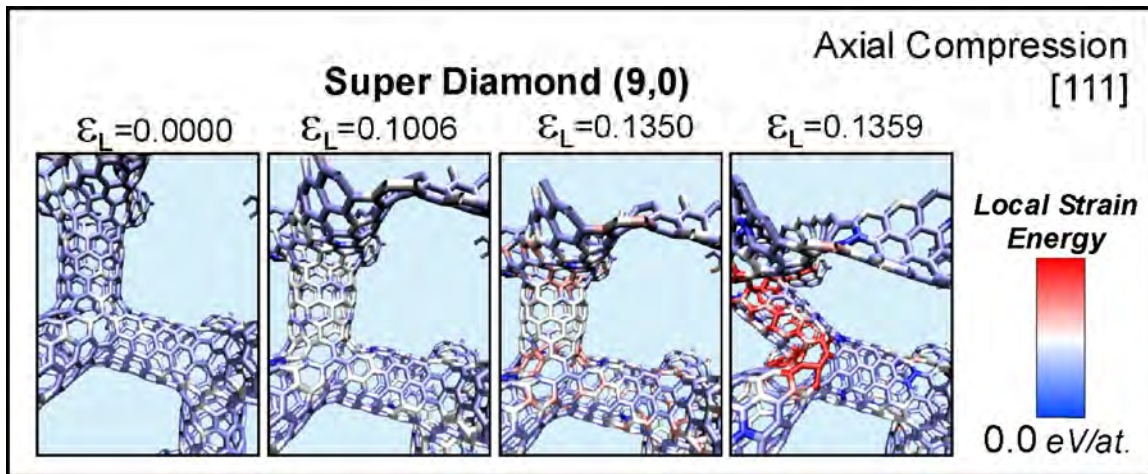


Figure 2.16 This figure shows how the rigidity of the constructor block (CNTs) along its axis is exploited, when compressing the network along its [111] axis, due to the strategic assembly imposed by the architecture.

Therefore, these networks can be highly compressed due to their symmetrical architecture, taking advantage of the intrinsic flexibility of carbon nanotubes (animations with the axial compression along the [001] axis of the SD network and SC network, along [111] axis of the SD networks and volumetric compression of the SD network are available as supplementary material at <http://materials.ipicyt.edu.mx/galeria/>). The unusual high performance of these networks under unidirectional (axial) compression, suggests that they can be used as molecular shock absorbers. When comparing these architectures with conventional diamond structure (dashed line in Figure 2.13), we observe that diamond exhibits a superior rigidity (proportional to the second derivative of the curves) than the 3D ON-CNTs; however, it is the mechanical robustness, combining good rigidity and outstanding flexibility that makes the covalent networks so remarkable and different from other carbon-based materials. In the future, we envisage that one could control the mechanical properties of 2D and 3D nanowire (or nanorod) networks by combining their assembly (connectivity and symmetry) with the intrinsic mechanical properties of the constructor blocks.

2.5 Surface area

The surface area was calculated following the Connolly algorithm [18], designed to obtain solvent-accessible surfaces. For the Connolly surface area we used a 2.0 Å probe radius, simulating the longest axis length in the nitrogen molecule N₂, and the van der Waals surface area was obtained assuming the 1.7Å van der Waals radius for carbon. The porosity properties correspond to an average of the main axis in the pore, measured from the nine relaxed ON-CNTs presented above.

The pore size and surface area, together with the superbond (distance from node to node) corresponding to each of the nine ON-CNTs studied are presented in Table 2.iii.

	Porosity		Surface Area	
	Super Bond length [Å]	Pore size [Å]	van der Waals Surface [m ² /g]	Connolly Surface [m ² /g]
(6,6)-(10,0) SS	16.8	9	2668	2317
(6,6) SS	16.7	10	2708	2748
(10,0) SS	16.8	10	2755	2686
(6,6) SG	16.8	24	2735	2813
(10,0) SG	16.7	24	2693	2782
(6,6) SC	18.4	12	2658	2650
(10,0) SC	15.8	8	2574	2490
(6,6) SD	17.2	19	2753	2612
(9,0) SD	15.2	22	2726	2299

Table 2.iii Porosity and surface area values calculated for the ON-CNTs. Similar values of superbond are fixed to compare the pore size of the different architectures. The right columns present the van der Waals and Connolly surface area for the nine different networks.

Figure 2.17.a illustrates the difference between the van der Waals surface area and the Connolly one in the SD (9,0) networks. A molecule similar in size to nitrogen (N₂) would be trapped at the nodes; while the van der Waals surface area consists of continuous sheets with the feature that the network divides the space in two, presenting an internal surface by narrow channels and an external one with access to the network pores. In a similar way, the SG 2D network in Figure 2.17.b divides the space with two sheets (internal and external) composing its Connolly surface area.

The porosity of these systems makes them good candidates for exploring novel catalysts, sensors, filters or molecular storage properties. By varying the superbond distances of these networks, it is possible to observe other properties with additional potential applications. For example, one could modify the network pore size and surface area. Hollow 1D nanostructures (such as CNTs) would enhance the surface activity of the networks and could trap different molecules or metals such as Fullerenes inside the cylinders (superbonds).

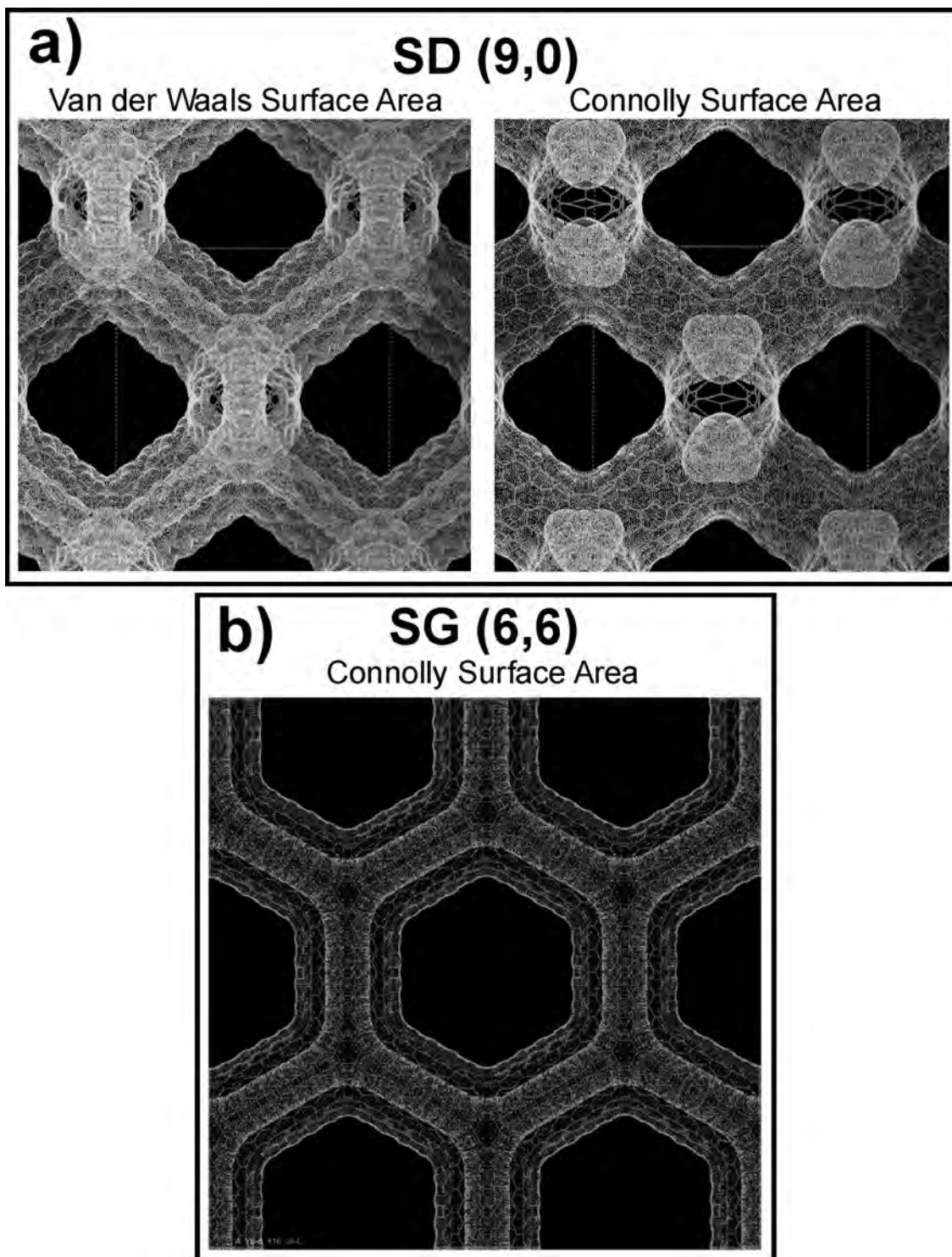


Figure 2.17 The images illustrate the van der Waals and Connolly surface areas. An internal and external accessible surfaces are present, the internal surface corresponding to narrow channels where molecules could be trapped. The external surface corresponds to the solvent accessible area at the network pores. Figure a) corresponds to theoretical simulations on the (9,0) SD networks, while b) presents the Connolly surface area simulation on the (6,6) SG architecture.



Appendix: *Calculation methods*

A.1 Euler's law and Gauss-Bonnet theorem

Using concepts from topology and differential geometry, one can apply the Gauss-Bonnet theorem to a closed orientable surface and Euler's law to a graphitic sheet, in which every atom is bonded to three other (sp^2 bonding), obtaining then the following relationship:

$$2N_4 + N_5 - N_7 - 2N_8 = 12(1 - g) \quad (1)$$

where:

$N_m \equiv$ number of non hexagonal rings with m sides.

$g \equiv$ genus of the structure (complexity of the arrangements; in particular for closed structures without any hole crossing it is zero).

In this case, we can make use of relation 1 to find the total amount of defects (non-hexagonal rings) needed in the building blocks. In order to apply it, we must have a closed orientable surface. We can obtain this by closing each terminal of the building block with a cap, like half of a C_{60} fullerene (this kind of cap will contribute with 6 pentagons each). Closing the building block in such a manner will produce a 'zero-hole' structure (*i.e.* $g = 0$). These considerations will convert expression 1 to:

$$2N_4 + N_5 - N_7 - 2N_8 = 12 - 6t \quad (2)$$

$N_m \equiv$ number of non hexagonal rings with m sides.

$t \equiv$ number of terminals in the specific building block.

\Rightarrow **(6,6) SuperCubic case**

The building blocks from this architecture have six terminals and considering that we are not interested using squares or pentagons in this case, expression 2 will show:

$$2N_4 + N_5 - N_7 - 2N_8 = 12 - 6(6) \quad (3)$$

$$N_7 + 2N_8 = 24 \quad (4)$$

as a final requirement, the (6,6) CNTs symmetry imposes the use of octagons, in order to keep the connectivity between each pair of CNTs at the required angles. This will reveal:

$$N_7 + 2N_8 = 24 \tag{5}$$

$$N_8 = 12 \tag{6}$$

We will need a total amount of 12 octagons distributed strategically at each 90° angle between pair of CNTs (*i.e.* one per 90° angle).

⇒ **(9,0) SuperDiamond case**

This building block has four terminals, and without the presence of squares or pentagons, expression 2 will show:

$$N_7 + 2N_8 = 12 \tag{7}$$

$$\tag{8}$$

the (9,0) CNTs symmetry will impose the use of heptagons, to being able to interconnect trios of CNTs, giving as a result:

$$N_7 = 12 \tag{9}$$

Since we have four interconnection sites of trios of CNTs along this building block, We will require to assemble three heptagons at each of these sites (total of 12 heptagons).

A.2 Landauer Büttiker Formalism

The Landauer-Büttiker formalism [8] has proved to be very useful in describing transport properties. The main idea of the Landauer approach [19] consists in expressing the current through a conductor in terms of the probability that an electron can be transmitted through it; then, the conductance of a sample ought to be proportional to the ease with which electrons can be transmitted through it.

Historically, the formalism was obtained in two steps: it began with Landauer, who related the linear response conductance to the transmission probability; and later was extended by Büttiker [20] to describe multi-terminal measurements.

The conductance of large macroscopic samples obeys Ohm's Law: $V = IR$, where the *resistance* R is defined as the inverse of the *conductance* $G = R^{-1}$. This conductance follows an ohmic scaling law:

$$G \equiv \frac{\sigma W}{L} \tag{10}$$

$W \equiv$ device's width.

$L \equiv$ device's length.

$\sigma \equiv$ conductivity (material parameter).

However, as we go to smaller dimensions there are two corrections to this law: *i)* there is an interface resistance independent of the length L of the device; *ii)* the conductance does not decrease linearly with the width W . Instead, it depends on the number of transverse modes in the conductor and goes down in discrete steps [8]. These corrections are taken into account in the Landauer formula:

$$G = \frac{2e^2}{h}MT \quad (11)$$

$e \equiv$ electronic Charge ($-1.6 \times 10^{-19} C$)

$h \equiv$ Planck's Constant ($6.63 \times 10^{-34} Js$)

$M \equiv$ number of modes in the device.

$T \equiv$ probability that an electron entering at one of the device's terminal will be transmitted to the other terminal.

The discrete steps mentioned above are not evident if the conductor is many thousands of wavelengths wide, since a very small fractional change in W moves M by many integers.

Expression (11) can be extended to a *many terminals* device, where the conductance under the *Landauer-Büttiker* formalism would be given by:

$$G_{pq} \equiv \frac{2e^2}{h}T_{p \leftarrow q} \quad (12)$$

$p \equiv$ terminal p of the device.

$q \equiv$ terminal q of the device.

$T_{p \leftarrow q} \equiv$ transmittance from terminal q to terminal p

To calculate the conductance, it is necessary to calculate the transmission probability. The transmission function can be expressed in terms of the Green's functions of the device and the coupling of the device with the leads as [8],[21]:

$$T_{pq} = Tr[\Gamma_p G_D^R \Gamma_q G_D^A] \quad (13)$$

$\Gamma_{p,q} \equiv$ coupling functions of the device with the leads p or q .

$G_D^{R,A} \equiv$ retarded (R) and advanced (A) Green function of the device.

The difficulty arises from the fact that we are dealing with *open systems*, this is, nonperiodic devices connected to leads that stretch out to infinity. If we remember that the Green's function $G^R(r, r')$ can be viewed as a mathematical entity that allow us to describe the response at any point r due to an excitation at point r' , we would be having a matrix of infinite size. The main idea for solving the problem is that a conductor connected to infinite leads can be replaced by a finite conductor with the effect of the leads incorporated through a 'self-energy' function.

Starting from the equation for the Green's function of the whole system we would have:

$$(\epsilon - H)G = I \quad (14)$$

$\epsilon = E + i\eta$ (η arbitrarily small).

$E \equiv$ energies of the system.

$I \equiv$ Identity matrix.
 $H \equiv$ Hamiltonian matrix of the system.

The Green's function in equation (14) can be partitioned into submatrices that correspond to the individual subsystems, lets just briefly illustrate it with the lead p and the device as the subsystems:

$$\begin{pmatrix} G_p & G_{pD} \\ G_{Dp} & G_D \end{pmatrix} = \begin{pmatrix} (\epsilon - H_p) & h_{pD} \\ h_{pD}^\dagger & (\epsilon - H_D) \end{pmatrix}^{-1} \quad (15)$$

where the matrix $(\epsilon - H_D)$ represents the finite isolated conductor, $(\epsilon - H_p)$ represent the infinite lead p , and h_{pD} are the coupling matrices that will be nonzero only for adjacent points in the device and the lead, respectively. Following this equation, it can be probed that the explicit expression for G_D is [8]:

$$G_D = (\epsilon - H_D - \Sigma_p)^{-1} \quad (16)$$

where: $\Sigma_p = h_{pD}^\dagger g_p h_{pD}$ corresponds to the *Self-energy* term due to the semi-infinite lead p and $g_p = (\epsilon - H_p)^{-1}$ corresponds to the p lead's Green's function. In fact, equation (16) can be extended to many leads as:

$$G_D = (\epsilon - H_D - \Sigma)^{-1} \quad (17)$$

where: $\Sigma \equiv \sum_{leads} \Sigma_l$

Then it is seen that G_D represents the propagation of electrons between two points inside the device, taking into account the effect of the leads through the term Σ . Actually, the term Σ can be viewed as an effective Hamiltonian arising from the interaction of the conductor with the leads. However, Σ is not hermitian.

Once the Green's functions are known, the coupling functions Γ needed to obtain the transmission function from equation (13) can be easily calculated from [8]:

$$\Gamma_p = i [\Sigma_p^R - \Sigma_p^A] \quad (18)$$

where R and A denote *Retarded* and *Advanced* functions, respectively.

Similarly, the electronic density of states can be obtained from the expression:

$$\rho(E) = -\frac{1}{\pi} \text{Im} [\text{Tr} G_D(E)] \quad (19)$$

While the electronic local density of states corresponding to site i and orbital α is given as:

$$\rho_{i,\alpha}(E) = -\frac{1}{\pi} \text{Im} [G_{Di,\alpha}(E)] \quad (20)$$

A.1 Electronic transport in extended systems

So far, the problem reduces to calculate the self-energy terms $\Sigma_{\{p,q\}}$. In the case of ON-CNTs as systems, they correspond to a discrete array of carbon atoms, this suggest the Linear Combination of Atomic Orbitals (LCAO) as an

efficient basis to extend the wave functions of our system with a Tight-Binding formalism. In this context, Marco B. Nardelli developed a scheme applicable to any general Hamiltonian that can be described within a localized orbital basis [22]. In his work, Nardelli deduced expression for the self-energy terms, using the formalism of principal layers [23] in the framework of the surface Green's function matching theory [24].

The main idea of this approach consists of dividing the solid into an infinite stack of principal layers. This transforms the original system into a linear chain of principal layers, where a *principal layer* can be defined as the smallest group of neighboring atomic layers such that only nearest-neighbor interactions between principal layers exist. The latest definition implicitly imposes the condition that there are only interactions between nearest-neighbor layers. Within this definition it is possible to define *intralayer transfer matrices* and *interlayer transfer matrices* (meaning *principal layer*), which will be the entities in charge of transmitting the response from any excitation through the system.

Then, following this framework Nardelli [22], [25] obtained:

$$\Sigma_p = h_{pD}^\dagger (\epsilon - H_{00}^p - (H_{01}^p)^\dagger \bar{T}_p) h_{pD} \quad (21)$$

$$\Sigma_q = h_{Dq} (\epsilon - H_{00}^q - H_{01}^q T_q)^{-1} h_{Dq}^\dagger \quad (22)$$

where $H_{nm}^{\{p,q\}}$ are the matrix elements of the Hamiltonian between the layer orbitals n and m of the p or q leads, respectively; and $T_{\{p,q\}}$ and $\bar{T}_{\{p,q\}}$ are the appropriate transfer matrices which are easily computed from the Hamiltonian matrix elements via an iterative procedure [22]. Correspondingly, h_{pD} and h_{Dq} are the coupling matrices between the Device and the leads.

The contribution of Nardelli's approach is that his scheme is applicable to any general Hamiltonian that can be described within a localized orbital basis. In this sense, it is the suitable approach to describe the electronic transport properties of extended systems such as the ON-CNTs, since the well known *Tight Binding Hamiltonians* represent an efficient technique to apply for the electronic properties of carbon nanostructures.

A.2 The Hamiltonian: *Tight-Binding Approximation*

The Tight-Binding method, as originally proposed by Bloch, consists in expanding the crystal states in linear combinations of atomic orbitals (LCAO) of the composing atoms.

The first step is to construct *Bloch sums* corresponding to the atomic orbitals. The *Bloch sum* of \mathbf{k} wavevector corresponding to the atomic orbital ϕ_i is given by:

$$\Phi_i(\mathbf{k}, \mathbf{r}) = \frac{1}{\sqrt{N}} \sum_{\mathbf{t}_m} e^{i\mathbf{k} \cdot \mathbf{t}_m} \phi_i(\mathbf{r} - \mathbf{t}_m) \quad (23)$$

where $\phi_i(\mathbf{r})$ is an atomic orbital of quantum number i and energy E_i of the atom centered in the reference unit cell; while $\phi_i(\mathbf{r} - \mathbf{t}_m)$ corresponds to the same orbital for the atom in the unit cell \mathbf{t}_m and N corresponds to the number of unit cells in the crystal.

The wave function of vector \mathbf{k} can be expanded as a linear combination of such a Bloch sums (*one per orbital per atom composing the unit cell*):

$$\psi(\mathbf{k}, \mathbf{r}) = \sum_i c_i(\mathbf{k}) \Phi_i(\mathbf{k}, \mathbf{r}) \quad (24)$$

where the coefficients $c_i(\mathbf{k})$ give a measure of the electronic probability in each state composing the wave function. These coefficients can be determined with standard variational methods.

Once defined a base (LCAO) to expand our Wave Functions, the next step is to solve the Schrödinger equation:

$$\hat{H}\psi(\mathbf{r}) = E\psi(\mathbf{r}) \quad (25)$$

where:

$$\hat{H} \equiv \frac{\hat{\mathbf{p}}^2}{2m} + \hat{V}(\mathbf{r}) \quad (26)$$

where $\hat{\mathbf{p}}$ is the quantum momentum operator and $\hat{V}(\mathbf{r})$ is the periodic crystalline potential [*i.e.* $V(\mathbf{r} + \mathbf{t}_m) = V(\mathbf{r})$].

The eigenstates ψ_i 's and its eigenenergies E_i 's can be obtained by solving the well known secular equation:

$$\| H_{ij} - ES_{ij}(\mathbf{k}) \| = 0 \quad (27)$$

where H_{ij} the matrix elements of the Hamiltonian previously described in equation (26), while S_{ij} correspond to the overlap matrix elements.

$$S_{ij} = \langle \psi_i | S | \psi_j \rangle \quad (28)$$

\Rightarrow *Slater-Koster Contribution*

The problem then reduces to obtain such a matrix elements H_{ij} 's and S_{ij} 's. This is not an easy problem without approximations, as J.C. Slater and G.F. Koster expose in their famous article [26]: “... *it becomes almost impossible difficult to carry out with full rigor (Bloch's method), on account of the enormous number of difficult integrals which must be computed ...*”. On the other hand, they showed some of the attractive qualitative features of the method, such as its capability to give solutions showing all the correct symmetry properties of the energy bands, and the fact that it is rather easy to get solutions for energy bands at any arbitrary point in the Brillouin zone. So, what Slater and Koster propose is to use it as an interpolation method, transforming the terms with complicated integrals into constants, to be chosen so that it would be possible to fit the result of more accurate calculation made by other methods.

In this context, Slater and Koster adapt some simplifications, which are going to be briefly described.

i Using Atomic Orbitals ϕ_i located on the atoms to form the Bloch sums (equation (23)), these won't be orthogonal to each other. This is solved by the Löwdin method, an orthogonalization method based on setting up new atomic orbitals φ_i , which are linear combinations of the original ones, but now orthogonal to each other.

This will make the secular problem much simplified. Besides, these Löwdin functions φ_i show symmetry properties like those of the original atomic orbitals ϕ_i . The new Bloch sums can be re-written as:

$$\Phi_i(\mathbf{k}, \mathbf{r}) = \frac{1}{\sqrt{N}} \sum_{\mathbf{t}_m} e^{i\mathbf{k}\cdot\mathbf{t}_m} \varphi_i(\mathbf{r} - \mathbf{t}_m) \quad (29)$$

ii The latest point reduces the S matrix to the *identity* matrix; while the new φ_i Löwdin functions are the ones involved in the integrals for H_{ij} :

$$S_{ij} = \begin{cases} 1 & \text{if } i = j \\ 0 & \text{if } i \neq j \end{cases} \quad (30)$$

$$H_{ij} = \sum_{\mathbf{t}_n} e^{i\mathbf{k}\cdot\mathbf{t}_n} \langle \varphi_i(\mathbf{r}) | \hat{H} | \varphi_j(\mathbf{r} - \mathbf{t}_n) \rangle \quad (31)$$

iii The Hamiltonian \hat{H} , including the periodic potential, can be written as the sum of a kinetic energy operator, and a potential, which is approximately a sum of spherically symmetrical potential wells V_a located at all the atoms of the crystal [*i.e.* $\hat{H} = \frac{\hat{\mathbf{p}}^2}{2m} + \sum_{\mathbf{t}_n} V_a(\mathbf{r} - \mathbf{t}_n)$].

Hence the original integral $\langle \varphi_i(\mathbf{r}) | \hat{H} | \varphi_j(\mathbf{r} - \mathbf{t}_n) \rangle$ corresponds to actually a linear combination of *three-center integrals*, whose calculation is difficult *per-se*, and the complications is even more when we remember the amount of such integrals.

iv A simplification is made noting that the integrals will get smaller numerically as the atoms included get farther apart. The natural simplification is to assume arbitrarily that all integrals are to be disregarded except those for neighbors lying closer than a certain minimum distance.

v A thing to be noticed is that many of the integrals can be related through demands of crystal symmetry.

vi Another simplification that we can make is to consider only certain atomic orbitals, whose energy is near that of the energy bands of interest. We couldn't make this approximation if we were making a rigorous calculation, but since we are choosing our parameters so as to fit certain accurately determined energies, we know that we cannot possibly make a serious error.

vii Finally, disregarding all the *three-center integrals* we would be retaining only the part of the potential energy corresponding to the sum of spherical potentials located on the two atoms on which the orbitals are located.

These assumptions allow us to arrive at integrals which only depend on the internuclear values $\mathbf{t}_n = \mathbf{R}_i - \mathbf{R}_j$ between sites where the orbitals involved are

centered on, and on the symmetry of such orbitals φ_i and φ_j . The latest can be taking into account by the direction cosines α , β and γ of the vector \mathbf{t}_n , since we can express each of the orbital functions φ_i as a sum of functions space quantized with respect to that *axis vector* \mathbf{t}_n . All this permits replacing the integrals with parameters depending on such variables, reexpressing equation (31) with the form:

$$H_{ij} = \sum_{\mathbf{t}_n} e^{i\mathbf{k}\cdot\mathbf{t}_n} h_{ij}(\mathbf{t}_n) G_{ij}(\alpha, \beta, \gamma) \quad (32)$$

Or following Slater and Koster notation:

$$h_{ij}(\mathbf{t}_n) G_{ij}(\alpha, \beta, \gamma) \equiv E_{\mu, \lambda}(\alpha, \beta, \gamma) \quad (33)$$

Where the right hand part stands for the parameters obtained as function of the direction cosines obtained between orbital μ and λ .

For further reference go to [26], where there is a table with the energy integrals for crystals in terms of two-center integrals.

⇒ *Charlier’s Parametrization.*

As it is mentioned by Goringe *et.al.* in their review on “*Tight-binding modelling of materials*” [27]: “... *The starting point for any discussion of the tight-binding method for electronic and atomic structure calculations must be Slater and Koster (1954) ...*”. Where the main contribution, the idea which underlies all tight-binding calculations, is the idea of replacing the integrals appearing in the expression of the *Hamiltonian Matrix* with parameters which depends only upon the internuclear distance $|\mathbf{R}_i - \mathbf{R}_j|$ and the symmetry of the orbitals involved; parameters are fitted to results of more accurate calculations from other methods.

In this context, one of the parametrizations available in the literature, is the one made for sp^2 carbon by Jean Christoph Charlier *et.al.* [19]. Their parametrization consists in a Slater-Koster Hamiltonian with parameters close to the set used for graphite in [28], obtained by fitting the *ab-initio* calculated band structure of bulk graphite.

There are four orbitals per atom, with s level located at $\varepsilon_S = -7.3eV$ below the triply-degenerated p levels taken as the zero of energy (*i.e.* $\varepsilon_p = 0$). The Slater-Koster hopping parameters for nearest-neighbor pairs are $V_{SS\sigma} = -4.30eV$, $V_{Sp\sigma} = 4.98eV$, $V_{pp\sigma} = 6.38eV$, and $V_{pp\pi} = -2.66eV$.

Second-neighbor interactions are taken into account using $V_{SS\sigma} = -0.18\Upsilon$, $V_{Sp\sigma} = 0$, $V_{pp\sigma} = 0.35\Upsilon$, and $V_{pp\pi} = -0.10\Upsilon$, where $\Upsilon = (3.335/r_{ij})^2$ is a scaling factor depending on the interatomic distance r_{ij} expressed in Å .

This set of tight-binding parameters has been successfully used to study SWNTs with polygonized cross section [19], coherent transport in carbon nanotubes mechanically deformed [22], [25] electronic properties of metal-metal intramolecular junctions of SWNTs [29], Quantum Conductance of a Nanotube Superlattice [30], and Quantum Conductance through crossed and parallel carbon nanotubes [31], among others.

A.3 Compression approach

The starting point to perform the volumetric compression was the relaxed structure. This equilibrium structure was compressed by a factor Δ in each of the three orthogonal directions x, y, z and the new compressed coordinates were relaxed and its configuration energy calculated. The new relaxed structure was once more compressed by the same factor Δ in the three directions and the new coordinates relaxed again. This procedure was repeated subsequently. The volumetric strain applied at each step was $\Delta\varepsilon_V=0.002$. Such volumetric strain is defined by:

$$\varepsilon_V = \frac{V_0 - V}{V_0} \quad (34)$$

$V_0 \equiv$ original volume of the equilibrium structure.

$V \equiv$ volume of the structure at each step.

While the Δ factor (defined as $\Delta = \frac{l}{l_0}$) is related by:

$$\Delta = [1 - \varepsilon_V]^{1/3} \quad (35)$$

The unidirectional compression was performed by a similar approach. This time the Δ factor for compression is applied only along one axis. This is:

$$\varepsilon_L = \frac{L_0 - L}{L_0} \quad (36)$$

$L_0 \equiv$ original length on the compression axis.

$L \equiv$ length of the structure on the compression axis at each step.

The compression factor is related by:

$$\Delta = 1 - \varepsilon_L \quad (37)$$

A.4 Connolly algorithm

A Connolly surface is the van der Waals surface of the model that is accessible to a solvent molecule having a nonzero radius. The surface is generated by rolling a spherical probe of a specified radius over the van der Waals surface of the model (see illustrative *Figure(A.1)*). A van der Waals surface is generated when the probe radius is zero.

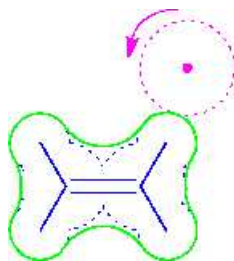


Figure A.1: Illustrative diagram showing the Connolly surface algorithm. The dashed circle represents the van der Waals surface area of the probe while the solid line around the molecule represents the Connolly surface area felt by the probe.

Where the probe contacts only one atom of the model, the Connolly surface is equivalent to the van der Waals surface of the model. Where the probe contacts two or three atoms simultaneously, the Connolly surface is equivalent to the van der Waals surface of the probe (*Figure(A.1)*). The resulting surface represents the solvent-accessible surface of the molecule (assuming that a molecule of solvent is a sphere with the same radius as the probe)

References.

- [1] Mackay, A. & Terrones, H. Diamond from graphite. **Nature** **352**, 762 (1991).
- [2] Terrones, H. & Mackay, A. The geometry of hypothetical curved graphite structures. **Carbon** **30**, 1251-1260 (1992).
- [3] Terrones, H., Terrones, M. & Moran-López, J.L. Curved nanomaterials. **Curr.Sci.** **81** (9), 1011-1029 (2001).
- [4] Tersoff, J. Empirical interatomic potential for carbon, with applications to amorphous carbon. **Phys. Rev. Lett.** **61**, 2879-2882 (1988).
- [5] Brenner, D.W. Empirical potential for hydrocarbons for use in simulating the chemical vapor deposition of diamond films. **Phys. Rev. B** **42** (15), 9458-9471 (1990).
- [6] Robertson, D.H., Brenner, D.W. & Mintmire, J.W. Energetics of nanoscale graphitic tubules. **Phys. Rev. B** **45**, 12592-12595 (1992).
- [7] Kroto, H.W., Heath, J.R., O'Brien, S.C., Curl, R.F. & Smalley, R.E. C₆₀: Buckminsterfullerene. **Nature** **318**, 162-163 (1985).
- [8] Datta, S. Electronic Transport in Mesoscopic Systems. **Cambridge University Press** (1995).
- [9] Charlier, J.-C., Lambin, Ph. & Ebbesen, T.W. Electronic properties of carbon nanotubes with polygonized cross sections. **Phys. Rev. B** **54** (12), R8377-R8380 (1996).
- [10] Choi, H.J., Ihm, J., Louie, S.G. & Cohen, M.L. Defects, Quasibound States, and Quantum Conductance in Metallic Carbon Nanotubes. **Phys. Rev. Lett.** **84** (13), 2917-2920 (2000).
- [11] Yakobson, B.I., Brabec, C.J. & Bernholc, J. Nanomechanics of carbon tubes: Instabilities beyond linear response. **Phys. Rev. Lett.** **76** (14), 2511-2514 (1996).
- [12] Iijima, S., Brabec, C.J., Maiti, A. & Bernholc, J. Structural flexibility of carbon nanotubes. **J. Chem. Phys.** **104** (5), 2089-2092 (1996).
- [13] Nardelli, M.B., Yakobson, B.I. & Bernholc, J. Mechanism of strain release in carbon nanotubes. **Phys. Rev. B** **57** (8), R4277-R4280 (1998).
- [14] Hernández, E., Goze, C., Bernier, P. & Rubio, A. Elastic properties of c and b_xc_yn_z composite nanotubes. **Phys. Rev. Lett.** **80** (20), 4502-4505 (1998).
- [15] Sanchez-Portal, D., Artacho, E., Soler, J.M. Rubio, A. & Ordejon, P. Ab initio structural, elastic, and vibrational properties of carbon nanotubes. **Phys. Rev. B** **59** (19), 12678-12688 (1999).
- [16] Huan, J.Y., *et al.* Superplastic carbon nanotubes. **Nature** **439**, 281 (2006).
- [17] Falvo, M.R., *et al.* Bending and buckling of carbon nanotubes under large strain. **Nature** **389**, 582-584 (1997).
- [18] Connolly, M.L. Solvent-accessible surfaces of proteins and nucleic acids. **Science** **221**, 709-713 (1983).
- [19] Landauer, R. Electrical resistance of disordered one-dimensional lattices. **Philos. Mag.** **21** (172): 863 (1970).
- [20] Büttiker, M. Four-Terminal Phase-Coherent Conductance. **Phys. Rev. Lett.** **57** (14): 1761-1764 (1986).
- [21] Fisher, D.S. & Lee, P.A. Relation between conductivity and transmission matrix. **Phys. Rev. B** **23**, 6851 (1981).
- [22] Nardelli, M.B. Electronic transport in extended systems: Application to carbon nanotubes. **Phys. Rev. B** **60** (11), 7828-7833 (1999).
- [23] Lee, D.H. & Joannopoulos, D. Simple scheme for surface-band calculations. **Phys. Rev. B** **23** (10), 4988-4996 (1981).
- [24] Garcia-Moliner, F. & Velasco, V.R. Theory of Single and Multiple Inter-faces. **World Scientific Publishing Co.Pte.Ltd** (1992).
- [25] Nardelli, M.B. & Bernholc, J. Mechanical deformations and coherent transport in carbon nanotubes. **Phys. Rev. B** **60** (24), R16338-R16341 (1999).
- [26] Slater, J.C. & Koster, G.F. Simplified Icao method for the periodic potential problem. **Phys. Rev.** **94** (6): 1498 (1954).
- [27] Goringe, C.M., Bowler, D.R. & Hernandez, E. Tight-binding modelling of materials. **Rep. Prog. Phys.** **60**, 1447 (1997).
- [28] Tomanek, D & Louie, S.G. First-principles calculation of highly asymmetric structure in scanning-tunneling-microscopy images of graphite. **Phys. Rev. B** **37** (14), 8327 (1998).

-
- [29] Fa, W., Chen, J., Liu, H. & Dong, J. Structural and electronic properties of the metal-metal intramolecular junctions of single-walled carbon nanotubes. **Phys. Rev. B 69**, 235413 (2004).
- [30] Lu, W., Wang, E.G. & Guo, H. Quantum conductance of a carbon nanotube superlattice. **Phys. Rev. B 68**, 075407 (2003).
- [31] Dag, S., Senger, R.T. & Ciraci, S. Theoretical study of crossed and parallel carbon nanotube junctions and three-dimensional grid structures. **Phys. Rev. B 70**, 205407 (2004).

Chapter 3. Defect engineering in ON-CNTs: *guiding current*

Abstract

The limitations of miniaturization in electronics by conventional top-down manufacturing constitute an important barrier to overcome in nanotechnology. The assembly of nanocircuits from nanowires and self integrated nanodevices is a challenge to pursuit.

CNTs are excellent candidates for electronic applications due to their conductor or semiconductor behavior and ballistic transport properties (electricity conductor with coherence length larger than their physical length). The introduction of defects in the carbon lattice could lead to unusual properties and novel nanodevices. While defects have been studied in isolated nanotubes, a next step is their study in CNT networks and nanocircuits.

This chapter begins with the scattering process occurring by the presence of a single Stone Wales defect (SW) in a CNT at the eigenchannel level. The charge arrangement produces 90° phase shifts of incoming electrons (total reflectance) or total transmittance, when appropriate symmetry is preserved between the defect and the CNT. By increasing the amount of SW defects, delocalization of ring charge is produced (concentric to the CNT axis) eventually resulting in a complete suppression of transport.

It is then proposed to incorporate defects strategically in ON-CNTs following the Hierarchy Algorithm [10] (previously described in [chapter 2](#)), in order to guide current within a nanocircuit. The conductance calculations reveal that arrays of defects can enhance the conductance through specific electronic paths maintaining zero conductance along the rest of them.

When SWs are distributed asymmetrically in the basic SG block, an accumulation of charge close to specific terminals is observed, thereby leading to higher electronic conductance for specific paths. This demonstrates that current guiding along specific paths in the network is possible by simply positioning strategically a number of SW defects.

By incorporating SW defects one by one into the SG block the superbond can be transformed into a Haeckelite (carbon nanotubes, where the rolling sheet is composed by pentagons, hexagons and heptagons rings [40]) to study the effect of defects. This reveals a simple explanation of the two basic phenomena producing the driving of current along the network. First, there is a behavior of a *'patch of defects'* which produces the delocalization of the defective quasibound states when the SW are close to each other. Second, this patch of defects promotes the enhancement in conductance by reflecting the incoming travelling electron and driving it through the chosen electronic path.

Therefore, arrays of defects can be seen as intrinsic devices to guide current through specific paths in ON-CNTs. Organic nanocircuits are envisaged to be working as an addressable array. By tuning the energy of the travelling electrons, different eigenchannels can be opened or closed and different electronic paths can be turned on and off within the nanocircuit.

3.1 Introduction	57
3.2 Effect of individual Stone-Wales (SW) defects in perfect CNTs	59
3.2.1 An individual SW and its implications at the eigen channel level	59
3.2.2 Different types of SWs produce different eigen channel behaviors.	64
3.2.3 Increasing the amount of SWs.	66
3.3 Patches of defects (Haeckelite) in ON-CNT	70
3.4 Enhancement of current through specific paths	71
3.4.1 Individual Stone Wales case.	73
3.4.2 Effect of an asymmetric distribution of defects.	76
3.4.3 Conductance enhancement of specific path	78
3.5 Conclusions	86
References	87

3.1 Introduction

The limits of miniaturization in electronics by conventional top-down manufacturing presents an important task to overcome in nanotechnology. The assembly of nanocircuits, from the bottom-up approach, with nanowires and self integrated nanodevices is a challenge to pursuit. In that respect, nanoscale components such as nanoclusters (0D) and nanowires (1D) represent attractive building blocks for hierarchical assembly of functional arrays.

The hierarchical assembly of molecular building blocks has been the subject of intense development. Possible networks could be built from DNA and RNA (Bio blocks) [1-3], the synthesis of ordered 3D lattices from atomic clusters (0D blocks) [4-6], and even ordered arrays of assembled inorganic nanowires (1D blocks) [7-9]. Recently, different architectures of Ordered Networks built from 1D blocks have been reported in the literature, where the final properties are dictated by the specific architecture. A general algorithm was proposed to design different types of architectures and theoretically explored [10] (*described in chapter 2*).

Basic electronic components based on isolated nanotubes have been reported. This includes molecular quantum wires [11], intramolecular junctions [12] behaving like rectifying diodes [13], room temperature transistors [14], and voltage inverters logic gates [15]. A further step was achieved when a single cross of nanowires was shown to perform like nanoscale avalanche photodiodes [16] and programmable nonvolatile memory devices [17]. However, this is only the first step toward nanoelectronic systems. Indeed, the next challenge is to go beyond single molecule components and to integrate such building blocks into organized architectures.

To that respect, initial success has been achieved with inorganic (Si or GaN) nanowires where a 3x1 network (3 nodes) is reported to perform as AND or NOR logic gates [18] and a 4x4 network (16 nodes) was made to work as an addressable decoder nanosystem [19]. Specifically, Zhong *et al.* [19] focus on schemes to address elements in nano arrays. These authors use field effect transistors positioned at each crossed-nanowires (each node of the network). By performing modifications at the molecular level on specific cross points, it is possible to define address codes that enable nanowires input lines to be turned on and off.

Along the possible 1D building blocks, CNTs are excellent candidates due to their ballistic conductor or semiconductor behavior and their robust mechanical properties. Experimentally, it has been demonstrated that *non-covalent* 2D networks (e.g. 3-12 nodes) could be obtained from CNTs [20]. For instance, a CNT based nonvolatile Random Access Memory (RAM) was proposed for non-covalent networks configurations, where each device element is based on a suspended crossed nanotube geometry that leads to bi-stable electrostatically switchable on/off states [21]. Covalently bonded 2D and 3D Ordered Networks based on CNTs (ON-CNTs) constitute a step further to experimentally achieve, because unusual physico-chemical properties have been theoretically reported [10]. Uptodate, it has been possible to assemble inorganic nanowires into stacked (non covalent) ordered arrays using the Langmuir-Blodgett technique [8], showing an astonishing control for both the spacing between parallel 1D blocks and their

architecture. While these nanowires were not connected covalently, it has been shown theoretically and experimentally that single- and double-walled carbon nanotubes can be merged covalently, either individually using controlled electron irradiation at high temperatures [22], or randomly in higher yields using atomic welders (e.g. B atoms) during heat treatments [23]. Therefore, by extrapolating the concept of welding CNTs into self assembled arrays, it seems possible to experimentally obtain experimentally novel architectures consisting of *covalently bonded* 2D and 3D CNTs networks using CNTs as building blocks.

The development of nanoelectronics based on carbon nanotubes has been inspired due to their ballistic transport properties (i.e. the electron coherence length is larger than the tube dimension). Interestingly, the introduction of defects in the carbon lattice can lead to interesting properties and novel nanodevices [24]. For instance, different types of defects have been studied in isolated nanotubes such as the quantum conductance effect of a vacancy [25] and its most stable configuration [26]. Another well known defect is the Stone Wales (SW) defect originally proposed in fullerenes [27]. The *generalized SW* defect consists of a 90° rotation of one bond producing non hexagonal rings in the case of a CNT. This defect can be used to tune the band gap [28]; while 5-7 pair defects (one pentagon and one heptagon ring) have been used to design quantum dots along a CNT by connecting metal and semiconductor tubes [29]. Furthermore, SW defects have been studied under mechanical strain showing that they can evolve into 5-7 pairs or patches and migrate, thereby generating quantum dot segments [30]. These defects can be generated by irradiation, using either an electron beam [31] or argon ion doses [32]. Doping species (such as boron [33] or nitrogen [34]) constitute another type of defect that modifies the electronic properties of nanotubes. For example, electrical switching has been reported for metallic CNTs doped with either a boron or nitrogen impurity under an electric field [35]. Along this line, the next step is to study the effect of defects within CNT based networks.

The present chapter explores the effect of topological defects (non hexagonal rings) in the electronic transport properties of ON-CNTs, from a single SW to a patch of defects (a full superbond composed by 12 SW defects, i.e. a Haeckelite). These patches of defects behave as intradevices within the network. It is shown how the strategic positioning of these patches of defects allow current guidance along the nanocircuit.

3.2 Effect of individual Stone-Wales (SW) defects in perfect CNTs

Different types of defects can occur in CNTs: vacancies, impurities of different chemical elements, non hexagonal carbon rings, and Stone Wales (SW) type rotations.

It is known that the main role of a defect in a CNT corresponds to the presence of localized charge around it (quasi bound states) which will be revealed as a peak in the DOS and a dip in the conductance because of resonant backscattering of conducting electrons near the quasibound state energies. In this case, the defect plays the role of a (coherent) scatterer damaging the transport properties [36].

3.2.1 An individual SW and its implications at the eigen channel level

In order to understand all the details governing the scattering process, we started our investigation with a (6,6) CNT with a single SW defect. The ballistic transport characteristic of the perfect CNT is modified by the presence of the SW defect (see Fig. 3.1). The main effect is the appearance of two well-defined dips in the conductance, one below the Fermi energy (E_-) and another one above the Fermi energy (E_+). Remarkably, the DOS exhibits a peak at those two energy values (E_+ and E_-), corresponding to quasi bound states associated with the SW

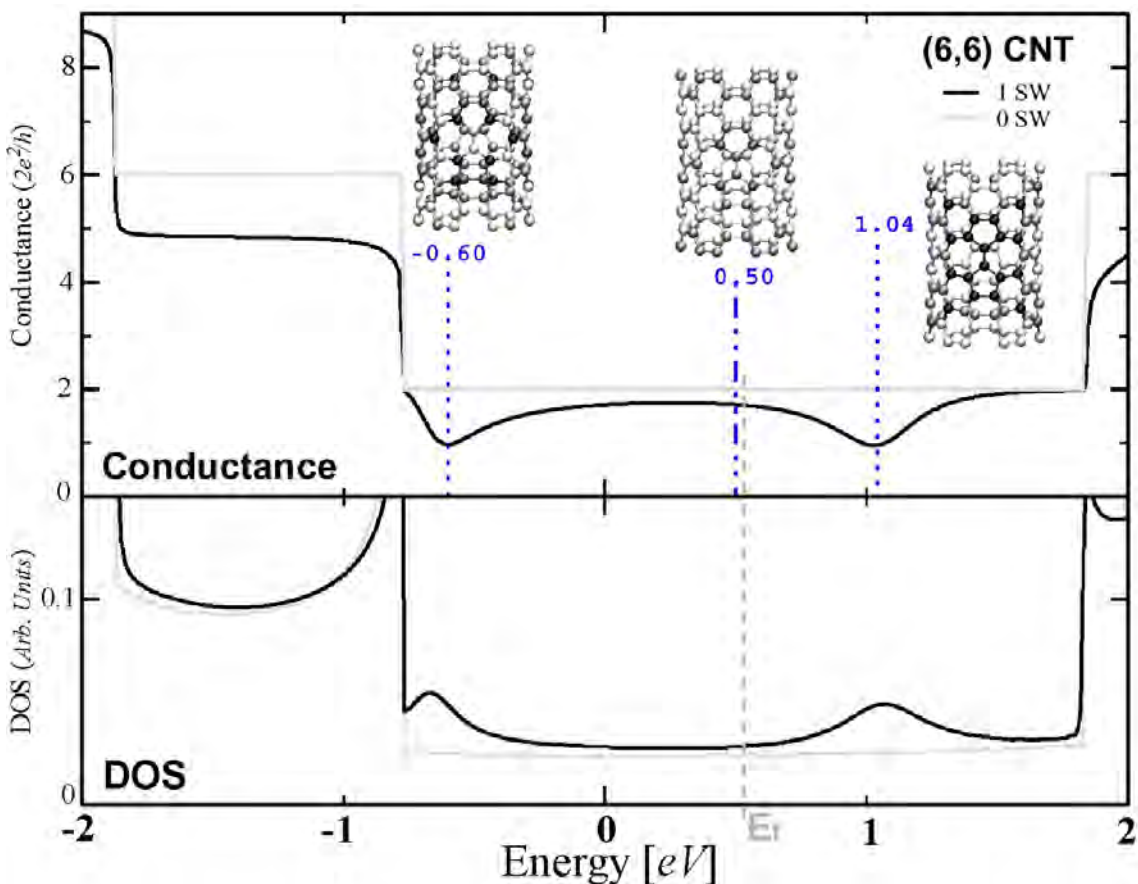


Figure 3.1: Conductance and DOS graphs for one SW case (black lines) along an armchair CNT. A comparison with the perfect CNT case is presented in grey lines. The inset shows the LDOS plot at the atomic sites, showing the quasibound states revealed as peaks on the DOS graph.

defect. The insets in [Figure 3.1](#) exhibits the LDOS on the CNT (black representing the highest amount of charge and white zero charge), showing an increase of localized charge around the defect due to the electronic quasibound state.

An important point to remark is that for both dips, the conductance is reduced from $2G_0$ to $1G_0$. First, it should be remembered that the metallic character of the armchair CNTs arises from two π bands crossing the Fermi level at wave vector $k_F \approx 2\pi/3a$ [37-38]. The two bands are conventionally denoted in CNTs as π (descending band corresponding to the bonding states) and π^* bands (ascending band corresponding to the antibonding state; see gray bands in schematic illustration in [Figure 3.3](#)). In the case of a perfect CNT, these two bands are those injecting two incoming electrons, hence yielding to a $2G_0$ total conductance in a pristine tube. Now, the important point to understand is how the presence of the SW rotation interacts with the two electrons coming from these two bands (here we model the electrodes as defect-free (6,6) tubes seamlessly connected to a portion of the same tube containing a defect). A convenient way to analyze the scattering process, is to study the conductance properties at the eigenchannel level at discrete energy values. The energy values chosen correspond to the two dips ($E_- = -0.60\text{eV}$ and $E_+ = 1.04\text{eV}$) and a third energy value close to the Fermi energy ($\sim E_f = 0.50\text{eV}$). The values of the conductance at those points are summarized in [table 3.i](#).

Transmitted Charge [G_0]

	Channel 1 π^* band	Channel 2 π band	Total Conductance
$E_- = -0.60\text{eV}$	0.000029	0.975469	0.975498
$E_+ = 1.04\text{eV}$	0.956777	0.002661	0.959438
$\sim E_f = 0.50\text{eV}$	0.905259	0.812171	1.717430

Table 3.i: Conductance values at the eigenchannel level for strategic energy values (the two conductance dips and close to the Fermi energy).

In addition, we also present real space amplitude plots of the scattered wave-functions at the various energies in [Figure 3.2](#).

The conductance values reveal that for both dips one eigen channel is totally reflected and the other one is completely transmitted. The reason for this effect can be explained by the arrangement of charge when the SW defect is incorporated, as shown on [Figure 3.2](#). To fully elucidate these plots, it is helpful to explain the scheme presented in [Figure 3.3](#).

The main arguments reduce to symmetry considerations. As it has been previously explained by Choi *et al.* [36], that the SW defect of [Figure 3.3](#) preserves structural symmetry under two mirror symmetry planes: perpendicular to the tube axis (M1) and the one containing the tube axis and the bond connecting the pentagons (M2), illustrated in [Figure 3.3.d](#). While in the perfect tube the π^* band state has an odd symmetry with respect the M2 plane, the π band state is even with respect to M2 (see c) in [Fig 3.3](#)). Since the SW defective tube can keep this symmetry under the M2 plane, the π^* and π bands do not mix and they remain as eigenchannels in this defective tube.

Now, let's focus on the π^* band states, they can either be even (represented by grey signs on Figure 3.3.d) or odd (represented by black signs) with respect to M1. In the even case (label by No. 1), we arrive to a *minus-minus* case for the rotated bond (marked by a grey circle) by which by one side makes it a bonding case and therefore energetically favoured than the odd case (label by No. 3). The rotated bond corresponds to a *minus-plus* case (antibonding case), but this *minus-*

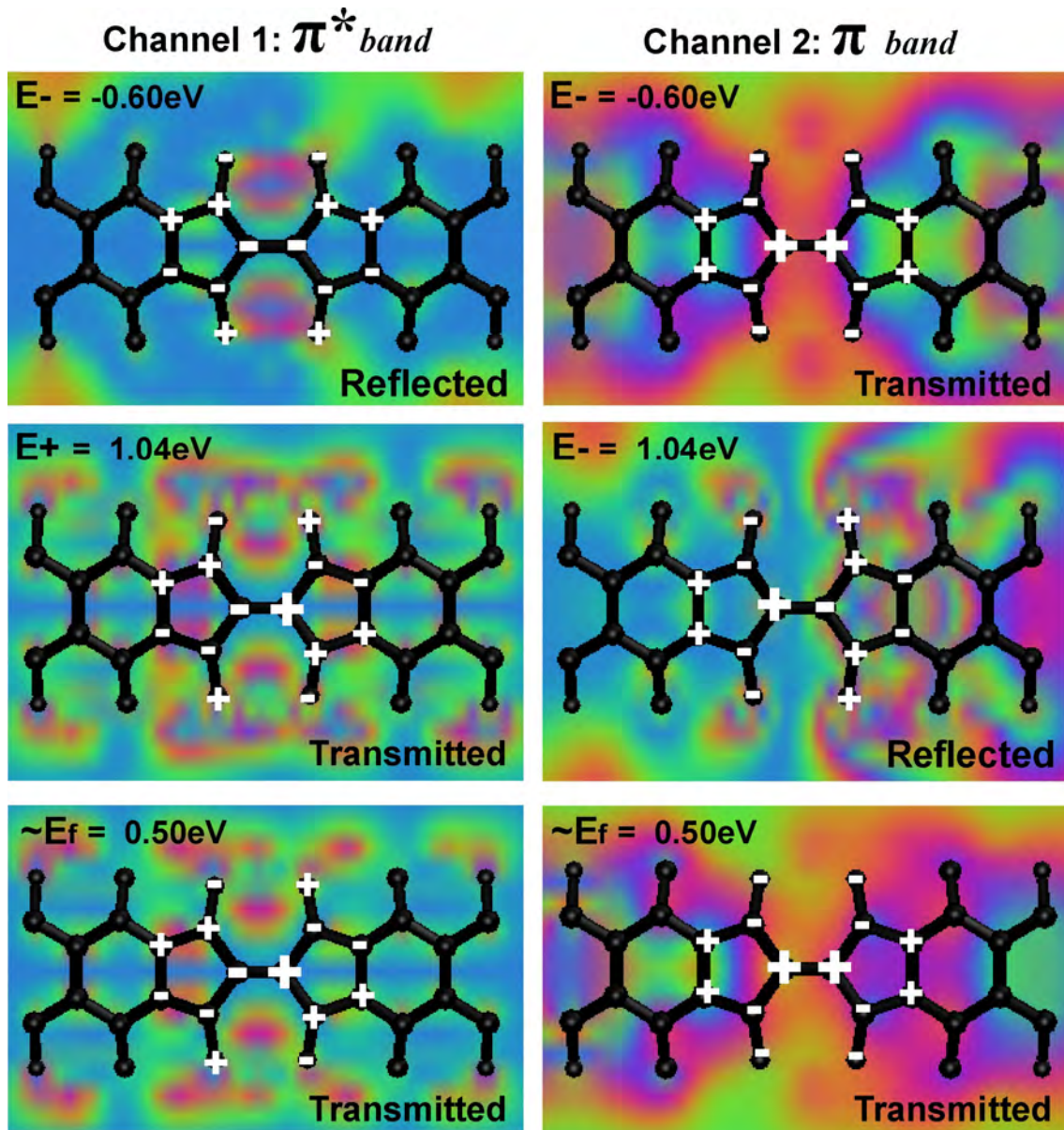


Figure 3.2: Real space amplitude of the scattered wave function at the eigenchannel level for the discrete energy values chosen. The CNT axis is located horizontally and the SW defect in the center of the tube. It is shown by white signs at the atomic sites the expected wave function signs due to the charge distribution observed, to emphasize the bonding and antibonding nature of the rotated bond and the symmetry needed from the wave function of the travelling electron to cross it. The right upper frame shows a transmitted case: the +,+ pair on the rotated bond preserve the symmetry of the vertical bonds, therefore allowing the travelling electron to transmit through the defect.

minus case at the rotated bond also implies a phase shift of 90° for the travelling incoming electron, which forces the state to be totally reflective, while the odd case with the *minus-plus* rotated bond has no need for a phase shift. It follows that particular state corresponds to total transmission.

A similar statement can be made for the π band states, where the even case (represented by black signs and label by No. 4) with respect to M1 turns out to have a *plus-plus* rotated bond (bonding, *i.e.* more energetically favourable) which do not imply any phase shift for the travelling electron coming from a π band; this corresponds to a total transmission case. The odd case (represented by grey signs and labeled by No. 2) with respect to M1 turns out to have a *plus-minus* rotated bond forcing a 90° phase shift for the incoming travelling electron and therefore resulting in a total reflected state.

Now that the symmetry arguments causing the scattering process by the SW defect have been explained, let's turn to study the charge density of the wave function presented in [Figure 3.2](#) and understand how this charge distribution points out to one of the states previously described (marked on the plot by white signs). In [Figure 3.2](#) it is displayed how at $E_- = -0.60\text{eV}$ the π band is the one transmitting the travelling electron since it corresponds to *plus-plus* case (bonding) for the rotated bond compatible with the symmetry of its travelling electron; while in the case of the π^* band it has *minus-minus* case (bonding) at the rotated bond, not compatible with the travelling electron symmetry, therefore imposing a 90° phase shift and causing total reflectance at this band. The opposite case is observed at $E_+ = 1.04\text{eV}$ (corresponding to the conductance dip over the Fermi energy), where the π^* band is the one conducting while the π band electron is the one totally reflected. It is important to point out the third energy case ($\sim E_f = 0.50\text{eV}$), in which the arrangement of charge of the wave function allows both eigen channels to conduct. It should be noted that the charge pattern of the π^* band at $\sim E_f$ is very similar to the one obtained at E_+ (both conducting cases). Similarly, the wave function charge pattern of the π band at $\sim E_f$ is very similar to the one obtained at E_- when conducting.

It should be mentioned, that the convention in signs used for the wave function of the perfect nanotube, as the starting point for all the analysis is similar to the one used by Rubio *et al.* [39]. The consistency with our results was confirmed by plotting the charge density wave function of the perfect tube (not shown here).

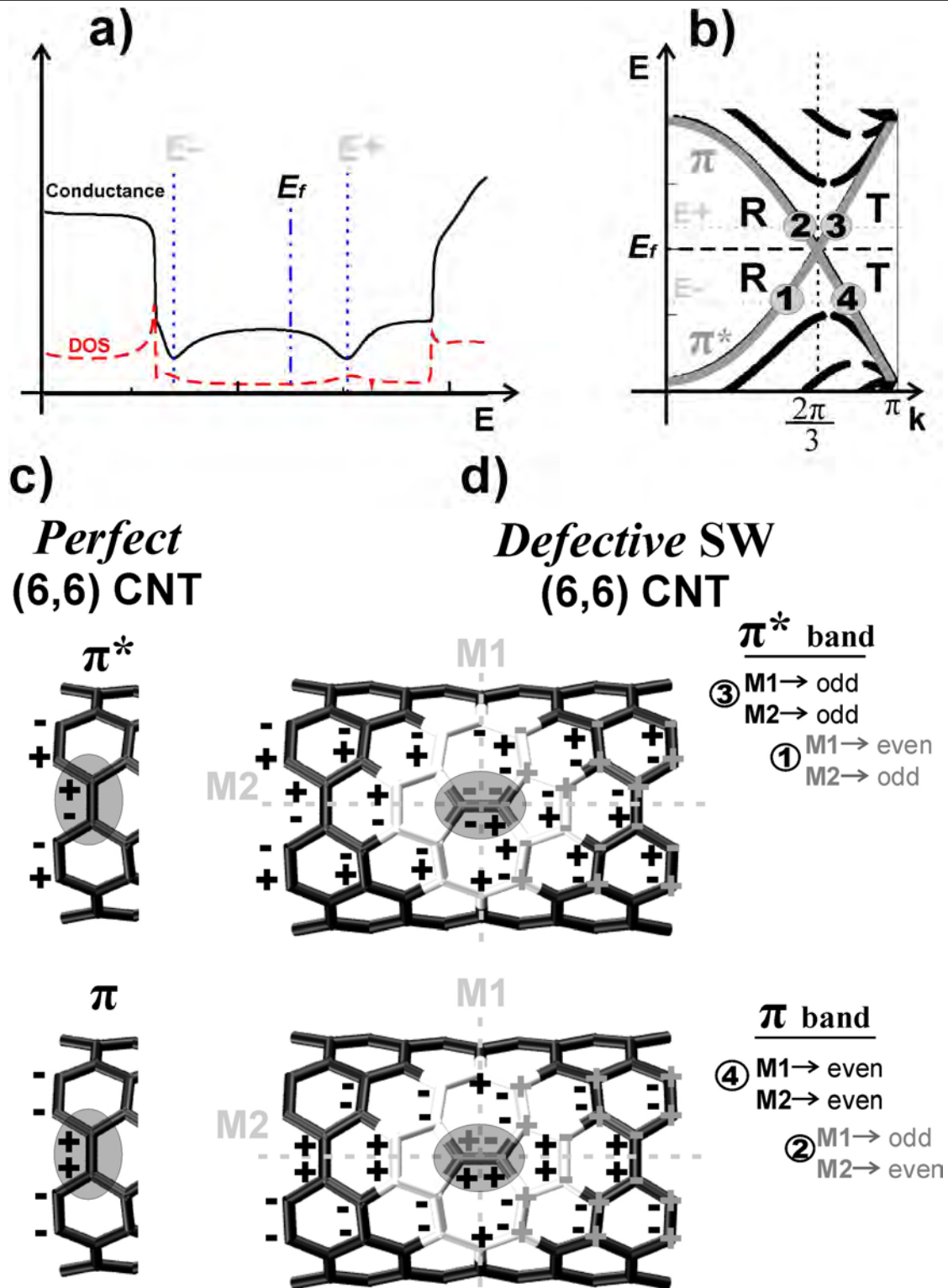


Figure 3.3: Illustrative scheme explaining the main symmetry argument governing the total reflectance (90° phase shift) or transmittance with the SW presence. a) presents the two energy points analysed at the conductance dips positions (E^- and E^+); b) shows a scheme with the two energy cases on an electronic band diagram for the armchair CNT, showing four available travelling electrons from the lead (semi-infinite CNT) and their corresponding eigenchannels (π and π^*). c) depicts the symmetry of the travelling electron along the perfect CNT in the two different eigenchannels. d) illustrates the symmetry of the wave function on the defective tube at the different energy cases for eigenchannel π and eigenchannel π^* . Grey circles mark the symmetry of the travelling electron on the vertical bonds on the leads (c) and the symmetry imposed by the rotated bond in the defective device (d).

3.2.2 Different types of SWs produce different eigen channel behaviors

A generalized Stone Wales defect can be obtained by rotating one of the bonds by an angle of 90° [27], thus producing an array of two pentagons and two heptagons around the rotated bond (also known as a 5775 defect). This gives two possible inequivalent SW defects in an armchair CNT, either rotating one of the bonds perpendicular to the tube axis (type **A**) or rotating one of the inclined bonds (type **B**); both types are illustrated in Figure 3.4.

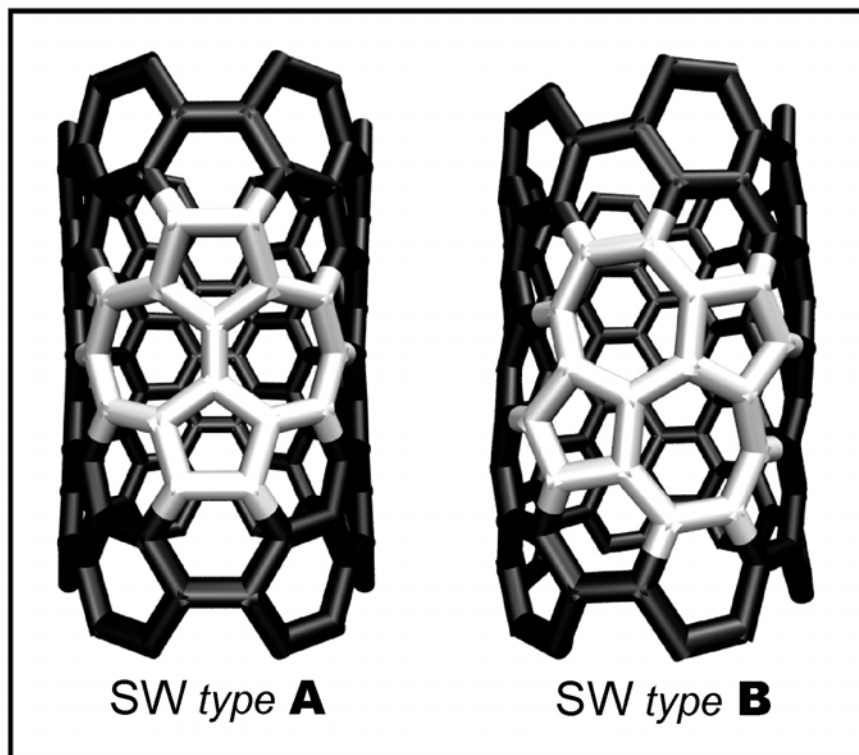


Figure 3.4: The two inequivalent SW position along an armchair CNT. The left case shows the rotated bond parallel to the nanotube axis; while the right case is obtained with the rotated bond inclined from the axis.

Case type A has been described in the previous section, using symmetry arguments. For case B, the symmetry under the mirror planes M1 and M2 is lost (see Fig 3.3.d). In the perfect tube, the π^* band state is odd and the π band state is even with respect to M2 (see Fig 3.3.c), but since the SW type B defect does not preserve this symmetry, the π^* and π bands mix and independent eigenchannels with completely transmitted or completely reflected states are no longer present.

In Figure 3.5 a similar behavior is observed for the conductance and DOS curves for both type A (black curve) and type B (grey curve) defects. They both reveal quasibound states with very well defined peaks in the DOS graph and dips in the conductance curve. Even when the dips in both cases (type A and type B) present $1G_0$, Table 3.ii reveals that in case B this $1G_0$ conductance at the dips is shared by both channels (Channel 1 $\rightarrow 0.71G_0$ and Channel 2 $\rightarrow 0.28G_0$ for the first dip; Channel 1 $\rightarrow 0.28G_0$ and Channel 2 $\rightarrow 0.66G_0$ for the second dip). The channels are not independent anymore, due to the lack of symmetry incorporated by the SW type B defect.

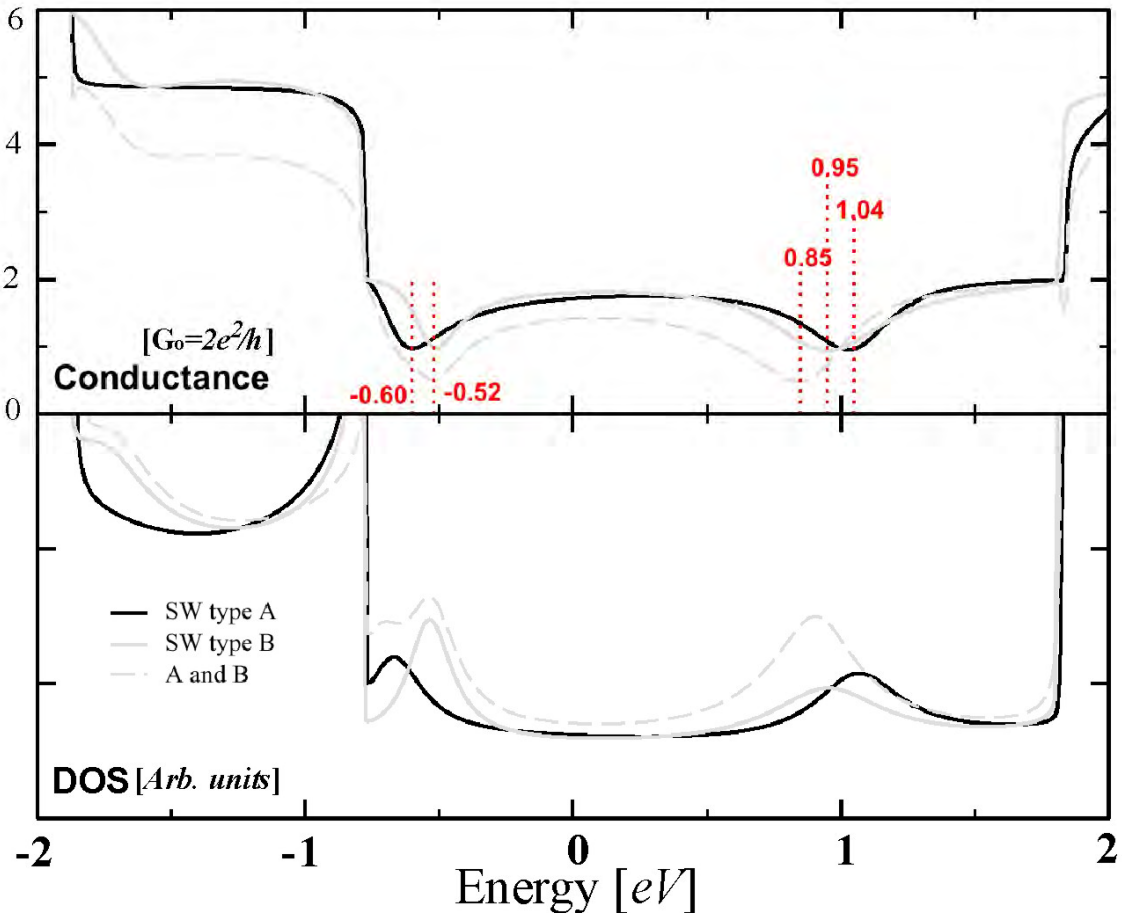


Figure 3.5: DOS and conductance curves comparing the inequivalent SW cases. The continuous curves correspond to the SW type A (black) or type B (grey), respectively; while the dashed line corresponds to a CNT with both type of SWs.

The gray dashed curves presented in Figure 3.5 correspond to the case when both types of SWs are included in the same tube. The DOS and conductance curves present an overlapping of both of the quasibound states (for each type of defect), below the Fermi energy. Above the Fermi level, even when the general behavior of having a quasibound state producing a dip in conductance is still present, it does not correspond to an overlap of the results found for the two cases of single defects. Instead, the trend now corresponds to a shift of the dip of conductance towards the Fermi level.

The other main trend is that the conductance for the grey dashed line has decreased all along the curve, as a consequence of having a greater amount of defects and therefore more localized charge and scattering centers in the conductor, thus blocking or decreasing the electronic flux through the tube.

Transmitted Charge [Go]

		Channel 1	Channel 2	Channel 1	Channel 2
		A to B	A to B	B to A	B to A
SW A	-0.60	0.00	0.98	0.00	0.98
SW B	-0.52	0.71	0.28	0.71	0.28
2SW A y B	-0.52	0.20	0.31	0.34	0.17
	-0.60	0.03	0.69	0.16	0.55
SW A	1.04	0.96	0.00	0.96	0.00
SW B	0.95	0.28	0.66	0.66	0.28
2SW A y B	0.85	0.17	0.31	0.34	0.14

Table 3.ii: Conductance values at the eigenchannel level for the different type of SW cases.

3.2.3 Increasing the amount of SWs

The amount of SW defects can be increased by adding a second SW at the opposite side of the nanotube (2 SWs case) and two more on the sides. The result is the formation of a ring of four SW defects (4 SWs case). [Figure 3.6](#) presents the DOS and conductance as the amount of SW is increased.

Below the Fermi level, there is a quasibound state at $E = -0.60$ eV for 1SW case, which disappears into a plateau in the energy axis when more defects are incorporated. The consequence is that the valley in the conductance spreads along the energy axis. At $E = -0.60$ eV, the LDOS does not longer present localized charge (black dots) coming from the quasibound state as in 1SW case (see [Figure 3.7](#)). They are replaced by a ring of grey points along the pentagons for the 2SWs and 4SWs cases, showing that the charge has delocalized in real space due to interference between defects causing delocalization of the quasibound state in the energy space as well.

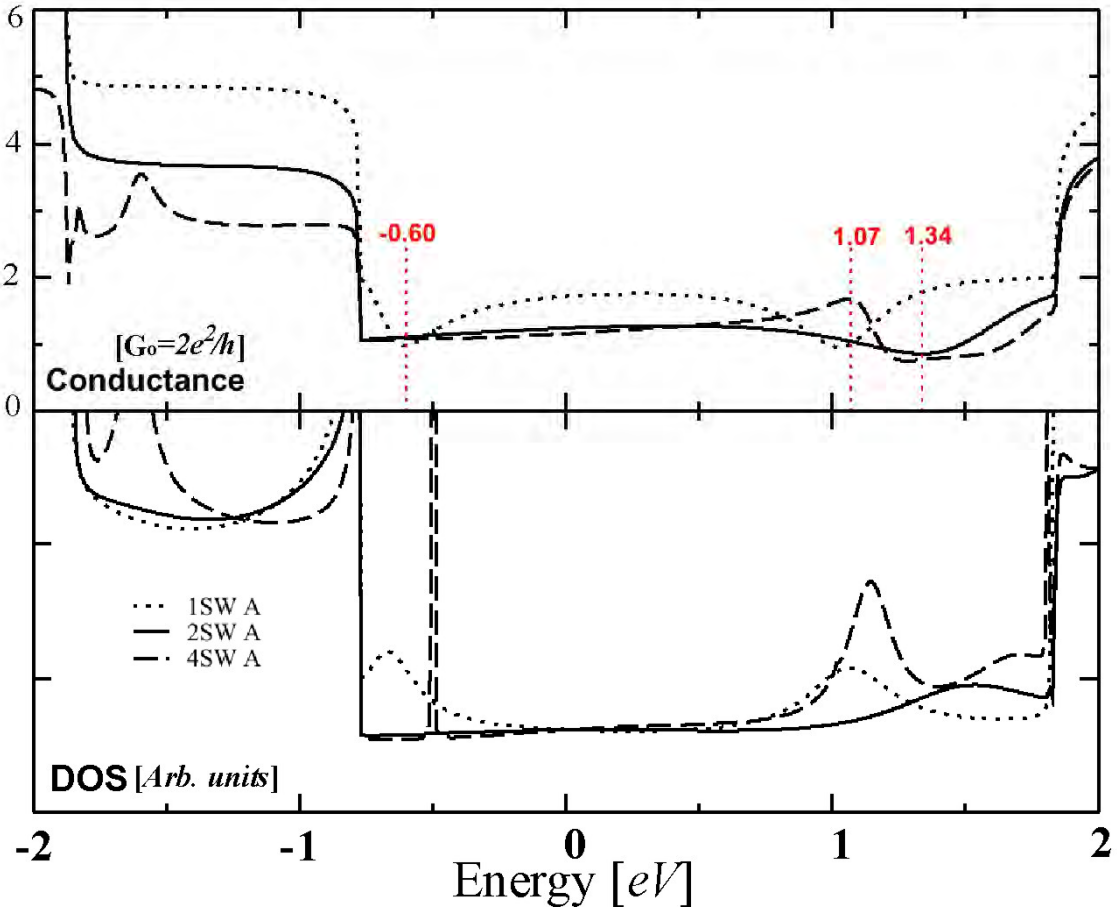


Figure 3.6: DOS and conductance curves as the amount of SWs is increased. One SW, two SW and four SW cases correspond to the pointed line, continuous line and dashed line, respectively. Three energy values marked on the conductance graph, are chosen for detailed analysis in [Figure 3.9](#).

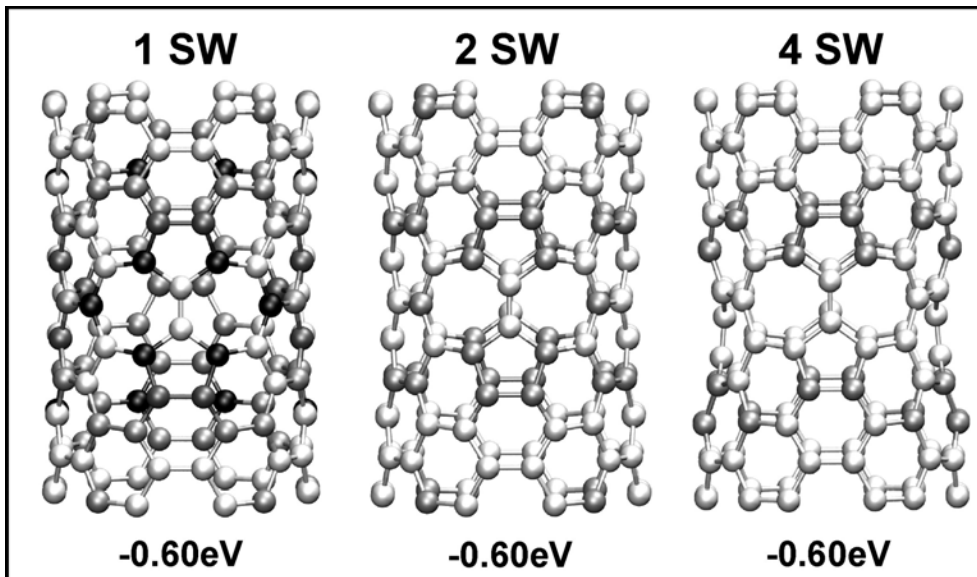


Figure 3.7: LDOS plot in real space as the amount of SWs is increased. It is observed that the quasibound charge from 1SW case delocalizes into a charge ring made by the pentagons.

Above the Fermi level, the peak of the quasibound state in the DOS graph at 1.07eV (1SW case) has shifted to the right and spread a little more along the energy axis; this causes valleys to form in the conductance graph (see 2SW case in Figure 3.6). The 4SW case exhibits a more complicated behavior above the Fermi level. This behavior is analyzed in Figure 3.9. At $E=1.34\text{eV}$ (where the conductance valley from 2SW case is located), it presents similar DOS and conductance characteristics when compared to the 2SW case. From Table 3.iii, it is observed that all the conductance originates from eigen channel 1 (π^* band). The LDOS plot in Figure 3.8 shows a delocalization of the charge in the heptagons of the two SW defects (case 2SW) and in a ring made by the 8 heptagons forming

Transmitted Charge [Go]

		Channel 1 A to B	Channel 2 A to B	Channel 1 B to A	Channel 2 B to A
1SW A	-0.60	0.00	0.98	0.00	0.98
2SW A	-0.60	0.27	0.84	0.27	0.84
4SW A	-0.60	0.13	0.95	0.13	0.95
1SW A	1.04	0.96	0.00	0.96	0.00
2SW A	1.34	0.85	0.00	0.85	0.00
4SW A	1.34	0.77	0.00	0.77	0.00

Figure 3.iii: Conductance values at the eigenchannel level as the amount of SWs is increased.

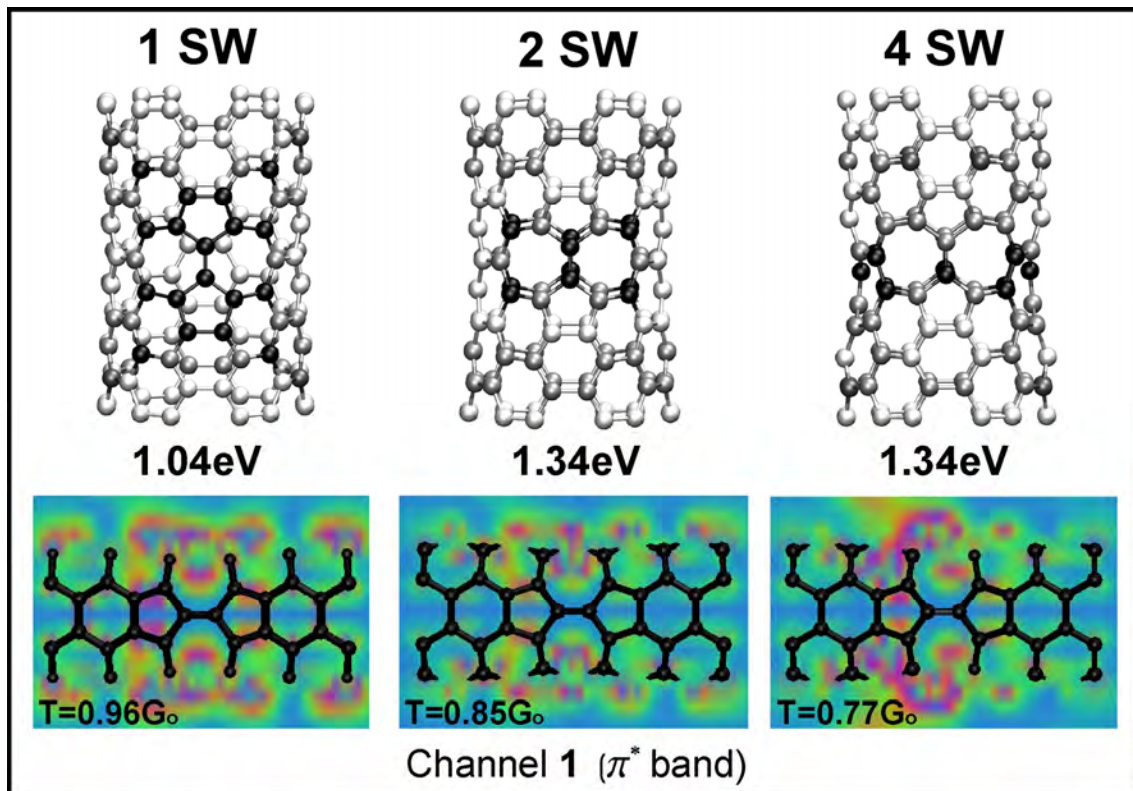


Figure 3.8: The LDOS as the amount of SWs is increased, showing a delocalization of the quasibound charge into rings around the tube axis (from interference between heptagons). The wave function plots show an increase in disturbance around the defective rings causing a decrease in transmittance.

the four SW defects (case 4SW). The charge density of the wave function of the travelling electron corresponding to the π^* band (shown in the lower panels of Figure 3.8) reveals an increase of disturbance in the charge pattern around the defective rings causing a smooth decrease in conductance as the amount of SW defects and delocalization of charge takes place.

Below the Fermi energy, the DOS curve starts increasing from the plateau at -0.60eV until a sharp peak (quasibound state) develops. The corresponding conductance curve follows the smooth increase but it reaches a maximum ($E=1.07\text{eV}$) just before the peak in DOS. After the peak, a sharp decrease in the conductance curve occurs (see Figure 3.6). A plateau ($E=-0.60\text{eV}$) of electronic states, originating from the pentagons and distributed by rings (see Figure 3.9), is present in the LDOS and conductance curves, where most of the conductance is coming from eigen channel 2 (π band). As we increase the energy, at $E=1.07\text{eV}$ (where the conductance is maximum just before the maximum in DOS), the charge has increased since electronic states from the heptagons have turned on and the wider ring formed by the four SW defects presents charge. This ‘turning on’ of the heptagons translates into ‘opening’ eigen channel 1 (π^* band) and therefore into an

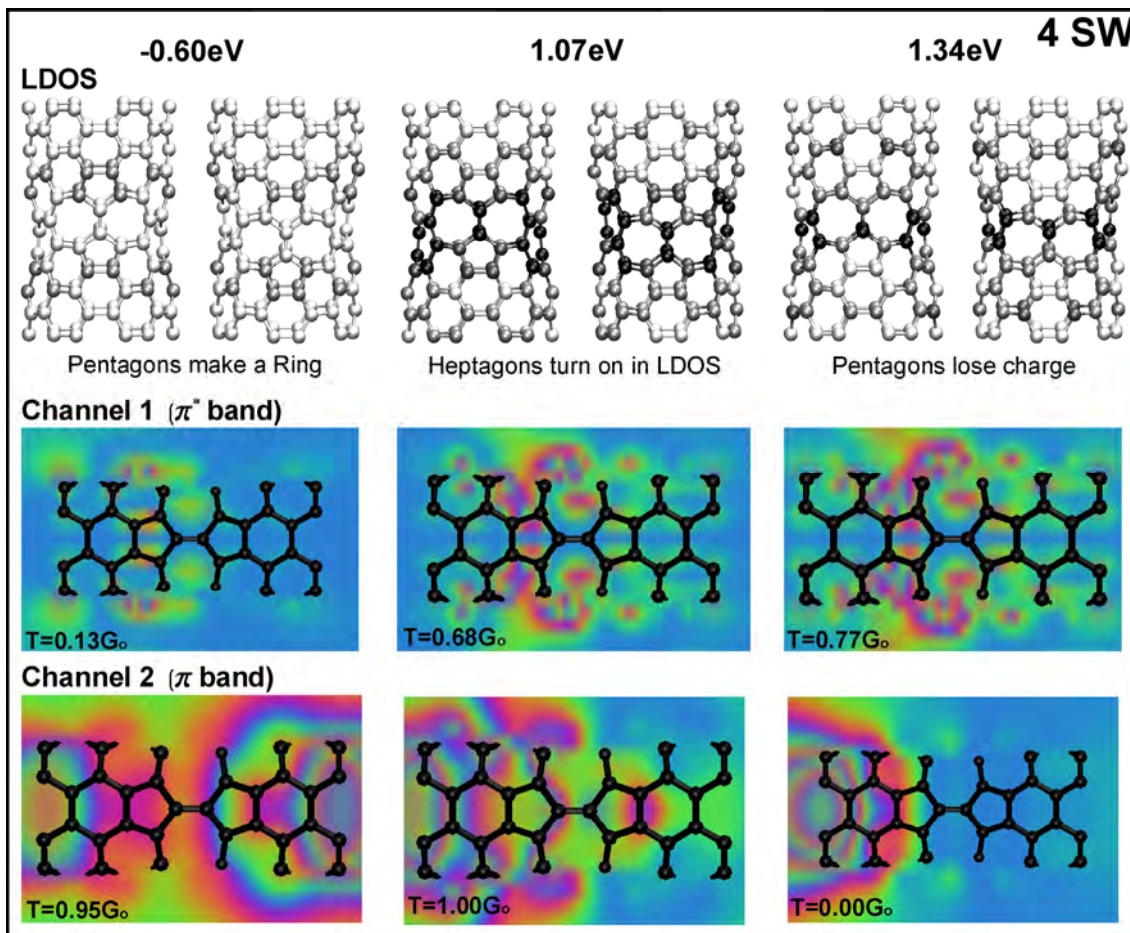


Figure 3.9: LDOS and wave function amplitude plots showing the behaviour of the 4SW case. The charge is delocalized into rings around the nanotube axis on the pentagons and then the charge is coming from the heptagons, depending the energy values; opening or closing different eigenchannels when different charge rings are activated.

increase of the total conductance when adding the two eigen channels. When we move further to $E=1.34\text{eV}$ (where the conductance decreased after the DOS peak) electronic states at the pentagons disappeared (causing the decrease in the DOS curve) and the only charge left is coming from the heptagons electronic states, 'closing' eigenchannel 2, therefore causing the sharp drop in the conductance curve.

It should be stressed that as the amount of SW defects is increased, they interfere with one another and the charge delocalizes into rings. Another observation is that rings of charge can block and open different eigen channels when coming from pentagon or heptagon electronic states.

3.3 Patches of defects (Haeckelite) in ON-CNT

Following the electronic transport studies on ON-CNTs, it is proposed a further step including defects in specific positions along the networks (repeated by translation operations).

In order to analyze the effect of defects in CNTs networks, hybrid networks have been designed by incorporating Haeckelite structures into the ON-CNTs. Haeckelite structures are carbon nanotubes, where the rolling sheet is not a graphene sheet but a carbon sheet composed by pentagons, hexagons and heptagons rings [40].

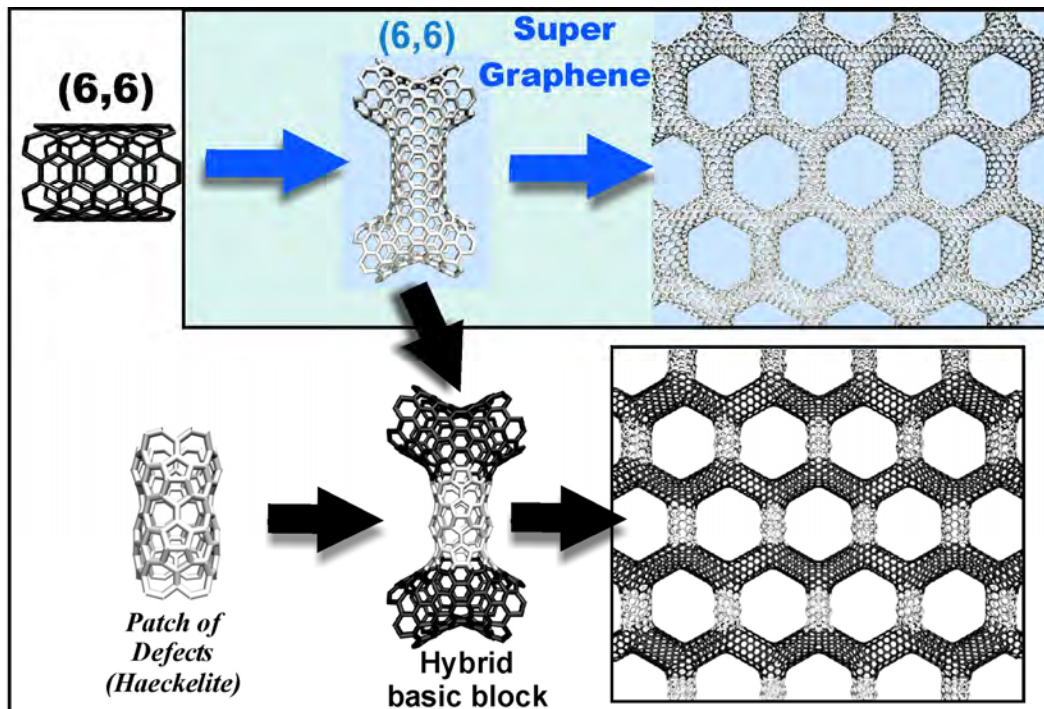


Figure 3.10: Schematic representation of the Hierarchy Algorithm used to strategically localize a patch of defects (Haeckelite) along a network. This is made by designing a hybrid multi-terminal block.

These hybrid networks can be obtained following the Hierarchy Algorithm previously described in [chapter 2](#). The hybrid basic block was designed starting from the (6,6) SG block (see [Fig. 2.2 and 2.10 in previous chapter](#)) and a portion of Haeckelite. As schematically shown in [Figure 3.10](#), a segment of the CNT

connecting both nodes in the basic block is removed and substituted by the portion of Haeckelite. The SG architecture was taken as toy model for two main reasons: i) the basic constructor block (a 4-terminals device) self-contains two nodes connected by a CNT (superbond), which allows the incorporation of patches of defects in the basic constructor block; ii) the (6,6) SG block shows conductor leads (due to its chirality) which guaranties incoming electrons at the Fermi level. Finally, the hybrid basic block is repeated by translation operations.

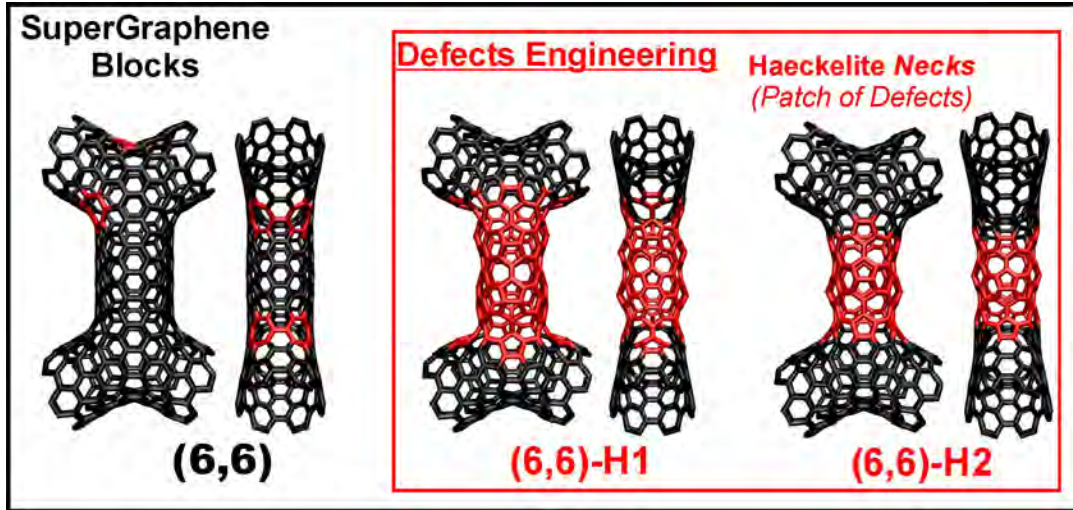


Figure 3.11: (6,6) SG block and two hybrid blocks designed by incorporating Haeckelite portions at the superbond location.

Following this approach, two different hybrid networks were designed. The difference was the type of Haeckelites used (i.e. different arrangements of the pentagons and heptagons inside the patch of defects) to observe the main effect of a patch of defects independently of the type of Haeckelite. The hybrid basic blocks are shown in Fig. 3.11 together with the basic (6,6) SG block. In the figure, red color represents the bonds of defective rings (i.e. pentagons and heptagons).

3.4 Enhancement of current through specific paths

In order to calculate the electronic transport properties of these hybrid networks, the Landauer-Buttiker formalism [41-43] and equilibrium Green functions were used, taking curvature into account by a semi-empirical Hamiltonian based on 4 orbitals (s, p_x, p_y, p_z) per carbon atom [44] (the technical details were described in the previous chapter).

The structure of the basic blocks is presented in Figure 3.12 in the upper panel and the conductance and DOS curves on the graphs at the bottom. Three inequivalent paths ($A \leftrightarrow D$, $A \leftrightarrow B$ and $A \leftrightarrow E$) are observed for the simple (6,6) SG block. Once the patch of defects is incorporated, the $A \leftrightarrow E$ path is not longer equivalent to the $D \leftrightarrow B$ one. This is due to the break of symmetry under the mirror plane perpendicular to the axis of the connecting cylinder between nodes. It follows that four inequivalent paths are obtained ($A \leftrightarrow D$, $A \leftrightarrow B$, $A \leftrightarrow E$ and $D \leftrightarrow B$).

The conductance curves exhibit a zero conductance at the Fermi level for the (6,6) SG block (as discussed in the previous chapter). Once the patch of defects is incorporated, conductance peaks around the Fermi energy appear for paths $A \leftrightarrow E$ and $D \leftrightarrow B$. The other two inequivalent paths $A \leftrightarrow D$ and $A \leftrightarrow B$ remain with zero conductance around the Fermi energy. It is remarkable that the role of the defect is here to improve the conductance properties along specific electronic paths. This is a phenomenon that can be exploited for driving current through well defined trajectories along a ON-CNT.

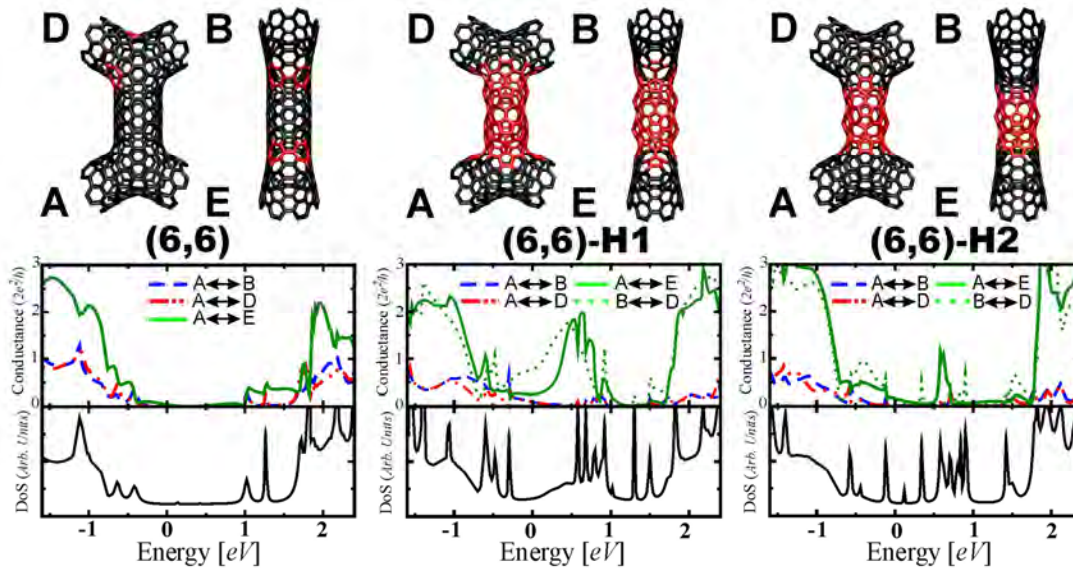


Figure 3.12: (6,6) SG block and the two hybrid blocks with their conductance and DOS graphs below. An enhanced conductance around the Fermi energy is revealed for path $A \leftrightarrow E$ and $B \leftrightarrow D$ in the hybrid cases, due to the incorporation of patches of defects.

A first basic explanation of the phenomenon can be given from the presence of pentagon and heptagon defects. It is known that the presence of a heptagon (pentagon) can cause an increase (decrease) of localized charge (quasi-bound electronic states) acting as scatterers on the transport properties [12, 36]. The position of these quasi-bound electronic states can affect the conductance through specific paths. These observations suggest that an array of defects can enhance the transport properties of specific electronic paths when blocking some other ones; raising the idea of guiding electronic current along networks based on CNTs.

In order to fully understand the phenomenon, a set of basic blocks was designed starting from the (6,6) SG block and incorporating one by one SW defects, until obtaining the (6,6)-H1 block. The set of blocks is schematically illustrated in Fig. 3.13 (the SW defects are in white color with an arrow marking its positions). Starting from this set of basic blocks, we performed an analysis of the DOS, conductance, LDOS and travelling electron wave function to study the conduction process between the (6,6) SG simple block and the (6,6)-H1 SG hybrid block. It should be noted that all the structures analysed in the present chapter were fully relaxed to obtain its minimum energy configuration based in the Tersoff-Brenner potential (see section 2.2.1 in previous chapter for further details).

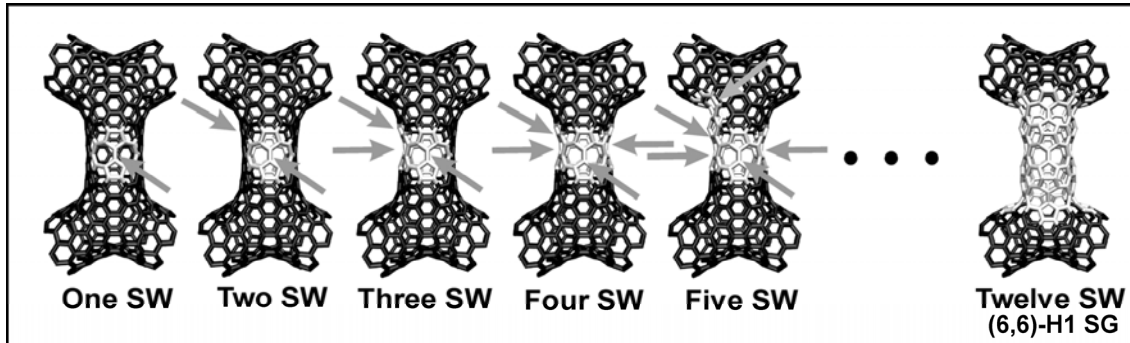


Figure 3.13: Schematic illustration of the one by one SW incorporation into the (6,6) SG block to finally transform it into the hybrid block.

3.4.1 Individual Stone Wales case

The simplest case introducing defects into a ON-CNT block corresponds to an individual Stone Wales defect (SW). A single SW was placed in two different positions as shown in Fig 3.14.

Case *Top* (see Fig 3.14) presents two main characteristics: the presence of the SW introduces electronic states into the conductor at specific energy values (new peaks in the DOS curves; see Fig. 3.15). At these specific energy values the conductance is increased. The LDOS plot at 0.35eV shows the appearance of electronic states on the CNT connecting both nodes when the SW is present

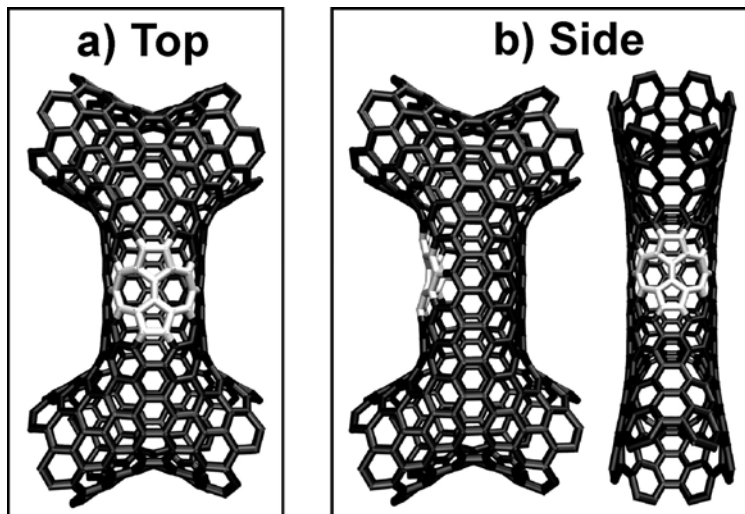


Figure 3.14: Two inequivalent positions where one SW is tested.

(marked by dotted rectangles on Fig 3.15). Then the presence of a SW incorporates new electronic states into the conductor which helps to increase its conductance.

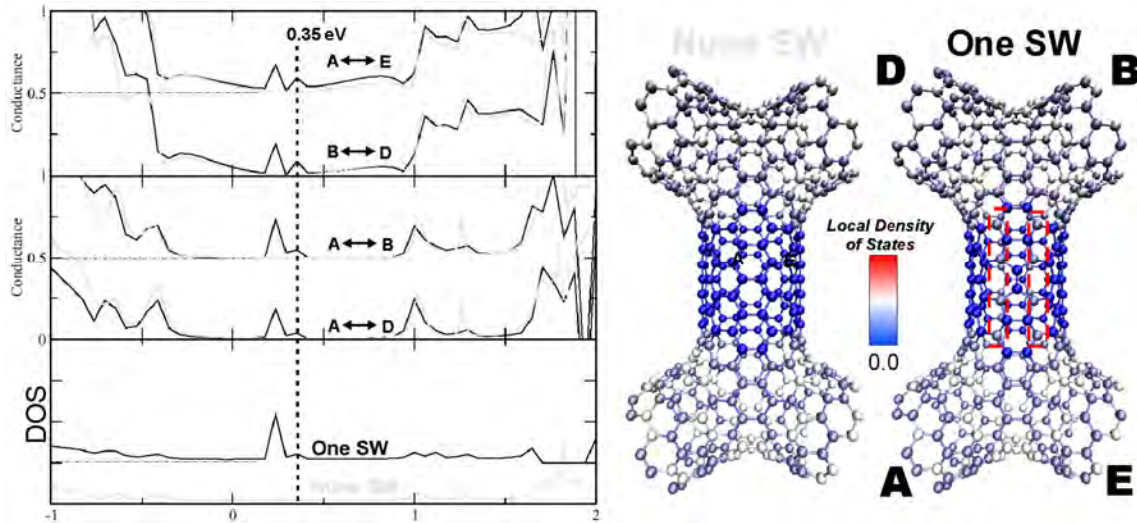


Figure 3.15: Left panel shows the DOS and conductance through the four inequivalent paths, revealing some conductance peaks when one SW is incorporated. The right panel shows the LDOS on the None SW and the One SW case at 0.35eV.

A similar analysis was performed for case *Side* (see Fig 3.14.b) and the same general trend was obtained, the SW presence incorporated electronic states which improved the conductance. However, the position of the SW is not symmetric anymore, improving the conductance better along certain paths. The LDOS at 0.95eV (see Fig 3.16) shows that the SW incorporates electronic states close to its position, with the new distribution of charge around path $A \leftrightarrow D$ and $B \leftrightarrow D$. This is consistent with an increase in conductance observed only for these two paths at 0.95eV. Therefore, the position of the SW can distribute asymmetrically the charge along the conductor, favouring the conductance of only specific paths. The -0.47eV case illustrates a similar trend, with the path $A \leftrightarrow D$ being the most favoured by the incorporation of electronic states and the one with the highest increase in conductance.

In summary, three main trends are observed: i) the incorporation of one SW increases the amount of electronic states at specific energy values; ii) the position of the SW is directly correlated with the distribution of the LDOS along the conductor; iii) this asymmetric increment of electronic states favours the conductance through specific electronic paths.

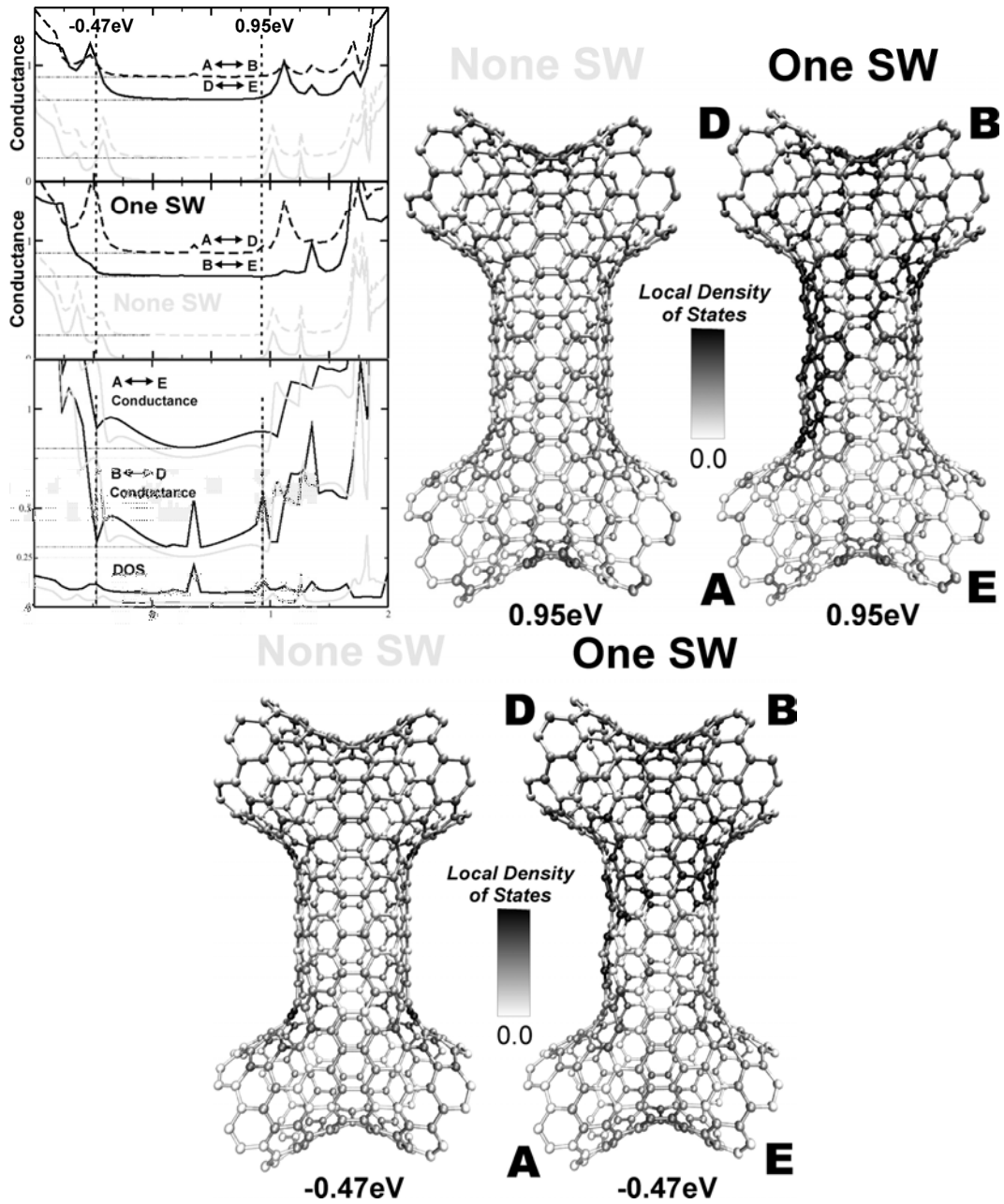


Figure 3.16: The LDOS at 0.95eV and -0.47eV , where conductance peaks appear for path $B \leftrightarrow D$ and $A \leftrightarrow D$ respectively, when one SW is present in the system. The 0.95eV case, with one SW, presents an appearance of more charge homogenously distributed around path $D \leftrightarrow B$ (darker zone). A similar trend is observed in -0.47eV for path $D \leftrightarrow A$ where the charge has increased along the path.

3.4.2 Effect of an asymmetric distribution of defects

An asymmetric effect was obtained when SW defects were added at the side of the superbond (see Fig. 3.17). An odd number of SW defects produces asymmetries with respect to the mirror plane that cuts the superbond in two equivalent pieces at the “None SW” basic block (perpendicular to the plane where the 2D SuperGraphene network resides). Interestingly, this asymmetry in localization of SW defects produces an asymmetric charge distribution of the multi-terminal device (basic block) favouring certain terminals and therefore guiding current through specific paths along the block.

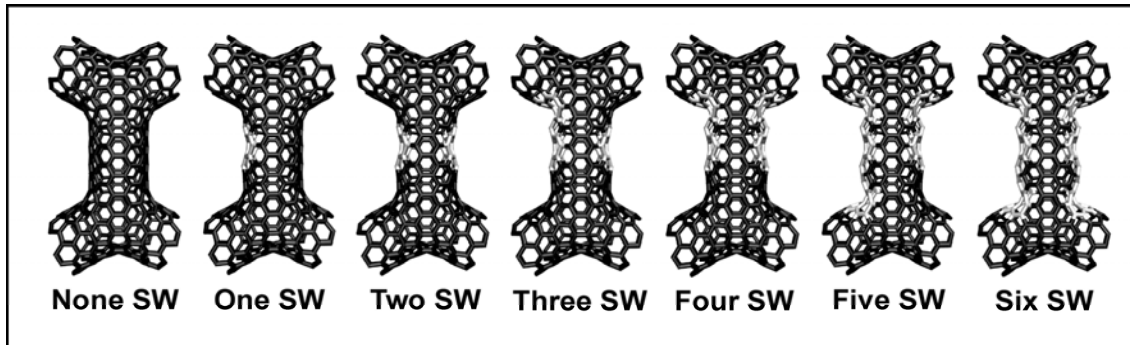


Figure 3.17: Stone Wales positions at the sides of the superbond, producing asymmetries when an odd amount of SW is present.

The DOS graph (see Fig. 3.18) shows a peak at 1.24eV as SW defects are added. When the conductance is analyzed for the paths crossing the superbond an interesting asymmetric effect is observed when three and five SW defects are present. Paths including terminal B are favoured for the three SW cases, while paths including terminal E have the higher conductance in the five SW case. The LDOS plot reveals an interesting phenomenon: in the three SW cases an increase of charge is found at the position where the fourth SW should be added in order to preserve symmetry (marked by an arrow in Fig 3.18.c). This accumulation of charge is located right at terminal B, thus favouring conductance through electronic paths including such a terminal, which at the same time avoids the SW defect located at terminal D. The same trend is observed in the five SW cases producing an accumulation of charge at the sixth SW position right at terminal E (see arrow in Fig 3.18.c), favouring then the conductance through paths including this terminal.

In the case of even number, the charge preserves symmetry, and the conductance paths crossing the superbond are equivalent.

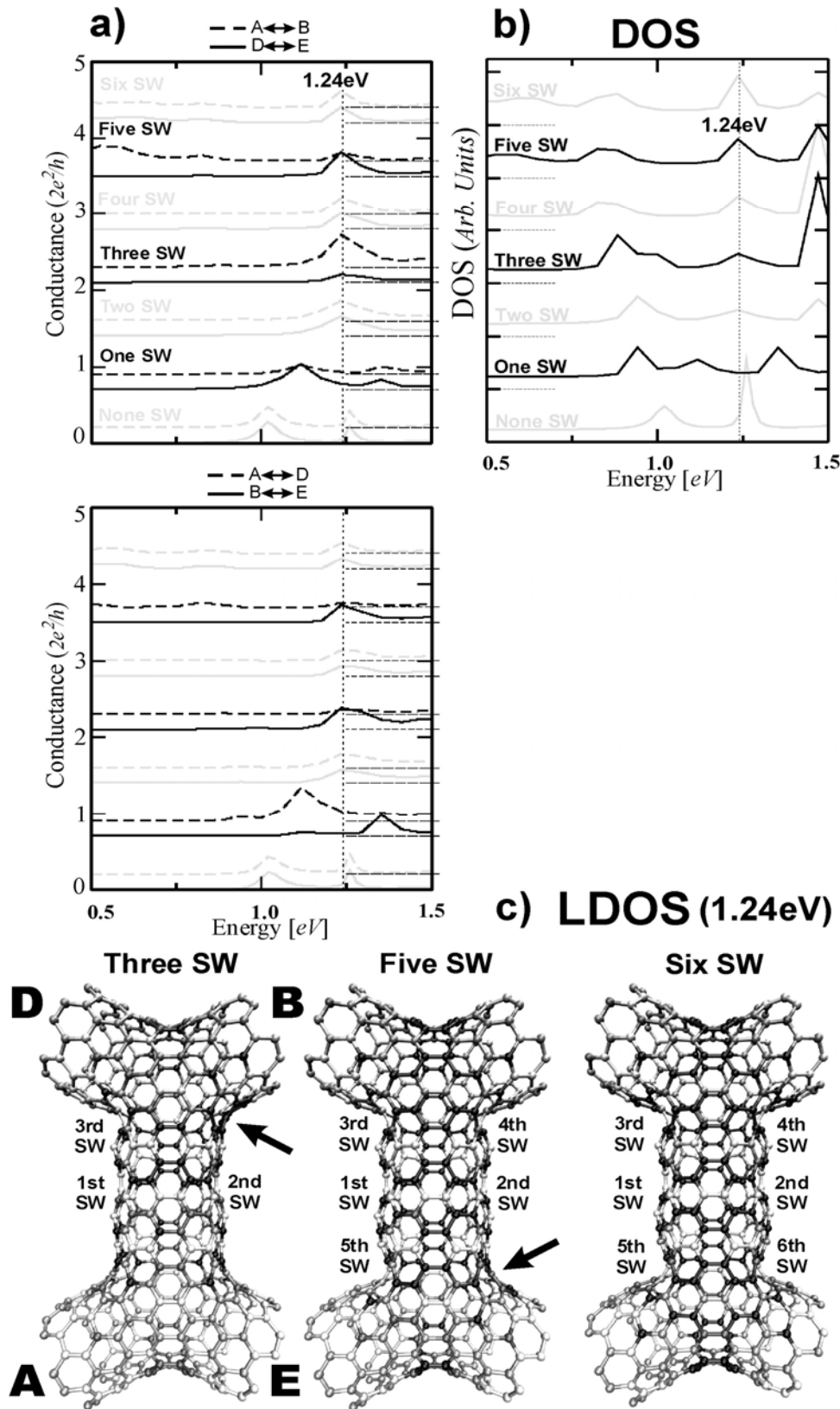


Figure 3.18: Analysis of the conductance peaks appearing at 1.24 eV. The LDOS shows that the asymmetry in defect positions originates asymmetry in the charge distribution favouring a specific terminal. The three SW case shows an increase in charge close to terminal B (marked by an arrow), when the conductance curves for this case are observed, it is seen that paths including terminal B are the electronic paths with conductance peaks. A similar behaviour is observed in the five SW case for terminal E. When an even number of defects is present the symmetry is preserved.

Figure 3.19 presents a similar case observed at 0.23eV, where the favoured conductance paths correspond to the paths including terminal A when five SW are present. The LDOS plot shows charge accumulation in such a terminal A induced by the fifth SW. The conductance curves corresponding to the six SW cases preserves the symmetry maintained by the even amount of SW defects.

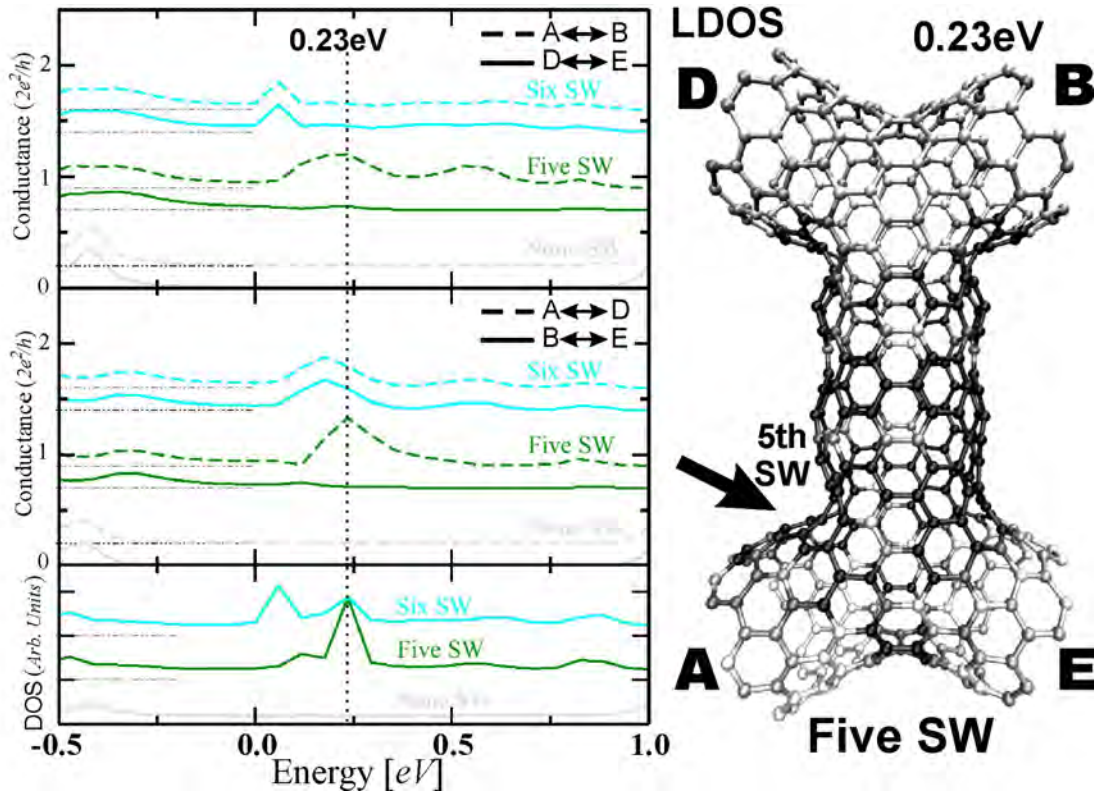


Figure 3.19: Conductance and DOS curves showing an increase in conductance on paths $A \leftrightarrow B$ and $A \leftrightarrow D$ at 0.23eV when Five SWs are present. The LDOS shows that the position of the Five SWs produces an increase in charge at terminal A favouring its electronic paths.

It should be remarked that the asymmetric distribution of SW defects causes charge accumulation favouring specific terminals, then producing higher conductance for specific electronic paths which translates into guiding current along the network when the SW defects are positioned strategically.

3.4.3 Conductance enhancement by path $A \leftrightarrow E$ and $D \leftrightarrow B$

The full study to understand the conductance enhancement obtained in path $A \leftrightarrow E$ and $D \leftrightarrow B$ is summarized in an analysis by rings shown in Figure 3.20. The upper panel shows the incorporation of the SW defects by rings including four SW defects each (it should be mentioned that the original block, *0 ring* structure, possesses a pair of heptagons at each 60° which produces a defect type 8558 with the bond rotation instead of the type 7557 known as a generalized SW at these positions).

The conductance graph shown in Figure 3.20.b displays the three inequivalent electronic paths (the array of defects breaks the symmetry between the $A \leftrightarrow E$ and $B \leftrightarrow D$ paths). A conductance enhancement appears for path

$B \leftrightarrow D$ and $A \leftrightarrow E$, between 0eV - 1eV . The increase in conductance for path $B \leftrightarrow D$ appears in the 2 ring block (solid black line in the graph) while path $A \leftrightarrow E$ reveals the conductance peak in the 3 ring case (solid grey line); these conductance peaks occur when the SW defects ring is closer to each electronic path in real space, respectively. The DOS is shown in Figure 3.20.c, where the inset corresponds to the energy region where the conductance enhancement occurs. From the dashed lines (0ring and 1ring cases), an increase is observed in electronic states to the solid lines (2ring and 3 ring cases) distributed broadly between 0.25eV - 0.6eV (see inset in Fig. 3.20). Conductance through path $A \leftrightarrow D$ (i.e. crossing the superbond) maintains a gap.

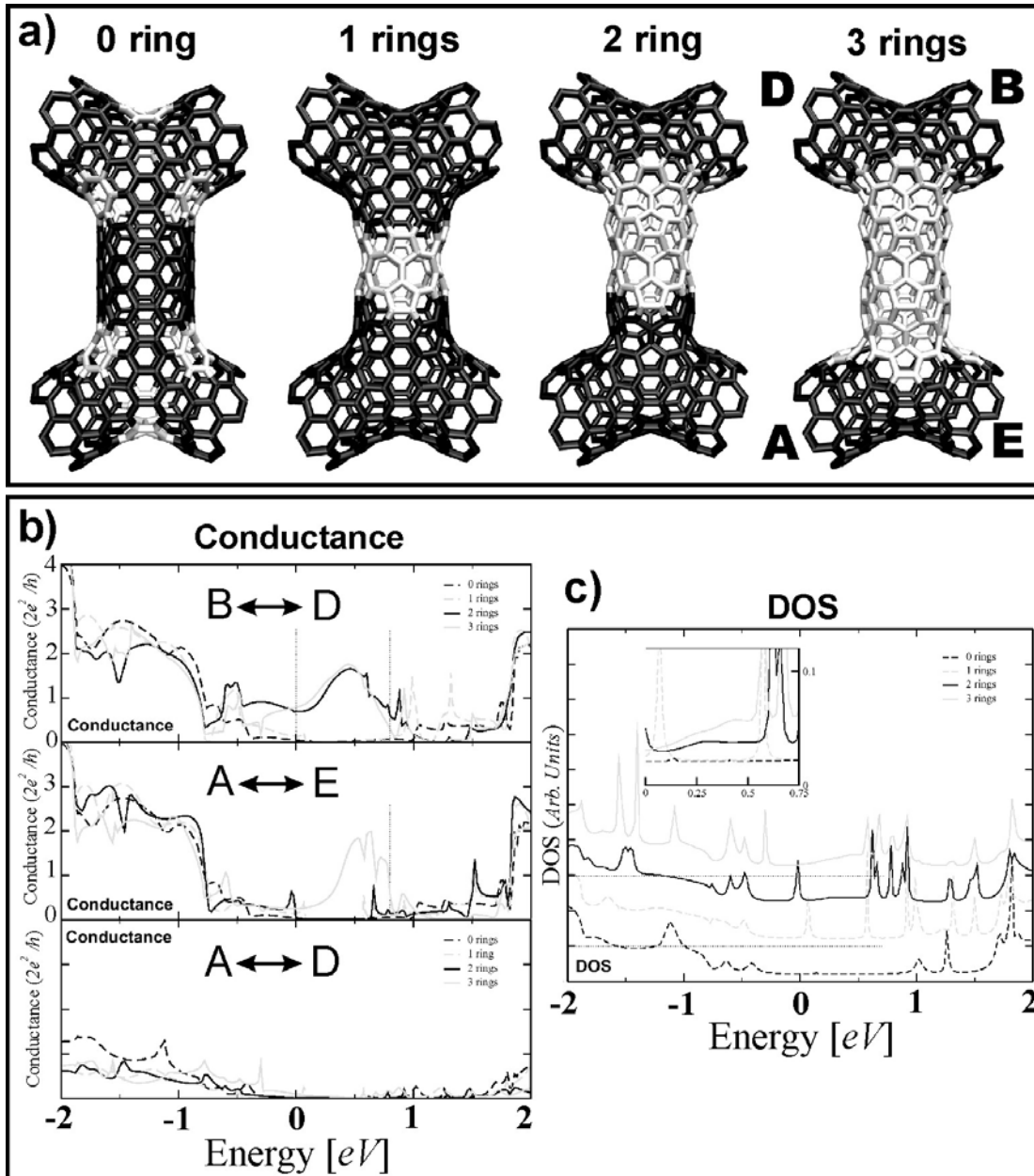


Figure 3.20: The top panel shows the incorporation of SWs by rings (4SWs at each ring). The bottom panel shows that the increase in conductance at path $B \leftrightarrow D$ appears when 2 and 3 rings are present while path $A \leftrightarrow E$ presents a conductance increase when 3 SW rings are present. These results are correlated with a delocalization in the energy space of the quasibound state as shown in the inset in the DOS graph.

In order to explore in detail the conductance increase, an analysis from the *1ring* case to the *2rings* case was performed by incorporating each individual SW defect one by one (illustrated in Figure 3.21.a). The first conductance peak for path $B \leftrightarrow D$ appeared at 0.30eV when 2SWs were incorporated (see Figure 3.21.b); with 3SWs a second conductance peak appears at 0.58eV and finally with the four SW defects (the second ring) the broad conductance peak is present. The conductance for path $A \leftrightarrow E$ remains with a gap as expected, since the defects were incorporated far away in real space from such terminals. When analyzing the DOS, the main region of interest corresponds to 0eV-0.6eV (presented in the inset of the graph, and increased in size in Figure 3.22). It is important to emphasize the

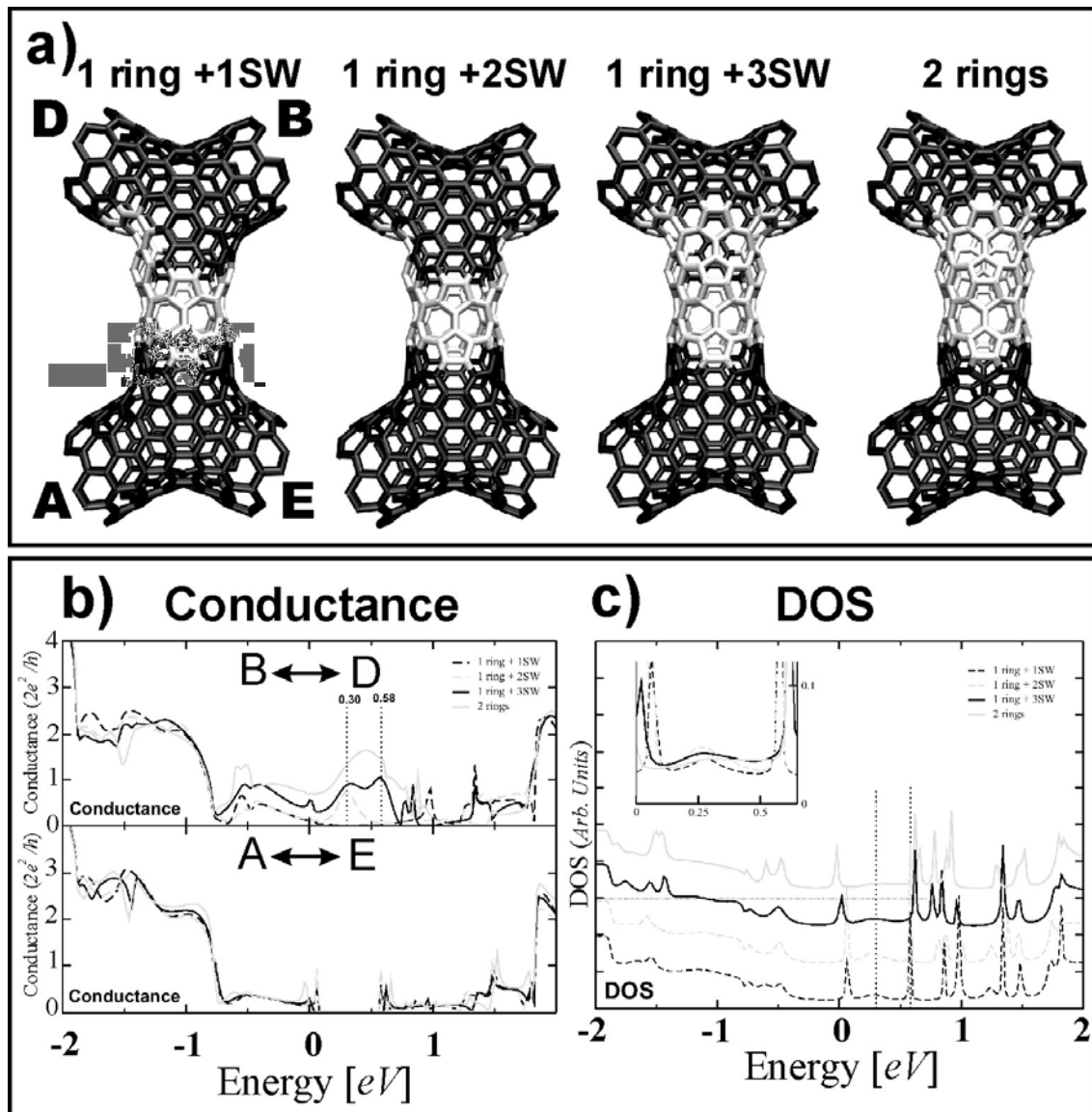


Figure 3.21: The top panel shows the incorporation of SWs one by one, from the first ring to the second ring. The bottom panel presents the conductance and DOS curves of the different blocks. A higher delocalization of charge is observed with broader peaks in the energy space when more SWs are incorporated (see inset in c), due to their interference since they are close to each other in real space. As the amount of SW is increased and the DOS peak close to 0.25 eV broadens, the conductance peak between 0.30eV and 0.58eV starts appearing.

evolution of the two peaks marked by vertical pointed lines in the conductance graph (at 0.30eV and 0.58eV; energy positions where the conductance peaks appeared); at 0.30eV the peak broadens in energy space whereas the very sharp peak (signature of a quasibound state) present at 0.58eV disappears from the 2SW to the 3SW case (when the conductance peak appeared), thus broadening the electronic states curve.

A detailed analysis of the DOS curves together with the LDOS reveals that the concept of '*patch of defects*' plays a critical role helping with the delocalization of charge. When we follow the evolution of the DOS peak at 0.30eV (see [Figure 3.22](#)), it is possible to observe the absence of peaks when only 1 ring of SW defects is present (dashed gray line in left graph), then a peak appears (black dashed line in right graph) when one SW is incorporated. As shown by the LDOS curve, an increase in electronic states is coming from the incorporated SW defects (red color indicating a maximum amount of electronic states). The important concept appears when the 2SWs are incorporated. In this case, there is an increase in states as expected, but the DOS peak starts widening in the energy space. This is an important fact, since the DOS is directly related to the probability to find an available electronic state after sampling the reciprocal space k , at certain energy values (DOS $\sim dk/dE$). A Dirac delta –like peak would mean all k states available for a specific energy value, therefore from the uncertainty principle ($\Delta k \Delta x \geq \hbar/2$), since all the k states are available, the uncertainty Δk is high and then the accessible position must be well known; this corresponds to localized charge in a specific position in real space from a bound state. As the peak starts broadening in the electronic space, the available k points are reduced for a specific energy and therefore the Δk uncertainty, which means an increment in position localization Δx uncertainty; this corresponds to the charge starting to delocalize in real space and increasing the electron mobility from the SW defects. This observation is confirmed by the LDOS plot. In this case it is observed by the presence of some white points (inside the dashed rectangle), this means that the two SW defects are close enough to feel each other and delocalize charge from one another. As more SW defects are incorporated, the DOS peak keeps broadening.

A similar phenomenon is observed at 0.58 eV in [Figure 3.21](#), where the second conductance peak appears. There is a sharp DOS peak when 1SW and 2SWs are incorporated (dashed curves). When 3SW are incorporated (which is when the conductance peak appeared), this sharp peak disappears and the increase in electronic states is distributed homogenously in the DOS curve (solid lines).

These observations indicate that even when an isolated SW defect generates quasibound states, an array of such defects close to each other in real space produces delocalization of such electronic states, thus helping the increase of conductance along certain electronic paths. Therefore the concept of a patch of defects plays a critical role in the electronic properties.

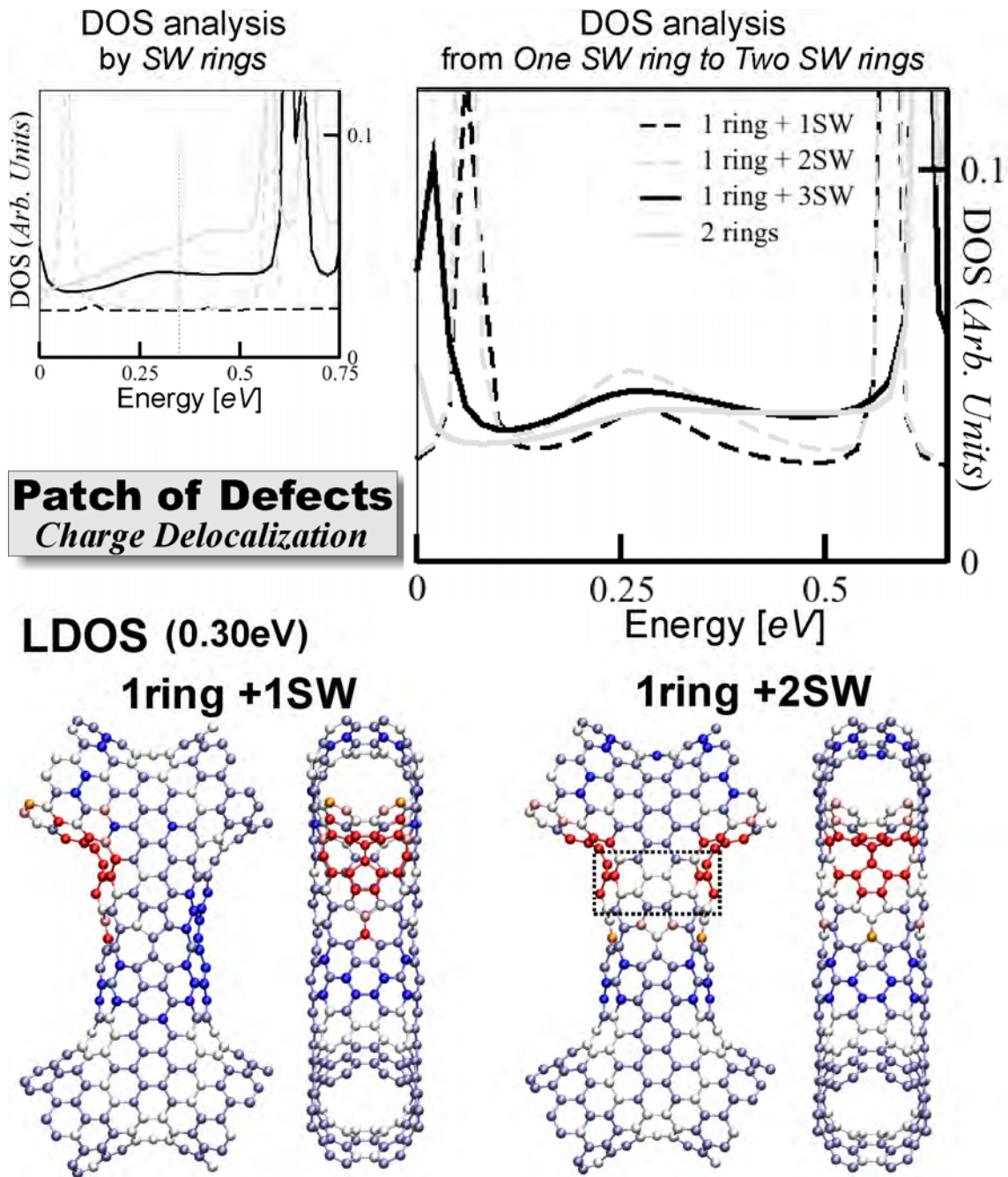


Figure 3.22: DOS and LDOS showing that the incorporation of a patch of defects (defects close enough to interfere) produce charge delocalization revealed here as broader peaks (quasibound states getting delocalized) on the energy axis at the DOS graphs. This is confirmed by the LDOS plot where the 1ring + 2SW case shows a charge ring when the two SW defects are close enough to interfere with each other (white spots inside the dotted rectangle).

The analysis was extended at the eigen channel level for the two energy points of interest. [Figure 3.23](#) depicts the 0.30eV case with the LDOS and the charge density of the wave function corresponding to the travelling electron together with a table showing the conductance values for each case in both eigen channels. The conductance values indicate that the peak appearing when 2SW defects are incorporated is coming from conduction by channel π . The charge density plots show how the travelling electron is reflected by the patch of defects (a “bouncing effect” on the travelling electron) and a smaller fraction is trapped at such a defect array ([see Channel \$\pi\$ plots](#)). When the ring of SW defects is fully incorporated, the reflectance of the travelling electron is improved. For channel π^* , most of the travelling electron charge is trapped by the middle ring of defects. When the second ring is fully incorporated, the charge in the middle ring decreases and becomes delocalized into the full patch including the upper ring (see purple and pink spots at the upper heptagons), which seems to improve the conductance through this channel by reflecting (‘bouncing’) the rest of the charge coming with the travelling electron.

A similar trend is observed in the 0.58eV case, shown in [Figure 3.24](#). The conductance peak appearing at 0.58eV when 3SW were incorporated, corresponds to the travelling electron coming from eigenchannel π^* . The charge density plots show how the travelling electron is reflected with the 60° angle opposite to the incoming terminal (see green color marked by the dashed rectangles) when no SW defects were present. This is consistent with the fact that the patch of defects promotes the reflection of the travelling electron. Plots from channel π^* show that most of the charge stays quasibounded at the defective sites in the 1ring+2SW case, while once 3SW are incorporated the charge delocalizes in the patch of defects helping the reflection of the incoming electron and improving the conductance to almost ballistic conductance by this eigenchannel.

Channel π^* shows a similar trend with most of the charge bounded to the defective sites and colliding with the 60° angle and finally when the second ring is fully incorporated, some charge can be reflected through path $B \leftarrow \rightarrow D$, thus increasing the conductance.

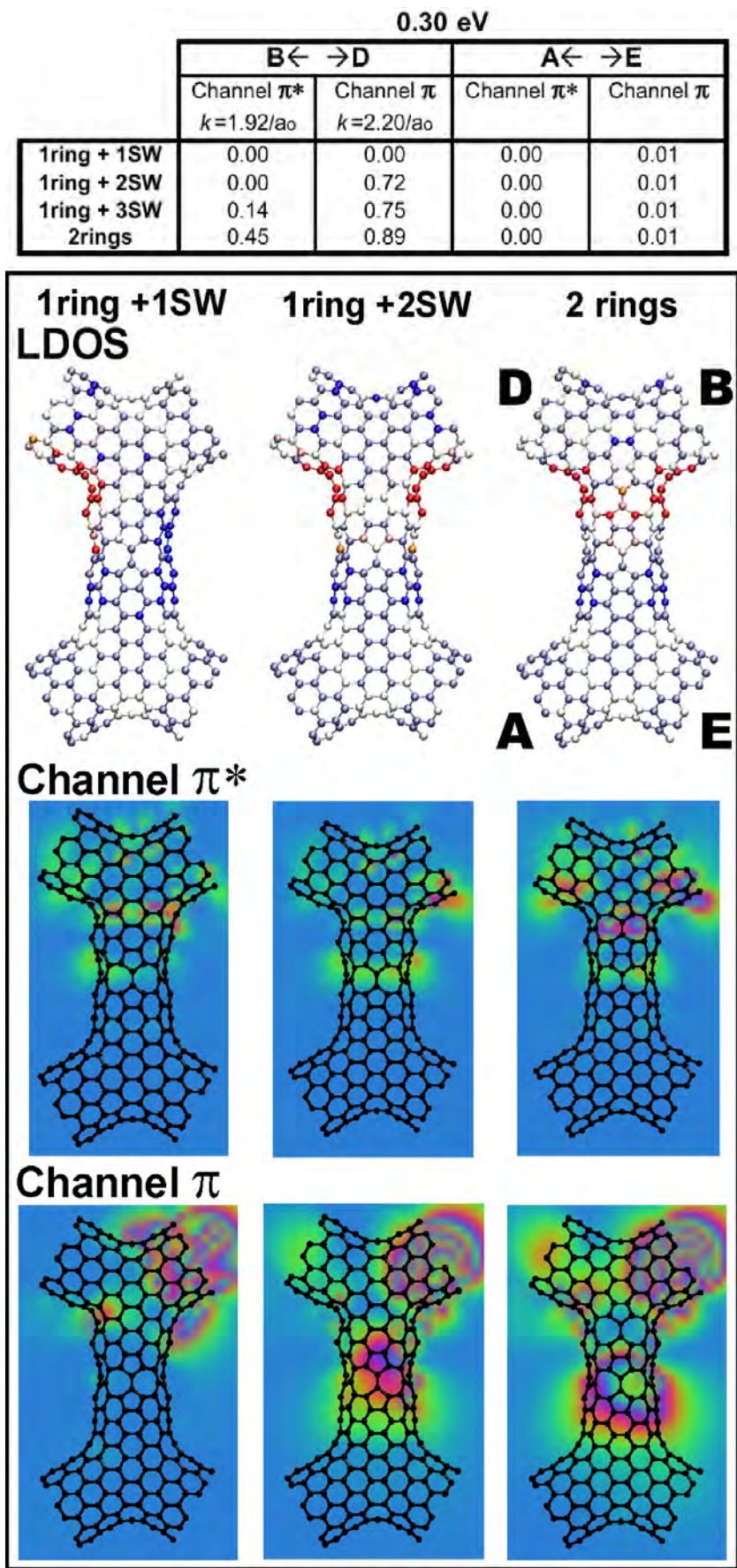


Figure 3.23: LDOS and travelling electron wave function analysis at 0.30eV, where the first conductance peak appears at the 1ring+2SW case. The conductance values show that the increase in conductance is coming from eigenchannel π , when 2SW interfere with each other causing charge delocalization into a ring which plays the role of bouncing barrier for the incoming travelling electron, reinjecting it into the favoured B \leftarrow \rightarrow D path. At the None SW case the incoming travelling electron is reflected by the 60° angle opposite to the incoming terminal; while with 4SW (2rings) the bouncing barrier is reinforced and the travelling electron better reinjected.

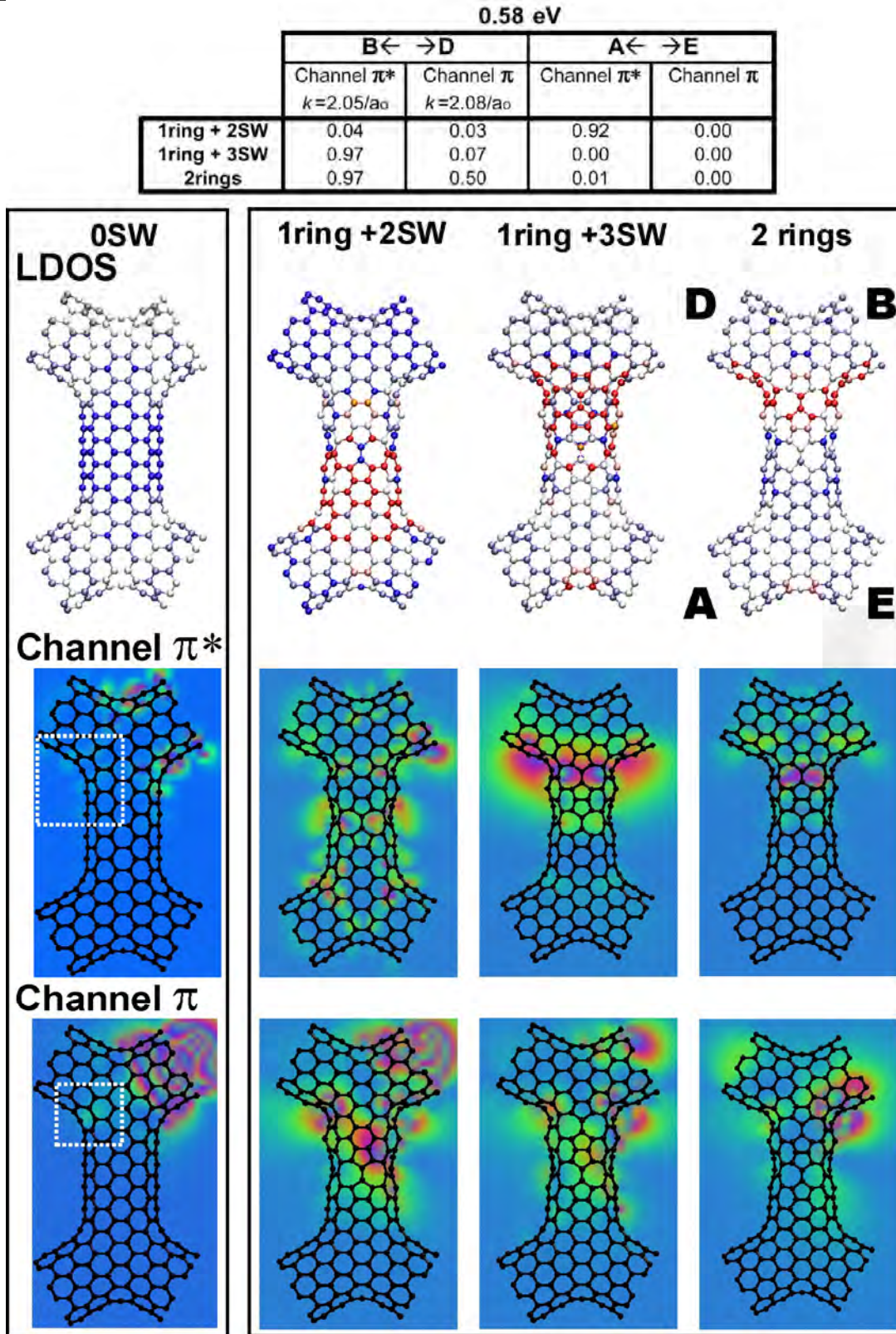


Figure 3.24: LDOS and travelling electron wave function analysis at 0.58eV, where the second conductance peak appears at the 1ring+3SW case. The charge delocalization from the patch of defects plays the role of a bouncing ring for the incoming travelling electron, reinjecting it into the favoured B←→D path. At the None SW case, the incoming travelling electron is reflected by the 60° angle opposite to the incoming terminal (marked with dotted rectangles).

3.5 Conclusions

Defects can be useful for electronic applications when their effect is fully understood and they are strategically utilized. The study performed in the present chapter started showing the scattering process of an individual SW defect in a CNT at the eigenchannel level, due to the charge arrangement producing 90° phase shifts of the incoming electrons (total reflectance) or total transmittance. When the amount of SW defects incorporated into the CNT is increased, they produce delocalization of charge by rings (concentric to the CNT axis) which could block or open different eigenchannels at different energy values.

Based on these results, we propose to incorporate defects strategically in ON-CNTs, to guide current along a nanocircuit. This has been demonstrated by designing a hybrid SG block (with a portion of Haeckelite) which is repeated by translation operations following the Hierarchy Algorithm. The conductance calculations revealed that such defect patches enhance the conductance through specific electronic paths maintaining zero conductance along the rest of them.

A detailed analysis was performed and the presence of a single SW defect in the SG block showed an increase in the amount of electronic states appearing in the DOS peaks at certain energy values, and the position of such defects was correlated with the LDOS distribution. When SW defects were distributed asymmetrically in the basic SG block, a charge accumulation was observed close to specific terminals, thus producing higher conductance for specific electronic paths which translates into guiding current along the network by the simple strategic localization of some SW defects.

The detailed analysis by incorporating SW defects one by one into the SG block, summarized by rings of 4SW (concentric to the superbond axis) explained the two main basic phenomena producing the conductance enhancement of paths $B \leftarrow \rightarrow D$ and $A \leftarrow \rightarrow E$ and therefore the driving of current along the network. First, the incorporation of 2rings and 3rings (the Haeckelite piece) showed a behavior of a *'patch of defects'* which produced the charge delocalization from the defective quasibound states. Second, this patch of defects promotes the enhancement in conductance by reflecting the incoming travelling electron and driving it through the correct electronic path.

Finally, our results indicate that arrays of defects can be seen as intrinsic devices along a CNT network able to guide current. This allows to envision an organic nanocircuit working as an addressable array, so that by tuning the energy of the travelling electron, different eigenchannels could be open or closed, and different electronic paths would be available within the nanocircuit.

References

- [1] Winfree, E., Liu, F., Wenzler, L.A. & Seeman, N.C. Design and self-assembly of two-dimensional DNA crystals. **Nature** **394**, 539-544 (1998).
- [2] Chworos, A., et al. Building Programmable Jigsaw Puzzles with RNA. **Science** **306**, 2068-2072 (2004).
- [3] Seeman, N.C. DNA in a material world. **Nature** **421**, 427-431 (2003).
- [4] Kalsin, A.M., et al. Electrostatic Self-Assembly of Binary Nanoparticle Crystals with a Diamond-Like Lattice. **Science** **312** 420-424 (2006).
- [5] Shevchenko, E.V., et al. Structural diversity in binary nanoparticle superlattices. **Nature** **439**, 55-59 (2006).
- [6] Redl, F.X., Cho, K.-S., Murray, C.B. & O'Brien, S. Three-dimensional binary superlattices of magnetic nanocrystals and semiconductor quantum dots. **Nature** **423**, 968-971 (2003).
- [7] Huang, Y., Duan, X., Wei, Q. & Lieber, C.M. Directed Assembly of One-Dimensional Nanostructures into Functional Networks. **Science** **291**, 630-633 (2001).
- [8] Whang, D., Jin, S., Wu, Y. & Lieber C.M. Large-Scale Hierarchical Organization of Nanowire Arrays for Integrated Nanosystems. **Nano Lett.** **3** (9), 1255-1259 (2003).
- [9] Tao, A., et al. Langmuir-Blodgett Silver Nanowire Monolayers for Molecular Sensing Using Surface-Enhanced Raman Spectroscopy. **Nano Lett.** **3** (9), 1229-1233 (2003).
- [10] Romo-Herrera, J.M., Terrones, M., Terrones, H., Sag, S., & Meunier, V. Covalent 2D and 3D Networks from 1D Nanostructures: Designing New Materials. **Nano Lett.** **7** (3), 570-576 (2007).
- [11] Tans, S.J., et al. Individual single-wall carbon nanotubes as quantum wires. **Nature** **386**, 474-477 (1997).
- [12] Chico, L., Crespi, V.H., Benedict, L.X., Louie, S.G., and Cohen, M.L. Pure Carbon Nanoscale Devices: Nanotube Heterojunctions. **Phys. Rev. Lett.** **76** (6), 971-974 (1996).
- [13] Yao, Z., Postma, H.W.Ch., Balents, L. & Dekker, C. Carbon nanotube intramolecular junctions. **Nature** **402**, 273-276 (1999).
- [14] Tans, S.J., Verschueren, A.R.M. & Dekker, C. Room-temperature transistor based on a single carbon nanotube. **Nature** **393**, 49-52 (1998).
- [15] Derycke, V., Martel, R., Appenzeller, J. & Avouris, Ph. Carbon Nanotube Inter- and Intramolecular Logic Gates. **Nano Lett.** **1** (9), 453-456 (2001).
- [16] Hayden, O., Agarwal, R. & Lieber, C.M. Nanoscale avalanche photodiodes for highly sensitive and spatially resolved photon detection. **Nature Materials** **5**, 352-356 (2006).
- [17] Duan, X., Huang, Y. & Lieber, C.M. Nonvolatile Memory and Programmable Logic from Molecule-Gated Nanowires. **Nano Lett.** **2** (5), 487-490 (2002).
- [18] Huang, Y., et al. Logic Gates and Computation from Assembled Nanowire Building Blocks. **Science** **294**, 1313-1317 (2001).
- [19] Zhong, Z., Wang, D., Cui, Y., Bockrath, M.W. & Lieber, C.M. Nanowire Crossbar Arrays as Address Decoders for Integrated Nanosystems. **Science** **302**, 1377-1379 (2003).
- [20] Ismach, A. & Joselevich, E. Orthogonal Self-Assembly of Carbon Nanotube Crossbar Architectures by Simultaneous Graphoepitaxy and Field-Directed Growth. **Nano Lett.** **6** (8), 1706-1710 (2006).
- [21] Rueckes, T., et al. Carbon Nanotube-Based Nonvolatile Random Access Memory for Molecular Computing. **Science** **289**, 94-97 (2000).
- [22] Terrones, M., et al. Molecular Junctions by Joining Single-Walled Carbon Nanotubes. **Phys. Rev. Lett.** **89** (7), 075505 (2002).
- [23] Endo, M., et al. Atomic Nanotube Welders: Boron Interstitials Triggering Connections in Double-Walled Carbon Nanotubes. **Nano Lett.** **5** (1), 1099-1105 (2005).
- [24] Charlier, J.-C. Defects in Carbon Nanotubes. **Acc. Chem. Res.** **35**, 1063-1069 (2002).
- [25] Chico, L., Benedict, L.X., Louie, S.G. & Cohen, M.L. Quantum conductance of carbon nanotubes with defects. **Phys. Rev. B** **54** (4), 2600-2606 (1996).
- [26] El-Barbary, A.A., Telling, R.H., Ewels, C.P., Heggie, M.I. & Briddon, P.R. Structure and energetics of the vacancy in graphite. **Phys. Rev. B** **68**, 144107 (2003).
- [27] Stone, A.J. & Wales, D.J. Theoretical studies of icosahedral C₆₀ and some related species. **Chem. Phys. Lett.** **128** (5-6), 501-503 (1986).

-
- [28] Crespi, V.H., Cohen, M.L. & Rubio, A. In Situ Band Gap Engineering of Carbon Nanotubes. **Phys. Rev. Lett.** **79** (11), 2093-2096 (1997).
- [29] Chico, L., López Sancho, M.P. & Muñoz, M.C. Carbon-Nanotube-Based Quantum Dot. **Phys. Rev. Lett.** **81** (6), 1278-1281 (1998).
- [30] Orlikowski, D., Nardelli, M.B., Bernholc, J. & Roland C. Theoretical STM signatures and transport properties of native defects in carbon nanotubes. **Phys. Rev. B** **61** (20), 14194-14203 (2000).
- [31] Ajayan, P.M., Ravikumar, V. & Charlier, J.-C. Surface Reconstructions and Dimensional Changes in Single-Walled Carbon Nanotubes. **Phys. Rev. Lett.** **81** (7), 1437-1440 (1998).
- [32] Gómez-Navarro, C., et al. Tuning the conductance of single-walled carbon nanotubes by ion irradiation in the Anderson localization regime. **Nature Materials** **4**, 534-539 (2005).
- [33] Carroll, D.L., et al. Effects of Nanodomain Formation on the Electronic Structure of Doped Carbon Nanotubes. **Phys. Rev. Lett.** **81** (11), 2332-2335 (1998).
- [34] Czerw, R., et al. Identification of Electron Donor States in N-Doped Carbon Nanotubes. **Nano Lett.** **1** (9), 457-460 (2001).
- [35] Son, Y.-W., Ihm, J., Cohen, M.L., Louie, S.G. & Choi, H.J. Electrical Switching in Metallic Carbon Nanotubes. **Phys. Rev. Lett.** **95**, 216602 (2005).
- [36] Choi, H.J., Ihm, J., Louie, S.G. & Cohen, M.L. Defects, Quasibound States, and Quantum Conductance in Metallic Carbon Nanotubes. **Phys. Rev. Lett.** **84** (13), 2917-2920 (2000).
- [37] Hamada, N., Sawada, S.-i. and Oshiyama, A. New one-dimensional conductors: Graphitic microtubules. **Phys. Rev. Lett.** **68** (10): 1579-1581 (1992).
- [38] Saito, R., Dresselhaus, G. & Dresselhaus, M.S. Physical Properties of Carbon Nanotubes. **Imperial College Press**, London UK (1998).
- [39] Rubio, A., Sanchez-Portal, D., Artacho, E., Ordejon, P. & Soler, J.M. Electronic States in a Finite Carbon Nanotube: A One-Dimensional Quantum Box. **Phys. Rev. Lett.** **82**, 3520-3523 (1999).
- [40] Terrones, H., Terrones, M., Hernández, E., Grobert, N., Charlier, J.-C. & Ajayan, P.M. New Metallic Allotropes of Planar and Tubular Carbon. **Phys. Rev. Lett.** **84**, 1717-1719 (2000).
- [41] Landauer, R. Electrical resistance of disordered one-dimensional lattices. **Philos. Mag.** **21** (172): 863 (1970).
- [42] Büttiker, M. Four-Terminal Phase-Coherent Conductance. **Phys. Rev. Lett.** **57** (14): 1761-1764 (1986).
- [43] Datta, S. Electronic Transport in Mesoscopic Systems. **Cambridge University Press**, UK (1995).
- [44] Charlier, J.-C., Lambin, Ph. & Ebbesen, T.W. Electronic properties of carbon nanotubes with polygonized cross sections. **Phys. Rev. B** **54** (12): R8377-R8380 (1996).

Chapter 4: CVD synthesis of CNT junctions and its Branching Mechanism

Abstract

Assembling nanostructures into ordered micro-networks remains a challenge in modern nanotechnology. 2D and 3D Ordered Networks based on Carbon Nanotubes (ON-CNTs) have shown intriguing mechanical and electronic properties of the assembled arrays [1]. The experimental realization of these types of networks, while quite challenging, can be greatly facilitated by studying the details of the branching mechanism during nanotube growth (multi-terminal junction of CNTs).

Since the first experimental observation of branched CNTs in 1995 [2], there have been significant developments to synthesize CNT junctions by different methods: i) by using templates [3], ii) by targeting an electron beam on crossing SWNTs in order to weld them into junctions [4], and iii) by gas phase synthesis approaches (either by arc discharge or CVD experiments) [5-13].

In this context, the aim of this chapter is to present a full study of the branching phenomena occurring during CNT junction synthesis. CVD growth in the absence of templates consists of the pyrolysis of hydrocarbons over a metallic catalyst, in the presence of carbon precursors containing sulfur [5-6,9,12,14]. Empirical observations have suggested that sulfur plays a key catalytic role in the branching mechanism [5-6,9,12], unfortunately without the characterization techniques to identify S in the CNT junctions successfully. Therefore, the branching phenomena by S atoms is not fully understood at the atomistic level.

The main idea of the experiment performed by Satishkumar et al. [5] was adapted in the laboratory (see section 4.2) and an exhaustive synthesis study was carried out modifying the amount of sulfur (e.g. thiophene), the temperature zone and the metallic catalyst. Drastic changes in morphology were observed and directly correlated to these variables (see section 4.3). Even more, five different types of covalent Y-junctions were identified when different experimental conditions were applied, from Y-junctions with arms of micrometers in diameter, Y-junctions of cone-stacked carbon cylinders to perfect multi-walled CNTs Y-junctions (see section 4.3.5).

Finally, a detailed high-resolution characterization of the Y junction nanostructures, complemented with first principles density functional theory (DFT) calculations, revealed the detailed atomistic model that elucidates the catalytic role of sulfur and the underlying branching mechanism in Y junctions (see section 4.4).

4.1 Introduction	91
4.1.1 Review of the literature	92
4.2 Experimental setup	93
4.2.1 Experimental method	93
4.2.2 Characterization techniques	95
4.3 CNT junctions results and discussion	95
4.3.1 Materials obtained in the external zone of the reactor	95
4.3.2 Material collected from the thermic insulator #1 zone (TI1)	98
4.3.2.1 Tree –like branches and Y junctions	98
4.3.2.2 Metallic balls entangled with carbon nanofibres	99
4.3.3 Effects of catalysts in the branching morphology.	104
4.3.3.1 Termination of CNTs when using Fe as catalyst	105
4.3.3.2 CNTs junctions	107
4.3.4 Effects of flow rates (thiophene concentration)	111
4.3.4.1 Minimum Ar flux through thiophene	111
4.3.4.1.a Random networks of 1D carbon blocks	111
4.3.4.1.b Micro tubular Junctions.	112
4.3.4.2 Medium Ar flux through thiophene	114
4.3.4.2.a Micro Patterns.	114
4.3.4.2.b Sea urchin –like nanostructures	115
4.3.5 Summary of Junctions produced	118
4.4 Branching Mechanism	119
4.4.1 Type of Junctions	119
4.4.2 Experimental and theoretical evidence	120
4.4.2.1 Detailed characterization at the branching points	120
4.4.2.2 DFT calculations: The importance of sulfur	122
4.4.2.3 HRTEM observations	124
4.4.3 Branching Mechanism and discussion	125
4.5 Conclusions	126
4.6 Open Issues	127
Calculation Methods	127
References	128

4.1 Introduction

Assembling nanostructures into ordered micro-networks remains a challenge in modern nanotechnology. 2D and 3D Ordered Networks based on Carbon nanotubes (ON-CNTs) have been proposed, showing intriguing mechanical and electronic properties of the assembled arrays [1], as exposed in chapter 2. The experimental realization of these types of networks, while quite challenging, can be greatly facilitated by studying the details of the formation mechanism of a branching node during nanotube growth (multi-terminal junction of CNTs).

CNT multi-terminal junctions (i.e. junctions with at least 3 terminals) were first proposed theoretically as “Y” junctions [15-16]. They have prompted special interest due to their potential electronic properties as nanodevices [17-18]. Tremendous efforts have been made to synthesize and control these structures.

Since the first experimental observation of branched CNTs in 1995 [2], there have been significant developments to synthesize CNT junctions by different methods. First, templates as mechanical constraints were used to obtain three terminal junctions [3]. Second, it was shown that targetting an electron beam on crossing SWNTs allowed researchers to weld them into junctions [4]. Finally, more recent results have focused on a gas phase synthesis process where the branching takes place *in-situ* during synthesis, either by arc discharge or CVD experiments. [5-13].

The overall morphology of junctions obtained using templates corresponds to the so-called “finger-like” shape [3], with the branches growing parallel to one another. In addition, high resolution characterization indicates that this type of material shows rather poorly graphitized side-walls. These two characteristics are detrimental for potential applications of ordered CNT networks. On the other hand, while the electron beam irradiation approach [4] is the only clear report of a covalent junction using *single-walled* nanotubes to date, it seems very unlikely that this technique could be scaled up for mass production. It is therefore clear that obtaining high quality nanoscale junctions is only viable if it is performed using CVD approaches, under conditions favourable for large-scale production, in which the *in-situ* branching phenomenon it is to understand and to control the fabrication of CNT junctions.

In this context, it is the aim of this chapter to present a detailed study of the branching phenomena occurring in this type of junctions. CVD growth in the absence of templates, consists of a simple pyrolysis procedure for synthesizing nickelocene along with thiophene for producing Y-junction CNTs [5]. Several subsequent studies followed a similar approach of pyrolysing a metallic catalyst, a carbon source and most of the time a sulfur containing species [5-6,9,12,14]. Empirical observations have suggested that the presence of sulfur in the synthesis process plays a key catalytic role in the branching mechanism [5-6,9,12]. Unfortunately without characterization evidence or a substantial and clear model for sulfur-mediated growth. Up to this time, the branching phenomena is not yet fully understood at the atomistic level.

When the main idea of the experiment by Satishkumar et al. [5] was adapted by our laboratory, an exhaustive synthesis study was performed, modifying the amount of sulfur (thiophene) and carrier flux, temperature zone and metallic

catalyst used in the experiment. The next sections of this chapter show the drastic changes in morphology that are directly correlated to these variables. Furthermore, five different types of covalent Y-junctions were obtained when different experimental conditions were applied (amount of thiophene or type of catalyst), ranging from Y-junctions with arms of micrometers in diameter, to Y-junctions of cone-stacked carbon cylinders, to perfect multi-walled CNTs Y-junctions.

Finally, the detailed high-resolution characterization of the Y junction nanostructures, complemented by first principles density functional theory calculations, revealed the detailed atomistic model that elucidates the catalytic role of sulfur and the underlying branching mechanism in Y junctions.

4.1.1 Review of the literature

The first experimental observation of branched CNTs was reported in 1995 from a sample prepared by the arc discharge technique [2]. After that, Nagy *et al.* claimed the synthesis of junctions of SWNTs, nevertheless their only characterization was carried out by STM without any conclusive TEM picture [19]; their sample was prepared by the thermal decomposition of C₆₀ in the presence of transition metals. The same year branching CNTs were reported as a by-product of diamond thick films in a hot filament CVD system using acetone and hydrogen. The authors of that study correlated the branching phenomenon to the presence of copper as a contaminant in their system [20]. Months later, Satishkumar *et al.* reported a simple CVD procedure of using nickelocene together with thiophene for producing CNT Y-junctions [5]. The next year the same group tested different types of organometallic compounds such as ferrocene and cobaltocene together with thiophene, thus yielding Y-junctions (it should be pointed out that the HRTEM studies revealed that these junctions consisted of branched cup-stacked fibres) [6]. The following year, Gu *et al.* reported Y-branching MWCNTs with a bamboo-like structure by CVD from a C-H-N gas system together with B₂O₃ and Ti [8]. During the same year two more reports appeared using iron and sulfur as a catalyst for the branching phenomenon [9,14]. In 2004, a different CVD approach was reported for CNT junctions, in which the new contribution is to dope the iron catalyst with small amounts of titanium [10]; nevertheless, the junctions obtained by this method exhibit a “finger-like” shape. In 2005, Heyning *et al.* claimed to synthesize, in high yield, Y-branched nanotubes, and reported that all MWCNTs in the sample are Y-junction nanotubes together with other carbon nanostructures [11]. These authors used the pyrolysis of a ferrocene:salt water solution together with methane. Finally, two new works appeared last year, the first one obtaining branched CNTs using the arc discharge technique from coal with CuO as a catalyst, emphasizing the presence of sulfur species in the coal sample [12]; and the second one reporting the fabrication of Y-junction bamboo-type carbon nanotubes by reduction of carbon dioxide (CO₂) with sodium borohydride (NaBH₄) [13].

After P. Nagy’s report, 11 works can be found in the literature describing CNT junctions: two corresponding to “finger-like” junctions [10,14], one to very symmetric CNTs Y-junctions [7], and a total of eight publications reporting CNT Y-junctions with very similar shape [5-6,8-9,11-13,20]. In this context, the main trend

observed in these eight works corresponds to the pyrolysis of a metallic catalyst, a carbon source and most of the time a sulfur-containing precursor.

A common feature found in these 8 publications is that these CNT junctions consist of joint cup-stacked nanofibres and not concentric tubules. Specifically, four of the works [5-6, 12-13] presented HRTEM images where the arrangement of the graphene layers consists of cone-stacked structure whereas the other three reports [8,11,20] do not show any HRTEM micrograph, and H. Zhu *et al.* reported a “blurry stacking of graphene sheets ...” within their nanostructures [9]. Therefore cone-stacked structures and sulfur appear to be somehow correlated.

Finally, it is worthy to point out the work performed by Li *et al.* since it appears to be the only report on CNT junctions consisting of concentric graphene cylinders [7].

4.2 Experimental setup

The experimental device was designed to reproduce the results reported by Satishkumar *et al.* [5]. The main elements to consider were the presence of nickelocene (NiCp_2), thiophene ($\text{C}_4\text{H}_4\text{S}$) and hydrogen.

The main issue to be solved was to have all the elements in a gaseous mixture for the CVD. In order to achieve this, a set of two tubular furnaces with a quartz tube were used as a reactor; the first furnace was used to sublime the nickelocene powder (introduced in an alumina crucible in the middle of the first furnace) whereas the second furnace would be used as the reaction furnace. To introduce the thiophene into the system in small amounts, this liquid was bubbled by the carrier gas (a mixture of 95% by vol. of Ar and 5% by vol. of H_2) before entering into the quartz tube. It was necessary to use a valve system, since thiophene needed to be introduced only during nanotube growth. Since the CVD system must be fed by an inert atmosphere during the heating of the furnaces system, a second gas line was adapted by the valve system with only Argon or Ar: H_2 mixtures (see Figure 4.1).

4.2.1 Experimental method

The first step was to heat up the second furnace to 1000°C under an argon atmosphere. Once the second furnace is ready, the first furnace is turned on and heated up to 400°C . It is important to start heating up the first furnace once everything is ready, since the experiment will start at the nickelocene subliming temperature ($\sim 260^\circ\text{C}$). When the first furnace reaches this temperature, the valve system must be switched to allow the introduction of the mixture gas line ($\text{Ar}+\text{H}_2+\text{C}_4\text{H}_4\text{S}$). All these compounds should be mixed while they pass through the first furnace and be pre-heated for the reaction in the second furnace. Once the first furnace temperature reaches 260°C and the reaction starts (seen by dark smoke coming out through the quartz tube and then out from the second furnace), five minutes are measured before changing the valves back to the inert gas line and allowing the whole system to cool down to room temperature.

It is known that one of the most critical variables in a CVD experiment corresponds to the temperature. The experimental device described above, displays different temperature zones along the quartz tube. Five different zones

were defined in our experiments (see Figure 4.1) and were labeled systematically to study the temperature effect and to identify the temperature region where each specific nanostructure is synthesized. The first zone was labeled as *thermic insulator #1 (TI1)* and corresponds to a steep gradient of temperature from 400°C to 1000°C in ~5cm; the second zone is *furnace #2 (F2)* corresponding to the interior of the second furnace which should be at an average temperature of 1000°C; the third zone is *thermic insulator #2 (TI2)* located at the outlet of F2 (~5cm, with a steep temperature gradient from 1000°C); after zone TI2 (where some black powder could be collected) the tube was divided in two more regions: *exterior #1 (Ex1)* and *exterior #2 (Ex2)*, the first one corresponding to ~3cm next to TI2, whereas the second one corresponds to the remainder of the quartz tube. In order to collect the samples, the quartz tube was marked with the different zones by measuring them.

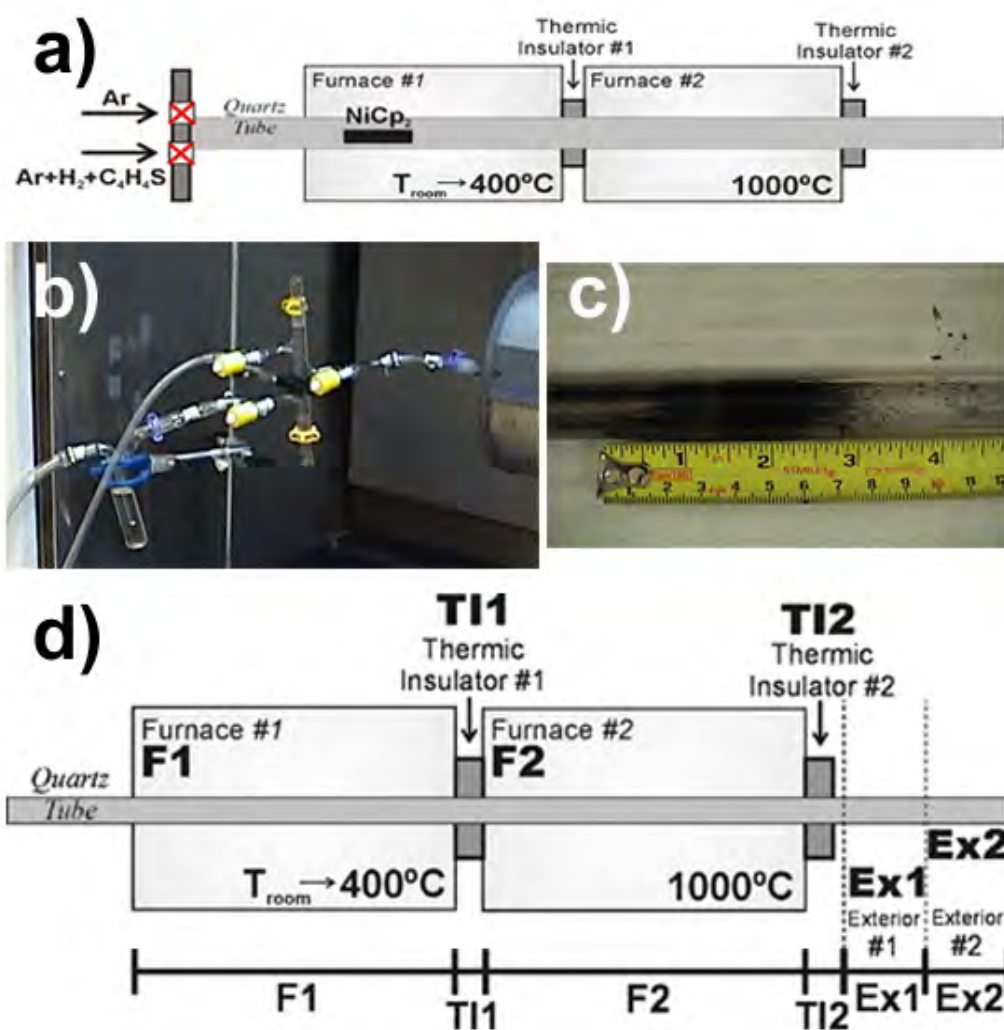


Figure 4.1: Experimental setup and temperature zones defined. Figure a) displays the scheme of the experimental set up; b) shows a picture of the thiophene bubbler before the valve system used to introduce the carrier gas; c) illustrates how to measure the quartz tube after the reaction to identify each different zone; finally d) presents the experimental setup with the labels at each different zone of the reactor.

In our studies two more variables were studied: i) the gas mixture flux and ii) the metallic catalyst employed. The gas mixture flux appears to play a crucial role since it regulates the amount of thiophene (sulfur) inserted into the system (as a carrier it imposes the feeding rate of the chemical reactives to the synthesis and together with the temperature dictates the local environment by the convection currents along the experimental device). The metallic catalyst is well known to act as the seed in the synthesis of nanotube structures, and will directly influence the specific structure obtained in the resulting sample.

4.2.2 Characterization techniques

The samples collected from the different experiments and different temperature zones were structurally characterized by: scanning electron microscopy (SEM, Philips FEG-XL30; operated 10-20 keV), scanning electron transmission microscopy (STEM, Philips FEG-XL30; operated 10-20 keV), transmission electron microscopy (TEM, Philips CM200; operated 200 keV) and high resolution electron microscopy (HRTEM, Philips CM200; operated 200 keV; and Jeol 4000EX operated at 400 keV); and analytically characterized by energy dispersive X-rays (EDX, in column Philips FEG-XL30 and in column Philips CM200) and electron energy loss spectroscopy (EELS, attached to the Philips CM200).

4.3 CNT junctions results and discussion

The exhaustive characterization shows the ability of the experimental method to synthesize different types of covalent junctions. Nevertheless, obtaining these junctions requires very specific conditions, precisely identified with this study. Some other types of nanostructures can be obtained when appropriate changes in carrier gas mixture flux, temperature or metallic catalyst are applied.

4.3.1 Materials obtained in the external zones of the reactor

Zones labeled as F2, Ex1 and Ex2 (see Fig 4.2) mainly contain carbonaceous spheres, known as carbon black. The main trend in morphology observed as we move further away from the furnace, is that the spheres decrease in diameter (see SEM images in Fig 4.2).

The second observation is that some of the carbon spheres encapsulate metals (observed by the difference in contrast of the TEM images and confirmed by EDX measurements); where nickel is encapsulated inside the spheres that are less rounded and exhibits the presence of more graphitized material. The second column in Figure 4.2 shows representative TEM images of round spheres without a darker core, while the third column shows the less rounded spheres with darker cores (each line in Fig 4.2 corresponds to a different temperature zone). Figure 4.3 shows EDX analysis of the three types of spheres: rounded (without the Ni signal), less rounded with dark core (showing the Ni and S peaks) and less rounded with several small dark particles (displaying the Ni and S signals).

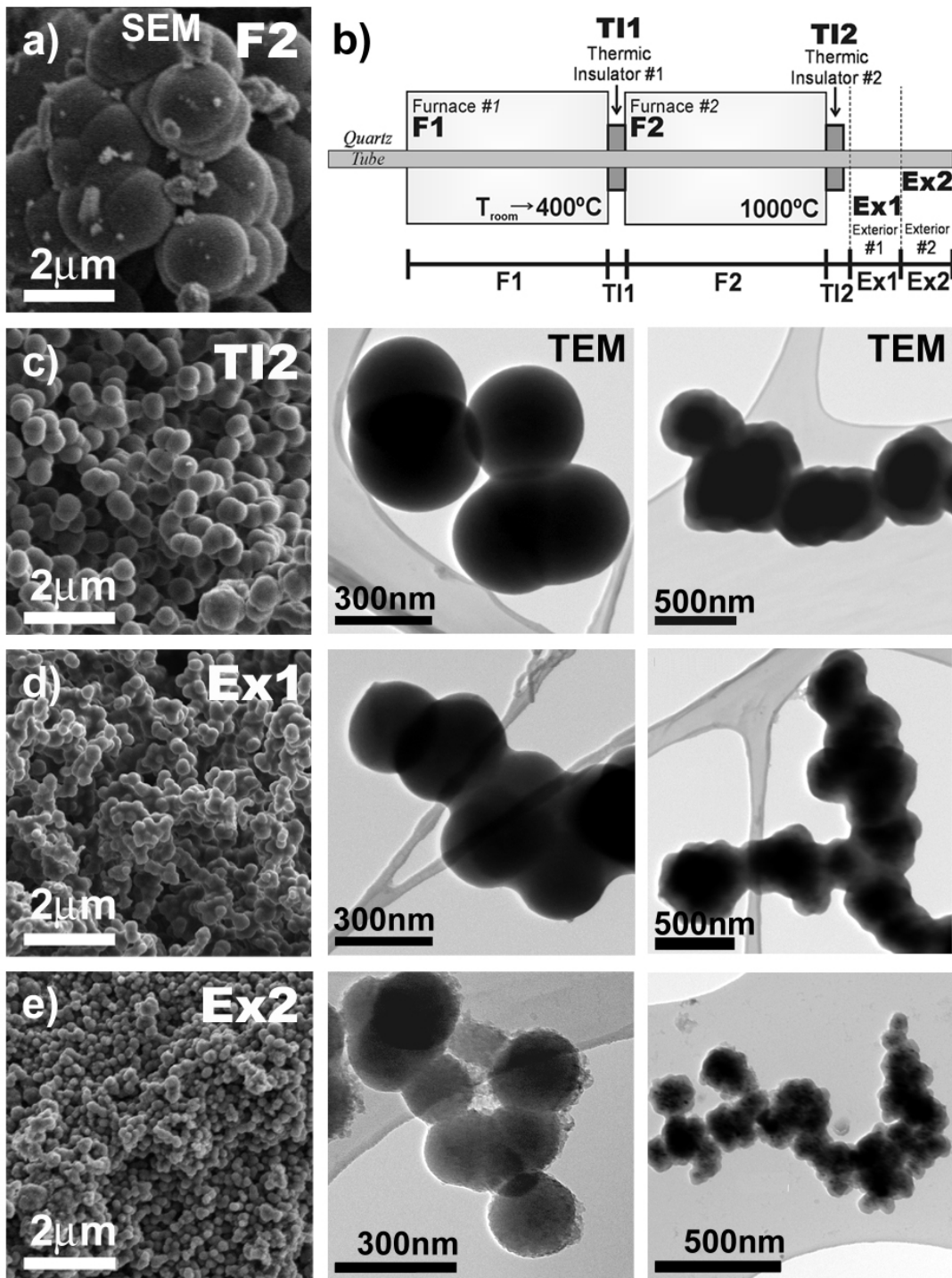


Figure 4.2: The material obtained at the exterior zones corresponds to carbon balls. Figure a) show the SEM image with the appearance and size of the balls of the sample collected from F2 while b) shows the schematic representation of the reactor labelled at each of the different zone. Figures c), d) and e) display the SEM and TEM images with the appearance of the material and their shape at higher magnifications, respectively, from the samples collected at the exterior zones.

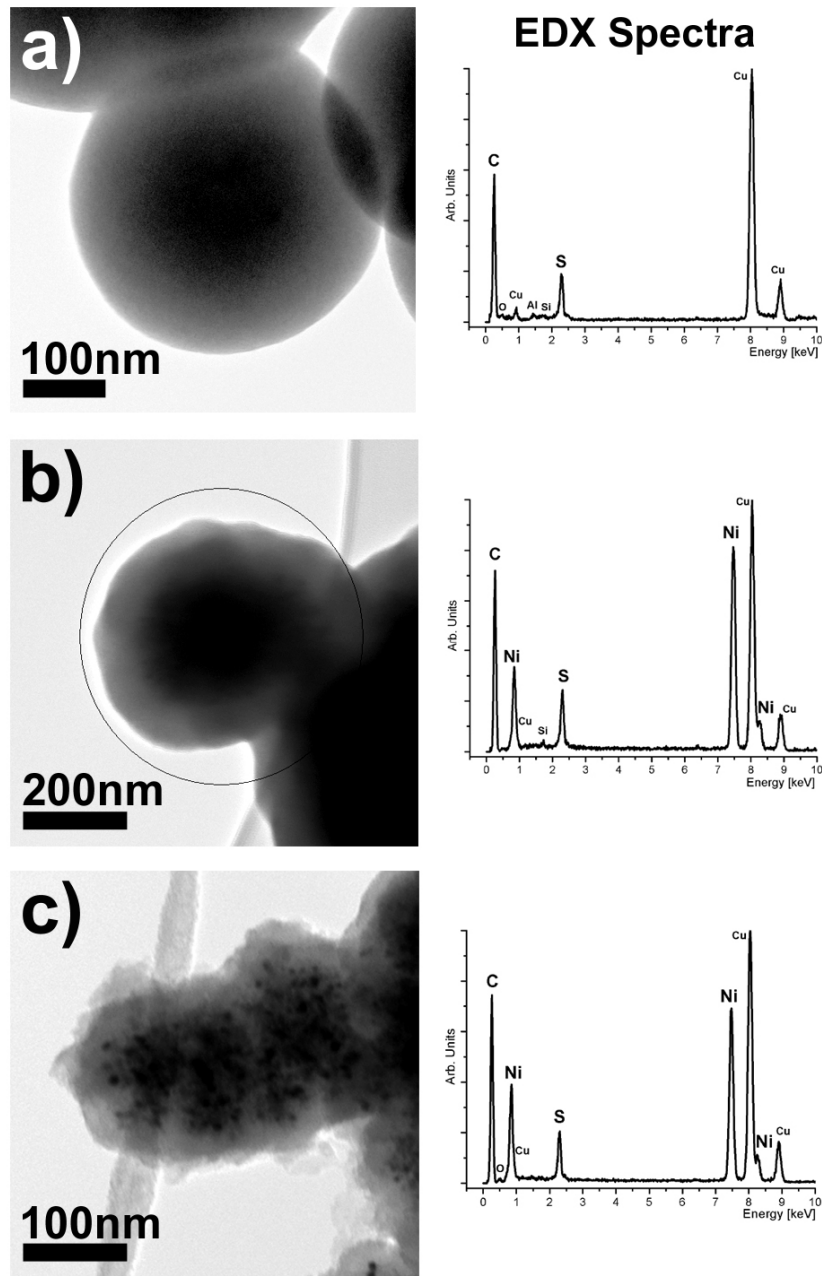


Figure 4.3: TEM images and their corresponding EDX analysis, showing in a) carbon spheres with very rounded shape and non Ni signal but S; b) displaying a dark interior corresponding to encapsulated Ni and S, and c) revealing small darker encapsulated particles which correspond to Ni and S according to the EDX spectrum.

4.3.2 Material collected from the thermic insulator #1 zone (TI1)

It is in this zone where Y-junctions were observed (as also reported by [5]). The sample collected from this zone showed two types of materials with different morphologies coexisting under these particular experimental conditions. The first type was predominantly composed by *tree branches* like material (see Fig 4.4), as the Y-junctions previously reported [5]. The second type of material corresponds to flakes of millimeter size composed of carbon fibres entangled with metallic spheres (see Fig 4.5.a).

4.3.2.1 Tree –like branches and Y junctions

This material has the general morphology of tree branches as shown in Fig 4.4. It is worth mentioning that this material was also observed in a sample collected in the TI2 zone, which is consistent with the existence of a steep temperature gradient.

This specific material was the main motivation for the present study, in order to reproduce the results previously reported [5], and to characterize in full detail the obtained samples. With this new information, theoretical studies are carried out in order to elucidate the branching mechanism (see Section 4.4)

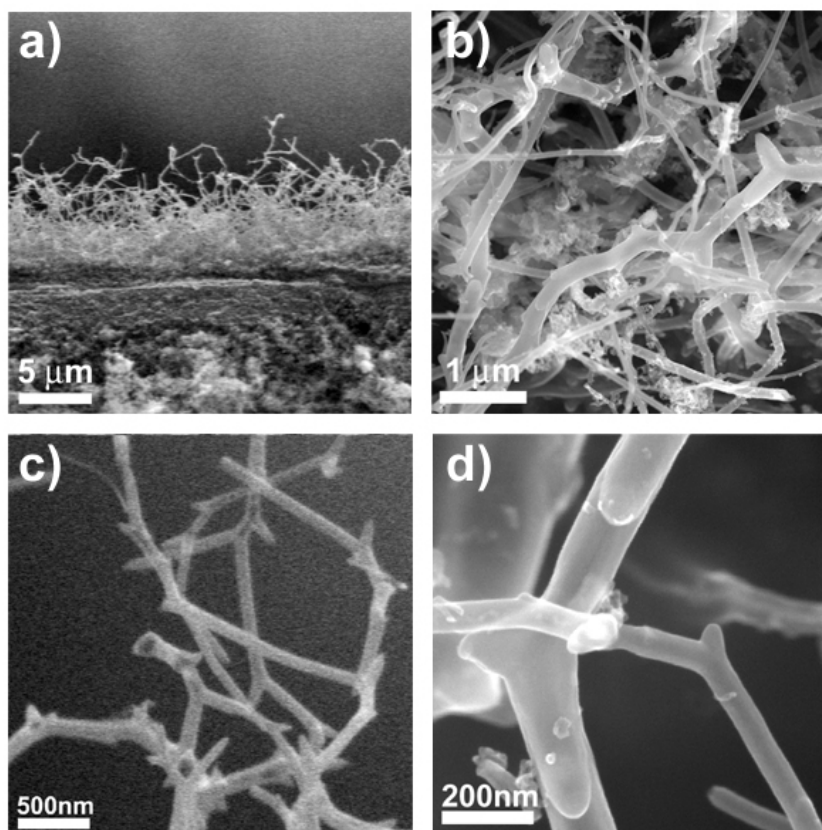


Figure 4.4: Tree branch –like material. Figure a) shows the low magnification SEM image with a shrub appearance; b) displays an average sample with high yield of branched material; c) shows a high density of branching points along the CNTs; d) reveals the morphology of the junctions in a higher magnification SEM image. The material has a similar appearance to the Y junctions reported in the literature [5].

4.3.2.2 Metallic balls entangled with carbon nanofibres

Low magnification SEM images depicted in Figure 4.5 reveal the entanglement of these carbon fibres. TEM images of the same sample show the internal structure of the fibres (see Fig 4.6). According to the HRTEM images, these fibre walls correspond to the stacking of graphene layers almost perpendicular to their axis (see Fig 4.6).

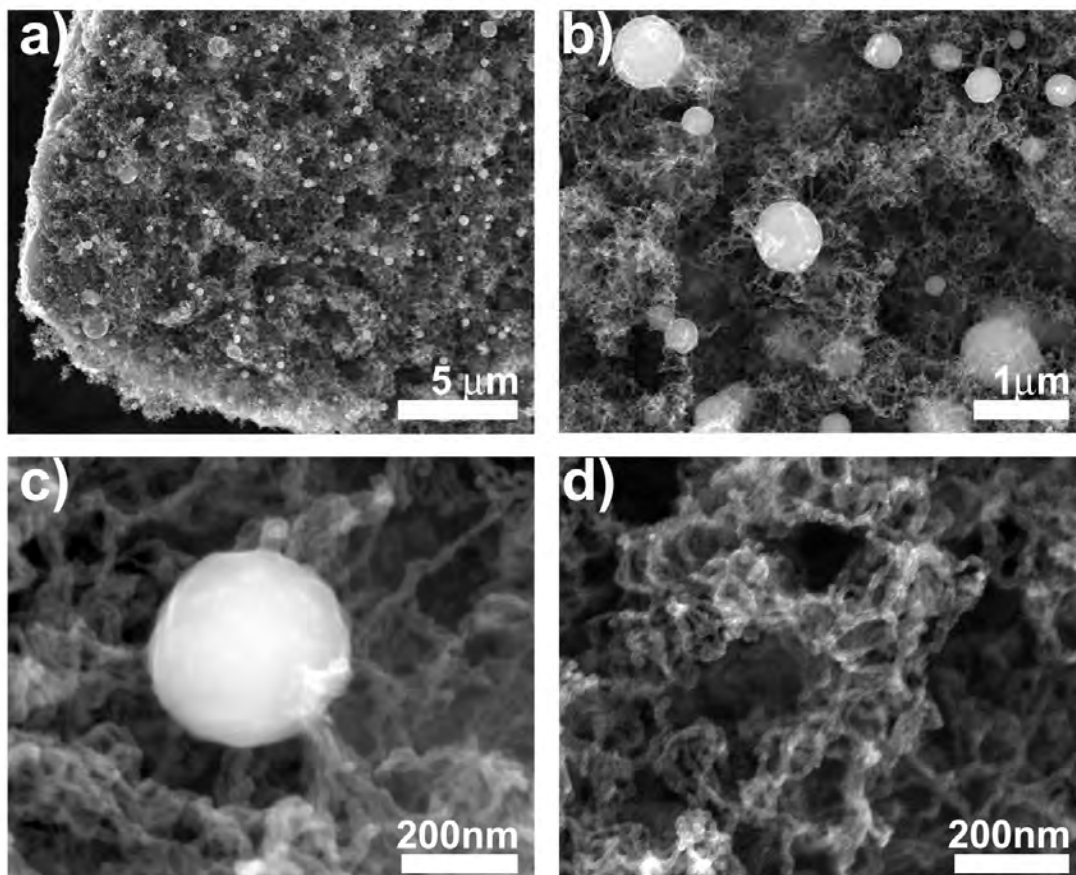


Figure 4.5: SEM images showing the entanglement of carbon fibres together with metallic balls. Figure a) shows the low magnification SEM image displaying the high yield of metallic balls in a carbon fibre entanglement along a flake; b) presents the high density of metallic balls of different sizes; Figure c) displays the spherical morphology of such balls; while d) corresponds to the general morphology of the carbon fibre entanglement.

Together with the entangled fibres, several metallic spheres can be observed from SEM images (see Fig 4.5). When the material was dispersed on TEM carbon grids, and analysed by SEM and TEM as presented in Figure 4.7, it is shown that these metallic balls are surrounded by a carbon coating from where carbon fibres start to grow. This shows that these metallic balls are actually attached to the grown carbon fibres.

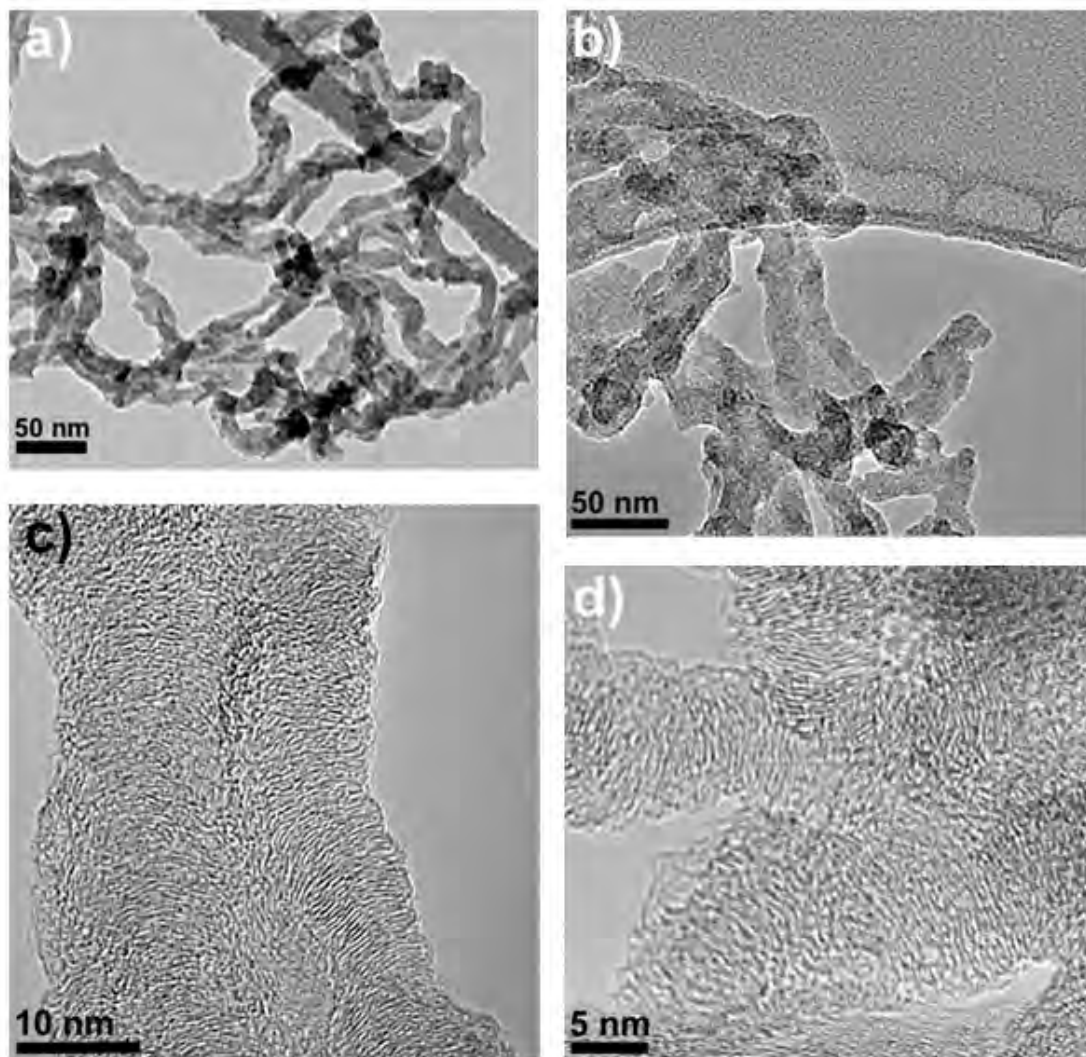


Figure 4.6: TEM and HRTEM images of the carbon fibres. Figure a) presents the low magnification TEM image of a small entanglement; b) displays hollow fibres with thick walls; c) shows the high resolution TEM image with the structure of the thick walls made from graphene layers stacked perpendicular to the fibres axis and d) fibres with a similar perpendicular stacking of the graphene layers to the axis.

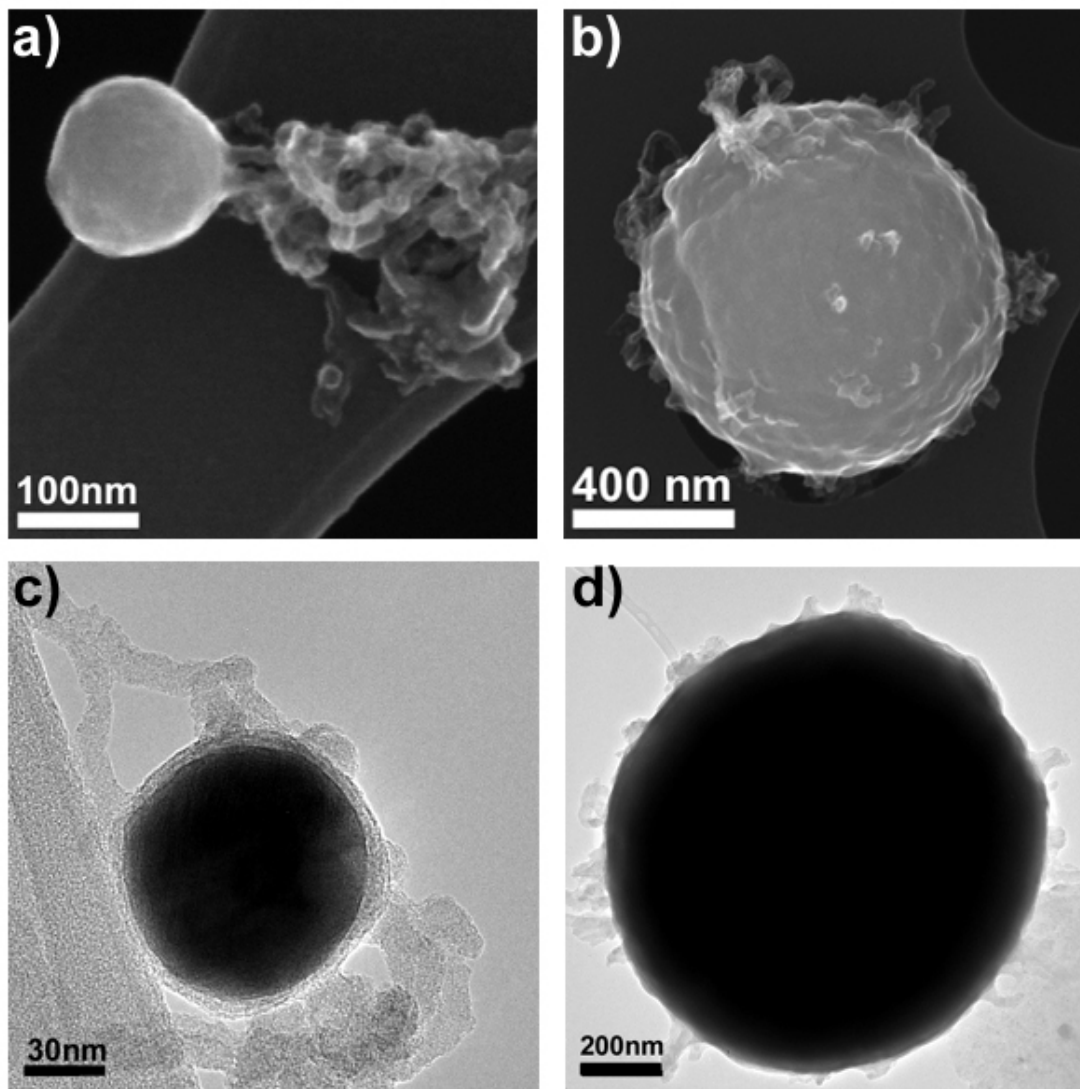


Figure 4.7: SEM and TEM images showing that the metallic balls are covered by a carbon layer from where fibres start to grow attaching the balls into the entanglement. Figure a) presents the SEM image of a metallic sphere attached to the fibre entanglement; b) shows a coating of the metallic ball; c) displays TEM image revealing a contrast difference in the core of the sphere from its metallic nature and its onion-like cover composed of carbon layers; d) presents the TEM image of a different metallic sphere.

The elemental composition of the material was analyzed and this revealed that some of the balls correspond to nickel spheres while some others correspond to nickel sulfide clusters. The elemental map shown in [Figure 4.8](#) displays a typical zone within the sample, in which most of the spheres show a sulfur signal together with nickel. Some other cases (marked by an arrow) to show only a nickel and a non sulfur signal. EDX line scans at the TEM shows some balls with sulfur signal following the nickel profile ([Figure 4.9.a](#)), and some other balls with only nickel signal ([Figure 4.9.b](#)).

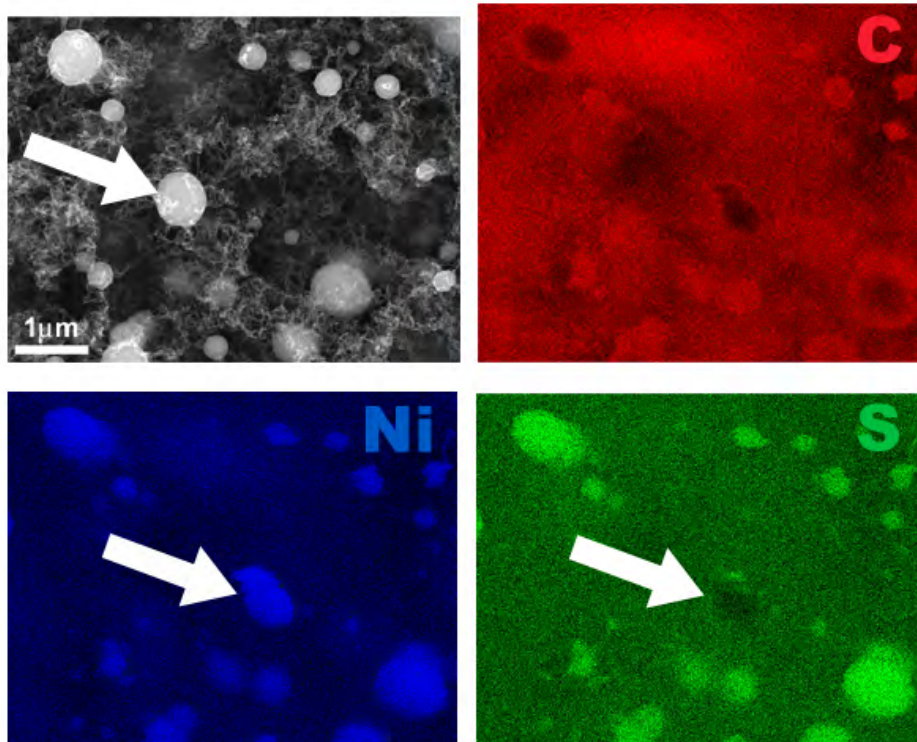


Figure 4.8: EDX elemental map, showing that the spheres correspond to nickel and some of them contain sulfur. The arrow points to a specific sphere without sulfur. Therefore the existence of both Ni and NiS_x is possible.

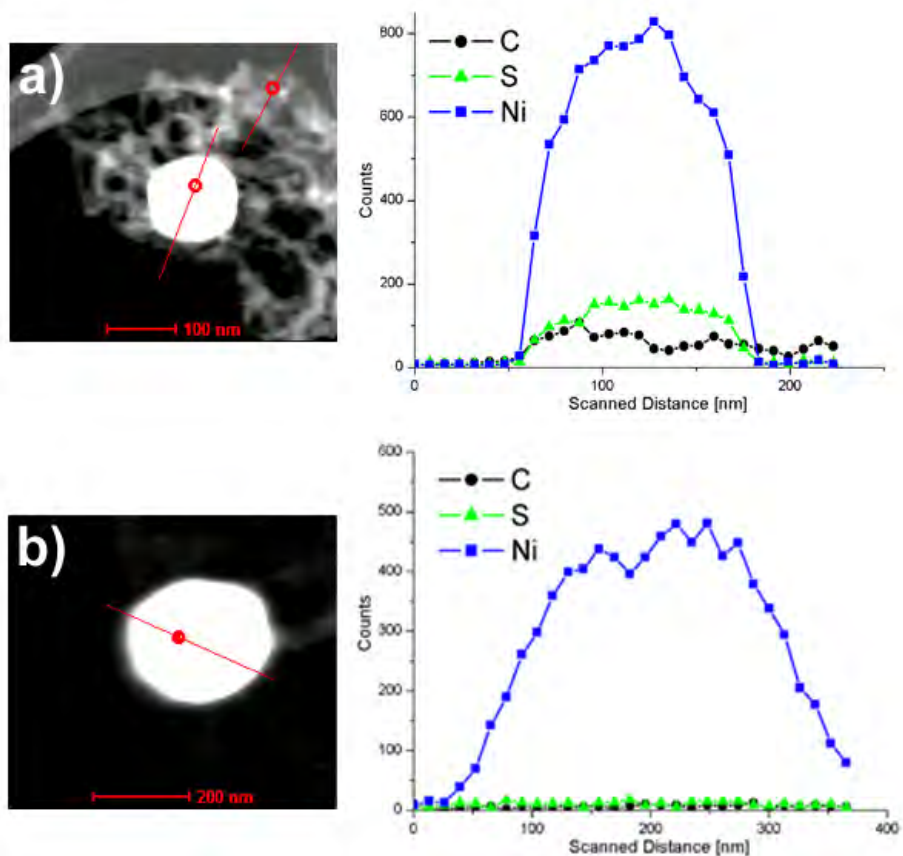


Figure 4.9: High resolution EDX linescans on metallic particles showing a nickel sphere with sulfur in a) and a pure nickel particle in b).

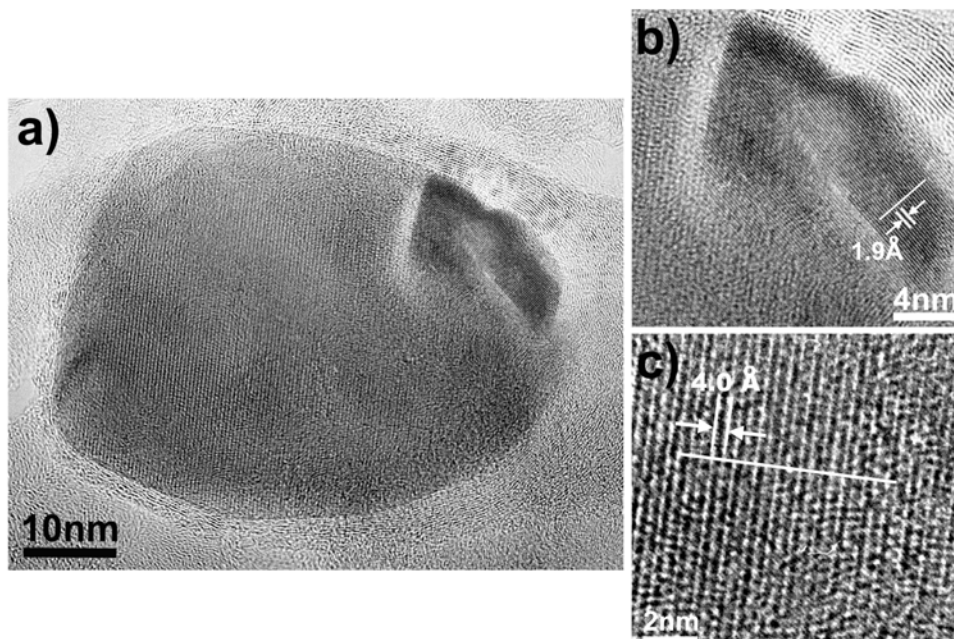


Figure 4.10: Catalyst particle with two domains with a different crystalline structure. Figure b) presents a zoom in the smaller domain contained in the bigger particle; while c) presents the crystalline structure of the main cluster.

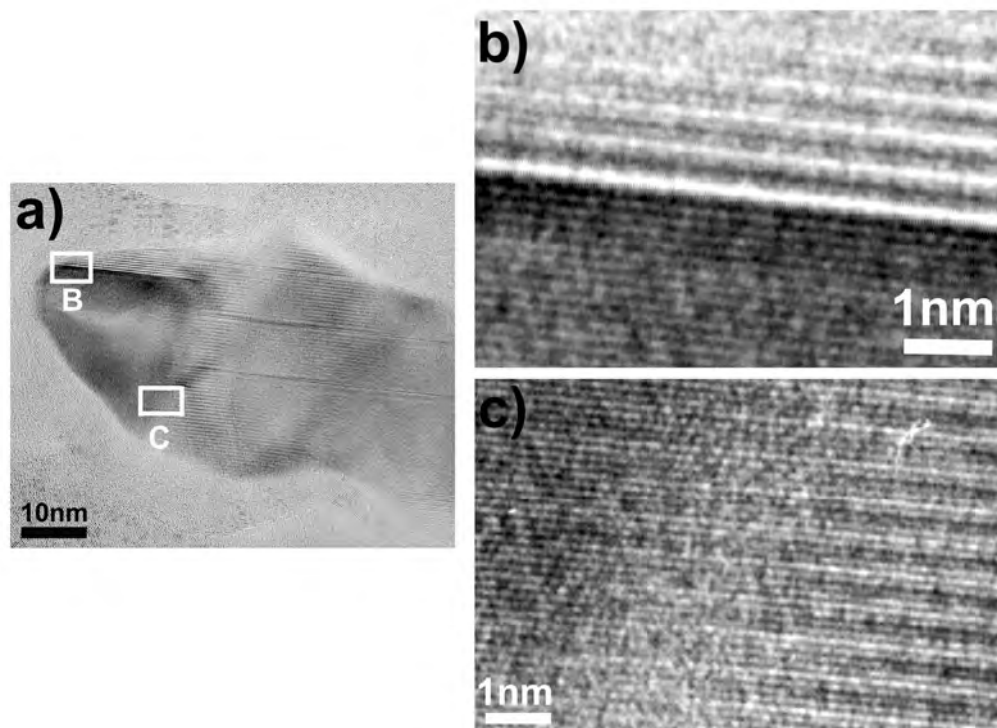


Figure 4.11: Two domains coexisting in a different catalyst particle. Figure b) and c) present the zoom in with the crystalline structure right at the borders.

Furthermore, HRTEM studies of metallic clusters from this sample reveal that in the same cluster, domains with different crystal structures as shown in [Figure 4.10](#) and [4.11](#) could coexist. [Figure 4.10.c](#) presents the planes observed from the main particle, while [Figure 4.10.b](#) shows the crystalline structure of the

smaller domain contained in the cluster. Similar results are observed in the particle exhibited in [Figure 4.11.a](#), where two different crystalline domains coexist in the same catalyst particle. [Figure 4.11.b](#) and [4.11.c](#) reveal the borders between the two domains. Further HRTEM should be done in order to elucidate the precise crystalline phase of the domains and the correct assignment of the indexes of the layer planes.

4.3.3 Effects of catalysts in the branching morphology

The use of ferrocene (FeCp_2) instead of nickelocene (NiCp_2) completely changed the resulting material. At the T11 zone, where interesting type of nanostructures appeared with nickelocene, only carbon black (carbon spheres) aggregates were obtained with ferrocene with few CNTs growing from them (see [Fig. 4.12.a](#) and [Fig. 4.12.b](#)). Now the interesting material appeared in the F2 zone,

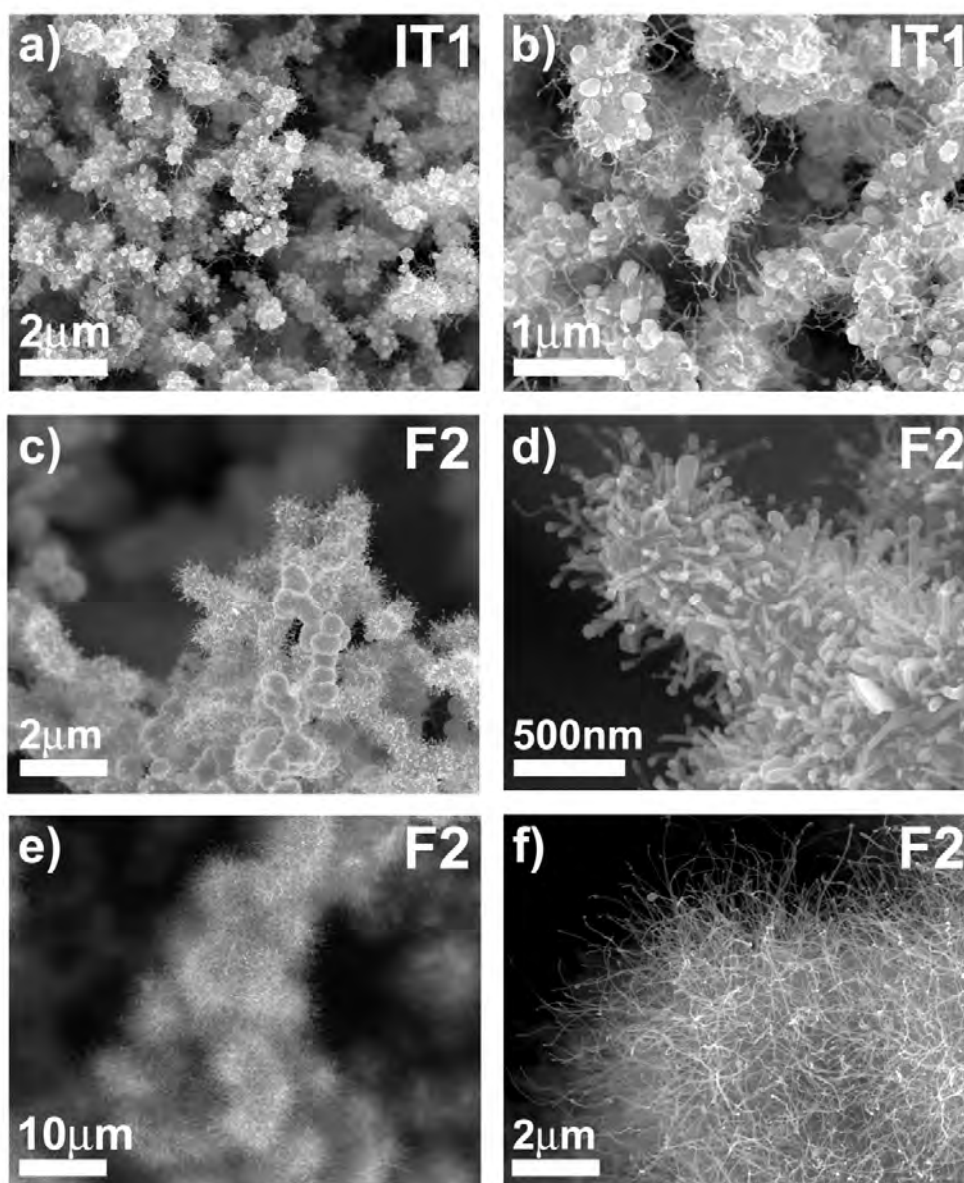


Figure 4.12: General morphology obtained by SEM of the material obtained when ferrocene is used instead of nickelocene. Frames a) and b) correspond to zone IT1, while frames c)-f) show CNTs growing out from carbon balls obtained from zone F2.

which corresponds to CNTs growing out from carbon spheres, showing small worm-like nanotubes (see Fig. 4.12.c and 4.12.d) in addition to longer and well crystallized CNTs (see Fig. 4.12.e and 4.12.f).

The high magnification SEM images taken from these CNTs revealed a peculiar termination (see Fig. 4.13.a and Fig. 4.13.b).

CNTs junctions were also obtained in the F2 zone, showing a concentric graphene cylinder structure (see Fig. 4.15 and Fig. 4.16).

4.3.3.1 Termination of CNTs when using Fe as catalyst

The peculiar termination of the CNTs showed a metallic particle at the tip. A thinner nanotube usually grows from such a tip, encapsulating a second metallic particle. The SEM image shown in Figure 13.c reveals the general morphology of these peculiar terminations, whereas Figures 4.13.d and 4.13.e depict dark field and bright field STEM images, respectively, in which the difference in contrast indicates the presence of the metallic particles. TEM images shown in Figures

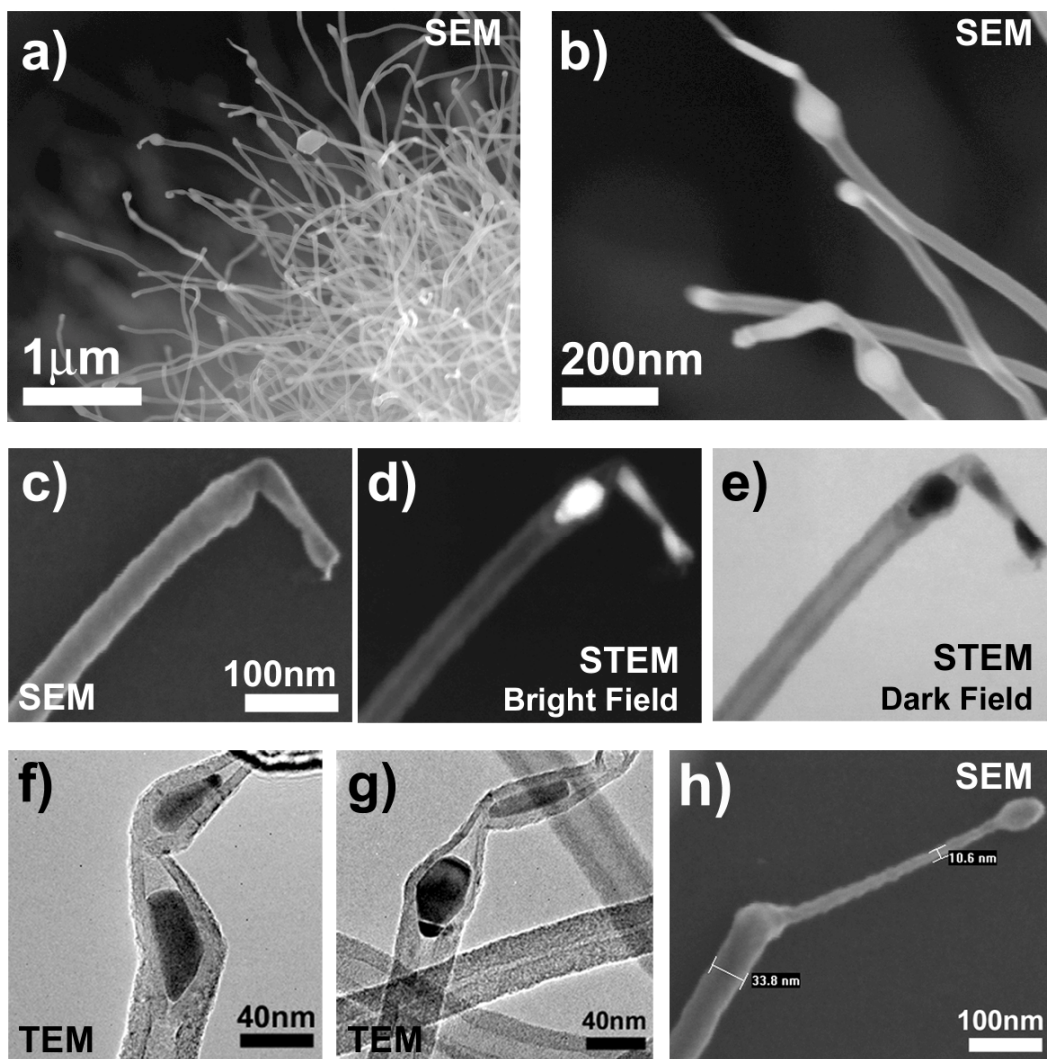


Figure 4.13: The nanotubes obtained exhibit a characteristic termination, in which a second and thinner nanotube is grown from the thicker one. Bright and dark field images are shown in d) and e) indicating the position of the metal particles; while TEM frames f) and g) show how the thinner nanotube is an extension of the thicker one.

4.13.f and 4.13.g indicate how the thinner nanotube is grown from the thicker CNT. Figure 4.13.h provides an estimation of the tube thickness showing a thinner nanotube of approximately 10 nm wide in diameter.

The EDX line scan measurement (see Fig. 4.14), revealed that the metal particles correspond to Fe and sometimes to FeS_x . Even when there is not an evident correlation between the sulfur presence and a change in morphology of the tips, the particles from the thinner nanotubes indicated the same compositions as those from the thicker tubes, suggesting that the thinner nanotube was grown from a piece of metallic cluster located in the thicker tube.

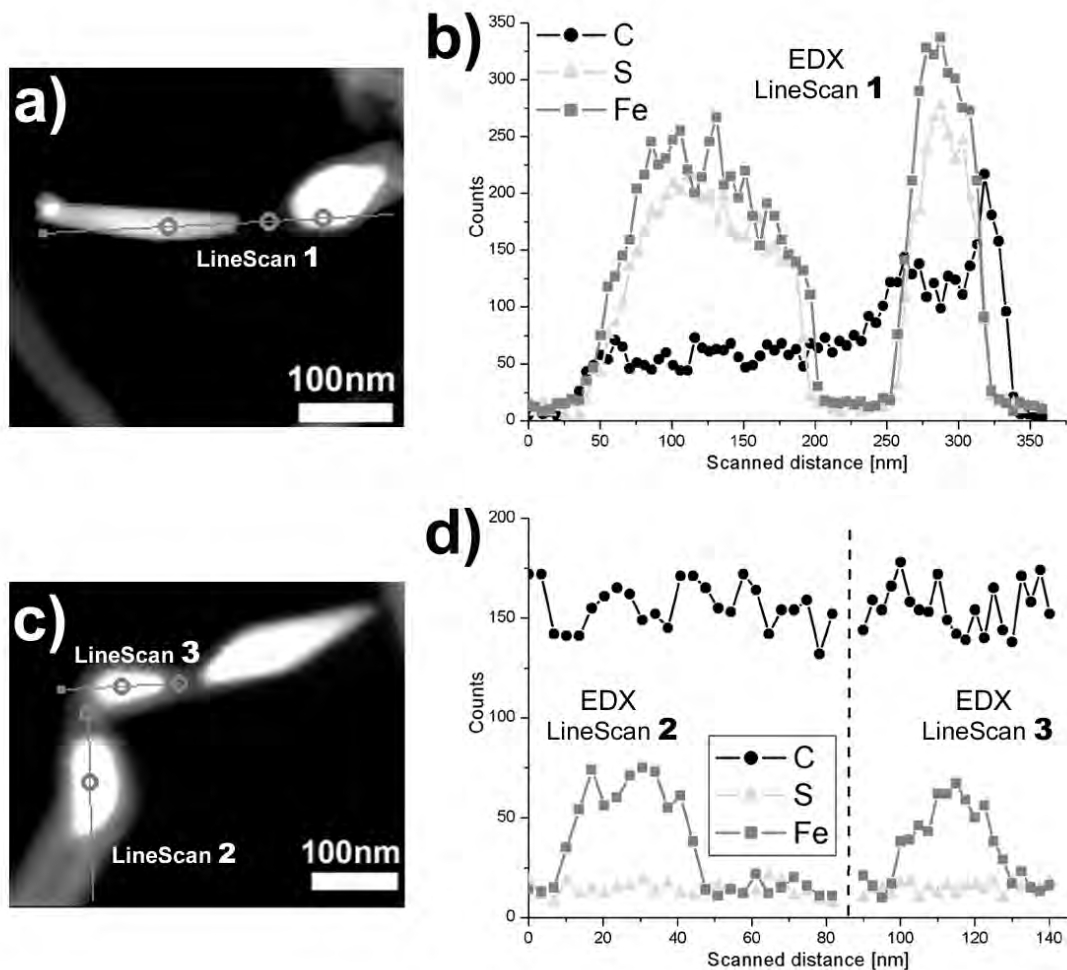


Figure 4.14: EDX line scans showing the composition of the metallic particles at the nanotubes tips. Frame b) shows an iron sulfide particle while frame d) shows the presence of pure iron particles. In both cases, the particle located in the thinner nanotube has the same composition found in the original thicker tube.

4.3.3.2 CNTs junctions

Figure 4.15 depicts TEM images of covalent Y-junctions obtained with Fe. The HRTEM evidence presented in Figure 4.16 indicates that the structure corresponds to graphene cylinders parallel to the nanotube axis; this should be remarked since most of the Y-junctions reported until now display either a stacked cone structure [5-6,8-9,11-13,20] (see section 4.3) or a finger-like morphology [10,14].

It is important to mention that the yield of this type of tubular junctions is low within the sample (< 5%), although it is indeed possible to obtain a concentric cylinder structure instead of cone stacked structures when iron and sulfur are present in the CVD process.

EDX line scan measurements have revealed that the metallic particles encapsulated close to the node of a Y-junction exhibit S and Fe, indicating that the metallic particle corresponds to iron sulfide (see Fig. 4.17), with a 1:1 stoichiometry. When EDX spectra were recorded on the carbon walls of the CNT Y-junction, sulfur traces were observed (see Fig. 4.17.c and 4.17.d).

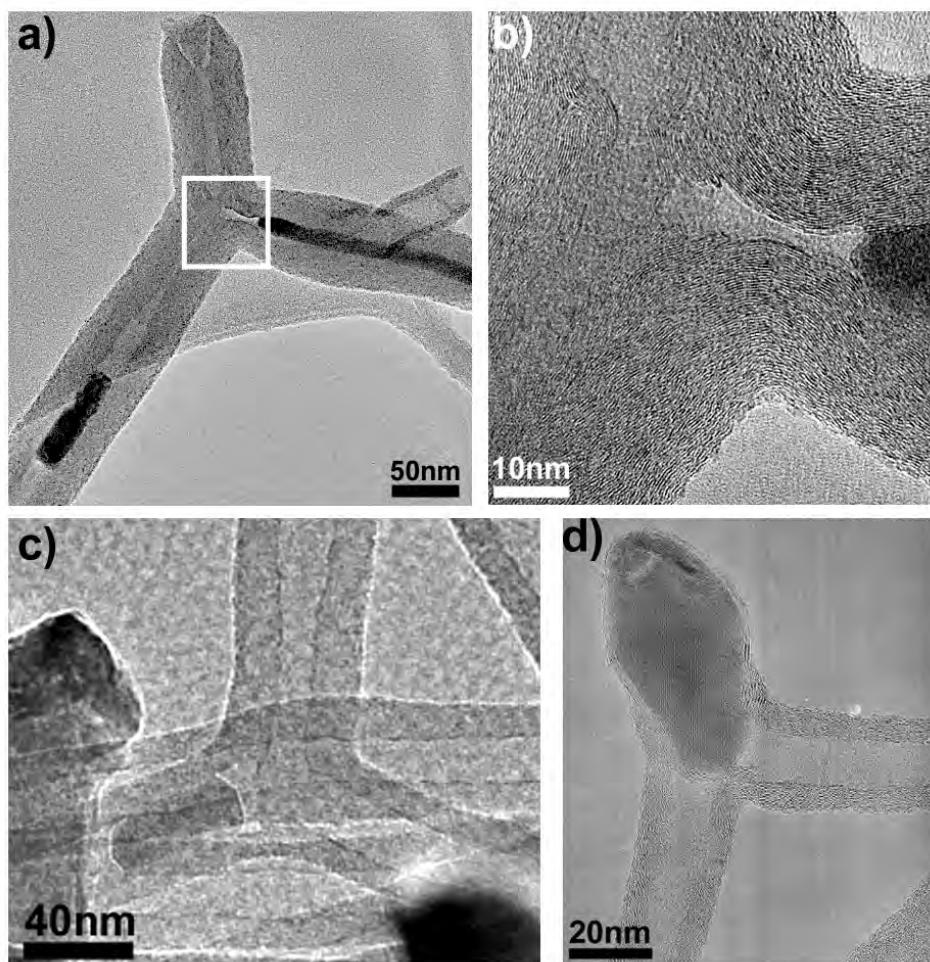


Figure 4.15: Y junctions obtained when ferrocene was used instead of nickelocene. Figure a) presents the low magnification TEM of a hollow Y junction and b) displays the junction zone at a higher magnification with a hollow interior. Figures c) and d) correspond to two other different junctions.

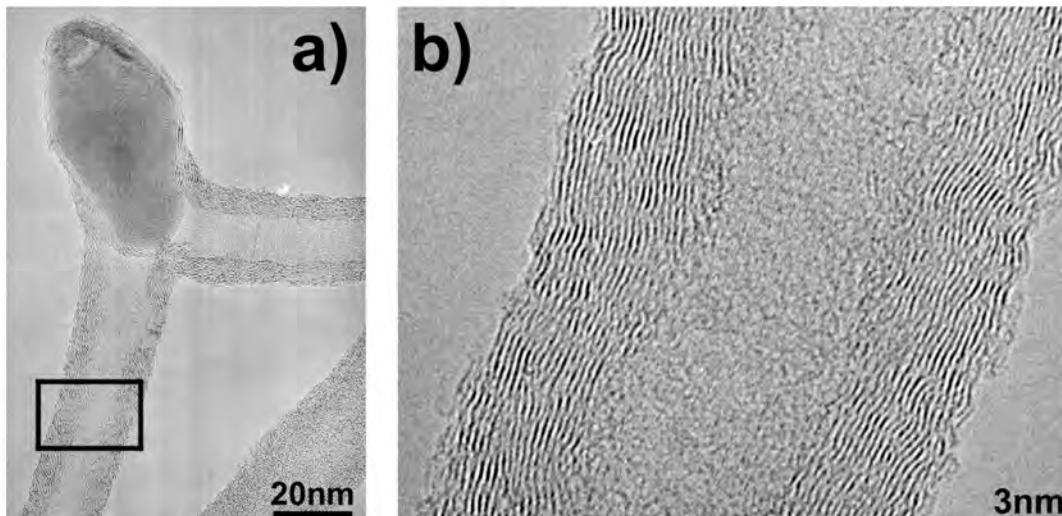


Figure 4.16: HRTEM images from one of the arms of the junctions shown in [Figure 4.15.d](#) indicating that the graphene layers are parallel to the tube axis. These nanotube junctions are not observed for nickelocene because cone-stacked fibres are always present (see [Fig. 4.30.b](#)).

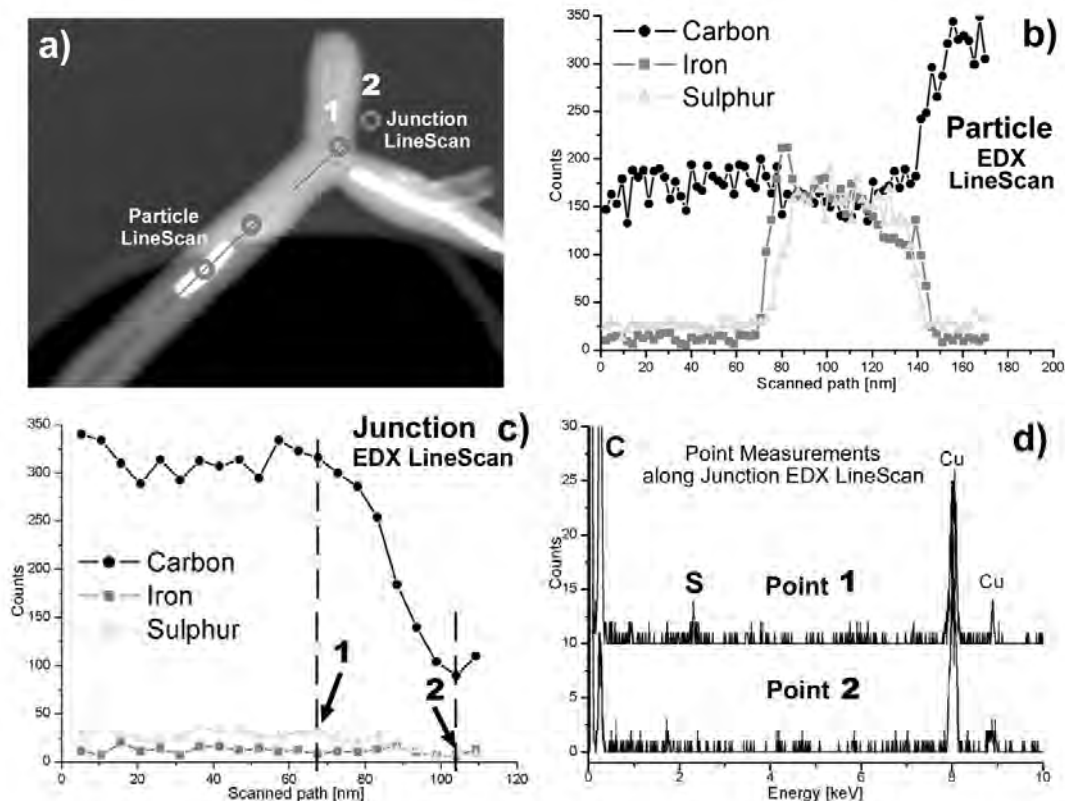


Figure 4.17: EDX line scans performed on the CNT Y junction. Frame b) shows that the metallic encapsulated particle corresponds to FeS_x ; c) indicates traces of sulfur on the carbon walls, confirmed by the point measurements shown in frame d).

The junction shown in Figure 4.15.d illustrates how the catalyst particle stayed trapped at the junction position and did not continue growing. Figure 4.18 displays a detailed HRTEM characterization of such a junction in order to elucidate a possible growth scenario.

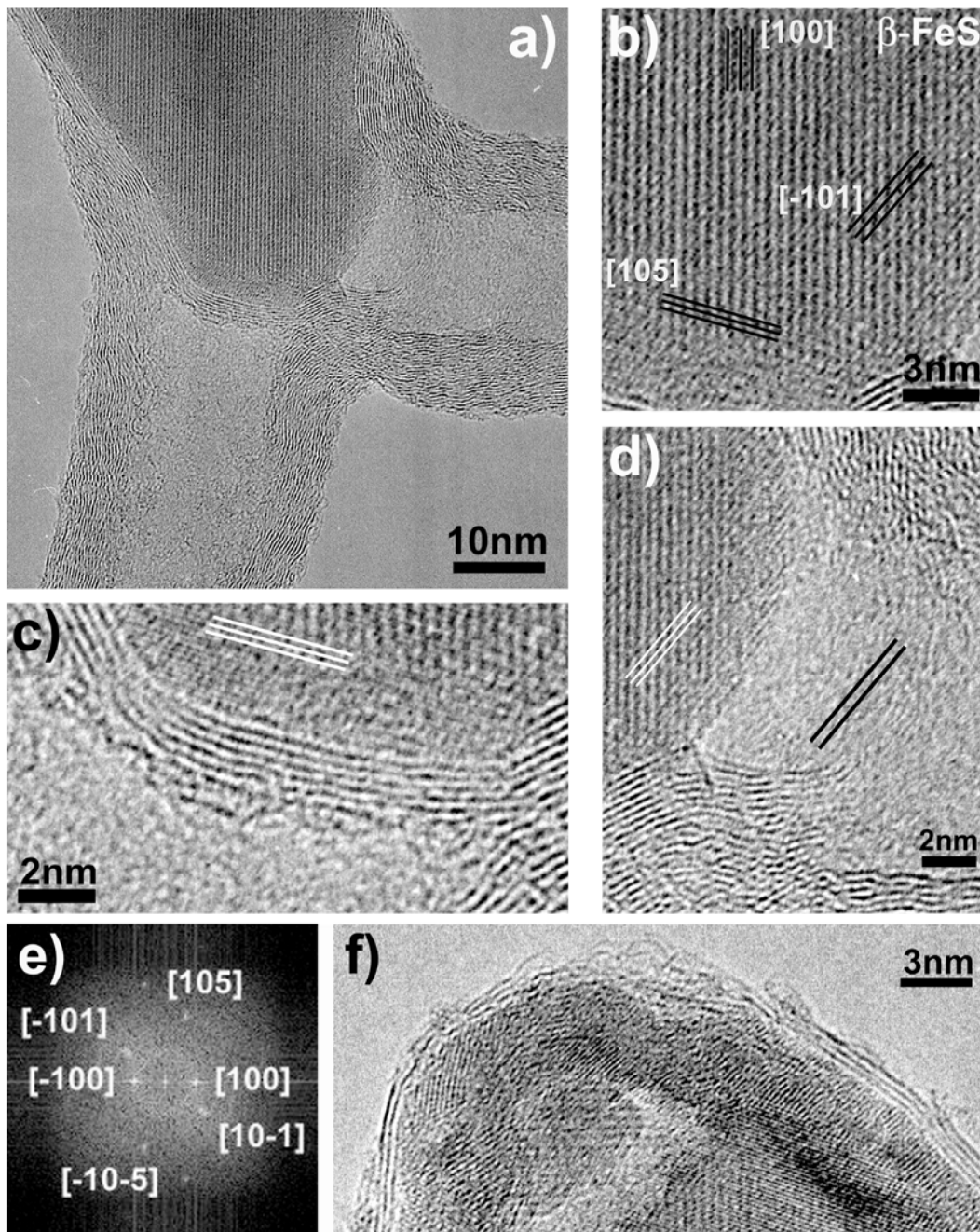


Figure 4.18: HRTEM study on a Y junction where the catalyst particle stayed trapped at the junction point. Frame b) shows the crystalline structure of the metallic catalyst, where three different planes are present. Frames c) and d) reveal the catalyst planes [105] and [-101] right at the edge of the catalyst particle, in a parallel arrangement with respect to the outgoing graphene layers; suggesting an epitaxial growth of the junction arms (marked by white and black lines). Frame e) shows the FFT calculation from the catalyst particle on image b); where the three different planes are detected and indexed. Finally, f) presents the top part of the particle with polycrystalline structure, starting with blurry graphene layers at the center part and growing into 2, 3 and 4 stacked graphene layers as it is moved towards the sides.

Figure 4.18.a shows the branching region, whereas Figure 4.18.b depicts the metallic particle structure where three different families of planes are detected. The FeS binary alloy phase diagram exhibits three different crystallographic types to exist in nature with the correct stoichiometry: γ -FeS, α -FeS and β -FeS. Powder x-ray spectrum simulations and their interplane distances together with the real space crystal simulation and HRTEM images allowed to discriminate between the three types being the β -FeS, the crystal phase of the FeS particle displayed in Figure 4.18. Figure 4.18.e exhibits the FFT obtained from the HRTEM images, which after comparison with the corresponding simulation of an electron diffraction pattern allowed to index the family planes as presented.

Interestingly, Figure 4.18.c and 4.18.d show the crystallographic planes of the metallic particle right at the edge from where the two CNT arms grow. It is noted that the metallic planes (501) and (-101) are observed always parallel to the graphene layers. When observing the top part of the metal particle (Figure 4.18.f), it can be noticed that it is polycrystalline and goes from blurry graphene layers at the middle part, to two, three and four well stacked graphene layers as we moved further away to the right side (similar trend leftwards).

The last observation suggests that the carbon source is being taken in by the top part of the particle letting carbon atoms diffuse towards the bottom in order to form the two branched nanotubes. It is clear that the metal planes (501) and (-101) are parallel to the graphene walls. It is assumed then that C diffuses through the planes so that it precipitates as graphite on its surface following the plane directions.

4.3.4 Effects of flow rates (thiophene concentration)

Dramatic changes were observed in the sample obtained in T11 zone when the mixture of gases containing thiophene was modified. For example, when a *minimum flux* (minimum observable amount) was employed, networks of carbon micro tubes were obtained. If the flux was slightly raised to *medium flux* of Ar passing through the thiophene (~0.1 l/min) millimeter size flakes with patterns at the microscale were observed; they contained different types of nanostructures such as filamentous carbon fibres with a nickel nanocrystal at the end (see Figure 4.23.j and 4.23.k).

4.3.4.1 Minimum Ar flux through thiophene

4.3.4.1.a Random Networks of 1D carbon blocks

Millimeter size flakes composed of networks of micrometer carbon tubes were obtained. These correspond to random networks covalently joined at multiple node points as shown in [Figure 4.19](#) (several node points are marked by arrows).

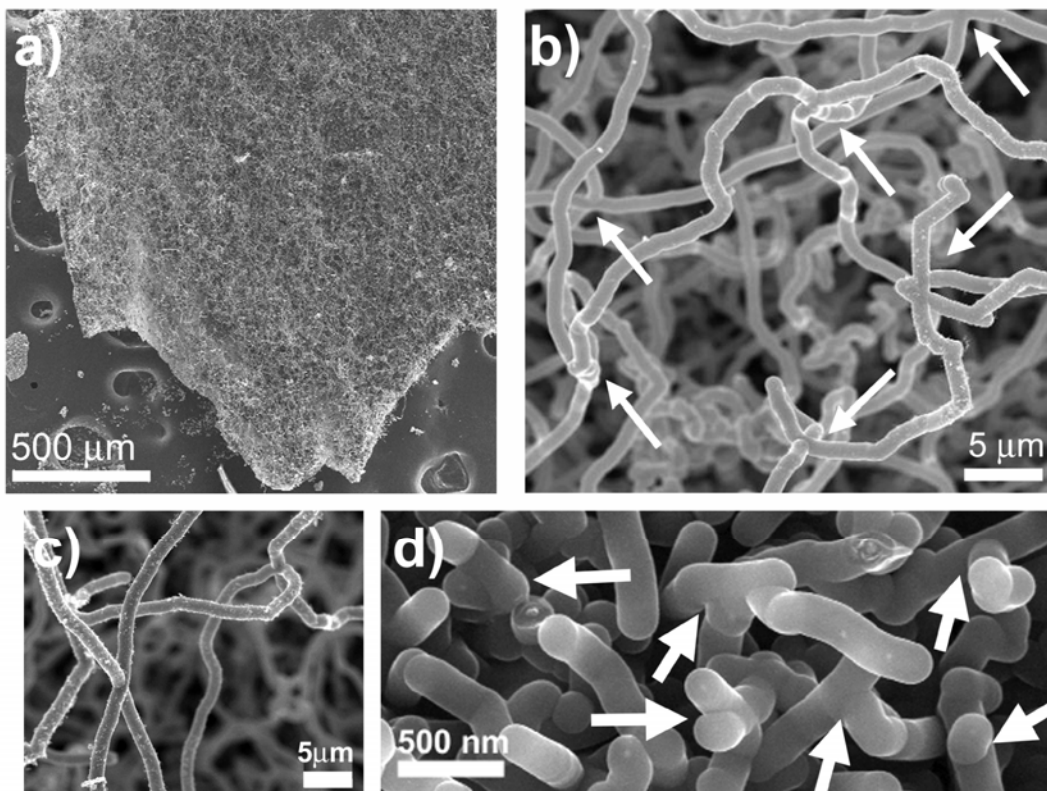


Figure 4.19: SEM images of random networks at different magnifications showing how tubular fibres are interconnected covalently in different ways.

4.3.4.1.b Micro tubular junctions

When the network nodes were studied by SEM, different geometries were found to be experimentally stable (see [Figure 4.20](#)). Specifically SEM [image 4.20.c](#) shows 90° angles between micro tubes; whereas [image 4.20.d](#) is close to have 60° angles similar to hexagonal geometry. [Figures 4.20.a](#) and [4.20.b](#) display the right angles to fit in a square framework.

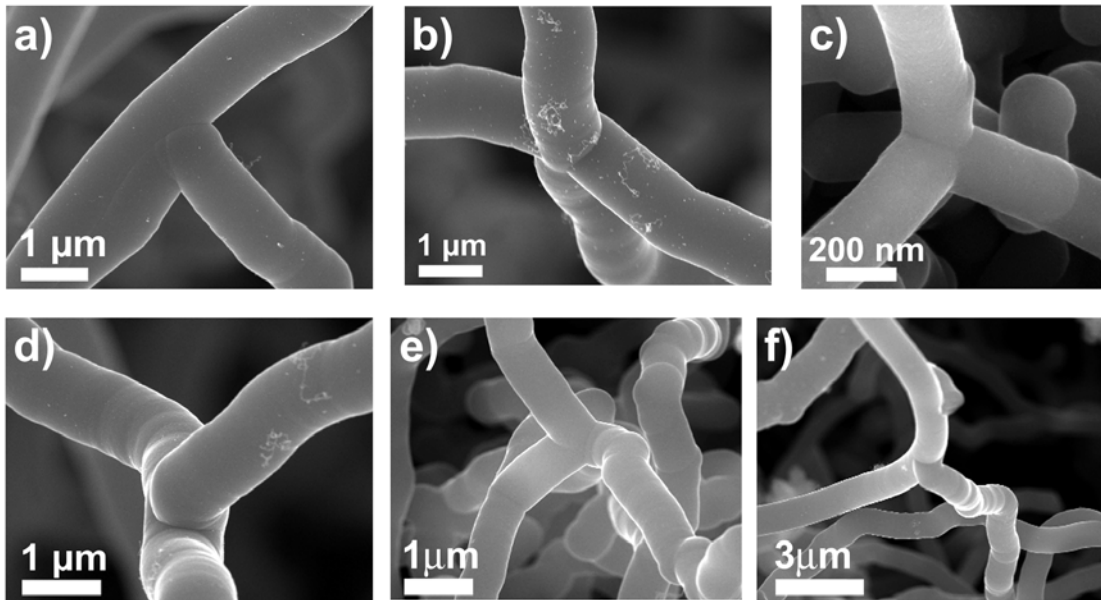


Figure 4.20: Carbon microtube junctions demonstrating the energetic stability of different type of geometries. Junctions in a) and b) exhibit right angles to build a square framework; junction c) could be used to construct a cube (3D) network whereas junction d) shows angles close to 60° resembling a hexagonal lattice.

TEM characterization of such covalent junctions indicates that they correspond to microtubes formed by graphene layers and they all exhibit a hollow core. These hollow cores are joined and kept hollow right at the node (marked by an arrow in Figure 4.21). It is noteworthy that these tubular microstructures are similar to Endo's fibres [21]. EDX studies revealed traces of sulfur along the tubular structures (see Figure 4.22).

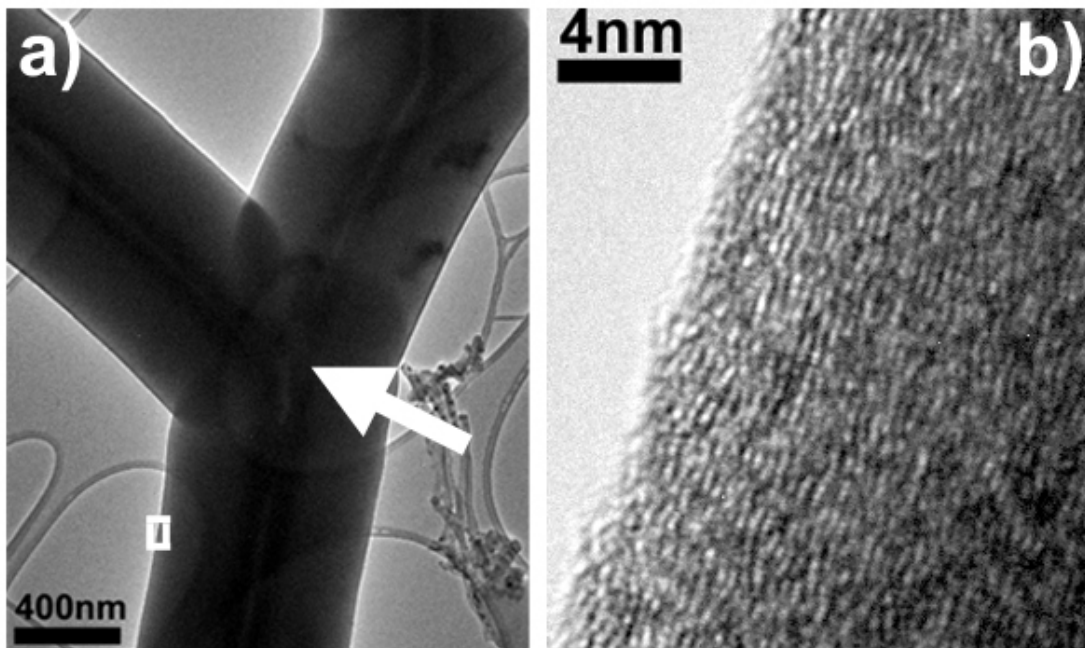


Figure 4.21: TEM and HRTEM images of the carbon microjunctions; a) reveals the hollow core inside the junctions (even at the node region; see arrow); b) HRTEM image showing the outer layers of the microtubules which consist of concentric graphene tubes; outer tubes appear to be more disordered than the inner tubules.

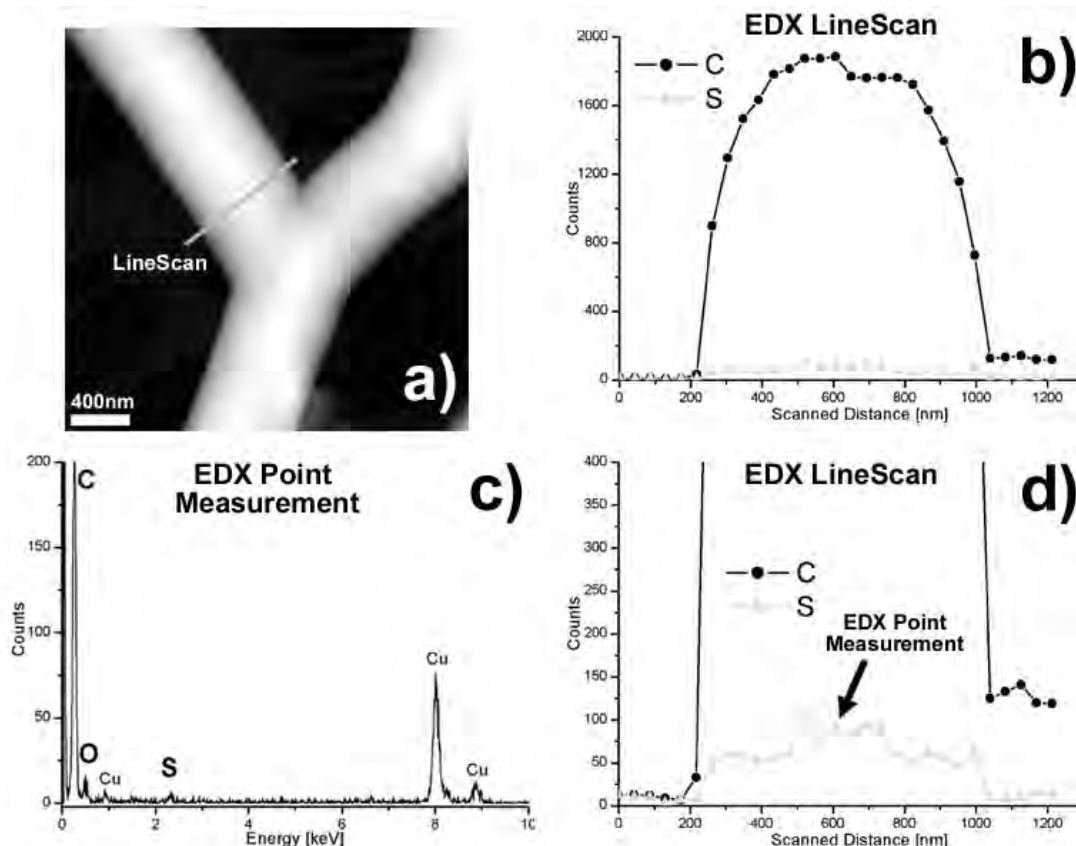


Figure 4.22: The high resolution EDX studies on the microneetworks were able to detect sulfur traces at the carbon microtubes. Figure a) shows the dark field TEM image of the study region; b) and d) correspond to the line scan from an arm of the microtube junction with the signal for C and S, revealing S traces following the C profile, observed in d) when a zoom in is performed in the data. Figure c) shows one of the point measurements from the linescan displaying the peaks features of a typical spectrum with the S trace detected.

4.3.4.2 Medium Ar flux through thiophene

4.3.4.2.a Micro Patterns

SEM images from [Figure 4.23](#) show the three types of millimeter-size flakes obtained from zone IT1. The second row displays microscale view where a well defined pattern is observed in [Figures 4.23.d](#) and [4.23.e](#), the third type does not reveal any pattern. When the magnification is increased ([third and fourth rows](#)), it is observed that each flake (or non pattern) is composed of different types of nanostructures. The EDX measurements ([first row in Figure 4.23](#)) indicates that patterns shown in [Figures 4.23.d](#) and [4.23.e](#) consist of similar proportions of Ni and S with respect to C, whereas the third type of flake has four times less amount of Ni and two times less amount of S when compared to the previous materials.

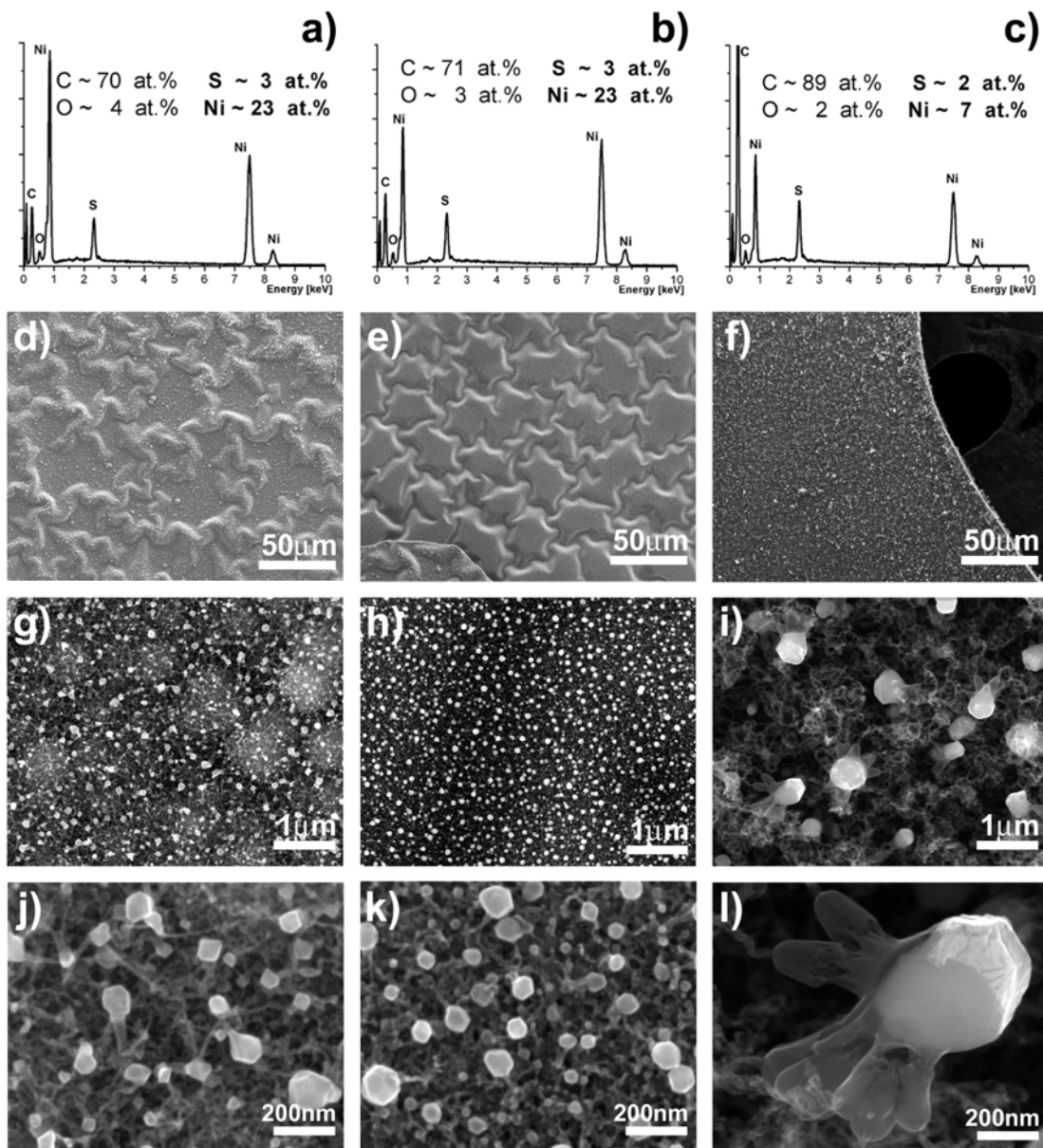


Figure 4.23: SEM images of flakes showing different types of micropatterns (each column corresponds to a specific flake). Samples were obtained in T11 zone when the Ar flux is reduced to medium flux. SEM images d), e) and f) indicate the microscale morphology; whereas j), k) and l) display the nanostructures contained in each type of pattern. Spectra in a), b) and c) show the elemental content of each type of micropattern measured by EDX.

It is important to mention that the micropatterns are composed by filament – like carbon structures which ends in a metallic nanocrystal; whereas the non patterned material contains *sea urchin* –like nanostructures (see fourth row in Fig. 4.23).

4.3.4.2.b Sea urchin –like nanostructures

As mentioned above, sea urchin –like nanostructures are always observed in microflakes that do not form patterns at the microscale. Interestingly, each protuberance finishes in a small needle –like carbon fibres which connects to the carbon fibre entanglements (see Fig. 4.24). This type of nanostructures exhibits a very complicated carbon coating with several negative and positive curvature zones. It should be mentioned that this type of nanostructures had been predicted theoretically in the past (see model in Fig. 4.24.e, courtesy of M.Terrones) [22].

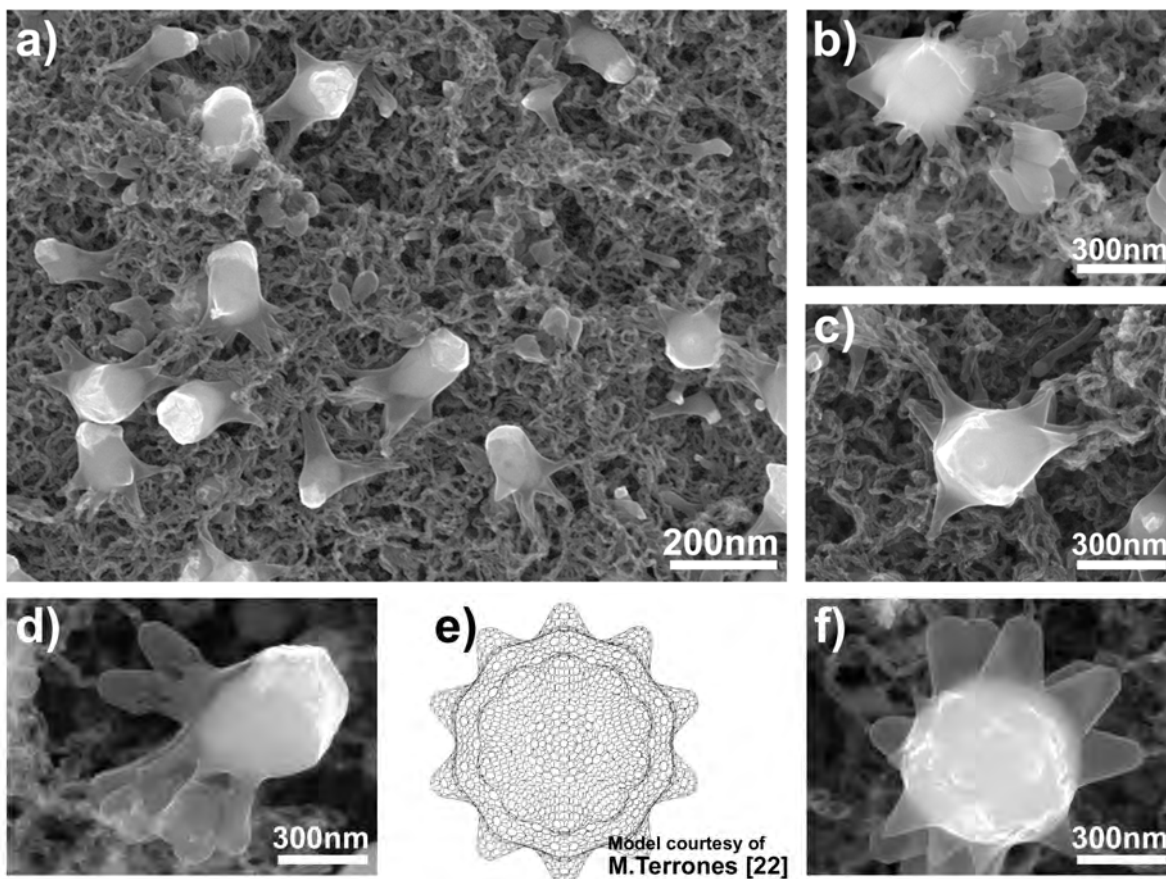


Figure 4.24: SEM images showing sea urchin –like nanostructures obtained in the non patterned flakes. This complex nanostructures are grown entangled and covalently bonded to nano fibres.

Figure 4.25 shows the detailed TEM and HRTEM characterization of the spikes forming the sea urchin –like structure. They are composed of well stacked graphene layers arranged perpendicular to the spike axis. The EELS elemental mapping shown in Figure 4.26 reveals that the coating mainly consists of carbon whereas the encapsulated particle contains mainly Ni. When EDX line scans were recorded across one spike, S followed the C profile (see Fig. 4.26.c and 4.26.d). It should be pointed out, that S is usually present in negative curvature regions.

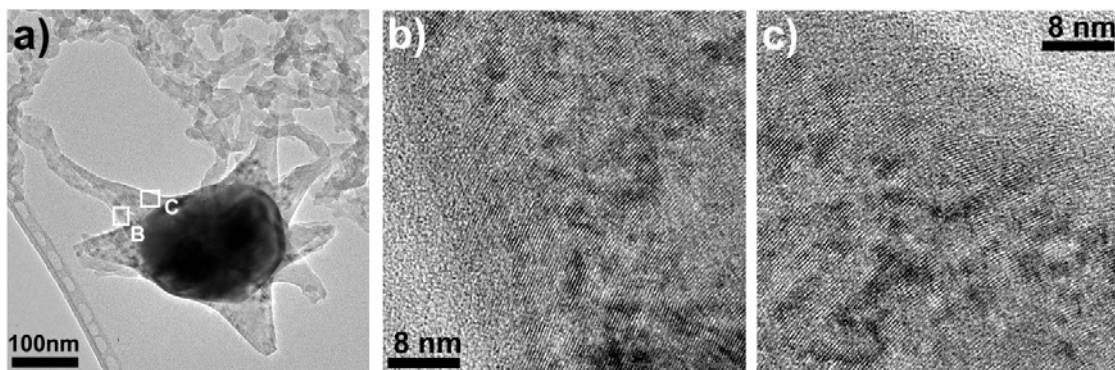


Figure 4.25: TEM and HRTEM images showing the structure of the sea urchin-like nanostructures, including the graphene layers stacking along the spikes.

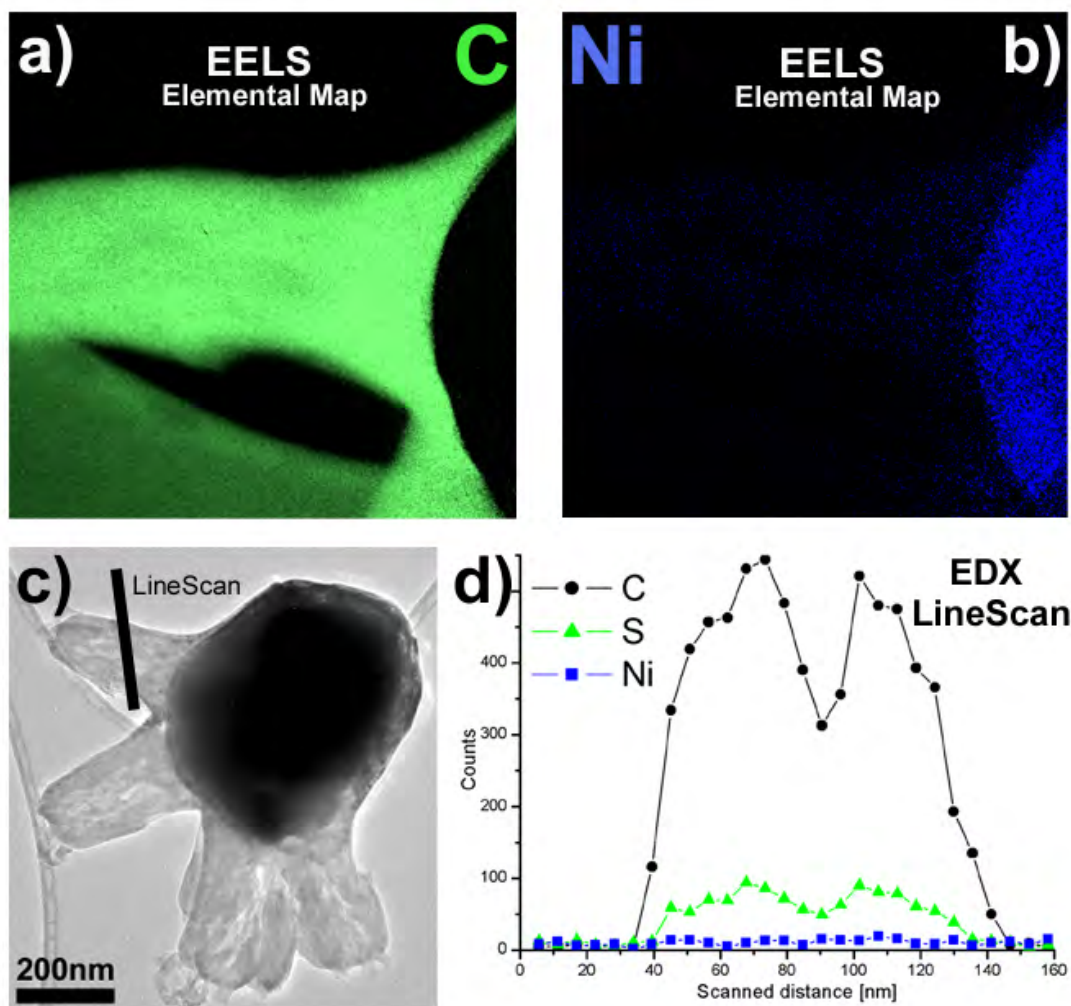


Figure 4.26: EELS elemental maps indicating that the encapsulated particle corresponds to Ni and the surrounding cover to C. The EDX linescan shown in frame c) and d) reveal the S signal which is commensurate with the carbon concentration.

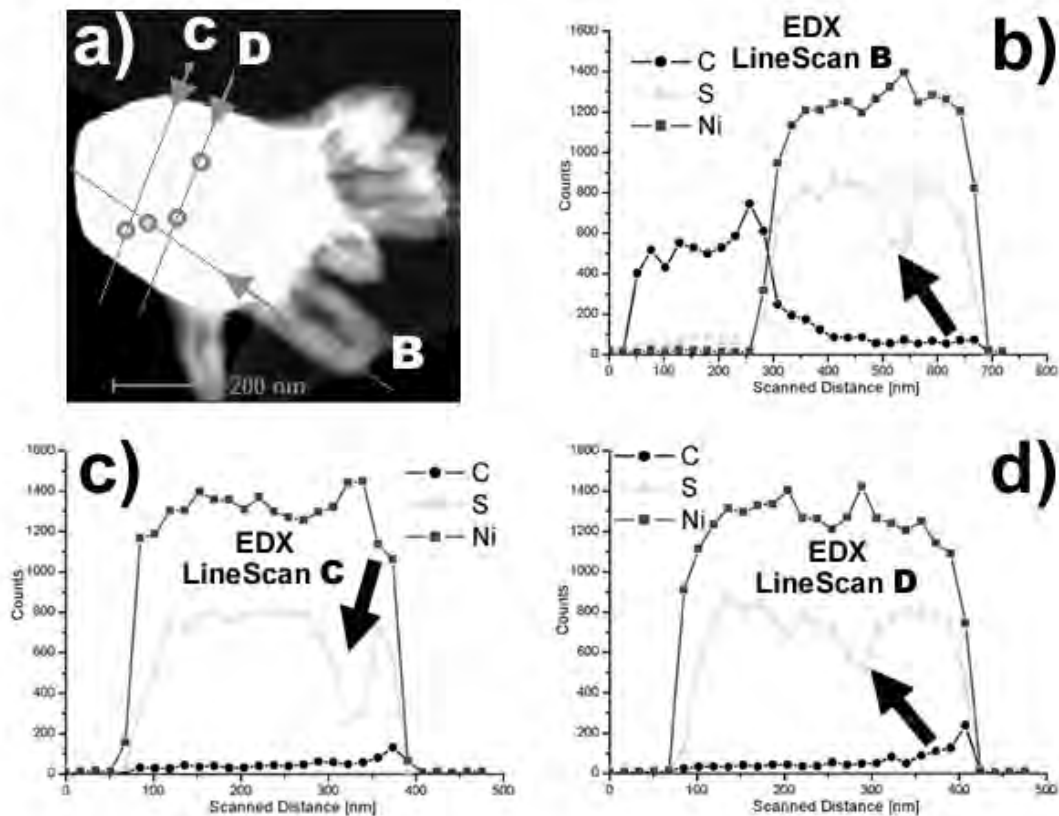


Figure 4.27: High resolution EDX linescans showing domains with different compositions along the encapsulated particle. The black arrows indicate a domain with less S corresponding to a crossing zone illustrated in the dark field image shown in a).

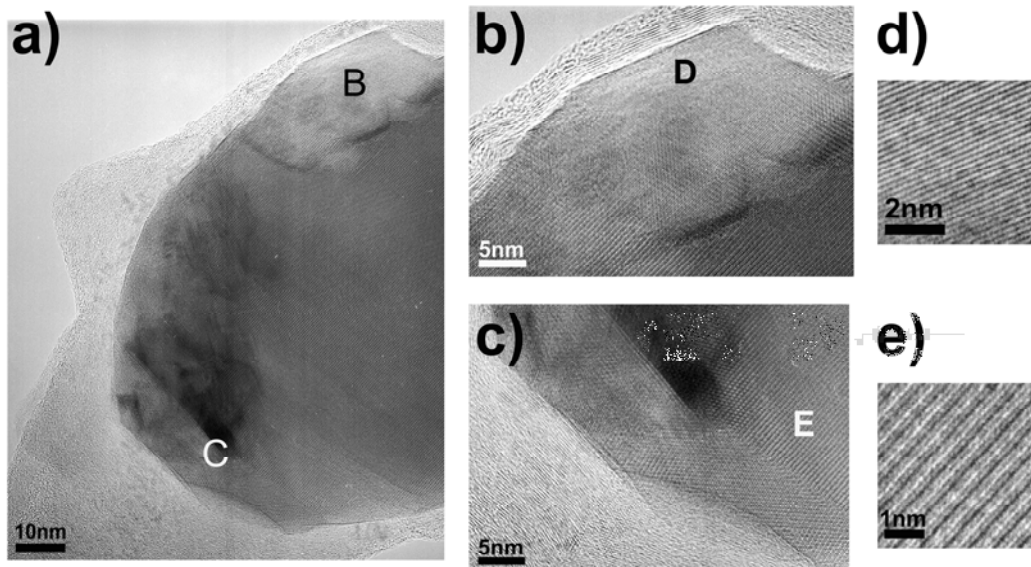


Figure 4.28: HRTEM images of an encapsulated particle displaying domains with two different crystalline structures coexisting in the same cluster. Frame b) corresponds to a zone in the upper part of the particle, and frame d) corresponds to the high resolution of the zone marked by D. The image shown in c) corresponds to a zone in the lower part of the particle, and frame e) shows the high resolution image of such a zone presenting a different crystalline structure than the zone showed in d).

The EDX line scans from the encapsulated metal exhibits the existence of domains with different elemental compositions. This is marked by arrows in the line scans (see Fig. 4.27), indicating a domain with a lesser amount of S. HRTEM characterization (see Fig. 4.28) confirmed the existence of two types of crystalline arrays coexisting in the cluster, presumably Ni and NiS_x, although further HRTEM analysis is needed to obtain the precise crystalline phase.

4.3.5 Summary of junctions produced

Among the different materials obtained when using different synthesis conditions, five different types of junctions were usually observed and are summarized in Figure 4.29. The tree branch-like junctions, as the material reported by Satishkumar et al. [5] was synthesized when nickelocene and an Ar flow through thiophene was used (e.g. 0.3 l/min). Three different types of junctions were identified in this material, some junctions with thick stems (diameters of c.a. 100-200nm), junctions with thin stem (diameters of c.a. 50nm) and junctions with multiple branching (Figure 4.29). When the Ar flow through thiophene was

Types of Junctions and synthesis conditions

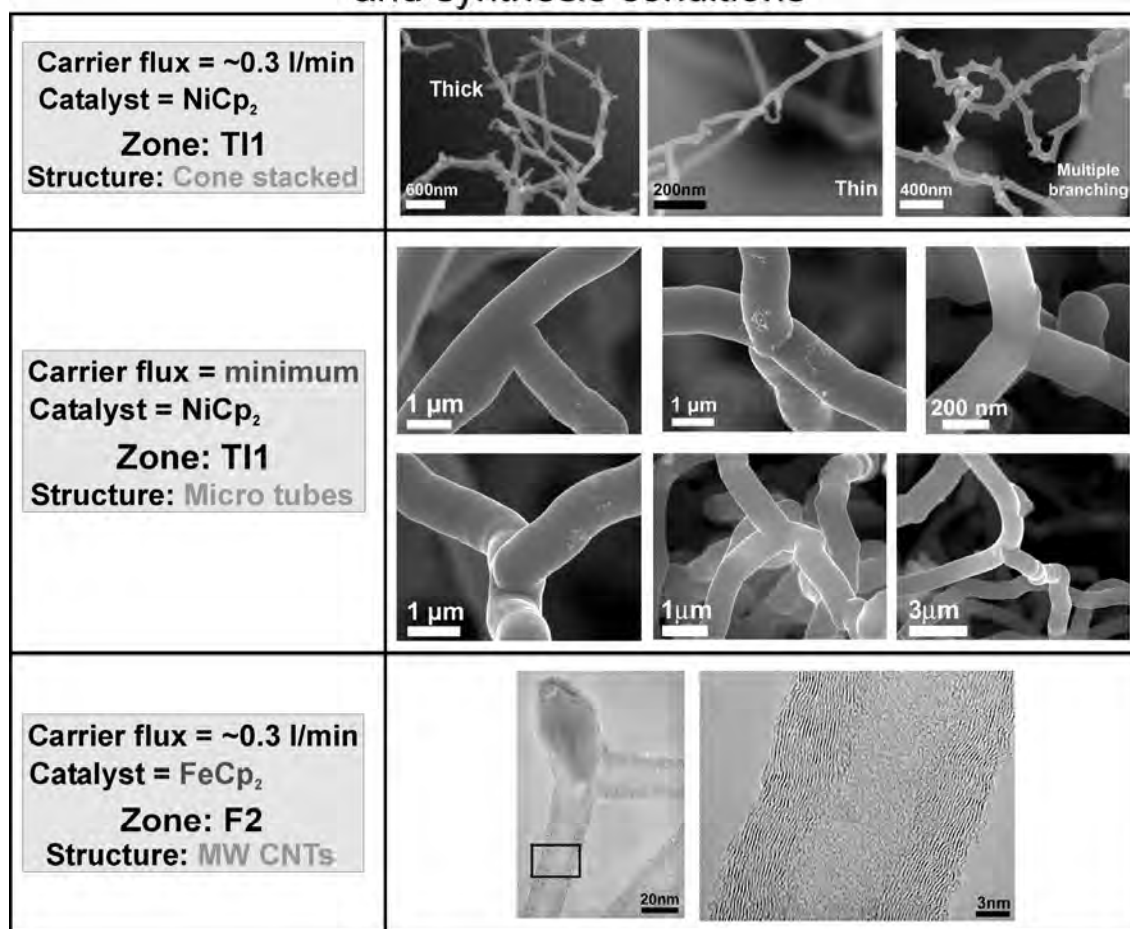


Figure 4.29: Schematic summary of the types of covalent junctions obtained under the different synthesis conditions. The first row corresponds to three different types of junctions exhibiting cone stacked structure; the second row shows junctions of carbon microtubes with hollow interior consisting of layered carbon; the third row depicts junctions consisting of graphene concentric cylinders structure.

reduced to a minimum, junctions of carbon microtubes were obtained (Figure 4.29), showing experimental stability of different types of angles, hollow interior and cone-stacked arrangements (see Fig. 4.21). Finally, when ferrocene replaced Ni, junctions of concentric graphene cylinders were obtained.

4.4 Branching mechanism

Once it was reproduced the branched nanotube material from reference [5], an exhaustive high resolution characterization together with first principles density functional theory calculations allowed us to elucidate the branching mechanism at the atomistic level and the importance of S atoms.

4.4.1 Type of junctions

Along the branched nanotube material, three main types of junctions were observed: junctions with thick stems (diameters of c.a. 100-200nm) as shown in Fig 4.30.a and 4.30.d; junctions with thin stems (diameters of c.a. 50nm) as shown in Fig 4.30.b and 4.30.e; and junctions with multiple branching (i.e. higher density of branching along a stem) as shown in Fig 4.30.c and 4.30.f.

Figures 4.30.g and 4.30.h reveal SEM and bright field images of junctions showing a hollow core. Figure 4.30.i corresponds to a TEM image of a junction

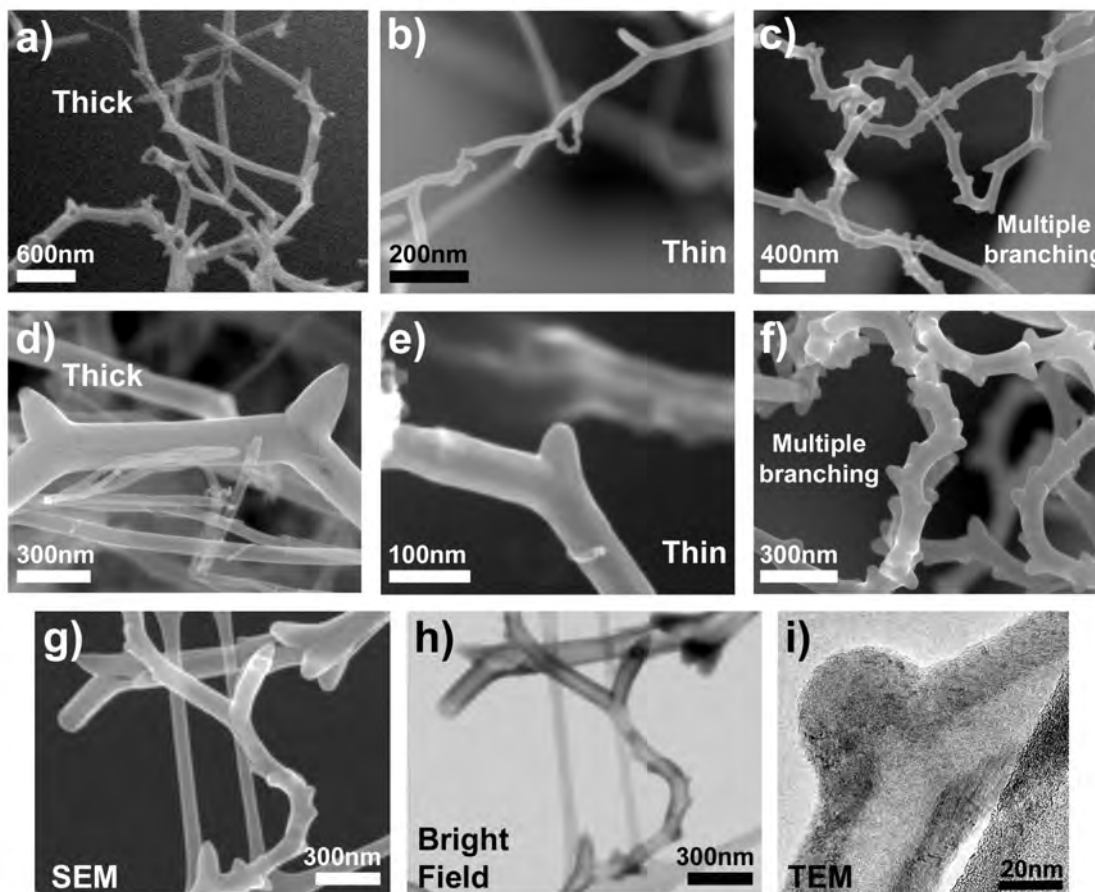


Figure 4.30: Frames a)-f) correspond to SEM images showing the types of tree branch –like junctions obtained. Frames g) and h) correspond to SEM and STEM bright field images revealing the hollow core of the junctions. The TEM image i) displays well stacked graphene layers.

exhibiting a well graphitized material. The appearance of the material at the microscopic level was previously shown in [Fig 4.4](#) at [section 4.2.2.1](#), showing shrub –like entanglements of such a material.

4.4.2 Experimental and theoretical evidence

An exhaustive high resolution characterization study revealed the presence of sulfur at the emerging branches which required modelling and motivated us to perform theoretical calculations in order to understand the role of sulfur at the atomistic level. This, together with HRTEM structural analysis, provides valuable understanding of the nanotube junction formation.

4.4.2.1 Detailed characterization at the branching points

The first step was to characterize at the nano-scale the branching nanotube points. The upper panel in [Figure 4.31](#) shows the presence of sulfur and the lower panel displays how the opening of a branch causes a tensile force which modifies the structure of the graphitized material.

Some reports in the literature mentioned empirical observations suggesting that the presence of sulfur in the experimental system (due to the use of sulfur containing precursors) should be playing a critical role in the branching formation [\[5-6,12-13\]](#); despite these empirical observations hinting to the role of sulfur, no experimental characterization evidence has been provided to verify the S presence. Therefore, detailed high resolution EDX measurements were performed and revealed S signal at the tip of an opening branch. [Figure 4.31](#) depicts the data obtained from this measurement. [Figure 4.31.a](#) shows the position of the line scan measurement, whereas in [Figure 4.31.b](#) a S signal can be seen at the tip (note that the S signal intensity is higher than the background signal). In order to ensure the reliability of this measurement, we compared an EDX point measurement in the vacuum (marked as point A in [Fig. 4.31.a](#)) with one point located at the tip (marked as point B in [Fig. 4.31.a](#)), thus indicating a signal at 2.3 keV characteristic of sulfur from point B but not from point A.

The second important analysis was performed from HRTEM, at the opposite side of each opening branch where a deformation in the stacking of the graphene layers was observed, consistent with the hypothesis of tensile forces coming from the opposite side in which a bump arises. The black and white lines marked on the HRTEM image of the lower panel in [Figure 4.31](#), illustrate the stacking variations on the observed graphene layers occurring in front of the emerging branch.

Branching Point

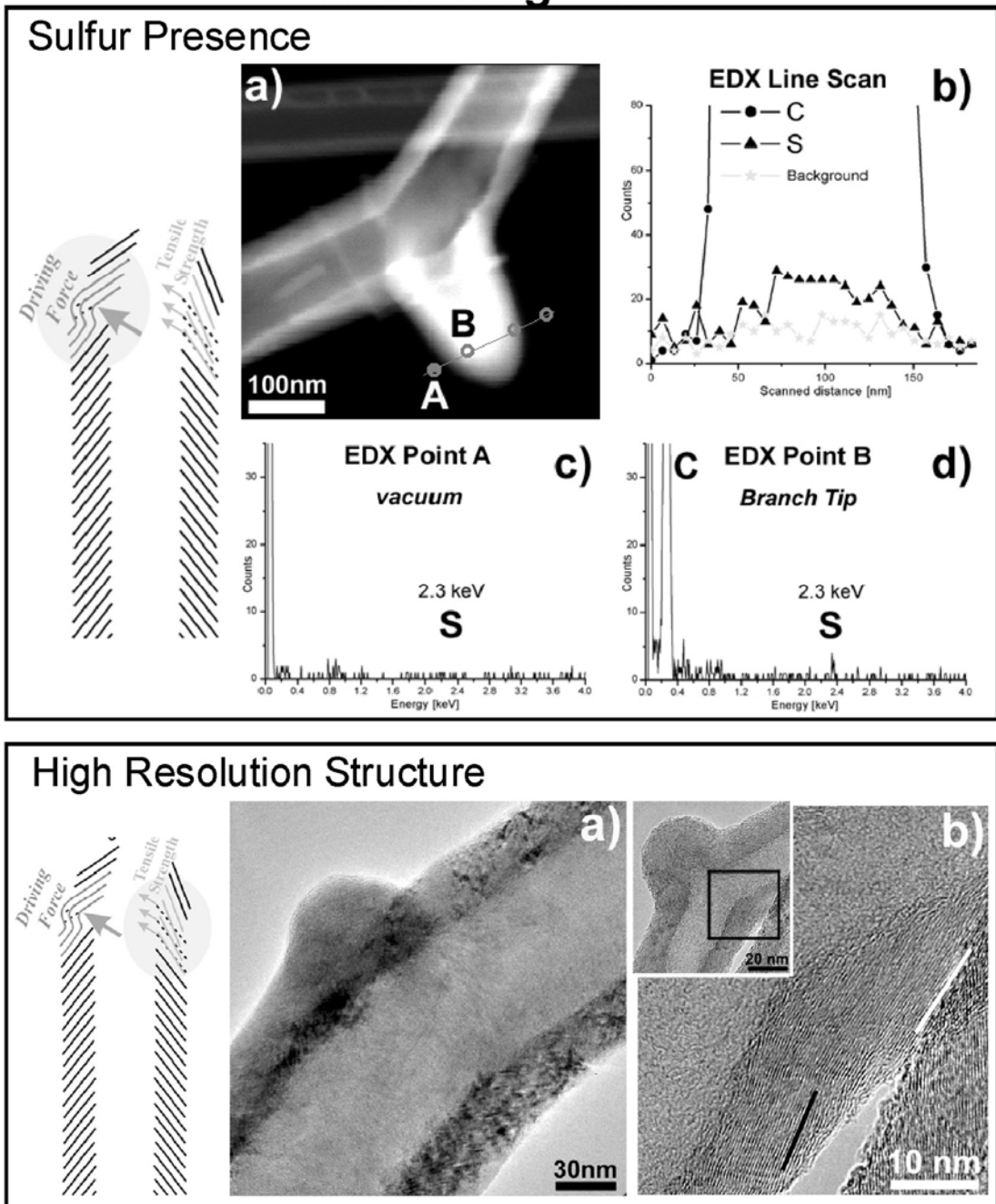


Figure 4.31: High resolution characterization at the branching point. The upper panels shows the EDX spectra showing traces of sulfur at the emerging branch. The lower panel depicts the change in the stacking angle of the graphene layers due to a tensile force caused by the emerging bump that causes branching along the growing fibre. Frame a) in the lower panel shows a direction change right in front of the opening bump; while b) presents the HRTEM image showing the stacking angle change of the graphene layers marked by the black and white line.

4.4.2.2 DFT calculations: the importance of sulfur

The presence of sulfur motivated to perform extensive calculations based on first principles density functional theory (both static and dynamic) to fully understand the sulfur role. Three different scenarios were studied: i) a ring of sulfur atoms was placed in a CNT (as shown in [Figure 4.32.a](#)); ii) a sulfur atom was placed in a graphene layer (see [Figure 4.32.c](#)); and iii) the energetic stability of a substitutional sulfur atom in a sp^2 carbon network was calculated under different type of environments (different type of curvature; i.e. pentagons, hexagons or heptagons. See [Figure 4.32.d](#)).

As shown in [Figure 4.32.a](#), the molecular dynamics calculations reveal that sulfur widens the diameter of a nanotube and promotes the formation of heptagons. This is consistent with the stacked-cone structure (see [Fig. 4.32.b](#)) observed in CNT junctions. When followed in detail, the molecular dynamics evolution, the formation of a pentagon and an heptagon can be seen (see [Fig. 4.32.e](#)), suggesting the ability of the sulfur to promote these types of non hexagonal rings in the sp^2 carbon network. When a sulfur atom was placed in a graphene layer, the S atom tends to move out from the carbon network, causing a bump on the graphene layer (see [Fig. 4.32.c](#)).

The energetic stability of the substitutional sulfur atom was calculated in a peanut –like model as shown in [Figure 4.32.d](#). This model contained positive curvature, negative curvature and hexagonal zones in the carbon network (see [section 4.6](#) for details in the model and calculation methods or [\[23\]](#)). These calculations clearly indicate that once sulfur is incorporated into the graphene network, it energetically favors pentagons and heptagons rings over hexagons, thereby introducing negative (heptagons) or positive (pentagons) curvature [\[24\]](#).

These three results can explain the sulfur role in promoting the opening of a branch as the driving force for cone-stacked fibres and CNT branches. The sulfur must be playing an important role generating the cone stacked structure that are observed; once the cone stacked structure is obtained, good enough concentration of sulfur is accumulated at a cone wall which will tend to promote a bump to emerge out of the cone. This is totally supported by the fact that sulfur will tend to promote the formation of heptagons and pentagons in the sp^2 carbon network, necessary to achieve negative curvature thus resulting in the formation of the branch.

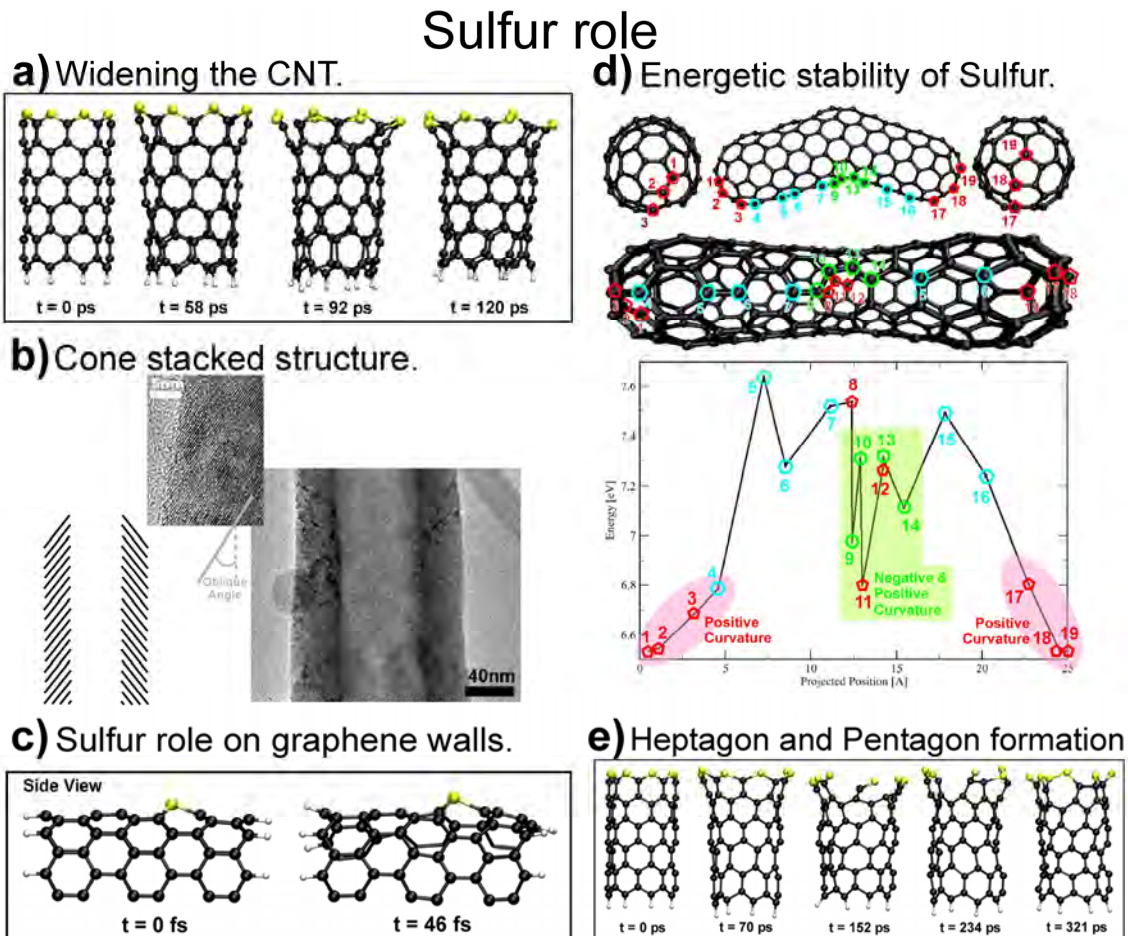


Figure 4.32: DFT calculation results summarizing the sulfur role. a) The snapshots from the molecular dynamics simulation show the effect of sulfur which results in the formation of heptagons that result in an opening of the growing tube. This inclination is also consistent with the cone stacked structure observed when sulfur is present as shown in b). Figure c) reveals a bump formation out of the graphene plane induced by the S atom presence. Figure d) summarizes the energetic stability results of sulfur embedded in a sp^2 carbon network, indicating that S tends to accommodate easily in curved regions containing either pentagons or heptagons. Figure e) presents the pentagon and heptagon ring formations observed from the molecular dynamics calculations, promoted by the sulfur presence.

4.4.2.3 HRTEM observations.

HRTEM studies are summarized in [Figure 4.33](#), where the main structural features of the Y junctions are highlighted. The left upper panel reveals how a change in direction of the main stem is accompanied by a branch opening. This is consistent with the variations in stacking angles of the graphene layers previously pointed out in [section 4.3.2.1](#).

The lower panel depicts the structure of the developing branch, showing graphitized layers that appear to be very well stacked with a hollow core; and the tip displays plain zones with well defined angles where the graphene layer curves. Finally, the resulting Y junction shown in the upper right panel consists of an array of graphene layers that are organized along two new arms at a given angle. Note that a cone stacked structure is preserved in the junction.

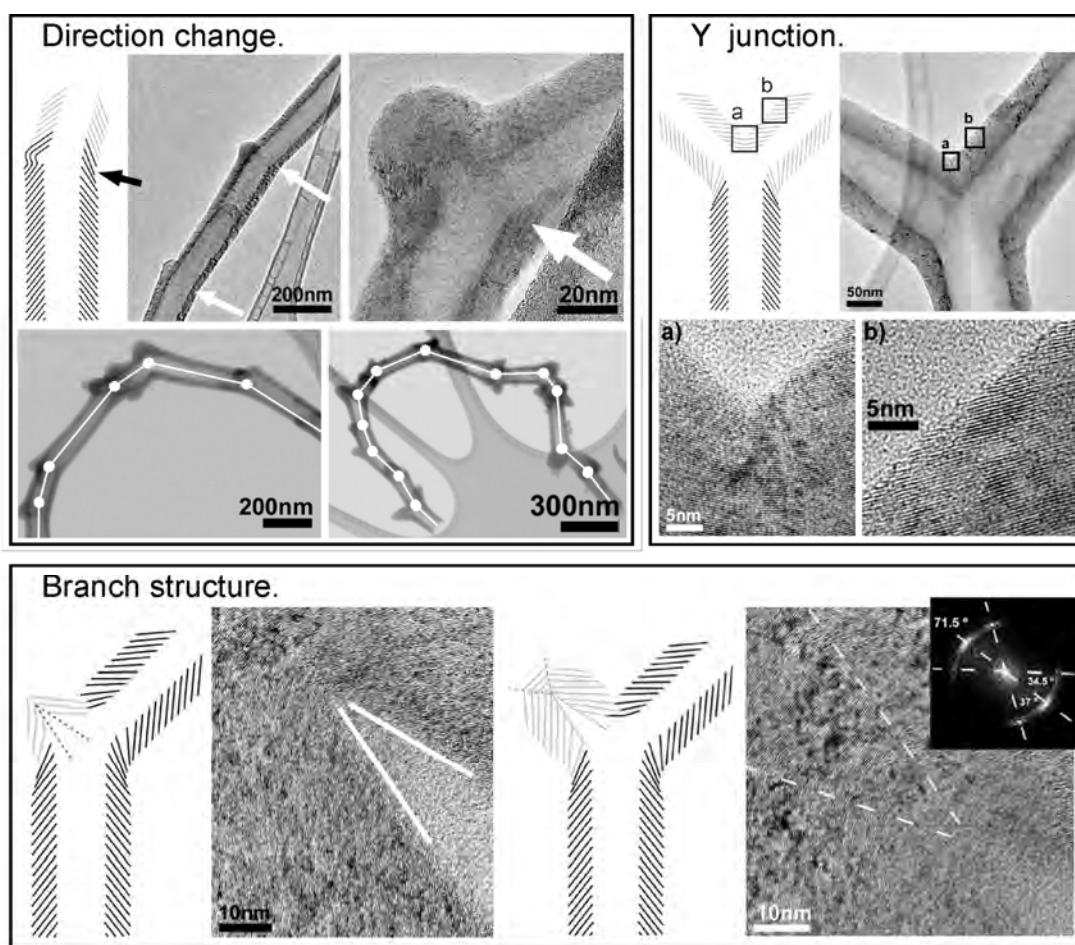


Figure 4.33: Structural HRTEM characterization of the branching formation. The left upper panel indicates the direction change observed every time a branch emerges. The lower panel displays the hollow interior and the graphene stacking of the developing branch. The upper right panel shows the final Y nanotube junction.

4.4.3 Branching mechanism and discussion

All the evidence provided in this chapter gives information to propose the branching mechanism of CNTs, summarized in Figure 4.34. The model starts with the formation of the main cylindrical stem with a cone stacked structure, favored by the presence of sulfur in the system, due to a widening effect on the nanotube (see Figure 4.32.a).

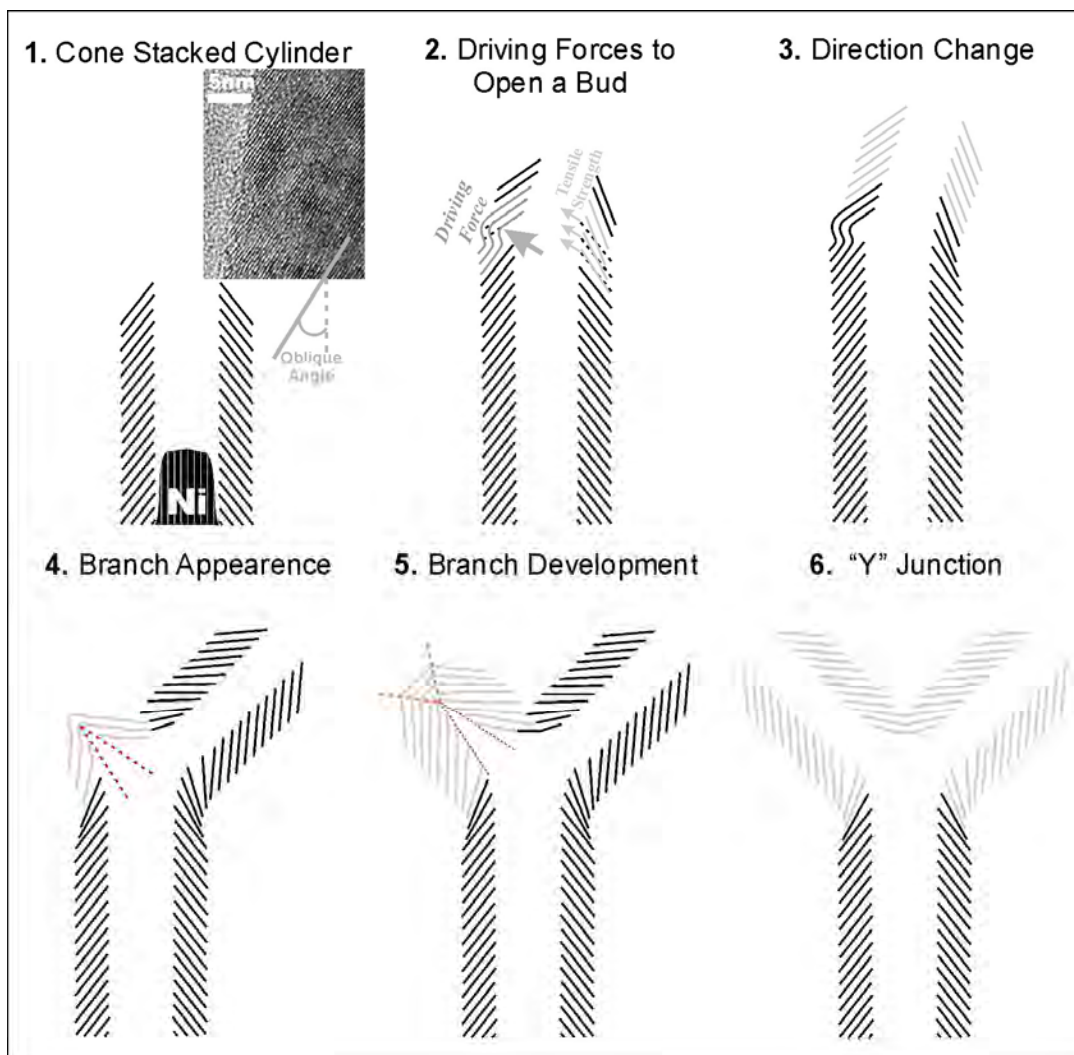


Figure 4.34: Schematic illustration of the Branching Mechanism. 1) Illustrates the cone stacked structure of the main stem due to the presence of sulfur in the system (see Fig. 4.32.a); 2) shows a bump appearance due to the sulfur ability to promote heptagons (see Fig. 4.32) as a driving force. As a consequence a tensile strength is generated on the opposite side therefore modifying the stacking angle; such stacking angle modification causes a change in direction of the main stem, displayed in 3), becoming the second arm of the junction; the bump keeps developing to become the third arm of the junctions as shown in 4), 5) and 6).

Accumulation of sulfur atoms on a cone wall then promotes the formation of a bump (see Figure 4.32.c), which induces deformations on the opposite side of the growing tubule. The bump formation is supported by the fact that sulfur tends to promote heptagon and pentagon rings in the sp^2 carbon network (see Figure 4.32.e). This step is essential for achieving negative curvature at the emerging

branch and positive curvature close to the branch tip (as indicated by the theoretical calculation results; see [Figure 4.32](#) and its discussion in [section 4.4.2.2](#)).

Following the initial stage of bump formation, the graphitic walls on the opposite side experience strong deformations which in turn cause a change in the stacking angle of the graphene layers. This change facilitates modification in the growth direction of the main stem, thus promoting the formation of the second arm (see [Figure 4.33](#)). On the opposite side, the bump will start developing a hollow interior and finally a closed tip with graphitized material to become the third arm of the junction (see [Figures 4.33](#) and [4.34.4 – 4.34.6](#)) to finally obtain the Y junction structure.

4.5 Conclusions

The synthesis study reported in this chapter allowed us to identify the specific zones in the reactor (temperature conditions) where the branched material is obtained (T11). In addition to the branched material, carbon fibre entanglements with metallic balls were also found. Interestingly, the encapsulated metal in these particles was identified as NiS_x and Ni.

When the Ar flow passing through thiophene was slightly modified, drastic changes were observed in the synthesized material. When medium flux was applied, flakes with micro patterns were observed. Those flakes were composed of nanocrystals at the end of filament –like carbon fibres. Some other flakes without any pattern were obtained in the same region, and consisted of carbon fibre entanglements in addition to sea urchin –like nanostructures. An important feature observed from HRTEM studies, is that the encapsulated material in the sea urchin –like nanostructures were polycrystals containing domains of Ni and NiS_x .

Random networks of 1D carbon blocks were obtained when minimum carrier flux was applied. Multiple covalent nodes were observed connected by micro tubular fibres. Those junctions exhibited different types of angles which could fit in cubic networks with square or hexagonal geometries. The structure of these junctions was analyzed by TEM and revealed a hollow interior.

Finally, when the catalyst was changed to ferrocene, some junctions were obtained in a different zone of the reactor. Interestingly, the structure of these junctions corresponds to concentric graphene cylinders; note that most of the CVD reported junctions exhibit the stacked-cone morphology.

High resolution characterization studies revealed the presence of sulfur at the emerging branch which motivated to perform first principles DFT calculations in order to understand, at the atomistic level, the sulfur role. This together with HRTEM structural analysis provides valuable evidence that help to understand the junction formation. All the evidence together allowed to propose the detailed atomistic model that elucidates the catalytic role of sulfur and the underlying branching mechanism in Y junctions.

4.6 Open Issues

The samples containing polycrystalline Ni and NiS_x domains coexisting in the same cluster would be of great interest for an *in-situ* HRTEM study at high temperatures in order to analyse the sulfur diffusion along the particle. A similar study on the *peculiar tip* material would also be of interest to see the live movement of the metallic particle at the tips and to study the carbon diffusion through them. Similarly, an *in-situ* heat treatment study under tension in the HRTEM for the tree – like material would be of importance.

The mechanical properties of the different type of junctions should also be studied by AFM or *in-situ* HRTEM; by stretching and compressing the different arms at different angles within the branched nanotubes.

Calculation methods

The calculations presented in this section were performed at Oak Ridge National Laboratory (ORNL), TN USA under the supervision of Bobby Sumpter and Vincent Meunier (collaborator and co-advisor of the present Ph.D. project). All calculations were performed using the periodic DFT program Vienna *ab initio* simulation package (VASP), version 4.6.6 [25-28]. The Kohn-Sham equations were solved using the projector augmented wave (PAW) approach and a plane-wave basis with a 400 eV energy cutoff [29-30]. The generalized gradient approximation (GGA) exchange-correlation functional of Perdew, Burke, and Ernzerhof (PBE) was utilized [31]. Electronic convergence was defined as a consistency between successive cycles of less than 10⁻⁵ eV.

Each nanotube system was placed in a cell that ensured at least 10 Å of vacuum in each Cartesian direction between the tube and its reflection. *k*-point sampling was restricted to a single point, the Γ point, a choice that is relevant for a cluster-like calculation as the one performed here.

The energetics were performed from full DFT-relaxation. The effects of temperature on S-doped CNTs was investigated with first principles molecular dynamics simulations using a 1 fs dynamical time step and a Nosé-Hoover thermostat to regulate the ion temperature to ~2500 K over 5 picoseconds (or ~1000 °K for the single S atom in the graphene wall).

The nano “peanut” studied consisted of a capped (9,0) and a (5,5) nanotube joined with a pentagon-heptagon pair. The calculation consisted of placing a single S atom at different substitutional positions (shown by red pentagons in case of belong to a pentagon, blue hexagon in case of belong to a hexagon and green heptagon in case of belonging to only hexagon rings; see Figure 4.30.c). Since the substitution of a carbon atom by a sulfur atom is associated with a significant structural reorganization, full DFT-relaxation for each case was performed.

References

- [1] Romo-Herrera, J.M. *et al.* Covalent 2D and 3D Networks from 1D Nanostructures: Designing New Materials. **Nano Lett.** **7** (3), 570-576 (2007).
- [2] Zhou, D. & Seraphin, S. Complex branching phenomena in the growth of carbon nanotubes. **Chem. Phys. Lett.** **238**, 286-289 (1995).
- [3] Li, J., Papadopoulos, C. & Xu, J. Nanoelectronics: Growing Y-junction carbon nanotubes. **Nature** **402**, 253-254 (1999).
- [4] Terrones, M., *et al.* Molecular Junctions by Joining Single-Walled Carbon Nanotubes. **Phys. Rev. Lett.** **89** (7), 075505 (2002).
- [5] Satishkumar, B.C., John Thomas, P. Govindaraj, A. & Rao, C.N.R. Y-junction carbon nanotubes. **Appl. Phys. Lett.** **77** (16), 2530-2532 (2000).
- [6] Deepak, F.L., Govindaraj, A. & Rao C.N.R. Synthetic strategies for Y-junction carbon nanotubes. **Chem. Phys. Lett** **345**, 5-10 (2001).
- [7] Li, W.Z., Wen, J.G. & Ren, Z.F. Straight carbon nanotube Y junctions. **Appl. Phys. Lett.** **79** (12), 1879-1881 (2001).
- [8] Gu, P., Zhao, J.H. & Li, G.H. Synthesis of Y-branching multiwalled carbon nanotubes with a bamboo like structure. **J.Mater.Res.** **17** (11), 2768-2770 (2002).
- [9] Zhu, H. *et al.* Growth mechanism of Y-junction carbon nanotubes. **Diam. & Rel. Mat.** **11**, 1349-1352 (2002).
- [10] Gothard, N. *et al.* Controlled growth of Y-junction nanotubes using Ti-doped vapor catalyst. **Nano Lett.** **4** (2), 213-217 (2004).
- [11] Heyning, O.T., Bernier, P. & Glerup, M. A low cost method for the direct synthesis of highly Y-branched nanotubes. **Chem. Phys. Lett** **409**, 43-47 (2005).
- [12] Wang, Z. *et al.* Synthesis of branched carbon nanotubes from coal. **Carbon** **44**, 1298-1352 (2006).
- [13] Lou, Z., Chen, C., Huang, H. & Zhao, D. Fabrication of Y-junction carbon nanotubes by reduction of carbon dioxide with sodium borohydride. **Diam. & Rel.Mat.** **15**, 1540-1543 (2006).
- [14] Huang, S., Dai, L. & Mau, A. Synthesis and structures of aligned branched carbon nanotubes produced by pyrolysis of iron (II) phthalocyanine. **Physica B** **323**, 336-338 (2002).
- [15] Scuseria, G.E. Negative curvature and hyperfullerenes. **Chem. Phys. Lett** **195**, 534-536 (1992).
- [16] Chernozatonskii, L. Carbon nanotube connectors and planar jungle gyms. **Phys. Lett. A** **172**, 177-176 (1992).
- [17] Andriotis, A.N. *et al.* Rectification properties of carbon nanotube "Y-Junctions". **Phys. Rev. Lett.** **87** (6), 066802 (2001).
- [18] Meunier, V. *et al.* Intrinsic electron transport properties of carbon nanotube Y-junctions. **Appl. Phys. Lett.** **81** (27), 5234-5236 (2002).
- [19] Nagy, P., Ehlich, R., Biró, L.P. & Gyulai, J. Y-branching of single walled carbon nanotubes. **Appl. Phys. A**, **70**: 481-483 (2000).
- [20] Oberlin, A., Endo, M. & Koyama, T. Filamentous growth of carbon through benzene decomposition. **J. Cryst. Growth.** **32**: 335-349 (1976).
- [21] Gan, B., *et al.* Branching carbon nanotubes deposited in HFCVD system. **Diam. and Rel. Mat.**, **9**: 897-900 (2000).
- [22] Terrones, M. **Ph.D. Thesis**: Production and Characterization of Novel Fullerene-related Materials: Nanotubes, Nanofibres and Giant Fullerenes. **University of Sussex, England** (1997).
- [23] Meunier, V., Henrard, L. & Lambin, Ph. Energetics of bent carbon nanotubes. **Phys. Rev. B** **57**, 2586-2591 (1998).
- [24] Mackay, A.L. & Terrones, H. Diamond from graphite. **Nature** **352**, 762 (1991).
- [25] Kresse, G. & Hafner, J. *Ab initio* molecular dynamics for liquid metals. **Phys. Rev. B** **47**, 558 (1993).
- [26] Kresse, G. & Hafner, J. *Ab initio* molecular-dynamics simulation of the liquid-metal-amorphous-semiconductor transition in germanium. **Phys. Rev. B** **49**, 14251 (1994).

Chapter 4: CVD synthesis of CNT junctions and its Branching Mechanism

- [27] Kresse, G. & Furthmuller, J. Efficiency of ab-initio total energy calculations for metals and semiconductors using a plane-wave basis set. **Comput. Mat. Sci.** **6**, 15 (1996).
- [28] Kresse, G. & Furthmuller, J. Efficient iterative schemes for *ab initio* total-energy calculations using a plane-wave basis set. **Phys. Rev. B** **54**, 11169 (1996).
- [29] Kresse, G. & Joubert, D. From ultrasoft pseudopotentials to the projector augmented-wave method. **Phys. Rev. B** **59**, 1758 (1999).
- [30] Blochl, P.E. Projector augmented-wave method. **Phys. Rev. B** **50**, 17953 (1994).
- [31] Perdew, J.P., Burke, K. & Ernzerhof, M. Generalized Gradient Approximation Made Simple. **Phys. Rev. Lett.** **77**, 3865 (1996).



Chapter 5. 1D Superlattices: *nitrogen doped and undoped segments*

Abstract

Miniaturization in electronics is the driving force for obtaining new functional nanodevices. The ability to design intramolecular devices along 1D nanostructures would result in molecular wires transporting electronic current with self integrated nanodevices. 1D Superlattices (or heteroatomic wires) with inorganic NWs [3] have been achieved showing axially [4-6], radially [8] and side-to-side [9] modulation of different type of materials. Regarding CNTs, extensive work has been performed connecting CNTs of different chirality (diameter) and characterizing their intramolecular interfaces [12-24]. Nevertheless, controlling chirality and the electronic properties of CNT segments during synthesis is an open problem. In this context, it is believed that the synthesis of doped CNTs with portions of undoped regions could act as efficient hetero-nanotubes with potential applications [26-27].

This chapter describes the formation of CN_x-pure CNTs using intermitent CVD (I-CVD) methods. The capabilities of this I-CVD method is well illustrated by successful synthesis of multiwalled CNTs exhibiting segments containing nitrogen and others without nitrogen (axially modulated doping). A first stage of synthesis experiments to callibrate the intermitent synthesis parameters (resulting in 825°C and 2.5 l/min as the best temperature and carrier flux parameters) is presented, showing enough experimental evidence to illustrate the multiwalled CNTs growth mechanism during the first 10 minutes of reaction. The exhaustive structural characterization together with the analytical measurements demonstrate the synthesis of these novel nanotubes. Finally, preliminary results demonstrate that the I-CVD method under the appropriate synthesis conditions could generate heteronanotubes containing tubules of different nitrogen composition (radially modulated doping).

5.1 Introduction	133
5.2 Experimental Setup	135
5.2.1 Experimental Device	135
5.2.2 Experimental Method	136
5.2.3 Characterization Techniques	136
5.3 Calibration Experiments	137
5.3.1 Temperature and Ar Flux.	137
5.3.2 Reaction Time	139
5.4 1D Superlattices	146
5.4.1 CNT heterojunction interfaces.	146
5.4.1.a Continuity along the interface	147
5.4.1.b Elbow –like structures in C-CNx heteronanotubes	149
5.4.2 Analytical (EDX) measurements.	152
5.4.3 Multiple segments.	155
5.4.4 Failed experiments	156
5.5 Conclusions	157
References	158

5.1 Introduction

Miniaturization in electronics is a driving force to obtain new functional nanodevices. The fabrication of nanocircuits remains a challenge. Specifically, 1D nanostructures represent suitable building blocks since they could act as nanowires transporting the electronic current. Furthermore, the ability to synthesize intramolecular devices along the wire is of interest in nanotechnology.

Electronic devices are based on 2D semiconductor interfaces, such as transistors, laser diodes, light emitting diodes and quantum cascade lasers. However, the formation of 1D heterostructures could replace existing electronics technology. In this context, the first attempts to interconnect two 1D nanostructures were reported with heterojunctions between a Si NW and a multiwalled CNT [1] and SWNTs and carbide nanorods [2]. It took three more years to actually obtain good quality 1D Superlattices [3] (1D SL) axially modulated with inorganic NWs [4-6]. This was obtained, on semiconductor GaAs NWs with segments of GaP by alternating laser ablation processes of solid GaP and GaAs targets [4]. In addition, Si/SiGe superlattices were synthesized by a hybrid pulsed laser ablation of Ge together with the chemical vapor deposition of Si species on Au which was used as catalyst [5]; similarly InAs/InP superlattices have been produced by chemical beam epitaxy on Au [6]. Subsequent work showed axial 1D SL performing as addressable arrays when different type of segments were locally electrical gating, along Si NWs where the dopant was modulated during growth in a n/n^+ superlattice [7]. Not only axially modulated SL have been obtained with NWs, but also the synthesis of Si/Ge core-shell and multishell NWs has been achieved [8] showing 1D SLs radially modulated. This was achieved by CVD, due to a more favorable diffusion of the vapor-phase into the NW surface than over the particle catalyst, allowing the epitaxial growth of the shells [8]. A third different geometry on 1D heterostructures has been reported, as *side-to-side* biaxial and triaxial NWs, where the final 1D nanostructure maintains its circular cross section, half of the circle composed of Si and the other half of ZnS (or ZnSe) in the biaxial case; these nanostructures were obtained by a two stage thermal evaporation of mixed SiO and ZnS (or ZnSe) powders [9]. A more complicated 1D axial SLs can be obtained when combining different type of nanostructured building blocks, such as the interconnecting 0D cluster with 1D nanostructures as the report of contacting Au nanoparticles with CNTs by self-assembly using the biotin-streptavidin molecules interaction [10]. Recently it was reported nanocrystal heterostructures in 3D with tetrapod-shape, where the core structure is composed of CdSe and the branching arms are axially grown epitaxially as CdTe wires or as a second generation of tetrapods at the end of each of the four arms [11].

Regarding CNTs, the connection of two different CNTs with different chiralities was theoretically proposed by the introduction of a pentagon-heptagon pair [12], thus producing metal-semiconductor or semiconductor-semiconductor heterojunctions. A first proposal of modelling the interconnection of different chirality CNTs was made two years before without any property calculation [13-a-b]. STM local electrical characterization along SWNTs [14] and four probe transport measurement on a kinked CNT [15] showed experimentally the existence of such intramolecular junctions. Three more reports appeared modelling the

interconnection of two different chirality and diameter CNTs and calculating their electronic properties, showing that localized states due to the pentagon-heptagon topological defects at the interface govern the electronic behavior around the Fermi level [16-18]. Subsequently, theoretical simulations of STM images and STS were performed on two connected CNTs in order to give a unique electronic signature to compare with experimental measurements [19]. Extensive work on interfaces of two different diameter CNTs interconnections has been reported, experimentally [20-21] and theoretically [22-23]. The reports showed that a metallic-semiconductor junction has an electronically sharp interface without localized electronic states, metallic-metallic junctions exhibit a more extended interface and low energy localized electronic states [20] while a semiconductor-semiconductor junction shows that localized electronic states from the defects on the interface exist in the energy gap and the extended states of the CNT penetrate and decay slowly into the other side [21]. Further efforts have reported a theoretical quantum transport study on a CNT superlattice, consisting of nanotube interfaces (diameter change from (9,0) to (12,0)) repeated periodically, showing a quantized conductance [24]. Even coaxial nanocables have been proposed, with a carbon nanotube core and a boron nitride nanotube as a shell. Ab initio calculations show that the electronic current is only carried by the inner CNT whereas the outer BN nanotube acts as an insulating shell [25].

All this theoretical work shows the importance of interfaces in CNT devices, nevertheless controlling chirality and therefore electronic segments of CNTs during synthesis remains a challenge hard to overcome towards applications. However, other alternatives have been explored by varying chemical doping along the tube, this by covering half of a SWNT (p-type nature) and exposing the other half to potassium, thus obtaining p-n junctions exhibiting rectifying characteristics along the nanotube [26]. A different electronic device was obtained when doping a segment of a SWNT with potassium, thus obtaining an intramolecular NOT logic gate [27].

The synthesis in mass production of CNT 1D SLs remains an important challenge. This chapter presents a proposal of intermittent CVD (I-CVD) synthesis method for producing CNTs, where two different carbon sources are continuously alternated to feed the CVD reactor. It should be mentioned that while this work was in progress a work appeared reporting similar 1D CNT SLs by flowing different carrier gases during the reaction [28]. The present chapter illustrates the capabilities of the I-CVD method with multiwalled CNTs by N-doping alternation. The first stage of synthesis experiments, producing undoped CNTs (MW) and nitrogen doped CNTs (CNx) independently, was performed to calibrate the most efficient experimental parameters. An exhaustive structural characterization together with the analytical measurements demonstrate the successful production of NT heterojunctions. We also observed that is possible to generate sandwich cylinders (radial modulation) of N-doped and undoped carbon using this method under specific experimental conditions.

5.2 Experimental Setup

In order to obtain 1D CNT SLs by the CVD technique, it was necessary feed the synthesis reactor with two independent carbon sources continuously alternated.

5.2.1 Experimental Device

A modified standard CVD aerosol pyrolysis device (previously described by Pinault *et al.* [29]), was used to feed two different aerosols into the reactor continuously. The schematic diagram of the device is shown in Figure 5.1.a, in which two aerosol generators are connected together into the quartz reactor by a pyrex piece with valves. Such glass connectors are depicted in Figure 5.1.b; note that contains two aerosol lines with independent valves, and a third gas inlet to feed the inert gas upon heating or cooling of the furnace. The full experimental device is shown in Figure 5.1.c and Figure 5.1.d. The figures show two aerosol generators, a valve system, a quartz tube placed in a furnace and a condenser and trap for the exhausting gases.

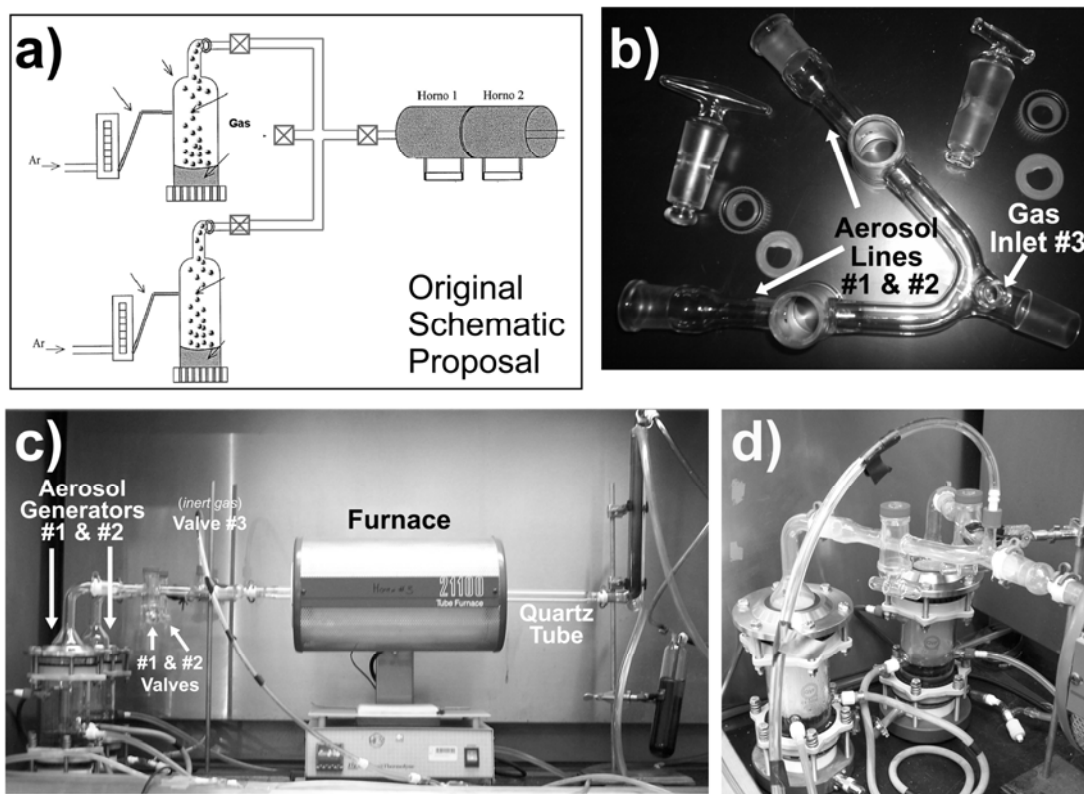


Figure 5.1: Adaptation to the CVD aerosol pyrolysis device to perform intermittent-CVD synthesis by continuously alternating the feeding aerosol sources. a) presents the original scheme with the modification proposal; b) exhibits a valves piece designed for the modification; c)-d) shows the experimental setup during a regular experiment.

5.2.2 Experimental Method

The CVD aerosol pyrolysis method, previously described [29], briefly consists of generating an aerosol from a solution containing a hydrocarbon as solvent and the metal precursor as solute. The aerosol is carried by an argon flow into the quartz tube inside a furnace system where the synthesis takes place.

Specifically in this work, the hydrocarbon solvent used for the N-doped CNTs corresponds to: benzylamine (C_7H_9N), self containing the nitrogen; while for the undoped CNTs, toluene (C_7H_8) was used as solvent. The metallic precursor used as solute in this study was ferrocene ($C_{10}H_{10}Fe$) in a 2.5 wt.% for both cases.

The other three important variables to define for the synthesis of CNTs by CVD are: temperature, gas flow and the reaction time. These three parameters were experimentally adjusted in a first experimental stage (see Section 5.3), in order to obtain the most efficient parameters to produce both type of segments: nitrogen doped CNTs (CN_x) from benzylamine and undoped CNTs (MW) from toluene to achieve the NT heterojunctions successfully.

Once performed the calibration stage (see Section 5.3), the Ar flow was set to 2.5l/min and the temperature to 825 °C. Subsequently, *intermittent CVD* experiments were performed, by alternating the aerosol feeding the benzylamine solution and the toluene solution. It should be remarked that only the first solution used contained the metallic precursor, while the second was only a hydrocarbon source. The latter ensured the continuous growth of the hetero-nanotube from the same active catalyst.

5.2.3 Characterization Techniques

The samples collected by scraping the central region (5cm long) of the quartz tube, were structurally characterized by: scanning electron microscopy (SEM, Philips FEG-XL30; operated 10-20 keV), high resolution electron microscopy (HRTEM, Philips CM200; operated 200 keV; and Jeol JEM 2010F operated at 200 keV), and analytically characterized by energy dispersive X-ray spectroscopy (EDX, in column Philips FEG-XL30).

5.3 Calibration Experiments

The first stage of experiments were performed to find the most suitable parameters such as temperature and Ar flow in the co-synthesis of CN_x and pure carbon (MW) heteronanotubes.

5.3.1 Temperature and Ar Flux

The two magnitudes measured were the amount of powder (black soot) material by their weight and the length of the CNTs by SEM micrographs. Since the 40cm furnace displays temperature gradients affecting the final quality of the sample. The material was always scraped from a 5cm zone right at the central region of the furnace to have a homogenous sample. Therefore, a Performance Coefficient was defined as:

$$\text{Performance Coefficient} = \frac{\text{Soot weight from 35cm remaining}}{\text{Soot weight from Central 5cm}}$$

in which the minimum value of such a coefficient should correspond to the most efficient conditions regarding the amount of material at the central 5cm zone with respect to the total amount of sample obtained.

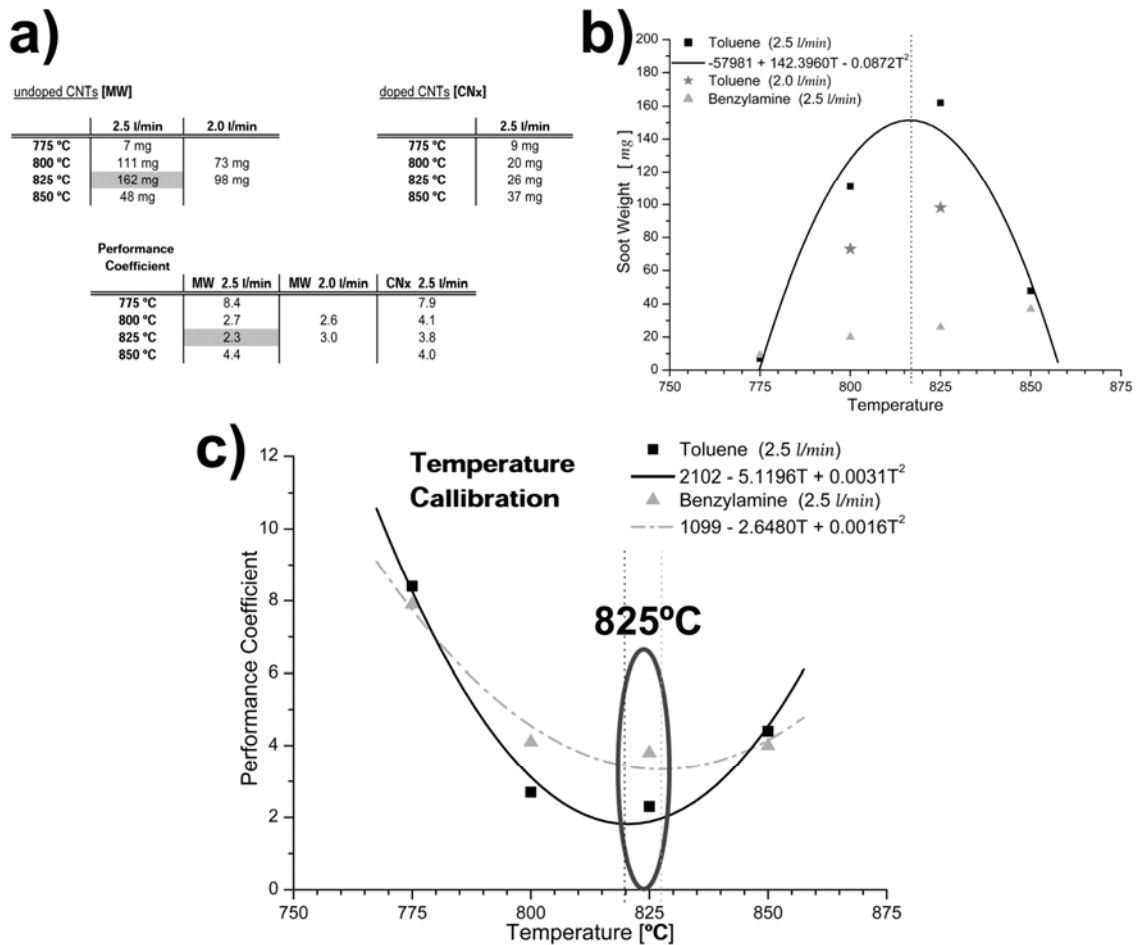


Figure 5.2: Results to obtain the most efficient carrier flux and temperature parameters for the co-synthesis of MW and CN_x CNTs. a) presents the obtained sample weights showing the performance at each different experimental condition; b)-c) exhibit graphs of the soot weight and the performance coefficient to find the most efficient experimental conditions.

Figure 5.2 summarizes the results concerning the optimal temperature and Ar flow used to maximize the amount of sample obtained. The weight tables shown in Figure 5.2.a, indicate 825°C as the best temperature for producing pure carbon CNTs using 2.0-2.5 l/min of Ar. When comparing to this data to the CNx CNTs results, it is observed that a larger amount of material is obtained at 850°C. When the performance coefficients were calculated, we noted that the minimum values correspond to **825°C** and **2.5 l/min** of Ar. The Ar flow for the CNx CNTs was not modified due to previous work performed in our laboratory (personal communication from A.Zamudio & A.L.Elías), finding 2.5 l/min of Ar as the best conditions for providing N-doped tubes.

Figure 5.2.b shows a graph indicating the sample's weights, which shows the maximum amount for MW CNTs produced at 825°C with flow rates of 2.5 l/min. Figure 5.2.c depicts a graph plotting the performance coefficient values. It was concluded that 825°C is the most efficient temperature for the synthesis when producing both type of nanotubes.

When the material was studied by SEM, it was observed that there is a direct correlation between the synthesis temperature and the length of the grown nanotubes for both cases (MW NTs and CNx NTs) as shown in Figure 5.3. These samples were always grown on quartz plates located at the central part of the furnace.

It should be emphasized that when using the same synthesis conditions (825°C, 2.5l/min and $\Delta t=10\text{min}$), MW CNTs were three times longer than CNx CNTs (see Figure 5.3.c).

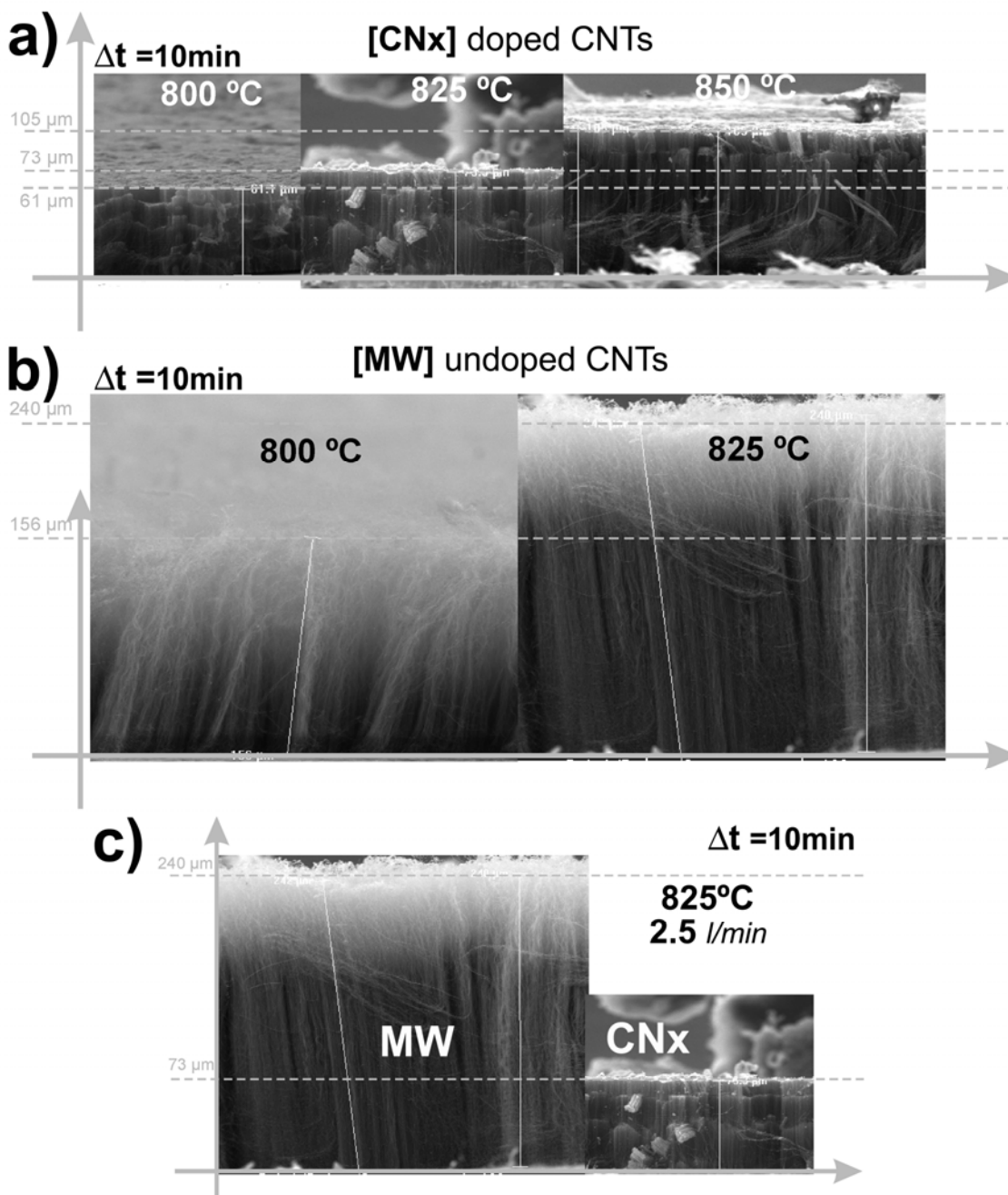


Figure 5.3: SEM micrographs showing the length dependence on the temperature of reaction. a) and b) corresponds to MW and CNx respectively; c) presents the direct length comparison between MW and CNx produced under the exact same synthesis conditions.

5.3.2 Reaction Time

Low magnification micrographs depicted in [Figure 5.4](#) for CNx CNTs show the overall morphology obtained of the carpet –like arrays. A general trend observed was an increase in the density of nanotubes ([compare Figure 5.4.d to 5.4.e](#) or [Figure 5.4.g to 5.4.h](#)).

Figure 5.4.g, 5.4.h and 5.4.i also show a length increase, confirmed by the measurements shown in Figure 5.6.

The SEM micrographs shown in Figure 5.5 indicate a similar trend for MW CNTs. A drastic change occurs when the reaction time changes from 5min to 8min. After 5min of reaction, short not well formed carpet-like arrays are produced (see Figure 5.5.d), while after 8min and 10min well aligned CNTs with higher density arrays are obtained. The drastic density increase is visually observed when comparing Figures 5.5.g, 5.5.h and 5.5.i.

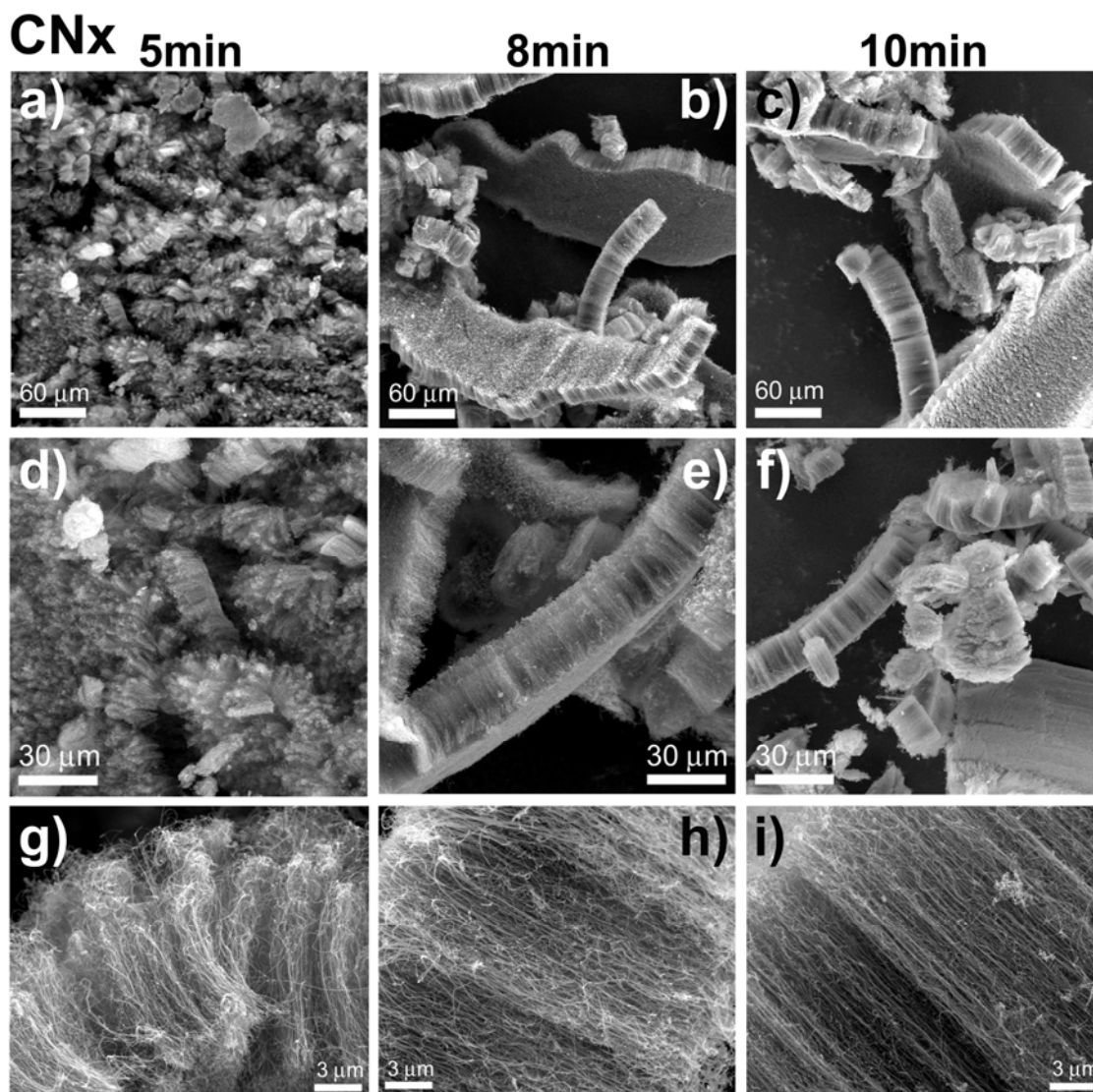


Figure 5.4: General shape of the CNx samples obtained as a function of the reaction time. Two major trends stand out: an increase of the density at the carpet like arrays and longer lengths are obtained with more reaction time.

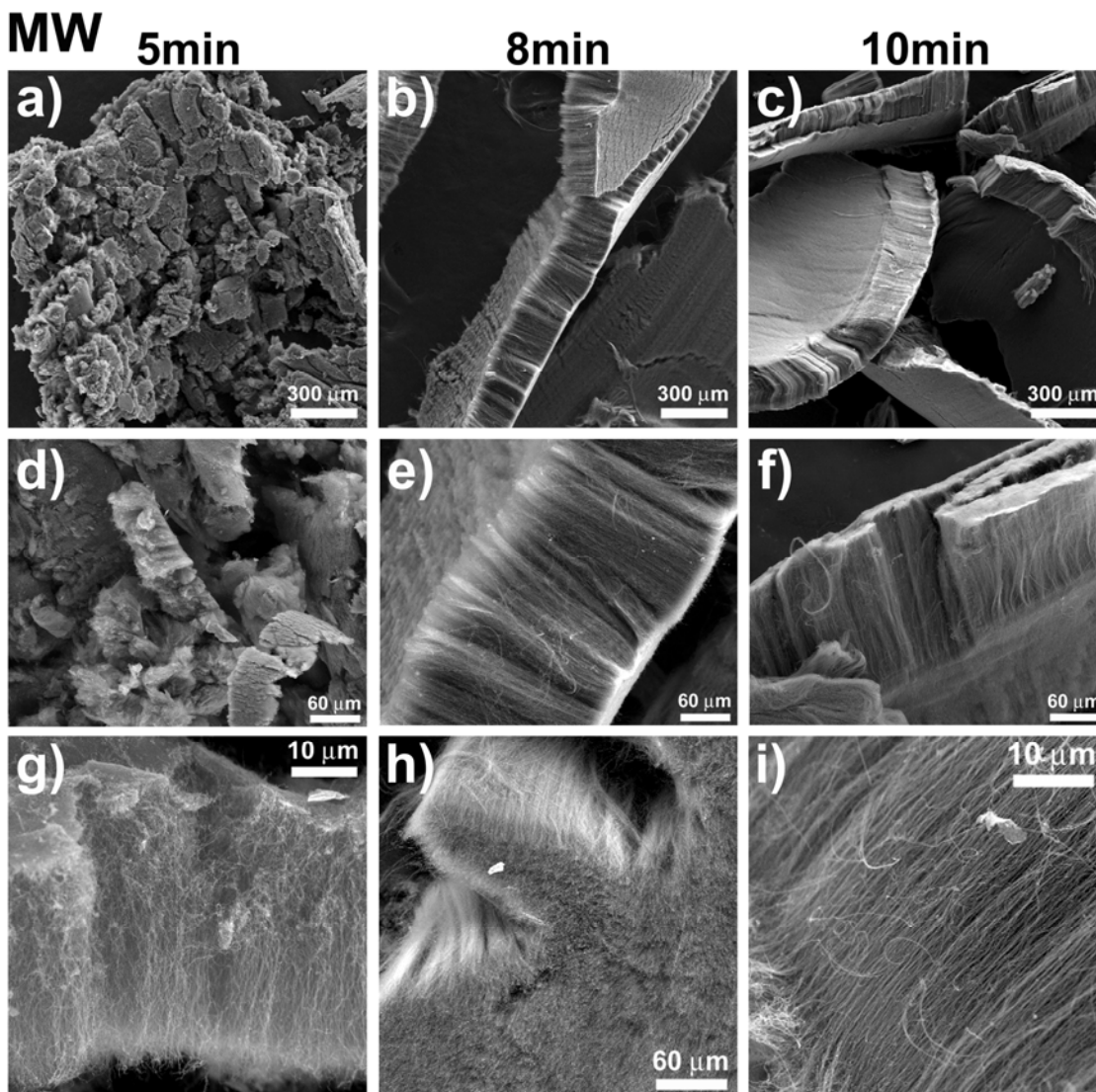


Figure 5.5: General shape of the MW samples obtained as function of the reaction time. Two major trends stand out: an increase of the density at the carpet-like arrays and longer length are obtained with more reaction time.

When the length of the CNTs is measured and plotted as a function of the reaction time, a linear relationship is obtained (see [Figure 5.6](#)). The graph in [Figure 5.6.b](#) shows the CN_x measurements from carpet-like arrays performed in the general soot powder (ball signs) and measurements from CN_x CNTs grown directly on quartz plates (diamond signs). This result suggests that we are working in the *elongation regime* according to the Endo & Koyama model [30-31]. The square signs in [Figure 5.6.b](#) represent the measurements performed from carpet-like arrays from the MW CNTs soot powder ([Figure 5.6.c](#)). The MW CNTs case presents an abrupt increase from 5 to 8 min, which according to the SEM micrograph observations is due to the lack of a good enough density of MW CNTs in the arrays at 5 minutes (see [Figure 5.5](#)). These results suggest that the *elongation regime* (Endo & Koyama model [30-31]) for MW CNTs is started after a

longer activation time than the CNx case, which is clearly achieved after 8 minutes of synthesis.

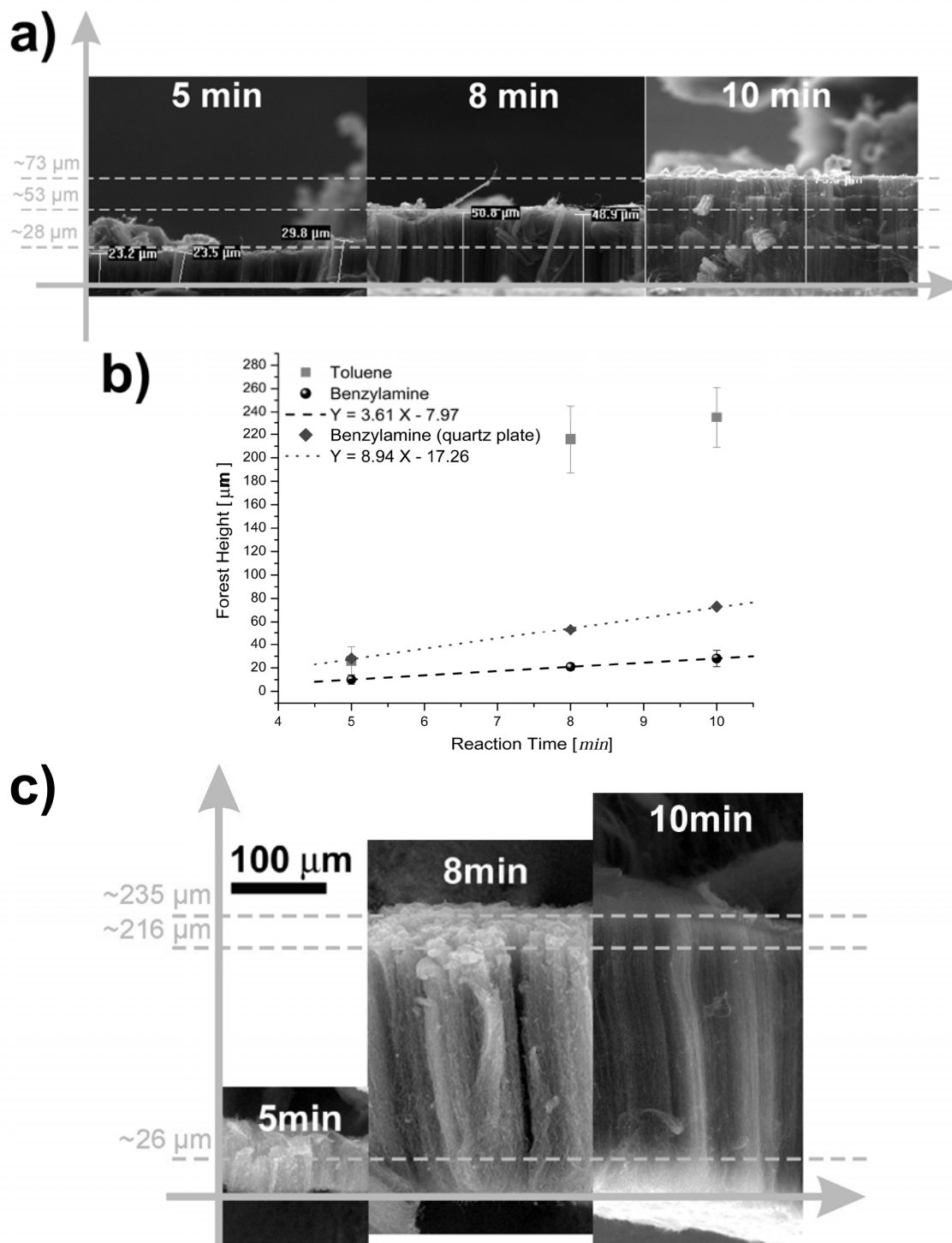


Figure 5.6: Length measurements of CNx CNTs in a) and MW CNTs in c). The graph presented in b) shows a lineal relation for CNx suggesting the elongation regime according to Endo & Koyoma model [29-30].

Diameter measurements were performed from higher magnification SEM micrographs (Figure 5.7). The CNx CNTs present a broad distribution between 20-90nm with the highest population in between 40-60nm in diameter. A diameter change was not observed as the reaction time increases.

MW CNTs reveal a broad diameter distribution between 30-100nm with the highest population between 40-80nm. A difference with respect to CNx CNTs is that MW CNTs start presenting a second group (less populated) of wider diameter tubes after 8min of synthesis (between 100-160nm). Statistic shows how MW CNTs in general show wider diameters when compared to CNx CNTs (this should be considered in the next section, when continuous Superlattices are going to be presented).

A clear diameter change as a function of reaction time was not observed in any of the cases, thus reinforcing the fact of being in the *elongation regime* from the Endo & Koyama model. According to such a model, the diameter increment starts after longer synthesis times when elongation has stopped [30-31].

The evidence obtained during this calibration stage allows to describe the growth mechanism of multi walled CNTs during the first 10 minutes of reaction. The first stage corresponds to a CNT density increment (catalyst activation) that results in carpet –like arrays; followed by a length increment of the CNTs, while no evident change in diameters is observed (elongation regime [30-31]). Figure 5.8 depicts the schematic representation of the Growth Mechanism of multiwalled CNTs by aerosol CVD, according to the evidence obtained in this study and also consistent with Endo & Koyoma [30-31]. According to them, the first ten minutes of reaction in our method correspond to a period of time before reaching the saturation length (i.e. $t_4 > 10min$). After the saturation length (L_{Sat} ; achieved when the catalyst has been poisoned), the diameters start widening during the next period of time.

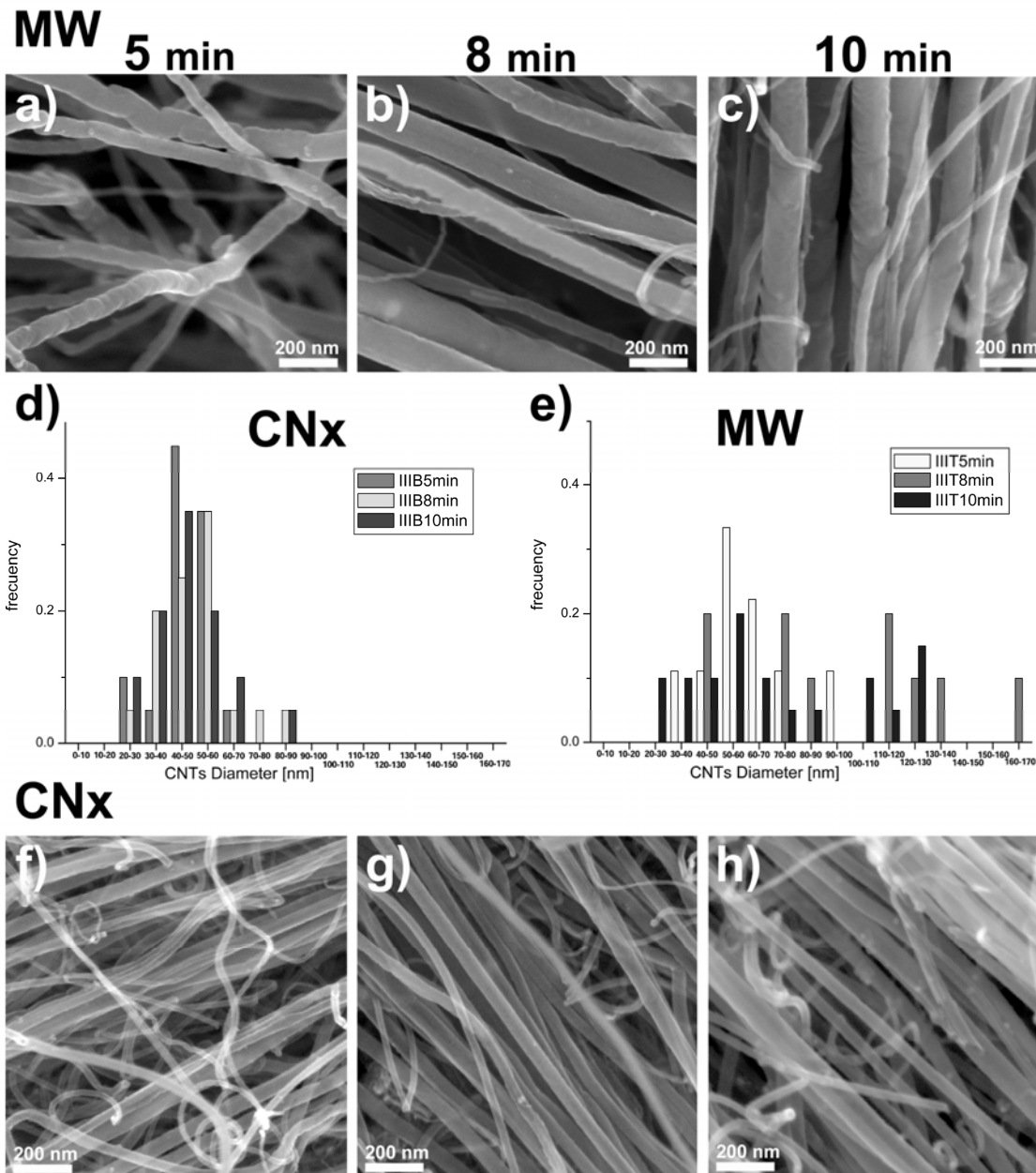


Figure 5.7: Diameter measurements from the different reaction times. a)-c) present typical MW CNTs obtained; while f)-g) show CNx typical appearance. d) and e) correspond to the diameter distributions for CNx CNTs and MW CNTs, respectively.

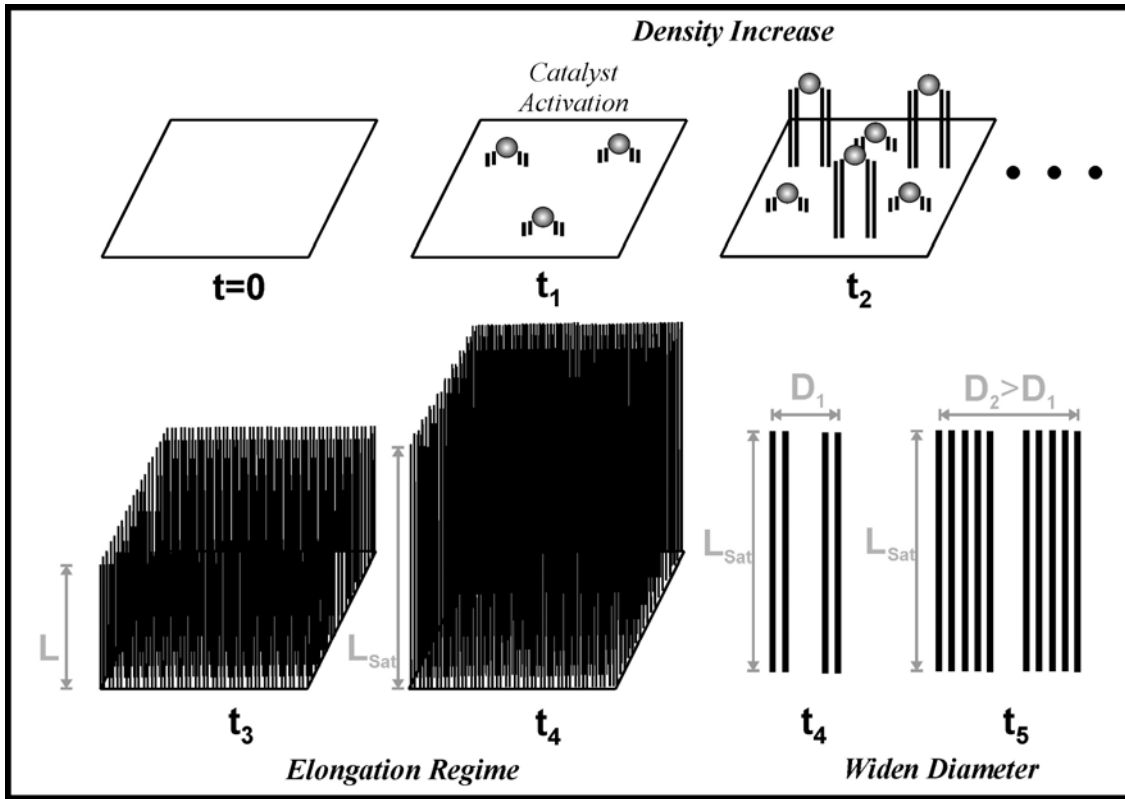


Figure 5.8: Schematic representation of the Growth Mechanism of multi walled CNTs by the aerosol CVD process. The reaction starts with a clean quartz substrate where iron particles start to develop the CNT growth (catalyst activation). As the first CNTs start growing, more iron aggregates keep catalysing new CNTs and therefore increasing the density of the arrays. When the density has increased a carpet-like array is obtained which keeps growing in length (elongation regime). Finally the catalysts stop their length growth and the CNTs keep widening their diameter.

5.4 1D Superlattices

This section describes the material obtained when the growth of non-doped (using toluene as precursor) and nitrogen-doped CNTs (using benzylamine as precursor) is continuously alternated during the CVD synthesis.

It should be noted, that while the first carbon source corresponds to a solution with the hydrocarbon solvent and ferrocene, the subsequent carbon source does not include any iron species (ferrocene) and only the hydrocarbon. This is important to remark, since the second stage of CNT synthesis is achieved using the iron catalyst coming from the Fe particles present in the CNTs produced in the first growing stage. This results in the formation of CNTs heterojunctions.

5.4.1 CNT heterojunction interfaces

The overall morphology of the heterojunction material obtained is shown in [Figure 5.9](#). Low magnification SEM micrographs ([Figure 5.9.a](#)) show the quality of the material obtained, which consists of carpet-like CNTs aggregates. [Figures 5.9.b-5.9.d](#) correspond to some of these carpets of CNTs, where there is marked separations (indicated by arrows) corresponding to the interface between the two segments composing the C-CNx heterojunctions.

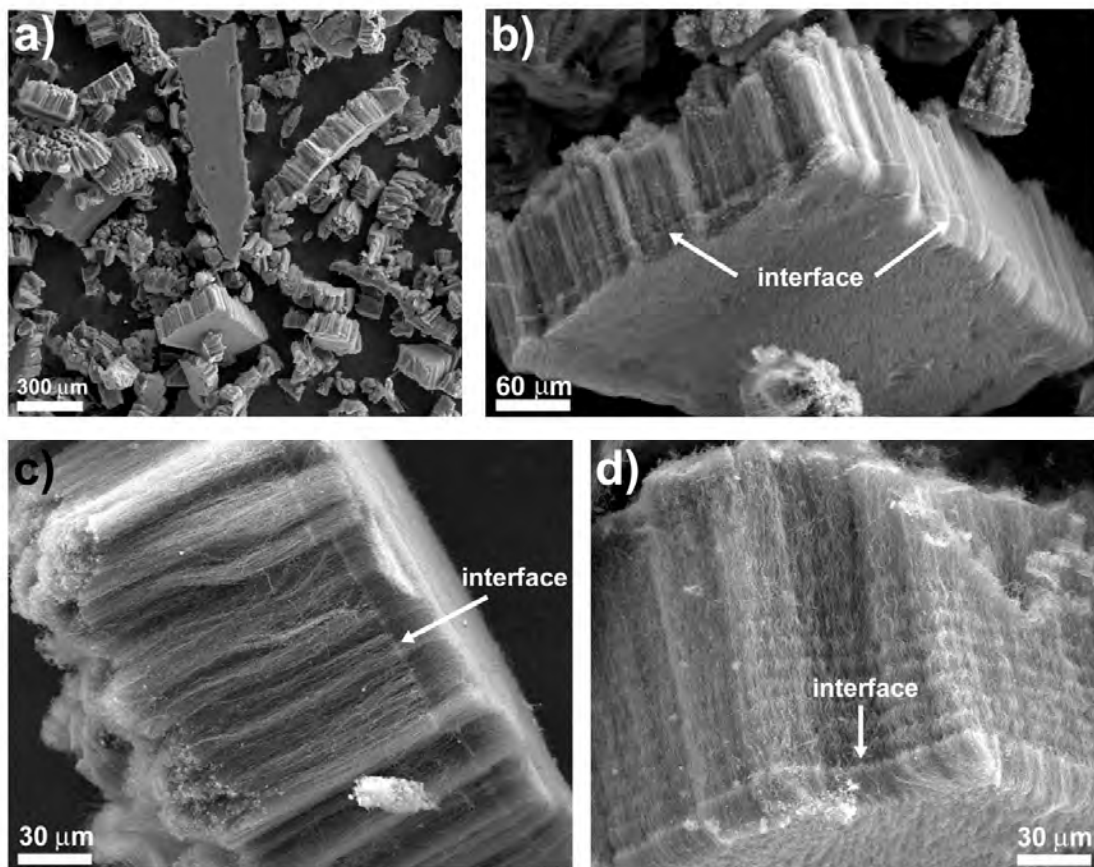


Figure 5.9: SEM images of aligned C-CNx heterojunction CNTs. a) overall morphology of the sample completely composed of carpet-like arrays; b)-d) typical carpet-like arrays where the C-CNx CNT interfaces (white lines) are marked by arrows.

5.4.1.a Continuity along the interface

Higher magnification SEM images presented in Figure 5.10, reveal the appearance of these interfaces. The zone marked in Figure 5.10.e, shows several continuous CNTs that appear at the interface, thus demonstrating the existence of heterojunctions composed of two different segments.

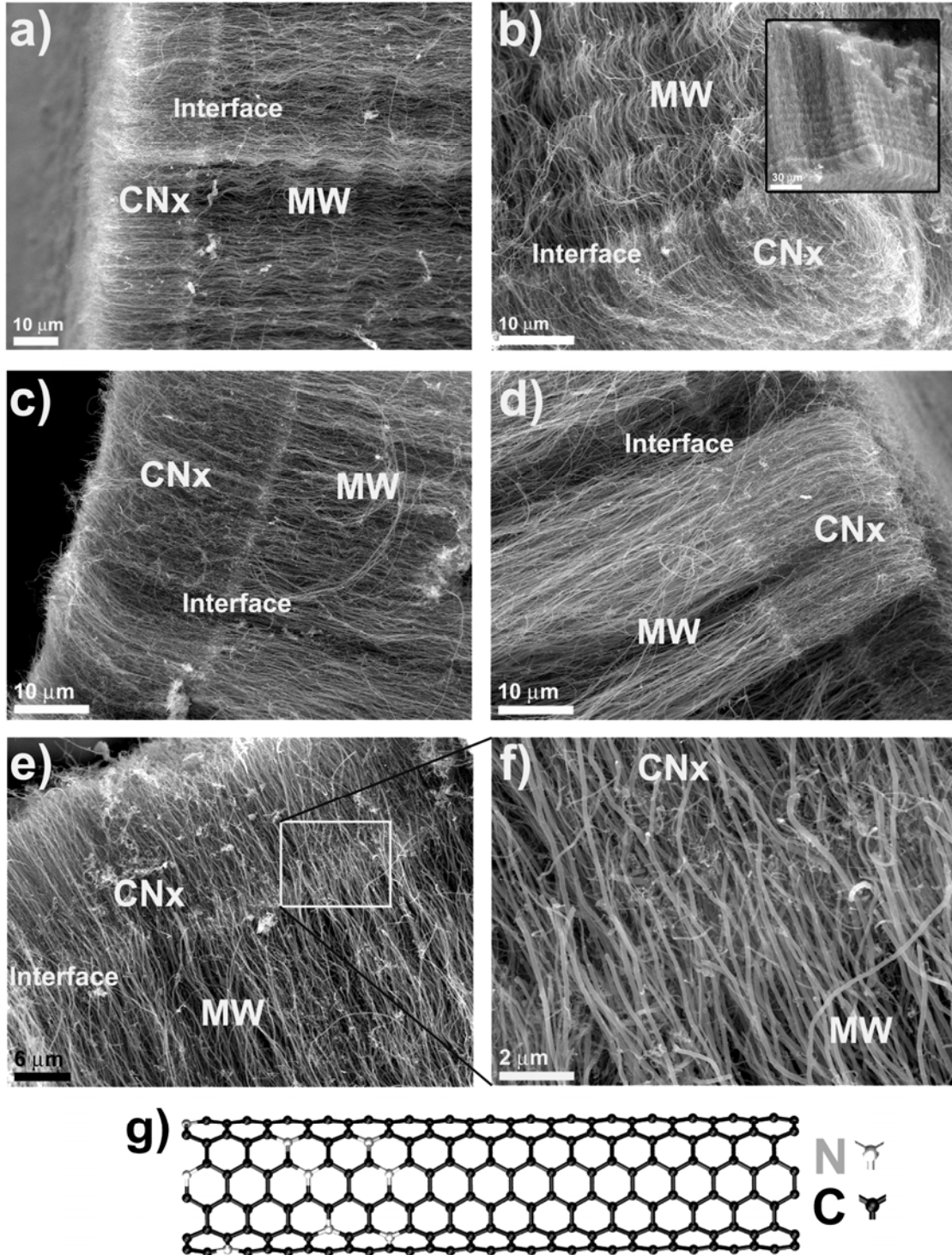


Figure 5.10: Higher magnification SEM micrographs showing the detailed structure of the interfaces. f) clearly shows continuity of several CNTs crossing the interface. g) corresponds to an atomic model illustrating a continuous C-CNx heterojunction.

In order to find further evidence regarding the heteroatomic interface, a statistic study measuring diameters was performed in the carpet-like aggregates. The first row in [Figure 5.11](#) shows the interface image, while [Figure 5.11.b](#) depicts a higher magnification image of the doped CNTs (CNx); the diameters were determined ([Figure 5.11.c](#)) presents a graph with a comparison between the diameters measurement obtained in the CNx side and the pristine CNx diameter distribution obtained from the calibration experiments (see subsection 5.4 and [Figure 5.7](#)) under exactly the same synthesis conditions (i.e. 8min reaction time). It is observed from [Figure 5.11.c](#) how the diameter distribution obtained in the superlattices sample is more populated with wider tubes (presumably influenced by growing from non-doped MW CNTs; see [Figure 5.7](#) in subsection 5.4). The second row ([Figure 5.11.d – 5.11.f](#)) plots a similar study in a different CNT carpet-like aggregate (the measurements were taken from zones at $\sim 5\mu\text{m}$ from the interface) showing an abrupt decrement in the population of thinner CNx nanotubes (when compared to the CNx nanotubes produced in non-intermittent CVD synthesis and which was used as calibration), while the distribution became drastically broader towards wider diameters, even reaching diameters usually observed only for non-doped CNTs (see [Figure 5.7](#) in subsection 5.4).

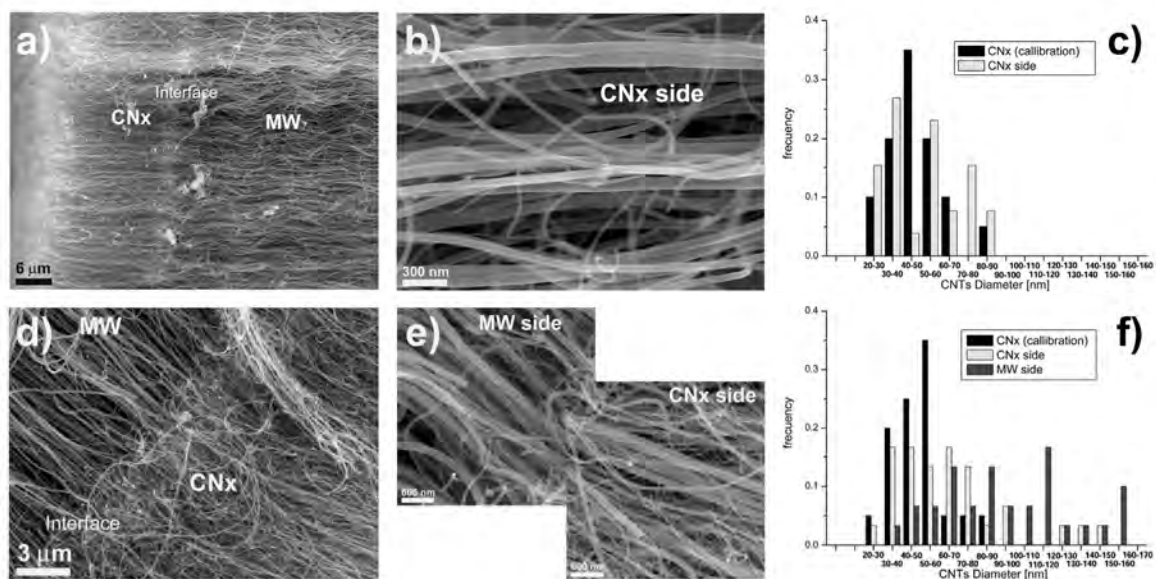


Figure 5.11: CNT diameters and distributions showing wider CNx segments, presumably induced by their growth from MW segments. a)-b) shows the SEM images from a CNx side; c) compares the diameters distribution of the CNx in a)-b) images with the CNx obtained during the calibration experiments. A similar comparison is performed in a different carpet-like array in d)-f) revealing wider CNx diameters when grown in a second stage from non-doped MW CNTs obtained in a previous synthesis stage.

This latter evidence suggests that the CNx segment is following the growth coming from the first synthesis stage of wider MW CNTs (see [Figure 5.7](#)).

5.4.1.b Elbow –like structures in C-CNx heteronanotubes.

Further evidence regarding the formation of C-CNx heterojunctions was obtained at the interface, where some elbow –like defects were observed. [Figure 5.12](#) shows SEM micrographs of such structures, which present an abrupt decrease in diameter at the interface. This is consistent with the shrinkage in diameters that is induced by the benzylamine (CNx CNTs are thinner than MW, as empirically observed from the calibration section; [see Figure 5.7](#)). Nevertheless, it should be noticed that the yield of such elbows was less than 5%, but represents complementary evidence confirming the existence of heteroatomic interfaces on the CNTs obtained from the I-CVD synthesis. These elbows could be forming when local growth conditions occur when exchanging the solvents.

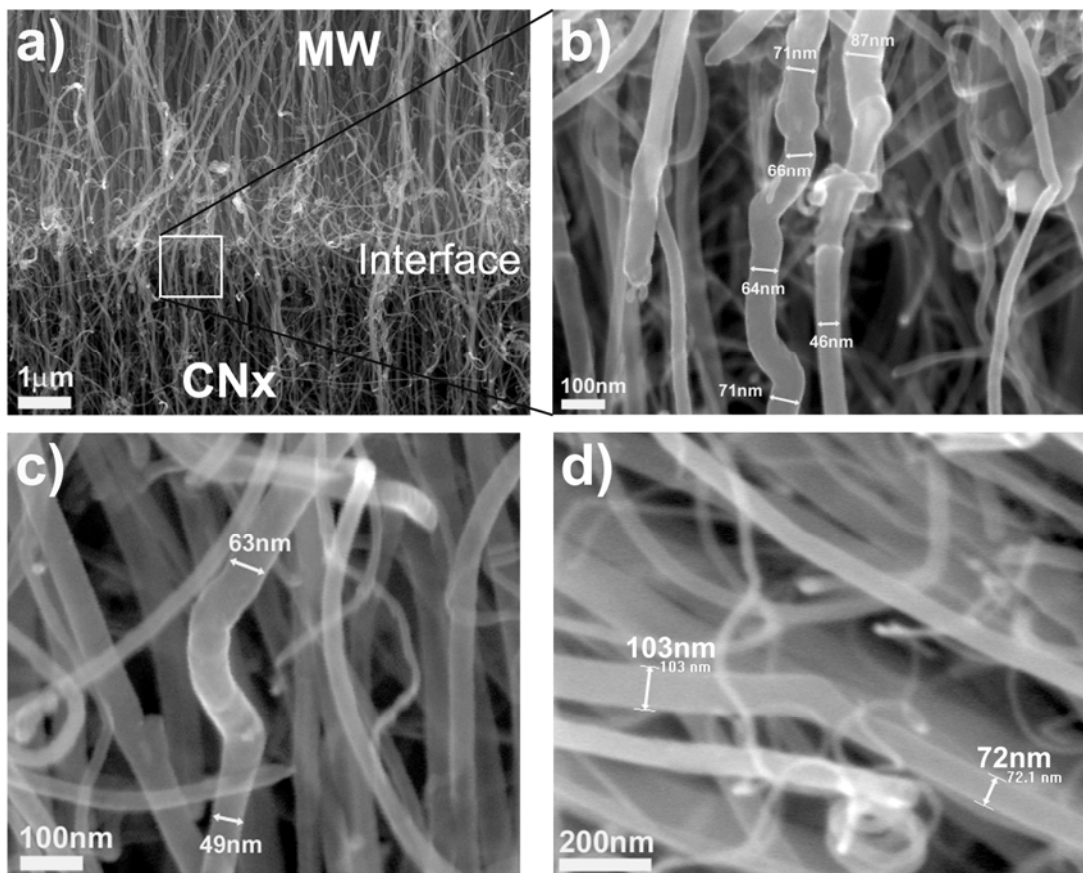


Figure 5.12: SEM images of elbow –like defects found at the interface zone, indicating an abrupt decrease in diameter along the CNT heterojunctions.

The TEM study was a challenge due to the lack of a reference to search for the interface zones. Nevertheless, some abrupt changes in diameter were observed along the same CNTs, as the one presented in [Figure 5.13.a](#). Some elbow-like features were also observed (see [Figure 5.13.b – 5.13.d](#)), and were studied structurally in more detail.

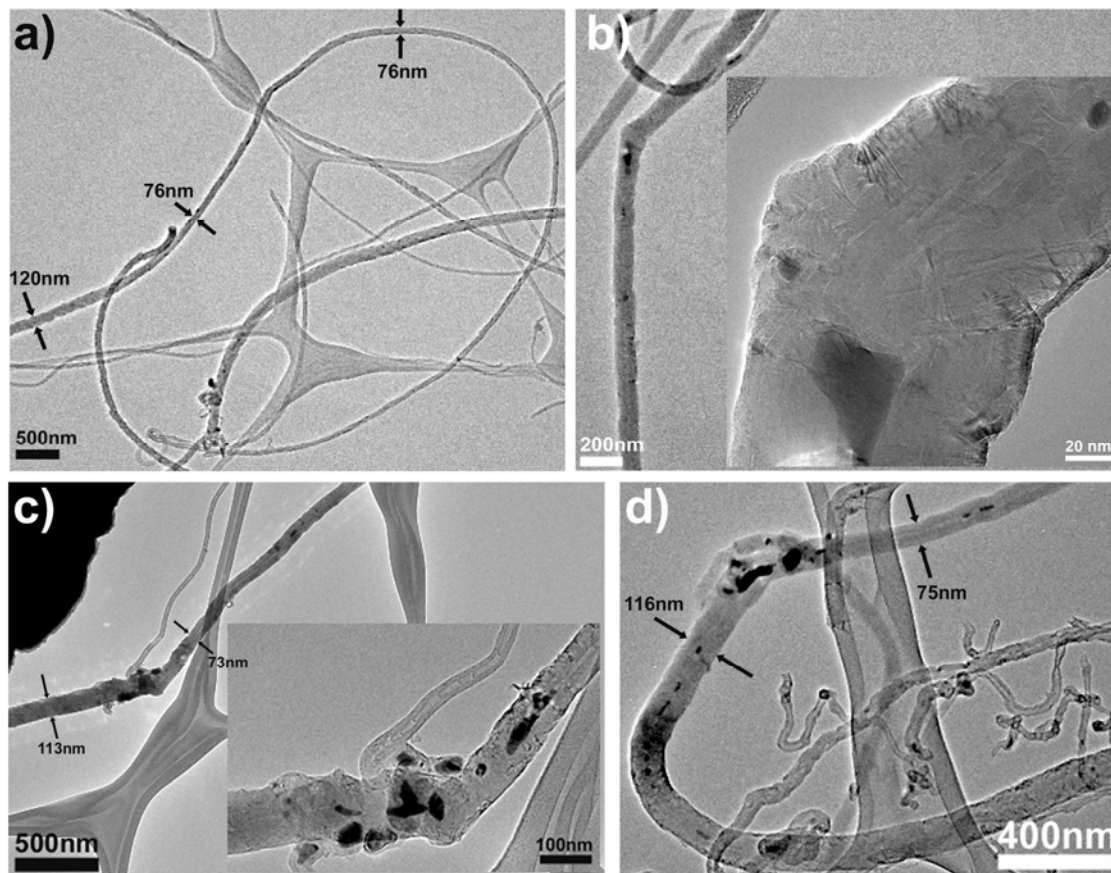


Figure 5.13: TEM micrographs showing in a) an abrupt decrement in diameter along the CNT; b)-d) elbow-like defective interface with change in diameter before and after the interface.

Besides the abrupt diameter change before and after the elbow feature, the high resolution structure of both segments was studied in order to obtain further insight into the formation mechanism of these defective interfaces.

A detailed structural study is presented in [Figure 5.14](#), where the side with the thicker segment is shown in [Figure 5.14.a](#) and [5.14.b](#) (from two HRTEM micrographs) being the zone in [Figure 5.14.b](#) the closest to the elbow region. [Figure 5.14.d](#) presents the structure of the thinner segment (presumably the CNx segment). The first point to stand out corresponds to the structural change from [Figure 5.14.a](#) where a hollow thick CNT is observed to [Figure 5.14.b](#) where more disordered graphite layers are observed in the zone closer to the elbow interface. The elbow interface is shown in [Figure 5.14.c](#) corresponding to a zone ~400nm long to finally continue with a thinner CNT segment with a hollow interior and some bamboo-like features starting to appear (marked by white arrows in [Figure 5.14.d](#)) characteristics of nitrogen doped CNTs [32]. These TEM observations suggest that

the MW segment starts growing as expected from the first stage of synthesis, and the introduction of the second source (in this case benzylamine) can create small zones of local turbulence causing some structurally disordered zones as starting in [Figure 5.14.b](#) and getting worse along the elbow interface until finally the flux gets stabilized to keep with the usual growth in the second stage of synthesis.

It should be noted that these heterojunctions have typical total lengths between $120\mu\text{m}$ - $160\mu\text{m}$ (see [Figure 5.9](#)), which makes this $\sim 400\text{nm}$ long interface to be less than 0.33% in length along the total superlattice.

Taking the data obtained from the calibration section (see [Figure 5.6](#)), a rough estimation provides a growing rate of $\sim 9\mu\text{m}/\text{min}$ and considering elbows interface lengths of the order of $\sim 400\text{nm}$, it would yield a turbulence reaction time of ~ 3 seconds (of course a rough estimation!!, since the synthesis kinetics totally would change without a stable flux).

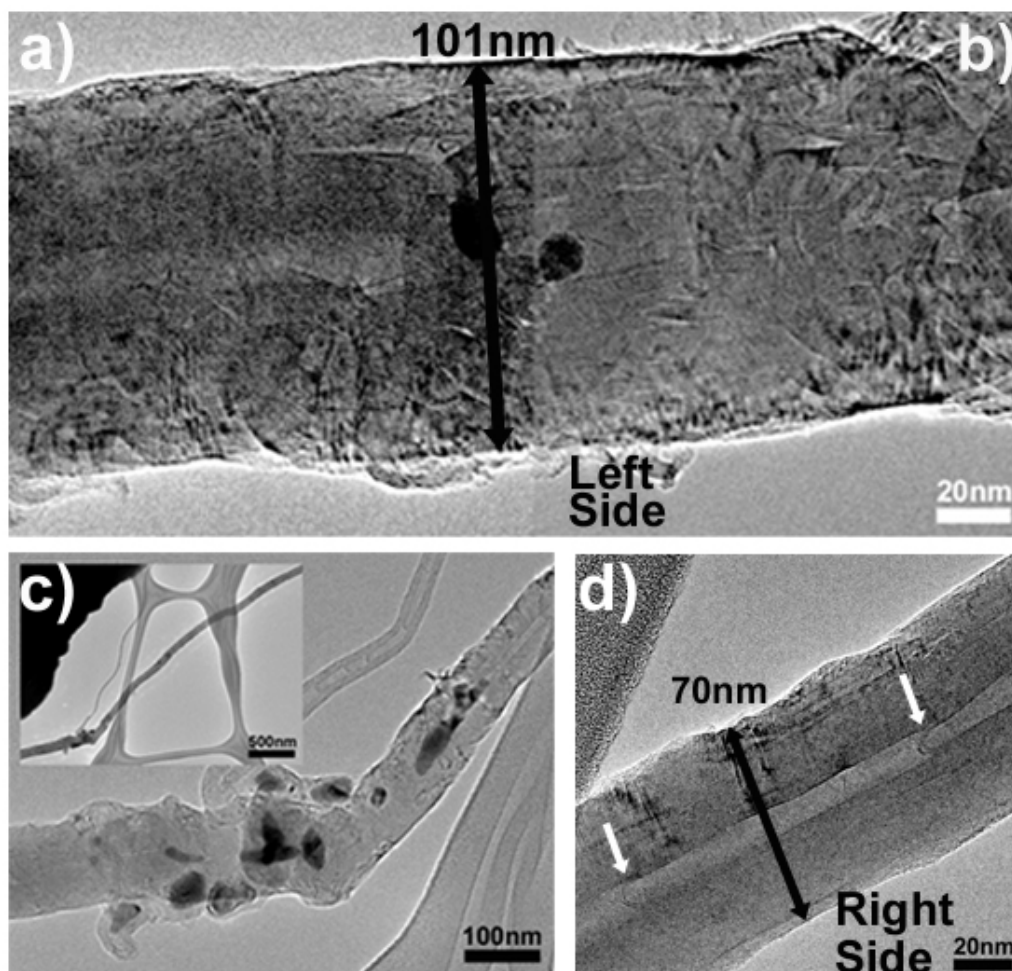


Figure 5.14: HRTEM micrographs showing the structure of the CNT before and after the elbow, showing in a) a hollow thick MW CNT which, presumably from turbulence, starts getting disordered in b) and finally into the defective interface c) (coming from left to right); then the CNT growth keeps going with bamboo-like features when the flux is stabilized back in d).

The use of a pure hydrocarbon solvent (without iron containing species) at the second stage of synthesis, complemented by the characterization evidence such as the higher magnification SEM micrograph showing continuity along the heterojunction zone (see Figure 5.10.f), together with the diameter statistics before and after the interface producing thicker CNx segments (see Figure 5.11), and the elbows –like features appearance (see Figure 5.12-5.14) at the interface allow to conclude the existence of covalent C-CN_x CNTs junctions.

5.4.2 Analytical (EDX) measurements

EDX analytical measurements were performed on different carpet –like arrays in order to demonstrate the nitrogen doping of certain segments of the 1D CNT Superlattice.

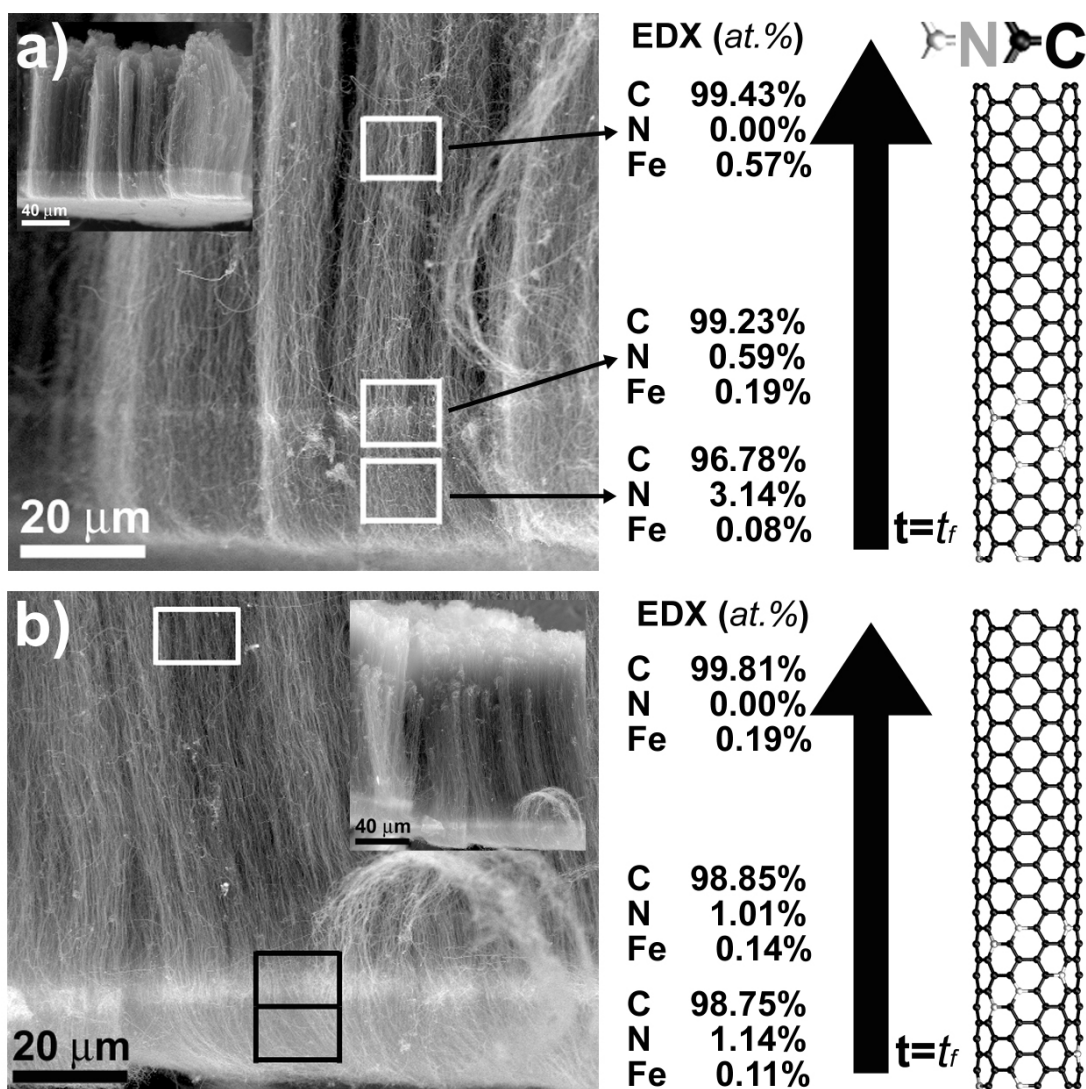


Figure 5.15: EDX measurement detects nitrogen content in the segment under the interface, where CN_x nanotubes were expected since benzylimine was the second synthesis stage reactant.

Figure 5.15 depicts measurements on samples obtained from an experiment performed with toluene and ferrocene at the first synthesis stage and only benzylamine during the second stage. The results clearly indicate the presence of nitrogen at the bottom of the carpet (Figure 5.15.a and 5.15.b). The measurement at the interface is consistent, detecting certain amount of nitrogen but in less quantity than in the CN_x portion.

The position of the segments reveal that the first stage reactants start the CNT growth upwards from the quartz substrate (as schematically represented in Figure 5.16 and indicated in Fig 5.15 by the black arrow on the right hand side); in this case the CN_x segment is located at the bottom (with a more flat ending as shown in Figure 5.15.a inset), confirming previous results on the kinetics of CNT growth [33].

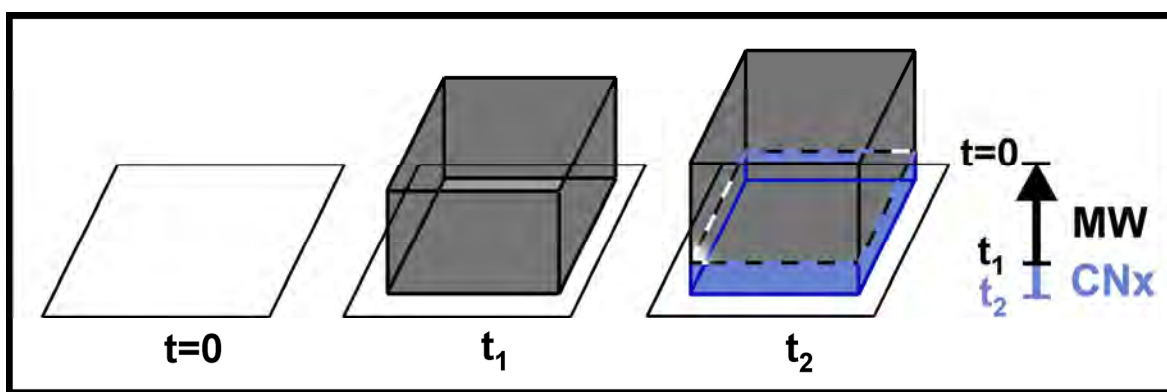


Figure 5.16: Schematic representation showing the spatial distribution of the CNTs segments in the heterojunctions as the reaction takes place during time.

Figure 5.17 shows EDX measurements on a sample obtained under different synthesis conditions, this time the first stage reactant corresponded to benzylamine and ferrocene while only toluene was used as the second stage reactant. Consistent with this, the higher amount of nitrogen was detected in the top zone while non nitrogen content was measured in the bottom zone. Interestingly, an abrupt interface was not detected an abrupt interface in this sample, while the nitrogen content was also measured to be decreasing (from top to bottom) continuously. This specific result, more than a Superlattice, represents CNTs with a nitrogen doping gradient along its length, which by itself should present interesting properties to study.

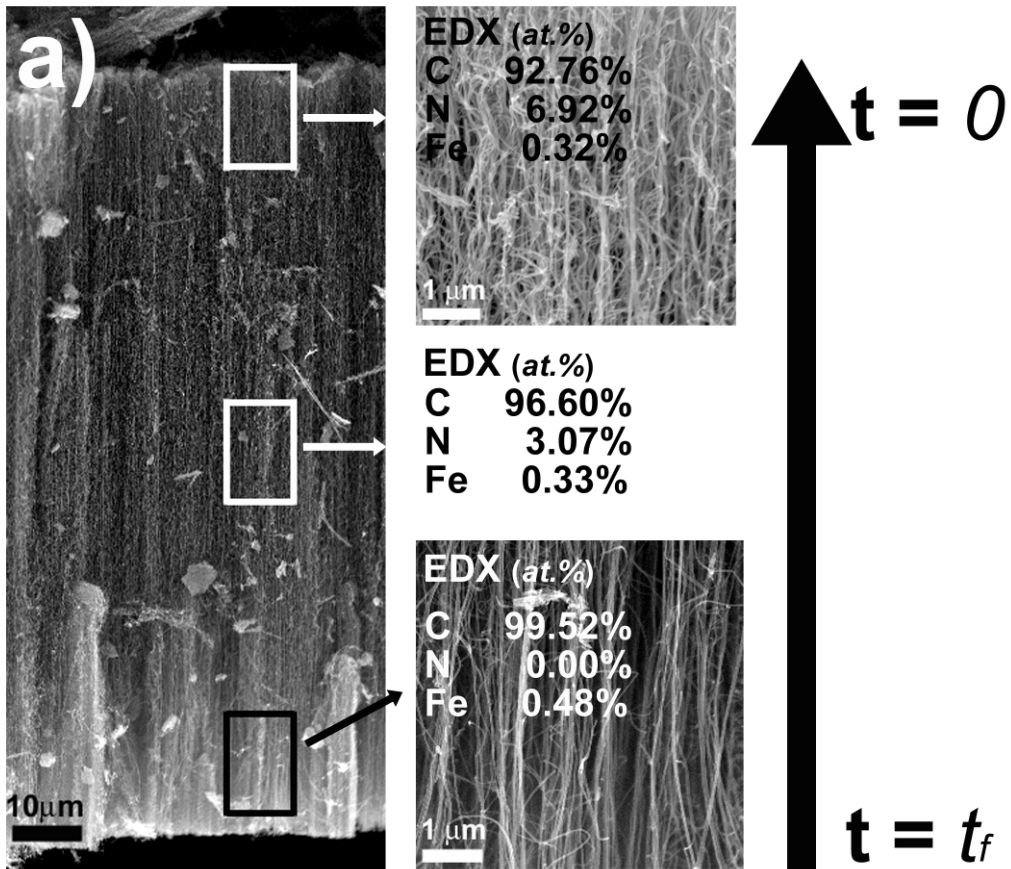


Figure 5.17: EDX measurement showing the presence of nitrogen at the top section where CNx were expected and the lack of N was found at the bottom section where non-doped MW appear. Abrupt heterojunctions were not detected in this case

5.4.3 Multiple segments

Finally, three segments were synthesized following a toluene/benzylamine/toluene sequence (Figure 5.18.a) and an inverse sequence of benzylamine/toluene/benzylamine (Figure 5.18.b). Figures 5.18.a1 and 5.18.a2 reveal interfaces dividing three different segments, while their EDX measurement indicated in Figure 5.18.a3 demonstrates that the highest nitrogen content is in the middle section; as expected. Figure 5.18.b1 shows an SEM micrograph of the carpet-like array with the longest segment (MW) in the middle, while Figure 5.18.b2 and 5.18.b3 present a close up at the upper interface showing the formation of continuous heterojunctions.

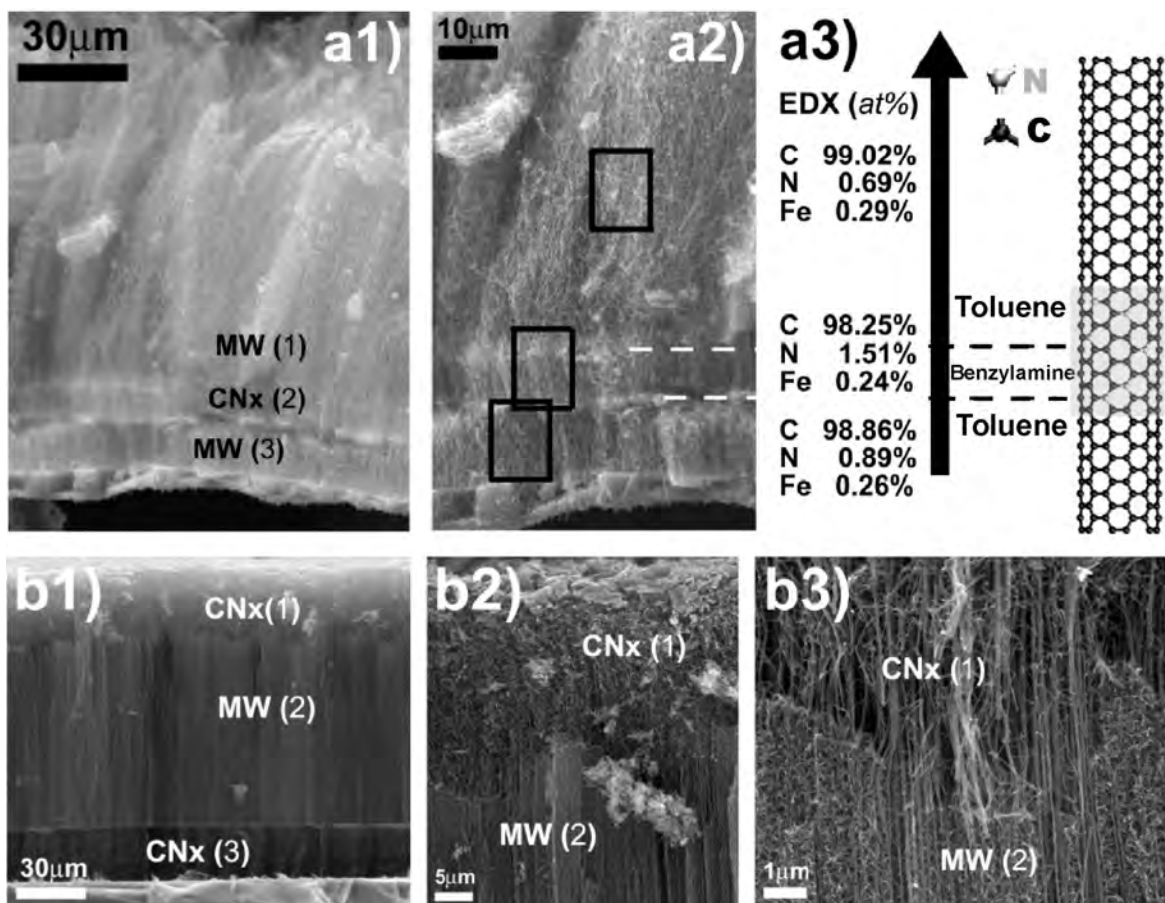


Figure 5.18: SEM images and EDX analyses of C-CNx-C and CNx-C-CNx heteronanotubes. The EDX measurements demonstrate the nitrogen presence in the expected CNx segment. An atomic model is presented to illustrate the intradvice obtained (a CNx segment) within the CNT in the middle region due to the N doping.

5.4.4 Failed experiments

The capability of the I-CVD method to synthesize different types of nanotube heterojunctions along 1D CNT Superlattices has been proved in the previous sections. Nevertheless, some failed experiments indicate crucial technical points that should be mentioned. The first corresponds to the hydrocarbon exchange during the CVD, which has to be done gently (when opening and closing valves) trying to avoid a big turbulence disturbance in the aerosol flux feeding the reactor. When the sources are abruptly exchanged, the turbulence could cause a lack of continuous heteronanotubes; in this case two independent carpets are formed (Figure 5.19.b). Nevertheless, a compromise should exist between a gentle change and trying to do it as fast as possible, since this would dictate the abruptness in interfaces along the superlattice.

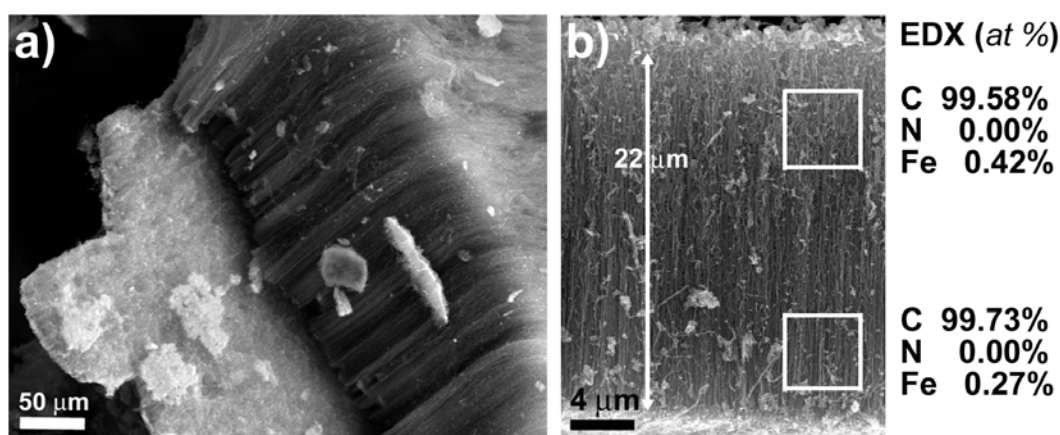


Figure 5.19: Representative results illustrating failed experiments.

Other failed experiments are shown in Figure 5.19.b. In this case the benzylimine/toluene interface was not clearly detected. In particular, the length of the carpet –like arrays ($\sim 20 \mu\text{m}$) correspond to a typical CN_x carpet length. Furthermore, when EDX measurements were performed, N was not detected. These three things together suggest that the incorporation of the toluene during the second synthesis stage should cover the CN_x nanotubes along the diameter, instead of maintaining the axial growth. Even when these are just preliminary results, they suggest that under appropriate synthesis conditions (trying to kill the catalyst to avoid further axial growth), radially modulated 1D CNT SLs could be achieved by the same I-CVD synthesis method.

5.5 Conclusions

An intermittent CVD method has been proposed to continuously alternate feeding sources during CVD synthesis to promote the formation of C-CN_x nanotube junctions.

A calibration stage was performed in order to obtain the most efficient synthesis parameters for the co-synthesis of MW and CN_x CNTs (resulting in 825°C and 2.5 l/min as the best temperature and carrier flux). This experimental stage allows to describe the MW and CN_x growth mechanism during the first 10 minutes of reaction, exhibiting first a density increased (catalyst activation) in the CNTs population within the carpet –like arrays, followed by a length increment of the CNTs (elongation regime [30-31]).

EDX studies confirm the presence of nitrogen on the CN_x segments, thus demonstrating the formation of CN_x-C NT interfaces. Furthermore, when appropriate alternation sequences of hydrocarbon sources are performed, multiple junctions are created.

The synthesis of these 1D Superlattices is not trivial and if experimental conditions are not carefully controlled the formation of unexpected structures can be obtained. For example, a gradual N-concentration along the CNT could be found and the formation of radial layers with different N-concentration are possible.

References

- [1] Hu, J., Ouyang, M., Yang, P. & Lieber C.M. Controlled growth and electrical properties of heterojunctions of carbon nanotubes and silicon nanowires. **Nature** **399**, 48-51 (1999).
- [2] Zhang, Y., Ichihashi, T., Landree, E., Nihey, F. & Iijima, S. Heterostructures of Single-Walled Carbon Nanotubes and Carbide Nanorods. **Science** **285**, 1719-1722 (1999).
- [3] Lauhon, L.J., Gudiksen, M.S. & Lieber, C.M. Semiconductor nanowire heterostructures. **Phil. Trans. R. Soc. Lond. on A** **362**, 1247-1260 (2004).
- [4] Gudiksen, M.S., Lauhon, L.J., Wang, J., Smith, D.C. & Lieber, C.M. Growth of nanowire superlattice structures for nanoscale photonics and electronics. **Nature** **415**, 617-620 (2002).
- [5] Wu, Y., Fan, R. & Yang, P. Block-by-block Growth of Single-Crystalline Si/SiGe Superlattice Nanowires. **Nano Lett.** **2** (2), 83-86 (2002).
- [6] Björk, M.T., *et al.* One-dimensional heterostructures in semiconductor nanowhiskers. **Appl. Phys. Lett.** **80** (6), 1058-1060 (2002).
- [7] Yang, C., Zhong, Z. & Lieber, C.M. Encoding Electronic Properties by Synthesis of Axial Modulation-Doped Silicon Nanowires. **Science** **310**, 1304-1307 (2005).
- [8] Lauhon, L.J., Gudiksen, M.S., Wang, D. & Lieber, C.M. Epitaxial core-shell and core-multishell nanowire heterostructures. **Nature** **420**, 57-61 (2002).
- [9] Hu, J., *et al.* Epitaxial Heterostructures: Side-to-Side Si-ZnS, Si-ZnSe Biaxial Nanowires, and Sandwichlike ZnS-Si-ZnS Triaxial Nanowires. **J. Am. Chem. Soc.** **125**, 11306-11313 (2003).
- [10] Smorodin, T., Beierlein, U. & Kotthaus, J.P. Contacting gold nanoparticles with carbon nanotubes by self-assembly. **Nanotechnology** **16**, 1123-1125 (2005).
- [11] Milliron, D.J., *et al.* Colloidal nanocrystal heterostructures with linear and branched topology. **Nature** **430**, 190-194 (2004).
- [12] Chico, L., *et al.* Pure Carbon Nanoscale Devices: Nanotube Heterojunctions. **Phys. Rev. Lett.** **76** (6), 971-974 (1996).
- [13] Dunlap, B.I. Relating carbon tubules. **Phys. Rev. B** **49** (8), 5643-5650 (1994).
- [14] Collins, P.G., Zettl, A., Bando, H., Thess, A. & Smalley, R.E. Nanotube Nanodevice. **Science** **278**, 100-103 (1997).
- [15] Yao, Z., Postma, H.W.Ch., Balents, L. & Dekker, C. Carbon nanotube intramolecular junctions. **Nature** **402**, 273-276 (1999).
- [16] Saito, R., Dresselhaus, G. & Dresselhaus, M.S. Tunneling conductance of connected carbon nanotubes. **Phys. Rev. B** **53** (4), 2044-2050 (1996).
- [17] Charlier, J.-C., Ebbesen, T.W. & Lambin Ph. Structural and electronic properties of pentagon-heptagon pair defects in carbon nanotubes. **Phys. Rev. B** **53** (16), 11108-11113 (1996).
- [18] Chico, L., Benedict, L.X., Louie, S.G. & Cohen M.L. Quantum conductance of carbon nanotubes with defects. **Phys. Rev. B** **54** (4), 2600-2606 (1996).
- [19] Meunier, V., Senet, P. & Lambin, Ph. Scanning tunneling spectroscopy signature of finite-size and connected nanotubes: A tight-binding study. **Phys. Rev. B** **60** (11), 7792-7795 (1999).
- [20] Ouyang, M., Huang, J.-L., Cheung, C.L. & Lieber, C.M. Atomically Resolved Single-Walled Carbon Nanotubes Intramolecular Junctions. **Science** **291**, 97-100 (2001).
- [21] Kim, H., *et al.* Direct Observations of Localized Defect States in Semiconductor Nanotube Junctions. **Phys. Rev. Lett.** **90** (21), 216107 (2003).
- [22] Fa, W., Chen, J., Liu, H. & Dong, J. Structural and electronic properties of the metal-metal intramolecular junctions of single-walled carbon nanotubes. **Phys. Rev. B** **69**, 235413 (2004).
- [23] Son, Y.-W., Lee, S.B., Lee, C.-K. & Ihm, J. Electronic structure of straight semiconductor-semiconductor carbon nanotube junctions. **Phys. Rev. B** **71**, 205422 (2005).
- [24] Lu, W., Wang, E.G. & Guo, H. Quantum conductance of a carbon nanotube superlattice. **Phys. Rev. B** **68**, 075407 (2003).
- [25] Zhang, Z., Guo, W. & Tai, G. Coaxial nanocable: Carbon nanotube core sheathed with boron nitride nanotube. **Appl. Phys. Lett.** **90**, 133103 (2007).

- [26] Zhou, C. Kong, J., Yenilmez, E. & Dai, H. Modulated Chemical Doping of Individual Carbon Nanotubes. **Science** **290**, 1552-1555 (2000).
- [27] Derycke, V., Martel, R., Appenzeller, J. & Avouris, Ph. Carbon Nanotube Inter- and Intramolecular Logic Gates. **Nano Lett.** **1** (9), 453-456 (2001).
- [28] Wei, D., *et al.* A New Method to Synthesize Complicated Multibranched Carbon Nanotubes with Controlled Architecture and Composition. **Nano Lett.** **6** (2), 186-192 (2006).
- [29] Mayne, M., *et al.* Pyrolytic production of aligned carbon nanotubes from homogeneously dispersed benzene-based aerosols. **Chem. Phys. Lett.** **338** (2-3), 101-107 (2001).
- [30] Dresselhaus, M.S., Dresselhaus, G., Sugihara, K., Spain, I.L. & Goldberg, H.A. Graphite Fibers and Filaments. **Springer-Verlag**, Berlin Heidelberg (1988).
- [31] Endo, M. & Koyoma T. **Kotai Butsuri** **12**, 1 (1977) [*in Japanese*].
- [32] Sumpter, B.G., *et al.* The Importance of Nitrogen in Carbon Nanotube Growth: Narrow Diameter Metallic Tubes, Dispersible Bundles and Bamboo-like morphologies. **ACS Nano** **1** (4): 369-375 (2007).
- [33] Li, X., Cao, A., Jung, Y.J., Vajtai, R. & Ajayan, P.M. Bottom-Up Growth of Carbon Nanotube Multilayers: Unprecedented Growth. **Nano Lett.** **5** (10), 1997-2000 (2005).



Perspectives

The main proposal of assembling 2D and 3D ordered arrays from 1D building blocks, developed during the present project, motivates further research work with the vast range of combinations that building block composition, length and diameter, architecture type and dimensionality offer to explore combining creativity and scientific knowledge.

Specifically, the experiments and calculations presented here open new questions to work on in the near future. On the experimental side, CNT Y-junctions with concentric cylinders structure (see Figures 4.15 and 4.16) were observed instead of the commonly reported cone stacked (see Figures 4.32.b and 4.33) structure of Y-junctions. This was obtained when using ferrocene (FeCp_2) instead of nickelocene (NiCp_2) under the presence of thiophene (experiment details in Section 4.2). Nevertheless, the yield of such nanostructures is low (less than 5%) along the average sample; this result suggests a synthesis study in order to improve the yield of this type of nanostructures which should have properties closer to CNTs than the cone stacked structure characteristic of carbon fibres. Even more, a second project would be a state of the art high resolution characterization, in order to elucidate the junction formation in this type of nanostructures. A first effort was presented here (see Section 4.3.3.2), when analyzing composition of the catalyst generating the junctions (see Figure 4.17), resulting in an iron sulfide (FeS); the high resolution structure of the junction and its correlation with its catalyst particle trapped right and the junction point (see Figure 4.18) was studied, nevertheless to accurately obtain the crystallographic phase of the catalyst more HRTEM and electron diffraction pattern are needed and further in-situ TEM studied should be performed in order to obtain a better insight into the junction formation mechanism and the role that sulfur and the crystallographic array of the catalyst particle is playing in the CNT junction formation.

Another result from the same chapter was the obtention of particles with domains of metallic nickel and domains of nickel sulfide (see Figures 4.10, 4.11, 4.27 and 4.28) coexisting in the same cluster. This samples should work to perform HRTEM in-situ experiments with beam irradiation to analyze the sulfur diffusion along metallic nickel and the formation of nickel sulfides. Certainly the project developed in chapter 4 shows the importance of sulfur in carbon samples, promoting highly curved morphologies, which motivates further work around sulfur (thiophene) and carbon nanostructures.

Regarding the project presented in chapter 5, the production of CNTs 1D Superlattices, varying the composition along the axis of the tube presents samples with potential electronic properties to be explored. This type of nanostructures suggest the presence of electronic intradevices along the nanowire, which could be study experimentally by STM (scanning tunneling microscopy) techniques. This correlates directly with a theoretical study to simulate the electronic structure and electronic transport properties at the interface of a CNT heterojunction of nitrogen doped and undoped tubes to completely understand the phenomenon.

It has been proved in chapter 4 the crucial role that sulfur (thiophene) plays in the branching formation obtained in carbon nanostructures, while chapter 5 has

presented an experimental setup to intermittently modify the chemical gases into the CVD reactor; therefore combining both ideas suggest further synthesis studies by the intermittent incorporation of the sulfur agent into the CVD reactor to have a better control in the branching phenomenon during the experiment.

On the calculations side, the electronic properties studied during the present project have focused on individual nodes, the next step would be to analyse the transport properties when one of this nodes is surrounded by similar nodes (i.e. include the presence of neighbor nodes in the simulations), to compare the differences. On this line we have started some calculation and the study is in progress. One of the main problems of including several nodes in a simulation comes from the computational cost, since the atomic systems increase considerably their amount of atoms and therefore become hard to compute. To tackle this problem, we have started working in a theoretical formalism including the Scattering Matrix, to mathematically interconnect different nodes; this approach would allow to accurately calculate the scattering matrix of a single node (or basic block) with computational expensive methods such as first principle calculations; and once obtained its matrix (which includes all the transport information needed from the block) it can be connected or propagated to different nodes by simple linear algebra operations.

An interesting scenario to simulate would be the physico-chemical properties of ON-CNTs when doping agents (such as sulfur or nitrogen) are present in the networks, since the experiments reveal the presence of such chemical agents in the carbon nanostructures.

It is known that CNTs can be doped by different chemical agents such as nitrogen, boron, phosphorous or sulfur; and they seem to stabilize differently along the sp^2 carbon network of the nanotubes. An important question to elucidate would be to understand how the hybridization of doping agent and carbon atoms in the sp^2 network is performed to see how it influences the formation of pentagon, hexagon or heptagon rings and therefore the type of curvature that would be favoured by different type of chemical doping agents.

A major challenge to be achieved in the near future is the controlled production of experimental ON-CNTs. Along this line, the most efficient approach in our opinion corresponds to a two-steps method: where the first problem corresponds to the ordered assembly of the CNTs, and once correctly assembled them to interconnect them covalently. CNTs can be coalesced (merged covalently) by irradiation at high temperatures (e.g. Terrones M., *et al.* [Phys.Rev.Lett.](#) **89** (7), 075505; 2002) or by using atomic welders (e.g. B atoms) during heat treatments (e.g. Endo M., *et al.* [Nano Lett.](#) **5**, 1099-1105; 2005). On this line, we have started working in collaboration with E. Alvizo-Paez and the IFUASLP on the assembling of multi walled CNTs by langmuir-blodgett techniques; while M. Hofmann at Prof. M. Dresselhaus group in MIT, have developed an in-situ approach during CVD synthesis to obtain monolayers with horizontally aligned bundles of SWNTs. This two collaborations are works to be followed, in order to expose the obtained assemblies to ion irradiation or heat treatments toward obtaining experimental covalently bonded 2D and 3D CNTs networks.

➤ Research Articles

The results exposed along the chapters of the present thesis are being reported in research articles submitted to scientific journals:

- Romo-Herrera, J.M., Terrones, M., Terrones, H., Dag, S. & Meunier, V. "Covalent 2D and 3D Networks from 1D Nanostructures". **NanoLetters** **7(3)**: 570-576 (2007).
- Romo-Herrera, J.M., Sumpter, B.G., Cullen, D.A., Terrones, H., Cruz-Silva, E., Smith, D.J., Meunier, V. & Terrones, M. "An Atomistic Branching Mechanism for Carbon Nanotubes: Sulfur as triggering agent". (in press; **Angewante Chemie**).
- Romo-Herrera, J.M., Terrones, M., Terrones, H. & Meunier, V. "Transport properties of ordered networks based on carbon nanotubes (ON-CNTs)". (submitted).
- Romo-Herrera, J.M., Terrones, H., Terrones, M., & Meunier, V. "Defects engineering in ON-CNTs: guiding current". (to be submitted).
- Romo-Herrera, J.M., Cruz-Silva, E., Cullen, D.A., Terrones, H., Smith, D.J. & Terrones, M. "Temperature gradient and flux effect effect in the Pyrolysis of Thiophene and Nickelocene: from sea urchin -like nanostructures to five different types of Y-junctions". (to be submitted).
- Romo-Herrera, J.M., Zamudio, A., Cruz-Silva, E., Cullen, D.A., Smith, D.J., Terrones, H., Terrones, M., "1D Superlattices from nitrogen-doped and undoped CNTs segments". (in progress).

During the development of the present Ph.D. project in Prof. M.Terrones and Prof. H.Terrones group at IPICYT, research collaborations with groupmates turned out in scientific articles:

- J.J. Velásquez-Salazar, E. Muñoz-Sandoval, J.M. Romo-Herrera, F. Lupo, M. Rühle, H. Terrones and M. Terrones. "Synthesis and State of The Art Characterization of BN bamboo-like nanotubes: Evidence of a root growth mechanism catalyzed by Fe". **Chem. Phys. Lett.** **416**: 342-348 (2005).
- M. Terrones, J.M. Romo-Herrera, E. Cruz-Silva, F. López-Urías, E. Muñoz-Sandoval, J.J. Velásquez-Salazar, H. Terrones and Y. Bando. "Pure and Doped BN Nanotubes: Recent Synthetic Achievements and Perspectives". **Materials Today** **10(5)**: 30-38 (2007).
- B.G. Sumpter, V. Meunier, J.M. Romo-Herrera, E. Cruz-Silva, D.A. Cullen, H. Terrones, D.J. Smith and M. Terrones. "The Importance of Nitrogen in Carbon Nanotube Growth: Narrow Diameter Metallic Tubes, Dispersible Bundles and Bamboo-like morphologies". **ACS Nano** **1(4)**: 369-375 (2007).
- A.R. Botello-Méndez, J. Campos-Delgado, A. Morelos-Gómez, J.M. Romo-Herrera, A.G. Rodríguez, H. Navarro, M.A. Vidal, H. Terrones and M. Terrones. "Controlling the Dimensions, Reactivity and Crystallinity of Multiwalled Carbon Nanotubes using Low Ethanol Concentrations". **Chem. Phys. Lett.** **453**: 55-61 (2008).
- J.L. Hernández-López, E.R. Alvizo-Páez, J.M. Romo-Herrera, H. Terrones, M. Terrones and J. Ruiz-García. "Soft Purification of Nitrogen-Doped Multi-Walled Carbon Nanotubes". (in press; **Nanotechnology**).
- E. Cruz-Silva, D.A. Cullen, L. Gu, J.M. Romo-Herrera, E. Muñoz-Sandoval, F. López-Urías, B.G. Sumpter, V. Meunier, J.-C. Charlier, D.J. Smith, H. Terrones and M. Terrones. "Hetero-doped Nanotubes: Theory, Synthesis and Characterization of Phosphorus-Nitrogen Doped Multiwalled Carbon Nanotubes". (in press; **ACS Nano**).